Numerical Modelling of Structural Patterns in Tectonic Flow with Applications to the Neoarchean Crustal Dynamics

by

Qǐháng Wú

A thesis
presented to the University of Waterloo
in fulfilment of the
thesis requirement for the degree of
Doctor of Philosophy
in
Earth Sciences

Waterloo, Ontario, Canada, 2024

© Qǐháng Wú 2024

Examining Committee Membership

The following served on the Examining Committee for this thesis. The decision of the Examining Committee is by majority vote.

External Examiner:
Dazhi Jiang
Professor
Dept. of Earth Sciences
Western University

Supervisor(s):
Shoufa Lin
Professor
Dept. of Earth and Environmental Sciences
University of Waterloo

Internal Member(s):
André Unger
Associate Professor
Dept. of Earth and Environmental Sciences
University of Waterloo

Chris Yakymchuk
Associate Professor
Dept. of Earth and Environmental Sciences
University of Waterloo

Internal-External Member:
Shunde Yin
Associate Professor
Dept. of Civil and Environmental Engineering
University of Waterloo

Author's Declaration

This thesis consists of material all of which I authored or co-authored: see Statement of Contributions included in the thesis. This is a true copy of the thesis, including any required final revisions, as accepted by my examiners.

I understand that my thesis may be made electronically available to the public.

Statement of Contributions

Qǐháng Wú was the sole author for Chapters 1 and 5 which were written under the supervision of Dr. Shoufa Lin and were not written for publication. This thesis consists in part of three manuscripts written for publication. Exceptions to sole authorship of the material are as follows:

Research presented in Chapter 2:

This research is conducted by Qǐháng Wú under the supervision of Dr. Shoufa Lin and Dr. André Unger. Qǐháng Wú and Dr. Shoufa Lin conceptualized the end goal of the numerical model. Qǐháng Wú wrote the programming code for this study. Dr. André Unger contributed to the methodology, optimization and testing of the programming code. Qǐháng Wú wrote the draft manuscript, which all co-authors contributed intellectual input on.

Publication based on this chapter:
Wú, Q., Lin, S., & Unger, A. (2023). Modelling multi-material structural patterns in tectonic flow with a discontinuous Galerkin level set method. *Journal of Geophysical Research: Solid Earth*, 128, e2023JB026806.

Research presented in Chapter 3:

This research was conducted under the supervision of Dr. Shoufa Lin. The field component of this research was logistically supported by the Ontario Geological Survey under the supervision of Thomas Gemmell and Sonia Préfontaine. Qǐháng Wú collected the field data and performed the structural analysis. Qǐháng Wú set up the numerical model and interpreted the model results under the supervision of Dr. Shoufa Lin and Dr. André Unger. Qǐháng Wú wrote the draft manuscript.

Research presented in Chapter 4:

This research is conducted by Qǐháng Wú under the supervision of Dr. Shoufa Lin. Qǐháng Wú and Dr. Shoufa Lin conceptualized the end goal of the numerical model. Qǐháng Wú set up the numerical model under the supervision of Dr. André Unger and performed computations on the computation facilities of the Digital Research Alliance of Canada (alliancecan.ca). Dr. Chris Yakymchuk provided guidance on the rheological and thermal conditions applied in the numerical model. Qǐháng Wú interpreted the modelling results and the geological significance with the guidance of Dr. Shoufa Lin. Qǐháng Wú wrote the draft manuscript.

Abstract

We formulate a numerical framework, in both 2d and 3d, to model the structural patterns emerging from viscous tectonic flow by coupling a level set description of the material interface with a finite element flow solver. Our formulation has the advantage of straightforward extensibility to encompass complex rheology and versatile mesh geometry, as well as improved computational efficiency. A distinct novelty of our formulation is the capability to offer a fully dynamical approach to modelling structural patterns resulting from an inhomogeneous and non-steady tectonic flow. The model output, in the form of lithological distribution and deformation patterns, can be directly compared with the results of based geological mapping and structural analysis, thus offering the opportunity to ground-truth the abstract numerical models with concrete field observations.

As examples for the potential applications of our method, we apply our newly developed method to the modelling of the crustal dynamics of the Neoarchean granitoid-greenstone terranes in two case studies to shed light on the potential vertical- to horizontal-style tectonics. In the first case study, a field-based structural study is conducted in the Swayze greenstone belt in the Superior Craton and four generations (G_1–G_4) of ductile deformations are identified. Among them, G_2 structures are associated with an oblique shearing kinematics with a granitoid-up/greenstone-down movement in the vertical direction and a dextral sense of shear in the horizontal direction, as well as an opposing plunge directions of L_2 stretching lineation. The tectonic regime associated with G_2 is interpreted to be the operation of vertical-style tectonism in the form of sagduction/diapirism under the backdrop of horizontal-style tectonism in the form of regional dextral simple shearing. To test this interpretation, an isothermal numerical model is constructed for the Swayze greenstone belt. The model replicates the observed lithological and deformation pattern, confirming the synchronous vertical and horizontal tectonism model as a viable regime to explain the observed structural patterns.

To further explore whether the synchronous vertical and horizontal tectonism is applicable to the Neoarchean crustal dynamics in general, a thermomechanical model is constructed in the second case study with both thermal and rheological conditions appropriate for the Neoarchean granitoid-greenstone terranes. As in the first case study, many aspects of the crustal architecture and structural patterns are comparable to the observations in Neoarchean terranes worldwide. Due to the high competency of the cold upper crust, the density-induced sinking of the supracrustal assemblages into the granitoid domes operates by active diachronous pointwise "dripping" at triple junctions or by sheet-like sagduction with higher rate of horizontal

shearing. Furthermore, the transitional process of the crustal dynamics towards the modern-day conditions from the hotter Archean Earth is further explored by systematically decreasing the Moho heat flux, which results in a delayed initiation and a slower rate of the vertical tectonic process. The increase in the horizontal strain rate results in the promotion of sheet-like sagduction pattern, the elongation of granitoid domes, the preferential alignment of the high strain zones and the reduction of the rate of greenstone sagduction. It is therefore postulated that through the secular cooling of the crustal thermal condition, the role of density-induced sagduction/diapirism is suppressed, thereby completing the transition of the Earth's crustal dynamics from a dominantly vertical style in the early Earth's history to a present-day dominantly horizontal style, with the Neoarchean being the interlude period where both processes coexisted. Furthermore, taking into account that the Neoarchean lithospheric dynamics of the southeastern Superior Craton is interpreted to be terrane accretion under a plate tectonics-like regime, we conclude that the synchronous horizontal and vertical crustal dynamics is not contradictory to a framework of plate tectonics on a lithospheric scale. In fact, the Neoarchean transition in crustal dynamics may mirror a similar transition in lithospheric dynamics from the early stagnant-lid tectonics to the modern day plate tectonics.

Acknowledgements

First and foremost, I would like to extend my gratitude to my advising committee for the patience and dedication through the years. Thank you to Dr. André Unger for the discussions on numerical methods and introducing me to the techniques of linear solvers so that I can solve my modelling problems within my lifetime. Thank you to Dr. Chris Yakymchuk for the stimulating discussion on Archean thermal and rheological regimes. Most importantly, thank you to Dr. Shoufa Lin for your unwavering support and your insightful guidance. Your confidence in me has always been my inspiration to carry on even in the most difficult times.

I would like to extend my gratitude to Dr. Jian Zhang for showing me the fascinating subject of structural geology and introducing me to basic techniques of field-based structural analysis. Thank you to Dr. Bruno Lafrance for the field course in structural mapping, where I was thoroughly taught to identify and map overprinting relationships in a greenstone belt context for the first time.

Thank you to my colleagues and friends at the Ontario Geological Survey: Gary Beakhouse, Thomas Gemmell, Evan Hastie, Peter MacDonald and Sonia Préfontaine for the field training, logistic support as well as the stimulating discussions in the field. I would also like to thank my field crew for bearing with me and patiently showing me everything about the woods of the northern Ontario.

Thank you to my friends and colleagues at the University of Waterloo for putting up with my nerdy character and geeky interest. Thank you to Alex Krapf-Jones for the kind help and wonderful times for my first field season in a country far away from home, to Sabastien Dyer and Carson Kinney for tolerating my distracting you for prolonged talks about modelling, to Hang Meng and Jianyu Chen for handcrafting a computer together which later served as a workhorse for code development and testing for this project and to Zhaowei Huang for the thought-provoking conversations on matters physical, metaphysical and delusional. I am also grateful to many excellent courses taught by the faculties of mathematics and engineering at the University of Waterloo, which helps me immensely on understanding the underlying principles of numerical modelling.

Last but not least, my deepest gratitude goes to my family for their steadfast support. I am especially to indebted my wife for the unconditional understanding through all these years. For all the hard problems I face on this journey, you are the magical source of my passion, inspiration and motivation to seek the perfect solution.

Dedication

To my grandparents, Xìnqín Zhào and Yǒuchūn Wú.
Also to my wife, Shamshijamal.

Table of Contents

Examining Committee Membership ii

Author's Declaration iii

Statement of Contributions iv

Abstract v

Acknowledgements vii

Dedication viii

List of Figures xiv

List of Tables xvii

List of Abbreviations xix

1 Introduction 1

2 Modelling multi-material structural patterns in tectonic flow with a discontinuous Galerkin level set method 5

2.1 Introduction 5

2.2 Numerical methods 8

2.2.1 The Stokes flow solver . . . 9
2.2.2 The level set solver . . . 10
2.2.3 Deformation analysis . . . 16
2.3 Numerical benchmarks and applications . . . 18
2.3.1 Competent inclusion in simple shear flow . . . 19
2.3.2 Rayleigh-Taylor instability . . . 26
2.3.3 Sheared 3d Rayleigh-Taylor instability . . . 34
2.4 Discussion and conclusions . . . 40
2.4.1 Geological interpretation of the level set field . . . 40
2.4.2 Geological interpretation on deformation analysis . . . 40
2.4.3 Summary and future extensions . . . 42

3 Neoarchean synchronous vertical and horizontal tectonism in the southern Swayze greenstone belt, Superior Province: Insights from structural analysis and numerical modelling 44

3.1 Introduction . . . 44
3.2 Geological settings . . . 46
3.2.1 Supracrustal stratigraphy . . . 48
3.2.2 Kenogamissi batholith . . . 48
3.2.3 The Ridout deformation zone . . . 49
3.3 Deformation analysis . . . 50
3.3.1 The southern domain . . . 54
3.3.2 The northern domain . . . 56
3.3.3 Summary of deformation and timing . . . 58
3.4 Numerical modelling . . . 59
3.4.1 Modelling methods . . . 60
3.4.2 Model setup . . . 61
3.4.3 Modelling results and comparison with field data . . . 64
3.5 Discussion . . . 69

3.5.1 Model assumptions and limitations . . . 69
3.5.2 Implications for the Neoarchean tectonics . . . 70
3.6 Conclusion . . . 72

4 Neoarchean crustal architecture and structural patterns under synchronous horizontal and vertical tectonism: Insights from numerical modelling 74
4.1 Introduction . . . 74
4.2 Methodology and model setup . . . 77
4.2.1 Governing physics . . . 77
4.2.2 Model setup . . . 80
4.3 Modelling results . . . 84
4.3.1 Baseline model without horizontal shearing . . . 84
4.3.2 Models with horizontal shearing of varying strain rates . . . 88
4.3.3 Models with horizontal shearing at various basal heat fluxes . . . 92
4.3.4 Distribution of total pressure and deformation zones . . . 95
4.4 Discussions . . . 96
4.4.1 Model assumptions and limitations . . . 96
4.4.2 Comparison with previous modelling studies . . . 97
4.4.3 Comparison with field structural observations . . . 99
4.4.4 Transition mechanism of crustal dynamics . . . 101
4.4.5 Crustal-scale deformation zones . . . 101
4.5 Conclusions . . . 103

5 Summary of conclusions and future directions 105
5.1 Summary of conclusions . . . 105
5.1.1 The discontinuous Galerkin level set method for modelling structural patterns . . . 105
5.1.2 The deformation pattern and crustal dynamics of the Swayze greenstone belt . . . 106
5.1.3 Implications for Neoarchean tectonics in general . . . 107
5.2 Future directions . . . 108

References **110**

APPENDICES **133**

A Linear system solver details **134**

A.1 The Rayleigh-Taylor instability 134

A.2 Competent inclusion in simple shear flow 137

A.3 Discussions 138

B Level set details **143**

B.1 Level set reinitialization 143

B.2 Slope Limiting 145

B.3 Efficient coupling scheme 148

C Additional benchmark problems **150**

C.1 The lid-driven cavity flow 150

C.2 Zalesak's disk 155

D Details of deformation analysis of the Swayze greenstone belt and regional implications **158**

D.1 Details of deformation analysis 158

D.1.1 Deformation G_1 158

D.1.2 Deformation G_2 159

D.1.3 Deformation G_3 161

D.1.4 Deformation G_4 161

D.2 Timing of deformation 163

D.3 Regional considerations 165

E Geochronology dataset for the Swayze Greenstone Belt **169**

F `stgeotk`: A `Python` package for strain analysis **173**

F.1 Reading data from export files 173

F.2 Finite deformation analysis implementations 174

F.3 Stereographic projection 176

List of Figures

2.1 Concept of the level set function for the interface of an elliptical material domain on a 2d plane . . . 11

2.2 Flowchart showing the coupling between the finite element flow solver and the level set solver . . . 14

2.3 The pressure and the velocity field around a spherical inclusion at the center of the modelling domain, as a benchmark to reproduce the results of Bons et al. (1997) . . . 21

2.4 Model setup of a 3d deformable inclusion under simple shear . . . 24

2.5 Snapshots of the deformation for a 3d deformable inclusion in a shear box up to a shear strain $\gamma = 8$ for $\eta_p/\eta_m = 100$ and $\eta_p/\eta_m = 10$ . . . 24

2.6 Model setup and $\bar{v}$ evolution for the 2d Rayleigh-Taylor instability benchmark . . . 27

2.7 Snapshots of the mesh configuration and the level set field of the 2d Rayleigh-Taylor instability benchmark . . . 28

2.8 Snapshots of the finite strain distribution of a 3d isoviscous Rayleigh-Taylor instability . . . 32

2.9 Snapshots of the Flinn diagram of the strain ellipsoids at the interface between the denser material on top and the lighter material below in the 3d isoviscous Rayleigh-Taylor instability test case . . . 33

2.10 Model setup for the two-layer 3d Rayleigh-Taylor experiment with a sinistral shearing boundary conditions. . . . 35

2.11 Model results for the sheared 3d Rayleigh-Taylor instability at peak root-mean-square velocity . . . 36

2.12 Simulated geological map with structural patterns of the sheared 3d Rayleigh-Taylor instability model on a horizontal slice at 8.00 km depth 38

3.1 Location of the study area and the simplified geological map of the Swayze greenstone belt (SGB) . . . 46
3.2 Structural data and stereographic projections related to the G_2 deformation . . . 51
3.3 Field photos showing the strain patterns of the G_2 deformation . . . 52
3.4 Field photos and stereographic projections of G_2 structures in the southern domain . . . 54
3.5 Field photos and stereographic projections of G_2 structures in the northern domain . . . 56
3.6 Summary of major generations of structures in the Swayze greenstone belt . . . 58
3.7 The configuration of the numerical model for the synchronous vertical and horizontal tectonism for the Swayze greenstone belt . . . 62
3.8 3d results of the numerical model for the Swazye greenstone belt . . . 65
3.9 Modelled lithological distribution and structural pattern for the Swayze greenstone belt on a slice plane at *ca.* 8.00 km depth . . . 66
3.10 Simulated lineation and foliation patterns in the northern and southern domains of the numerical model . . . 68

4.1 Simplified geological maps of various parts of the Superior Craton representative of the Neoarchean granitoid-greenstone terranes . . . 75
4.2 Model setup and boundary conditions of the Neoarchean synchronous crustal-scale gravitational overturn and horizontal shearing . . . 81
4.3 3d geometry of the granitoid-greenstone interface and the strain ellipsoid distribution of the base model . . . 85
4.4 Structural patterns of the baseline model at *ca.* 8.00 km depth . . . 86
4.5 Viscosity profile and the evolution of maximum velocity magnitude under various horizontal shear strain rates . . . 88
4.6 The geometry of the strain ellipsoids at *ca.* 8.00 km depth and the granitoid-greenstone interface at various boundary shear speeds . . . 89
4.7 Foliation and lineation patterns at various shear speeds and depths . 90

4.8 Crustal temperature profile, effective viscosity profile and the temporal evolution of maximum velocity magnitude in the modelling domain under increasing basal heat fluxes q_m 93

4.9 Simulated crustal structure under various basal heat fluxes q_m 94

A.1 The zero level set contour of the 2d Rayleigh-Taylor benchmark. . . . 139

A.2 The zero level set contour of the 3d Rayleigh-Taylor experiment on a yz slice plane through the origin. 140

A.3 The zero level set contour of the 3d inclusion on a yz slice plane through the origin. 141

B.1 The minmod shock detector acting on the vertex $\boldsymbol{v}_1$ and $\boldsymbol{v}_2$ of the target cell Ω_0 with the barycentre at $\boldsymbol{c}_0$ 146

B.2 Illustration of a multithreaded level set-flow solver coupling scheme . 149

C.1 Model setup for the lid-driven cavity flow and the steady-state velocity magnitude at Re = 400 151

C.2 General procedure of the weighted least square (WLS)-particle-in-cell (PIC) method 152

C.3 The results of lid-driven cavity flow benchmark for Re = 100 and Re = 1000 154

C.4 Model setup and computational mesh for the Zalesak's disk benchmark 156

C.5 The interface trace of the Zalesak's disk before (dashed line) and after (solid line) one revolution 156

D.1 Field photos and measurements of the G_3 deformations 160

D.2 Field photos and measurements of the G_4 structures 162

D.3 Concordia diagrams of the samples for zircon U-Pb geochronology . . 163

List of Tables

2.1 Quantitative comparison between results obtained by Bons et al. (1997) and that measured from our study under various boundary conditions 23

2.2 Benchmark results for the isoviscous case ($\eta_0 = \eta_1 = 100$) 29

2.3 Benchmark results for the non-isoviscous case ($\eta_0 = 10$, $\eta_1 = 100$). . . 30

2.4 Convergence analysis for the 2d isoviscous and non-isoviscous Rayleigh-Taylor instability. 32

4.1 List of the values of material parameters used in the numerical model. 82

4.2 Maximum velocity magnitude ($v_{\max}$) and the time at which the gravitational overturn reaches peak velocity ($t_{\max}$) under increasing boundary shear velocity (v_s) 84

4.3 Maximum velocity magnitude ($v_{\max}$) and the time at which the gravitational overturn reaches peak velocity ($t_{\max}$) under increasing basal heat flux q_m (*i.e.* basal temperature) 87

A.1 Number of iterations and CPU time of the 2d Rayleigh-Taylor instability test case on an adaptively refined mesh up to 32×32 135

A.2 Number of iterations and CPU time of the 2d Rayleigh-Taylor instability test case on an adaptively refined mesh up to 64×64 135

A.3 Number of iterations and CPU time of the 3d Rayleigh-Taylor instability test case on an adaptively refined mesh up to $16 \times 16 \times 16$ . . . 136

A.4 Number of iterations and CPU time of the 3d Rayleigh-Taylor instability test case on an adaptively refined mesh up to $32 \times 32 \times 32$ . . . 136

A.5 Number of iterations and CPU time of the 3d inclusion test case on an adaptively refined mesh up to $16 \times 16 \times 16$ 137

A.6 Number of iterations and CPU time of the 3d inclusion test case on an adaptively refined mesh up to $32 \times 32 \times 32$ 137

C.1 Errors of the Zalesak's disk benchmark with increasing grid densities 157

D.1 Summary and comparison of the deformation history of the Ridout deformation zone (RDZ), Swayze greenstone belt (SGB) and the Cadillac-Larder Lake deformation zone (CLLDZ), Abitibi greenstone belt . . . 168

List of Abbreviations

AMG algebraic multigrid 10, 134, 141, 142

AMR adaptive mesh refinement 157

CG conjugate gradient 134, 138

CLLDZ Cadillac-Larder Lake deformation zone xviii, 50, 72, 100, 158, 165–168

DG discontinuous Galerkin 2, 7, 9, 12, 29–31, 42, 106, 108, 143

ENO essential non-oscillatory scheme 143

FC fully coupled 10, 134, 138

FLIP fluid implicit particle 153

GMRES generalized minimal residue 134, 138, 142

HJ Hamilton-Jacobi 108, 143, 144

ID-TIMS isotope dilution-thermal ionization mass spectrometry 163, 165

ILU incomplete LU 10, 134, 138, 141

ISA instantaneous strain axis 1, 16, 42

LA-ICP-MS laser ablation-inductively coupled plasma-mass spectrometry 163

LDG local discontinuous Galerkin 143

PIC particle-in-cell xvi, 2, 5, 8, 31, 151, 152

RDZ Ridout deformation zone xviii, 49, 50, 54, 59, 72, 100, 106, 158, 160, 161, 165–168

RK Runge-Kutta 12, 144

SCLM subcratonic lithospheric mantle 61

SCR Schur complement reduction 10, 134, 138

SGB Swayze greenstone belt xv, xviii, 2–4, 45, 46, 48–52, 54, 56, 58–60, 62, 64–66, 68–73, 106, 158, 159, 161, 163, 165, 166, 168

TTG tonalite-trondhjemite-granodiorite 35, 49, 50, 61, 80, 97, 158, 168

TVD total variance diminishing 12, 144

WENO weighted essential non-oscillatory scheme 13, 143, 145, 147

WLS weighted least square xvi, 151, 152

Chapter 1

Introduction

Numerical modelling of tectonic flow has provided the geoscience community with profound insights into the tectonic processes on various length and time scales by solving a set of partial differential equations describing the thermomechanical evolution of the lithospheric materials (*e.g.* Beaumont et al., 2001; Zhou et al., 2018; Sizova et al., 2010). In the traditional geodynamic modelling methods, the modelling results are typically compared to the real world lithospheric conditions and evolutions by means of indirect geophysical or petrological data (*e.g.* Yu et al., 2022; Beaumont et al., 2001). However, comparing and correlating the model results with direct field observations of mesoscale structures remains elusive. In this thesis, we propose a modelling methodology by capturing the interface between different materials (*i.e.* lithological units) with the level set method (Hillebrand et al., 2014; Samuel and Evonuk, 2010). Our method offers the distinct capability to extract not only the 3d lithological distribution but also the structural patterns from the tectonic flow in the form of instantaneous and finite deformation fields. The former, which includes information on *e.g.* the instantaneous strain axis (ISA), the shearing kinematics and the kinematic vorticity, can be directly computed from the tectonic flow velocity field. The latter, typically visualized by the geometry of the strain ellipsoids, foliation/lineation patterns and Flinn's K-value, can be obtained from the strain integration through time on judiciously-placed tracer particles in areas of interest. In this way, the material distribution of the model at any given erosion level may be compared to the lithological pattern on the geological map. The deformation of the level set contours can be interpreted as the folding pattern of the primary structures (*e.g.* bedding) on a regional scale. The simulated deformation field can be compared to the field analysis of structural patterns, thereby offering multiple pathways to test

the validity of the numerical model against real-world observations.

Our formulation also provides an efficient and extensible means to achieve the aforementioned goal by applying a discontinuous Galerkin (DG) method to solve the level set fields, the geometrical evolutions of which are directed by the flow velocity field obtained from a finite element Stokes flow solver. The unification of the level set solver and the flow solver under the finite element discretization allows for straightforward implementation for non-structured mesh geometry as well as non-linear and potentially anisotropic rheological relations. Moreover, in contrast to the traditional particle-in-cell (PIC) methods (Thieulot, 2014; Moresi et al., 2003; Gerya and Yuen, 2007), the deformation-tracking particles in our method serve only as passive "observers" of the finite strain rather than as active tracking mechanisms of material properties. In this sense, the clouds of particles do not have to achieve sufficient density to resolve the material distribution, nor is the computationally intensive two-way particle-mesh interpolation required.

The Archean crustal dynamics leading to the dome-and-keel geometry of the granitoid-greenstone terranes remains a controversial topic with ideas divided between a vertical- and horizontal-style tectonics. The former argues, on the ground of elevated heat flux and the presence of an inverted crustal density profile, that the dome-and-keel pattern is the result of crustal-scale gravitational overturn (also known as *sagduction/diapirism*, *Rayleigh-Taylor instability* or *partial convective overturn*) (*e.g.* Van Kranendonk et al., 2004; Chardon et al., 1996; Collins, 1989; Lin et al., 2013). On the other hand, several studies explain the dome-and-keel under a horizontal-style tectonic framework, where the crustal deformation is driven by the far-field tectonic forcing manifested as an orthogonal (Type 1) fold interference pattern or a metamorphic core complex (*e.g.* van der Velden et al., 2006; de Wit, 1998; Kusky and Polat, 1999).

However, such simplistic dichotomy of Archean tectonics is not supported by field structural studies in multiple granitoid-greenstone terranes in the Neoarchean Superior Craton, where the coexisting evidence of both a vertical- and horizontal-style tectonics is observed, leading to the conjecture that both mechanisms may have operated synchronously during Neoarchean (*e.g.* Bouhallier et al., 1993; Lin, 2005; Lin and Beakhouse, 2013). To test this hypothesis and at the same time illustrate the practical use case of our modelling framework, two case studies are computed with our formulation:

In the first case study, a field-based structural analysis based on overprinting relationship is conducted in the Swayze greenstone belt (SGB). Four generations (G_1–G_4) of ductile structures are identified. Among them, the G_2 deformation is the regional

deformation responsible for the formation of regional upright anticline-syncline folding, an oblique granitoid-up/greenstone-down shearing kinematics and an opposite plunge direction of L_2 mineral stretching lineation on opposing granitoid-greenstone belt boundaries. The structural pattern is compatible with a regional deformation field involving both components of vertical sagduction/diapirism movement and horizontal dextral shearing. This interpreted deformation field is subsequently used as the boundary condition of an isothermal mechanical model with horizontally layered granitoid greenstone as the initial configuration. The numerical model replicates the lithological distribution and the structural pattern (in terms of foliation/lineation pattern, strain distribution and shearing kinematics) of the G_2 deformation, thereby affirming the synchronous vertical and horizontal tectonism as a possible mechanism for establishing the crustal architecture in the SGB.

Building upon the SGB model, we proceed to construct a thermomechanical model with thermal and rheological conditions appropriate for the Neoarchean Earth to explore the secular development of crustal architecture and structural patterns under gravitational overturn synchronous with horizontal simple shearing. Our results show that the gravitational overturn process in the granitoid-greenstone terranes takes the form of diachronous active sagduction of the greenstone supracrustal assemblages in a pointwise geometry at triple junctions or in a sheet-like geometry in synclinal keels that are aligned parallel to the finite stretching axis. We conclude that a synchronous vertical and horizontal tectonic regime can be a viable explanation for the 3d crustal architecture, deformation patterns and high strain zone distribution in not only the SGB but also for multiple other Neoarchean granitoid-greenstone terranes. Furthermore, we explore the change in crustal behaviour with diminishing Moho heat flux and high horizontal strain rate, to explore the evolution of crustal architecture towards modern-day conditions. In both cases, the rate of greenstone sagduction is suppressed, while the former additionally results in delayed onset of the gravitational overturn process, supporting the diminishing role of gravitational overturn process in crustal deformation through time. In this context, the Neoarchean may represent a transition period in the Earth's history when the crustal dynamics gradually evolve from dominantly vertical re-organization due to density difference to horizontal interaction between rigid blocks, as is first proposed in (Lin, 2005). This shift in crustal dynamics mirrors a similar transition in lithospheric dynamics from the stagnant-lid like tectonics to the modern-day plate tectonics (*e.g.* Bédard, 2018; Johnson et al., 2014), suggesting the Neoarchean to be a possible global transition period of the Earth's tectonic regime on multiple scales (Lin, 2007).

The outline of this thesis is as follows. In Chapter 2 we describe in detail the the-

oretical background and the computational implementation of our modelling framework, as well as presenting benchmark cases to validate the numerical results. In Chapter 3, the field structural analysis of the SGB are compared to the results of a mechanical model to explore the possibility of explaining the crustal dynamics by synchronous horizontal and vertical tectonics. Building upon the mechanical model for SGB, we extend the model in Chapter 4 to incorporate both temperature- and strain rate-dependent viscosity, with thermal and mechanical conditions appropriate for the Neoarchean Earth and discuss the implications on the Neoarchean crustal dynamics in general.

Chapter 2

Modelling multi-material structural patterns in tectonic flow with a discontinuous Galerkin level set method

2.1 Introduction

Thermomechanical modelling of long-term tectonic flows has yielded insights into complicated geodynamic processes and has served as a virtual laboratory for probing into the evolution of dominant tectonic regimes at various stages of the Earth's history (*e.g.* Beaumont et al., 2001; Sizova et al., 2010; Zhou et al., 2018). The thermomechanical equations are combined with a rheological model, cast in an effectively viscous formulation, to simulate the slow creeping flow on a tectonic timescale. The numerical solution is typically obtained on a stationary mesh oblivious to the movement of different material units in the model (*e.g.* Kronbichler, 2021; May et al., 2014; Braun et al., 2008) to avoid the costs for remeshing under grid distortion (*e.g.* de Montserrat et al., 2019; Choi et al., 2013). Because the mesh retains no information about the movement of the material, some mechanism is required to inform the mesh of the material distribution.

In geodynamic modelling, the task of locating the material interface is typically achieved by some Lagrangian framework separate from the computational mesh, inevitably incurring additional computational costs. The particle-in-cell (PIC)

method represents the material domain with particles, which can possess nonzero volume (Moresi et al., 2003) or be abstract volumeless tracers (Gerya and Yuen, 2007; Thieulot, 2014; May et al., 2014). Resolving the movement of the material domains through time is equivalent to tracking the movement of a cloud of particles. The limitations of the particle approach are high memory consumption due to the large number of particles required to properly resolve the material field and the poor scalability due to the transfer of particle information from particles to the mesh and between CPUs in distributed memory computing. The front-tracking method, on the other hand, represents the material interface using a 2d mesh (in 3d model) or 1d curve (in 2d models) (Braun et al., 2008; Becker et al., 2008). The deformation of interface with the flow is described accurately at the expense of high computational costs due to the maintenance of the interface mesh, especially in 3d simulations. This method is also inflexible when it comes to handling complicated geometric changes in the form of splitting and merging behaviours (*e.g.* boudinage, melt coalescing, crustal delamination, etc.) (Tryggvason et al., 2001). The arbitrary Lagrangian Eulerian (ALE) method (Fullsack, 1995; Pysklywec et al., 2002) represents a middle ground between the two aforementioned methods, both in terms of strengths and weaknesses, by making the connectivity of the Lagrangian nodes optional and the background computational mesh vertically deformable.

Traditionally numerical geodynamic models enable us to visualize the dynamical evolution of material, strain rate, temperature and pressure distribution through space and time (*e.g.* Yu et al., 2022). Although the model results can be corroborated by indirect evidence of geophysical and petrological data, correlating the simulation to observable field evidence remains elusive. Meanwhile, in the structural geology modelling community, profound insights into the mechanism of meso- and microscale fabric development have been extracted from kinematic analysis under the assumption of a homogeneous strain field (Lin et al., 1998; Jiang and Williams, 1998; Ramsay and Graham, 1970; Ramsay, 1980). However, linking the kinematic picture to a regional-scale tectonic model with complete dynamics remains challenging (Jiang and Williams, 1999; Fletcher and Pollard, 1999). Recent developments in micromechanics have demonstrated the power of applying quasi-analytical solution to the analysis of multiscale tectonic flows through the inhomogeneities-in-inhomogeneities method (Jiang, 2014, 2023; Jiang and Bhandari, 2018; Bhandari and Jiang, 2021). However, these applications are based on quasi-analytical solutions and are limited to problems with simple geometry and boundary conditions.

The objectives of our tectonic modelling method are twofold. Firstly, our method implements an efficient and flexible method for capturing material interfaces on an

Eulerian mesh, in both 2d and 3d, without the necessity to involve additional Lagrangian mesh or particles. Secondly, we build the connection between abstract numerical models of crustal dynamics and concrete observations of geological mapping by formulating methodology to extract field-testable lithological distributions and deformation patterns from modelling results.

To achieve the first objective, we use the level set formulation, which is a method that is widely applied to the simulation of multimaterial flows in fluid dynamics (*e.g.* Kronbichler et al., 2018; Sussman et al., 1994). The level set formulation implicitly "captures" the interface between material domains by attaching a scalar field to the Eulerian mesh (Hillebrand et al., 2014; Samuel and Evonuk, 2010; Bourgouin et al., 2007). The solution of the level set formulation is achieved by the discontinuous Galerkin (DG) discretization, which is a variant of the finite element method optimized for the modelling of transport-type problems. Adaptive mesh refinement localized around the material interface is implemented to improve the accuracy of interface resolution and minimize the mass loss deficiency inherent to the level set method. To build the connection between the material distribution and the tectonic flow, we couple the DG level set solver with a continuous finite element Stokes flow solver. Additionally, we employ an efficient linear system solver technique to obtain fast solution on an adaptively refined mesh with viscosity contrasts. The strength of this combination is the unification of the level set solver and the flow solver under the finite element framework, which then enables us to fully exploit the advantages of the finite element method in terms of flexibility of mesh geometry, simplicity of implementing anisotropic rheology to model mesoscale structures (Ran et al., 2019; Jiang, 2016) as well as large-scale mantle processes (Fraters and Billen, 2021), and accurate treatment of material transport due to the highly scalable DG discretization (*e.g.* Hesthaven and Warburton, 2007). Our methodology is similar in spirit with Heister et al. (2017), with the difference that the latter computes the advection of the composition fields directly without retaining the geometrical information of the interface.

To achieve our second objective we combine the strengths of the level set description of the interface geometry, the kinematic analysis techniques in structural geology and the mesh-based geodynamic models. We seek a numerical solution of tectonic flow on a discretized mesh, which results in a simulated tectonic flow that is non-steady in time and inhomogeneous in space. Additionally, the distribution of the lithological units are recorded by the evolution of the level set field while the finite deformation field is continuously recorded by the massless tracer particles. A simulated geological map pattern can be constructed from the level set field at any

arbitrary level of depth. Regional folding of the lithological units can be visualized by constructing cross-sections perpendicular to the regional structural grain. Analysis of the deformation field on the stationary mesh as well as on the tracer particles yields structural information (*e.g.* bedding, foliation and lineation orientations) that can be compared with structural features observable in the field. We note that this approach differs from the traditional PIC in that the markers are entirely passive and therefore not essential to the modelling computations. The modeller has the liberty to choose a suitable number of particles in areas of the model where deformation tracking is needed.

Our modelling method is particularly suited for testing numerical models with observations acquired from field mapping in the form of the distribution of lithological units, regional folding patterns of stratigraphy, the distribution of strain characteristics and intensity, as well as the foliation/lineation patterns. Our present formulation is not confined to any particular scale as long as the viscous rheological law is applicable and the inertial effect of the flow is negligible (the "creeping" flow regime), thereby making it a versatile tool to explore instantaneous and finite strain patterns resulting from both regional crustal-scale deformation (*e.g.* Archean lithospheric-scale density inversions, Section 2.3.3) and the evolution of meso- to microscale structural features (*e.g.* deformation around rheologically distinct inclusions or porphyroclasts, Section 2.3.1).

In the following sections of the article we begin by briefly introducing the discretization scheme for both the tectonic flow solver and the level set interface solver in Section 2.2 as well as their mutual coupling. Also discussed in this section is the methodology to extract instantaneous and finite deformation patterns (Section 2.2.3) from the numerical model. We then present numerical experiments in Section 2.3 to showcase the validity of our modelling methods and its capability to produce simulation data that is relevant to field structures analysis. Finally, we discuss the correlation between the modelling results with real-world geological observations and our plan for future developments in Section 2.4.

2.2 Numerical methods

In our method, we couple two solution mechanisms to achieve multi-material simulation of the tectonic flow. The Stokes solver obtains the flow velocity and pressure while the level set solver captures the evolution of regions occupied by materials of different properties. The level set method has been widely applied to the modelling

of two-phase flows (*e.g.* Sussman et al., 1998), free-surface flows (*e.g.* Groß et al., 2006) and crystal growth (*e.g.* Merriman et al., 1994; Zhao et al., 1996). It has also been applied to the modelling of tectonic flows under a finite volume (Hillebrand et al., 2014; Samuel and Evonuk, 2010) or a traditional finite element discretization (Bourgouin et al., 2007).

The level set solver is discretized with a DG discretization. To the best knowledge of the authors, our study represents the first attempt to introduce DG level set formulation to modelling viscous tectonic flow. As the discontinuous variant of the finite element method, the DG method relaxes the inter-elemental continuity requirement in the traditional continuous finite element method and reintroduces the numerical flux into the finite element formulation. With this property the DG combines the stability of finite volume discretization for the modelling of hyperbolic problems and the compactness for high-order approximation of the finite element method. Because the approximation basis is local to each mesh cell, the DG method lends itself to massive parallelization and adaptive mesh refinement (Hesthaven and Warburton, 2007).

The DG discretization is originally formulated for the neutron transport problem (Reed and Hill, 1973) and has since been widely applied to the modelling of hyperbolic conservation laws (Cockburn and Shu, 1991; Shu, 2014). Besides its wide application in fluid dynamics (*e.g.* Rhebergen et al., 2013), the DG method has also been applied in the geophysical community for modelling seismic wave propagation (Chung et al., 2015; Zhang et al., 2019) and fault aseismic slips (Uphoff et al., 2022). It has also been utilized to discretize the level set formulation for multiphase fluid dynamics modelling. (*e.g.* Mousavi, 2014; Mousavi et al., 2016; Zhang and Yue, 2019; Owkes and Desjardins, 2013; Jibben and Herrmann, 2017)

In the following paragraphs of this section we describe the numerical strategies used to implement both solvers as well as the methodologies to extract information regarding finite deformation from the model results. The numerical procedures herein discussed are implemented in both 2d and 3d based on the finite element infrastructures provided by the `deal.II` library (Arndt et al., 2021).

2.2.1 The Stokes flow solver

The long-term tectonic flow of the Earth's crustal material can be approximated by a highly viscous creeping flow. Furthermore, if the volume change is negligible, the flow can be further approximated as incompressible, which leads to the following set

of governing equations:

$$\begin{cases} \boldsymbol{\nabla} \cdot \big(2\eta \boldsymbol{D}(\boldsymbol{v})\big) - \boldsymbol{\nabla} p + \rho \boldsymbol{g} = 0 \\ \boldsymbol{\nabla} \cdot \boldsymbol{v} = 0 \end{cases} \tag{2.1}$$

where $\boldsymbol{D}(\boldsymbol{v}) = {}^1\!/_2 \left(\boldsymbol{\nabla} v + (\boldsymbol{\nabla} v)^\top\right)$ is the rate-of-deformation tensor and $\boldsymbol{g}$ is the constant downward-pointing gravity vector. $\rho(\boldsymbol{x})$ and $\eta(\boldsymbol{x})$ are the spatially-variable material density and the effective viscosity respectively. At the current stage of development the effective viscosity η is a scalar due to the assumption of isotropic material. However, it is possible to model anisotropic material behaviour by extending viscosity to a tensorial quantity. A mixed finite element method is used to discretize the equation on an Eulerian quadrilateral mesh with a quadratic approximation for velocity and a linear approximation for pressure (*i.e.* the $\mathcal{Q}_2\mathcal{Q}_1$ elements) (Donéa, 2003). Complemented by the appropriate boundary conditions, the velocity $\boldsymbol{v}$ and pressure p can be obtained on the mesh by solving the following linear system:

$$\begin{bmatrix} \boldsymbol{A} & -\boldsymbol{B} \\ -\boldsymbol{B}^\top & \boldsymbol{0} \end{bmatrix} \begin{bmatrix} \hat{\boldsymbol{v}} \\ \hat{\boldsymbol{p}} \end{bmatrix} = \begin{bmatrix} \boldsymbol{f} \\ \boldsymbol{h} \end{bmatrix} \tag{2.2}$$

where $\boldsymbol{A}$ is the discrete viscosity matrix and $\boldsymbol{B}$ is the discrete gradient operator. $\hat{\boldsymbol{v}}$ and $\hat{\boldsymbol{p}}$ are arrays of expansion coefficients for velocity and pressure respectively. Equation (2.2) can either be solved monolithically with a fully coupled (FC) approach (Silvester and Wathen, 1994) or in a two-step manner by decoupling the pressure from velocity by Schur complement reduction (SCR) (Elman and Golub, 1994; Moresi and Solomatov, 1995). In both cases, solving the linear system efficiently hinges upon finding a high-quality preconditioner for $\boldsymbol{A}$. In this study we employ a level-based incomplete LU (ILU) preconditioner as well as an algebraic multigrid (AMG) preconditioner with one V-cycle sweep. An in-depth discussion of these solver properties, techniques as well as performance comparisons are available in Appendix A. In summary, we conclude that FC excels relative to SCR regardless of the choice of the preconditioner. In terms of the preconditioner for the FC approach, the ILU with a level-of-fill equal to one is the most cost-effective method for 2d problems. However, it is no longer as competent as the AMG method for 3d problems due to the large number of induced fills.

2.2.2 The level set solver

While the Eulerian formulation of the Stokes flow solver provides the dynamics of the flow, the passive movement of the regions of different material properties cannot

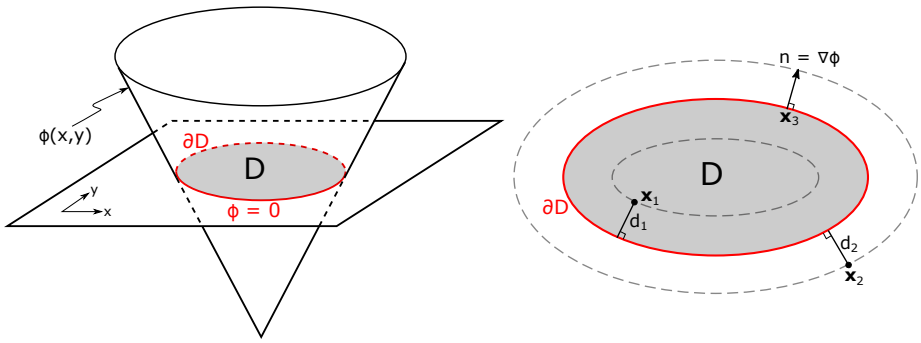


Figure 2.1: Concept of the level set function for the interface of an elliptical material domain on a 2d plane. $\boldsymbol{x}_1$ is inside the material domain D, $\boldsymbol{x}_2$ is outside the material domain and $\boldsymbol{x}_3$ is on the material interface. d_i is a shorthand of the distance to interface $d(\boldsymbol{x}_i, \partial D)$. In this case $\phi(\boldsymbol{x}_1) = -d_1$, $\phi(\boldsymbol{x}_2) = d_2$ and $\phi(\boldsymbol{x}_3) = 0$.

be resolved, thus necessitating the formulation of some material tracking mechanism. In this study, we utilize the level set method as a strategy to capture the material interface rather than representing the material domains with particles (*e.g.* Moresi et al., 2003; Gerya and Yuen, 2007) or tracking the interface with an independent mesh structure (*e.g.* Braun et al., 2008).

The level set method (Figure 2.1) captures the interface of a material domain D by associating it with a scalar level set function $\phi_D(\boldsymbol{x}, t)$. The magnitude of ϕ_D has a signed distance property that at an arbitrary point $\boldsymbol{x}$, $\phi_D(\boldsymbol{x})$ is by definition the distance from the point to the interface of D. Whether the point is "inside" or "outside" of the domain is reflected by the sign of ϕ_D. The level set field evaluates to zero on the interface ∂D. In this study, we follow the convention that a negative level set value is prescribed to a point inside D and a positive value if otherwise. These properties can be encapsulated in the following equation:

$$\phi_D(\boldsymbol{x}) = \begin{cases} d(\boldsymbol{x}, \partial D) & \boldsymbol{x} \in D \\ 0 & \boldsymbol{x} \in \partial D \\ -d(\boldsymbol{x}, \partial D) & \boldsymbol{x} \in \Omega \backslash \bar{D} \end{cases} \tag{2.3}$$

where $d(\boldsymbol{x}, \partial D)$ is the distance function from a point $\boldsymbol{x}$ to the interface of a domain D occupied by one single type of material. Due to its property as a signed distance field, the level set field has a unit gradient ($\|\boldsymbol{\nabla}\phi\| = 1$).

Modelling the evolution of the material domain with the level set method involves the solution of an advection problem followed by a reinitialization problem. Since

both problems are of hyperbolic nature, we implement the DG method to discretize the weak form of the equations representing both problems. The temporal integration is treated explicitly with a high-order explicit Runge-Kutta (RK) total variance diminishing (TVD) method.

The advection problem

The advection problem describes the passive movement of the level set field ϕ under the velocity field $\boldsymbol{v}$ provided by the flow solver:

$$\frac{\partial \phi}{\partial t} + \boldsymbol{v} \cdot \boldsymbol{\nabla} \phi = 0 \tag{2.4}$$

Because the DG discretization does not enforce continuity across cells, the discretized level set value ϕ_h is doubly-valued at the cell face. We use the following shorthand to describe the one-sided value of the interfacial ϕ_h from the viewpoint of cell Ω_e:

$$\phi_{h,e}^{\pm}(\boldsymbol{x}) = \lim_{\epsilon \to 0^{\pm}} \phi_h(\boldsymbol{x} + \epsilon \boldsymbol{n}_e) \tag{2.5}$$

where $\boldsymbol{n}_e$ is the outward-pointing normal at the cell face of the element Ω_e. From a geometric standpoint, $\phi_{h,e}^{-}$ is the value of ϕ_h at the cell face approximated by the polynomial basis internal to Ω_e, while $\phi_{h,e}^{+}$ is that approximated by the basis local to neighbouring cell sharing the same cell face.

By premultiplying with an arbitrary test function ψ and integrating over a finite element cell Ω_e, we arrive at the DG discretization of the advection problem:

$$\int_{\Omega_e} \psi_h \frac{\partial \phi_h}{\partial t} dV = \int_{\Omega_e} (\boldsymbol{v} \cdot \boldsymbol{\nabla} \psi_h)\, \phi_h \, d\Omega - \int_{\partial \Omega_e} \psi_h f(\phi_{h,e}^{-}, \phi_{h,e}^{+})\, dS \tag{2.6}$$

where the subscripts ϕ_h and ψ_h are the polynomial approximation of the level set function ϕ and test function ψ. $f(\cdot, \cdot)$ is the numerical flux located at the interface of the cell Ω_e and is upwinded with respect to the transport direction of the velocity field $\boldsymbol{v}$ for stability:

$$f(\phi_{h,e}^{+}, \phi_{h,e}^{-}) = (\boldsymbol{v} \cdot \boldsymbol{n}) \frac{\phi_{h,e}^{-} + \phi_{h,e}^{+}}{2} + |\boldsymbol{v} \cdot \boldsymbol{n}| \frac{\phi_{h,e}^{-} - \phi_{h,e}^{+}}{2} \tag{2.7}$$

The reinitialization problem

As the level set field is advected with the velocity of the flow through time, the magnitude of the level set gradient is not guaranteed to maintain unity. As a result, the level set field loses the signed distance property. Because the material parameters in the cells close to the interface are computed as a function of the level set values (see Section 2.2.2 for details), this deviation affects the numerical integration of material parameters in these cells. If left untreated, this deviation can then cause large errors in the simulated results. To correct for this deviation, we reinitialize the level set field by evolving the following reinitialization equation through pseudo-time τ to steady state:

$$\frac{\partial \phi}{\partial \tau} + \text{sgn}(\phi_0)\left(\|\boldsymbol{\nabla}\phi\| - 1\right) = 0 \tag{2.8}$$

where $\phi_0(\boldsymbol{x}) = \phi(\boldsymbol{x}, t)\big|_{t=0}$ is the not-yet-reinitialized value of ϕ and sgn is the signum function. The physical interpretation of this equation is to propagate the information of the unit divergence away from the interface. This is a Hamilton-Jacobi problem with the Hamilton-Jacobi operator H in the form of $H(\boldsymbol{\nabla}\phi) = \text{sgn}(\phi_0)\left(\|\boldsymbol{\nabla}\phi\| - 1\right)$. A local discontinuous Galerkin scheme is used to solve the reinitialization equation directly (Yan and Osher, 2011; Karakus et al., 2016b). Numerical instabilities that may develop in this formulation are smoothed by applying a weighted essential non-oscillatory scheme (WENO) limiter (Zhong and Shu, 2013). Detailed derivations of both the discretization and the limiting process are documented in sections 1 and 2 of Appendix B.

Flow solver coupling

Figure 2.2 illustrates the coupling between the Stokes flow solver and level set solver as a two-way process. From time t^n to t^{n+1}, the discrete velocity field $\hat{\boldsymbol{v}}^n$, obtained at each degree of freedom from the Stokes flow solver, is interpolated onto the quadrature points of each element cells via the finite element basis functions of velocity in the Stokes solver. The velocity values at the quadrature points are then employed in the level set update from ϕ^n to ϕ^{n+1} through volume and surface integration in Equation (2.6).

To inform the Stokes flow solver of the updated material distribution, the level set values ϕ^{n+1} are first interpolated onto the quadrature points of the Stokes flow solver. The relationship between the updated level set field and the material parameter θ (*e.g.* density ρ, viscosity η, etc.) in a two-material system is established by:

$$\theta(\boldsymbol{x}) = \theta_0 h_\epsilon(\phi(\boldsymbol{x})) + \theta_1\left(1 - h_\epsilon(\phi(\boldsymbol{x}))\right) \tag{2.9}$$

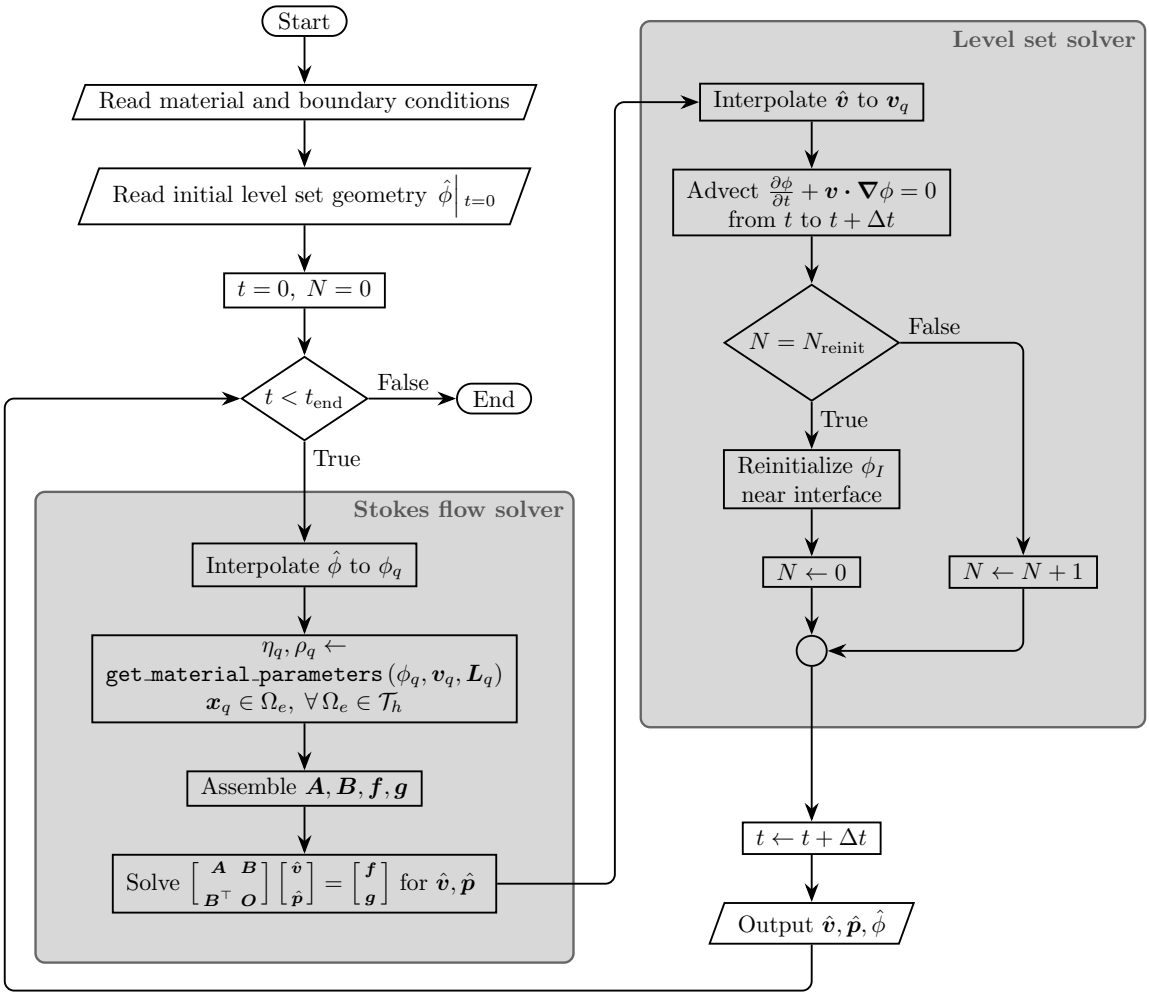


Figure 2.2: Flowchart showing the coupling between the finite element flow solver and the level set solver. The subscript q implies that the quantity is evaluated at the quadrature points.

where θ_1 is the material parameter associated with the domain where $\phi < 0$ and θ_0 is the "background" material. $h_\epsilon(\phi)$ is the smoothed Heaviside function:

$$h_\epsilon(\phi) = \begin{cases} 0 & \phi < -\epsilon \\ \frac{1}{2}\left(1 + \frac{\phi}{\epsilon} + \frac{1}{\pi}\sin\left(\frac{\pi\phi}{\epsilon}\right)\right) & -\epsilon \leqslant \phi \leqslant \epsilon \\ 1 & \phi > \epsilon \end{cases} \tag{2.10}$$

This method, which is typically used in two-phase flow problems (*e.g.* Tornberg and Engquist, 2000), creates a transition zone near the material interface of width 2ϵ so as to improve the accuracy of the numerical integration. The material parameters computed from Equation (2.9) will participate in the assembly of the elemental viscosity matrix in the Stokes flow solver.

In the case where more than two materials are present in the model, we define a background material which underlies all material domains. The overlying materials are each associated with a level set solver and ordered by their stratigraphical relationship. The stratigraphical relationship determines which material takes precedence over others when evaluating the level set functions. For example if the level set values for material A and B are both negative at point $\boldsymbol{x}$ (meaning in the material domain for both A and B), A overlies B implies the material definition for point $\boldsymbol{x}$ is A instead of B. The overlying relationship comes from the geological model. Geologically, this overlying relationship is equivalent to the stratigraphic order (or the "younging direction") of the modelled lithological units. The details of the efficient implementation of the coupling between the level set and the Stokes solver is discussed in section 3 of Appendix B.

To further reduce the computational cost, we notice that the level set values only enter the flow solver for cells within a narrow band of prescribed width around the zero level set. Therefore instead of solving Equation (2.8) to steady state, we iterate up to $\tau_{\max} = \gamma n h$. Here we assume the transition narrow band is of a width of $2n$ cell and γ is a constant coefficient to compensate for the non-unity propagation speed due to the signum function smoothing (Karakus et al., 2018). Since too frequent reinitialization introduces excessive interface movement, we trigger the reinitialization at a fixed interval N_{reinit} immediately prior to the adaptive mesh refinement of the cells close to the interface.

2.2.3 Deformation analysis

The modelling approach introduced in this study takes into account the complete dynamics and enables the modeller to analyse both the instantaneous and finite deformation patterns of the simulated flow. This is achieved by applying the methodology of the kinematic structural analysis to the simulated flow field. This process is discussed in detail in this section. The interested reader is also referred to Jiang (2023, chapter 5, and references therein) for a more in-depth and pedagogical account of the flow kinematics analysis.

The instantaneous deformation field is readily available by analysing the velocity field and the velocity gradient tensor $L_{ij} = \partial v_i / \partial v_j$. After decomposing the $\boldsymbol{L}$ into symmetric rate-of-deformation tensor $\boldsymbol{D}$ and anti-symmetric vorticity tensor $\boldsymbol{W}$, the following quantities can be evaluated at any arbitrary time and location in the numerical model:

1. The flow apophyses, or the "fabric attractors" (Passchier, 1998), can be obtained by taking the eigenvectors of $\boldsymbol{L}$. The eigenvectors represent the direction where the flow is attracted to, assuming $\boldsymbol{L}$ is constant in time;

2. The instantaneous strain axis (ISA) can be obtained from the eigendecomposition of the rate-of-deformation tensor $\boldsymbol{D}$;

3. The vorticity vector $\boldsymbol{\omega}$ can be computed by $\boldsymbol{\nabla} \times \boldsymbol{v}$. $\boldsymbol{\omega}$, which is the local sense of vorticity measured with respect to a fixed reference frame attached to the stationary mesh. We caution that this vorticity is not the same as the vorticity measured with respect to the local instantaneous principal strain rate axes and is therefore not objective (Means et al., 1980; Jiang, 1999).

4. The kinematic vorticity number W_k can be obtained by $\|W\| / \|D\|$. W_k measures a nonlinear ratio between the rotation component and the stretching component of the deformation (Tikoff and Fossen, 1995). In a plane strain scenario, $W_k = 0$ and $W_k = 1$ represent two end-member flow types. The former corresponds to pure shear and the latter to simple shear. Differentiating flow types based on W_k in 3d deformation is not straightforward, in which case $W_k = 1$ can only be treated as a necessary condition for simple shear flow (Jiang, 2023).

The above-mentioned quantities represent the instantaneous condition of the flow. However, the deformation structures observed in the natural geological materials are

commonly the results of accumulated deformation through a prolonged and complicated tectonic history. This process can be modelled by involving a Lagrangian tracking mechanism on top of the stationary mesh. In order to integrate finite deformation through time, tracer particles are injected into and around the regions of the model where deformation tracking is required. The particles are then advected in the modelling domain by the velocity interpolated from the mesh. The particle advection is computed by a forward Euler scheme as soon as the solution of the level set advection problem is completed.

To track finite deformation, each particle is associated with a deformation gradient tensor $\boldsymbol{F}(t)$, which is initialized to identity matrix $\boldsymbol{I}$ upon generation. For time step $\Delta t^n = t^{n+1} - t^n$, the approximated deformation tensor $\boldsymbol{F}^{n+1}$ can be integrated with the 1$^{\text{st}}$-order forward Euler scheme of the well-known relation $\dot{\boldsymbol{F}} = \boldsymbol{L}\boldsymbol{F}$ (Malvern, 1969, p.163):

$$\boldsymbol{F}^{n+1} = \left(\boldsymbol{I} + \Delta t^n \boldsymbol{L}(t^n)\right) \boldsymbol{F}^n \tag{2.11}$$

The power of the deformation gradient tensor lies in its potential correlation with the foliation and lineation orientations, thus building a bridge between the abstract numerical model and the concrete field observations. The foliation and lineation orientation can be extracted by computing the eigendecomposition of the left Cauchy-Green tensor $\boldsymbol{C} = \boldsymbol{F}\boldsymbol{F}^\top$, which in 3d space yields three positive eigenvalues ($\lambda_1 \geqslant \lambda_2 \geqslant \lambda_3$) and three corresponding mutually orthogonal eigenvectors ($\boldsymbol{\nu}_1, \boldsymbol{\nu}_2, \boldsymbol{\nu}_3$). The trend and plunge of the eigenvector $\boldsymbol{\nu}_1$ is the maximum stretching orientation of the finite strain and can be interpreted as the orientation of the stretching lineation. In the same way, the orientation of $\boldsymbol{\nu}_3$ corresponds to maximum finite shortening and can be interpreted as the pole to the foliation plane (*e.g.* Lin et al., 1998). Geometrically, the eigenvectors ($\boldsymbol{\nu}_1, \boldsymbol{\nu}_2, \boldsymbol{\nu}_3$) also correspond to the orientations of the three axes of the strain ellipsoid (Elliott, 1972). The square root of the eigenvalues ($\sqrt{\lambda_1}$, $\sqrt{\lambda_2}$ and $\sqrt{\lambda_3}$) are the length of the maximum, intermediate and minimum principal axes of the strain ellipsoid. Equipped with this knowledge, we can also compute the slope of any tracer particle on the Flinn diagram, or the Flinn's K-value:

$$K = \frac{\ln\left(\lambda_1/\lambda_2\right)}{\ln\left(\lambda_2/\lambda_3\right)} \tag{2.12}$$

Values of K significantly greater than 1 are dominated by prolate strain or "cigar-shaped" strain ellipsoids. These particles mark the locations which favours the development of L-tectonites. On the contrary, particles with K significantly smaller than 1 are dominated by oblate strain or "pancake-shaped" strain ellipsoids, which correspond to the places where the development of S-tectonites is expected. The

strain intensity N can also be computed by evaluating the deviation of the strain ellipsoids from a sphere (Ramsay and Huber, 1983):

$$N = \sqrt{\left(\sqrt{\frac{\lambda_1}{\lambda_2}} - 1\right)^2 + \left(\sqrt{\frac{\lambda_2}{\lambda_3}} - 1\right)^2} \tag{2.13}$$

These predictions can be compared with the field observations of the deformation style and the relative intensity of deformation for validation. In addition to the spatial distribution, the numerical model provides the continuous temporal evolution of the deformation pattern, *e.g.* the change of the foliation orientation through time. This information can also be compared to the results of the analysis of strain history typically obtained from the field analysis or overprinting relationships between multiple generations of structures.

2.3 Numerical benchmarks and applications

Three numerical experiments are presented to test the validity (Section 2.3.1 and Section 2.3.2) and showcase the real-world application of our technique (Section 2.3.3). We begin by computing two non-dimensional problems representing flow under simple shearing as well as density overturn. In 2d they serve as benchmarks with established numerical or near-analytical solutions so that we can verify the correctness of our results, evaluate the convergence of our numerical discretization, and establish the robustness of our solution technique for the linear system. We then extend the 2d benchmark cases to 3d to demonstrate the capability of our methods to characterize finite deformation patterns. Despite the non-dimensional nature of these numerical models, the results can be generalized to geological structures on multiple scales and in various tectonic settings as long as the governing equations and the linearly viscous rheology hold.

The reinterpretation of a non-dimensional variable (denoted with an overline, *e.g.* $\overline{\eta}$, $\overline{\boldsymbol{v}}$) to a corresponding variable with a physical unit (*e.g.* η, $\boldsymbol{v}$) can be carried out in the following manner: let l_c and t_c denote the characteristic length and temporal scales such that $\overline{\boldsymbol{x}} = \boldsymbol{x}/l_c$ and $\overline{t} = t/t_c$. The non-dimensional viscosity $\overline{\eta}$ can then be related to the physical viscosity η by $\overline{\eta} = \eta/t_c l_c$. The non-dimensional velocity $\overline{\boldsymbol{v}}$ and pressure $\overline{p}$ can then be scaled to their real-world counterparts by $\boldsymbol{v} = \overline{\boldsymbol{v}}\, l_c/t_c$ and $p = \overline{p}\, l_c$. We remark that this scaling analysis is only possible due to the linear nature of our problem and is not generally applicable under more complicated material models.

Finally, to demonstrate the geological application of our method to crustal-scale tectonic processes, we model a density overturn process operating under prescribed background shearing in Section 2.3.3. This model represents a possible scenario for the Neoarchean crustal dynamics when vertical tectonism in the form of sagduction and diapirism as well as horizontal tectonism in the form of modern-day-like plate tectonics operates simultaneously. In terms of the physical process, this experiment demonstrates the 3d interplay between a Rayleigh-Taylor instability discussed in Section 2.3.2 and the simultaneous deformation of the rheologically inhomogeneous crust under the simple shear flow akin to Section 2.3.1.

Besides the above-mentioned numerical experiments, we have also included our results for an additional set of benchmark problems in Appendices A and C.

2.3.1 Competent inclusion in simple shear flow

In this set of experiments we simulate the deformation field produced by a relatively competent spherical inclusion (with viscosity η_p) embedded in a viscous matrix (with viscosity η_m) under a simple shear regime in both 2d and 3d. This model can be viewed as an abstraction for describing the deformation field in and around a competent lithological inhomogeneity undergoing shear deformation on a larger scale. On micro- or mesoscale, such matrix-inclusion system emerges naturally from the study of asymmetric porphyroclasts as shear sense indicators (Zhang and Fossen, 2020), as kinematic vorticity gauges of the bulk flow (Stahr and Law, 2011) and as a proxy for modelling fabric development (Marques, 2016). On a regional scale, the model encapsulates, for example, the deformation field of less competent stratigraphy layers around a mechanically rigid pluton, both undergoing regional tectonic shearing.

Previous modelling of the matrix-inclusion system are typically based on one or more of the following assumptions:

1. The inclusion is considered as a rigid or deformable ellipsoid immersed in an infinitely viscous matrix. In the case of a rigid ellipsoid, the motion of the inclusion can be resolved in both 2d and 3d by applying Jeffery's theory (Jeffery, 1922) either analytically (*e.g.* Ghosh and Ramberg, 1976) or numerically (*e.g.* Jeẑek, 1994; Ježek et al., 1999; Jiang, 2007). If the ellipsoidal inclusion is considered deformable, the deformation of the inclusion can be obtained by Eshelby's theory for both linearly (Jiang, 2007) and power-law viscous rheology (Jiang, 2014).

2. The flow is assumed to be steady-state. This assumption is made in several one-step finite element modelling on a bounded domain. The inclusion can be modelled as a separate phase more viscous than the matrix (Bons et al., 1997) or as a domain boundary (Masuda and Mizuno, 1996; Pennacchioni et al., 2000).

Attempts to overcome these limitations are made in 2d by combining a front-tracking algorithm with viscoplastic fast Fourier transform algorithm (Griera et al., 2013) or by a Lagrangian finite element method with remeshing (Schmid and Podladchikov, 2005). By computing two sets of numerical experiments with our formulation, we show that firstly, the results of our approach are comparable to previous studies in 2d and secondly, our approach provides a method to relax the aforementioned assumptions in 3d even for large amount of deformation.

2d benchmark

In the first set of numerical experiments we reproduce the model setup by Bons et al. (1997). A steady-state flow field is computed for a circular inclusion with radius of $1/24$ centred at the origin of a $[-0.5, 0.5]^2$ square box. The matrix viscosity, denoted as η_m, is set at 1 and the inclusion viscosity, denoted as η_p, is set at 100.

The experiment is computed under three different boundary conditions specified in Bons et al. (1997, section 2.1), which we briefly summarize as:

1. On all boundaries, $v_y = 0$ and v_x varies linearly from 0.5 on the top boundary ($y = 1$) to -0.5 at the bottom boundary ($y = 0$)

2. $v_x = 0.5(-0.5)$ on the top (bottom) boundary and $v_y = 0.0$ on the left and right boundaries. Normal stresses on all boundaries are set to be equal to the background pressure.

3. $v_x = 0.5(-0.5)$ and $v_y = 0$ on the top (bottom) boundaries. On the left and right boundaries, $v_y = 0$ and the normal stresses is equal to background pressure.

The computation is carried out on a base grid of 512×512. The grid is refined up to an equivalent density of 8192×8192 at the inclusion-matrix interface for accurate resolution of interface pressure.

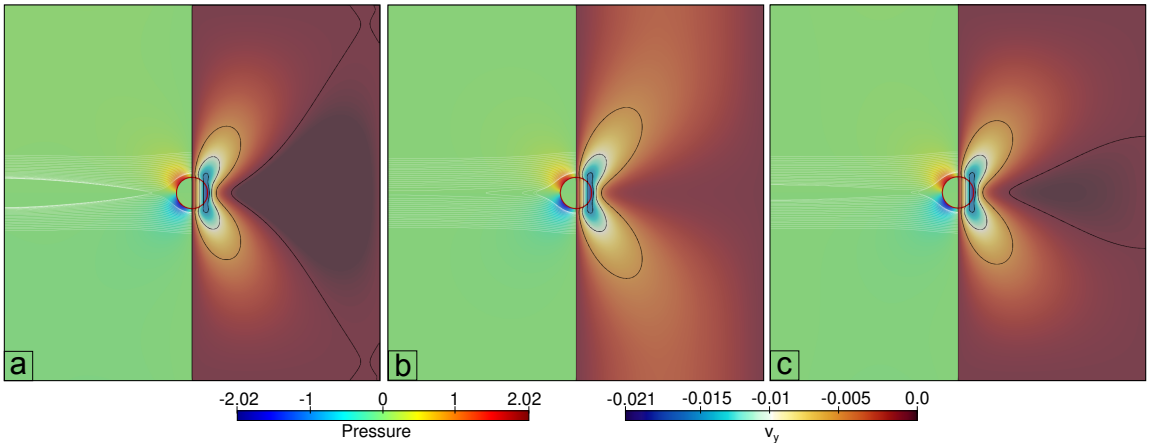


Figure 2.3: The pressure and the velocity field around a spherical inclusion at the centre of the modelling domain. Our model reproduces the results of Bons et al. (1997) for linearly viscous flow. The subfigures (a), (b) and (c) correspond to the boundary conditions 1, 2 and 3 (*i.e.* the figures 4a, 4d and 4g) in Bons et al. (1997). On the left half of each subfigure, the white contours are streamlines at ψ values of 0.0005, 0.001 0.0025, 0.005 and 0.01; the blue line is the flow separatrix and the colour shading represents the pressure field. The right half of each subfigure is shaded by the value of y-velocity and the black lines are the contours of y-velocity at -0.015, -0.010, -0.005 and 0.0. See text for discussion

To qualitatively compare the stream function ψ, y-velocity and pressure distributions of our results with that of Bons et al. (1997), Figure 2.3 is constructed to repeat the Figures 4a, 4d and 4g of Bons et al. (1997). The stream function values ψ at mesh nodes throughout the model can be obtained with the following equation, assuming the origin $(x_0, y_0) = (0, 0)$ to be the datum:

$$\psi(x, y) = -\int_{x_0}^{x} v_y(\hat{x}, y)\, d\hat{x} + \int_{y_0}^{y} v_x(x, \hat{y})\, d\hat{y} \tag{2.14}$$

The integral is computed numerically by a Gauss-Legendre quadrature along the cell faces outward from the datum. The contour patterns of the stream function ψ and y-velocity from the two studies show good agreement. The flow patterns of both studies are also mutually consistent: For boundary conditions 1 and 3 a bow-tie-shaped flow pattern is produced, while for boundary condition 2 the flow pattern is eye-shaped.

A quantitative comparison can be carried out by computing the stream function ψ value of the flow separatrix, the vertical distance D_s between the intersections of separatrix with the left boundary and the distance D_{sp} between the stagnation point to the origin. Both D_s and D_{sp} are normalized to the radius of the inclusion. In a

bow-tie flow pattern (obtained in boundary conditions 1 and 3), the flow separatrix separates regions of distinct flow patterns. For an eye-shaped flow pattern (obtained in boundary condition 2), the separatrix is defined as the streamline whose leftmost intersection point converges onto the left boundary. In this particular case, D_s and D_{sp} is undefined. The separatrices under various boundary conditions are plotted as the blue line in the left halves of Figure 2.3. Our results of the separatrix ψ-value, D_{sp} and D_s are tabulated in Table 2.1. Both the geometry of the separatices and the numerical values of ψ, D_{sp} and D_s are comparable to the results shown in Figure 4 and Table 1 of Bons et al. (1997).

Finally, the maximum absolute pressure value $|p|_{\max}$ of our model is obtained at the inclusion-matrix interface (listed in the last row of Table 2.1) and can be compared with the analytical solution $|p_a|_{\max}$ (Schmid and Podladchikov, 2003):

$$|p_a|_{\max} = \frac{2\eta_m(\eta_p - \eta_m)}{\eta_p + \eta_m}\sqrt{\dot{\gamma}^2 + 4\dot{\epsilon}^2} \tag{2.15}$$

where $\dot{\epsilon}$ and $\dot{\gamma}$ are the boundary pure strain rate and the simple shear strain rate. For this benchmark, $\dot{\epsilon} = 0$ and $\dot{\gamma} = 1$, thus yielding $|p_a|_{\max} = 1.9604$. We remark that the numerical model is computed on a finite domain whereas the analytical solution assumes that the boundary conditions are imposed at infinity. Despite this discrepancy, the $|p|_{\max}$ for all boundary conditions agrees well with $|p_a|_{\max}$ because the diameter of the inclusion is sufficiently small relative to the domain size.

3d experiment

In the second numerical experiment we investigate the evolution of the finite deformation through time of an inclusion-matrix system in a 3d box of dimensions $[-2, 2] \times [-0.5, 0.5] \times [-0.5, 0.5]$. The y- and z-components of the velocity are prescribed to be zero on all boundaries as a 3d non-steady extension to the previous 2d steady-state inclusion problem. The box is subject to dextral shearing by prescribing the x-velocity to be 1.0 on the top boundary and -1.0 on the bottom boundary. The x-velocity varies linearly with respect to the z-coordinate for all other boundary faces analogous to the boundary condition 1 in Section 2.3.1. The matrix viscosity η_m is set to 1. Two numerical models are computed, with inclusion viscosity η_p is set to a "more competent" value of 100 for one model and a "less competent" value of 10 for the other. The setup of the model is summarized in Figure 2.4. Tracking particles are generated within and around the inclusion for tracking the finite deformation. Both models are computed up to a shear strain $\gamma = 8$.

	BC 1		BC 2		BC 3	
	This study	Bons et al. (1997)	This study	Bons et al. (1997)	This study	Bons et al. (1997)
Separatrix	6.80×10^{-4}	7.30×10^{-4}	9.29×10^{-4}	9.27×10^{-4}	7.77×10^{-4}	7.72×10^{-4}
D_{sp}	2.34	2.62	n/a	n/a	3.23	3.42
D_s	1.91	1.87	n/a	n/a	0.90	0.89
$\lvert p \rvert_{\max}$	2.021	n/a	1.962	n/a	1.982	n/a

Table 2.1: Quantitative comparison between results obtained by Bons et al. (1997) and that measured from our study for boundary conditions (BC) 1, 2 and 3. See text for discussions.

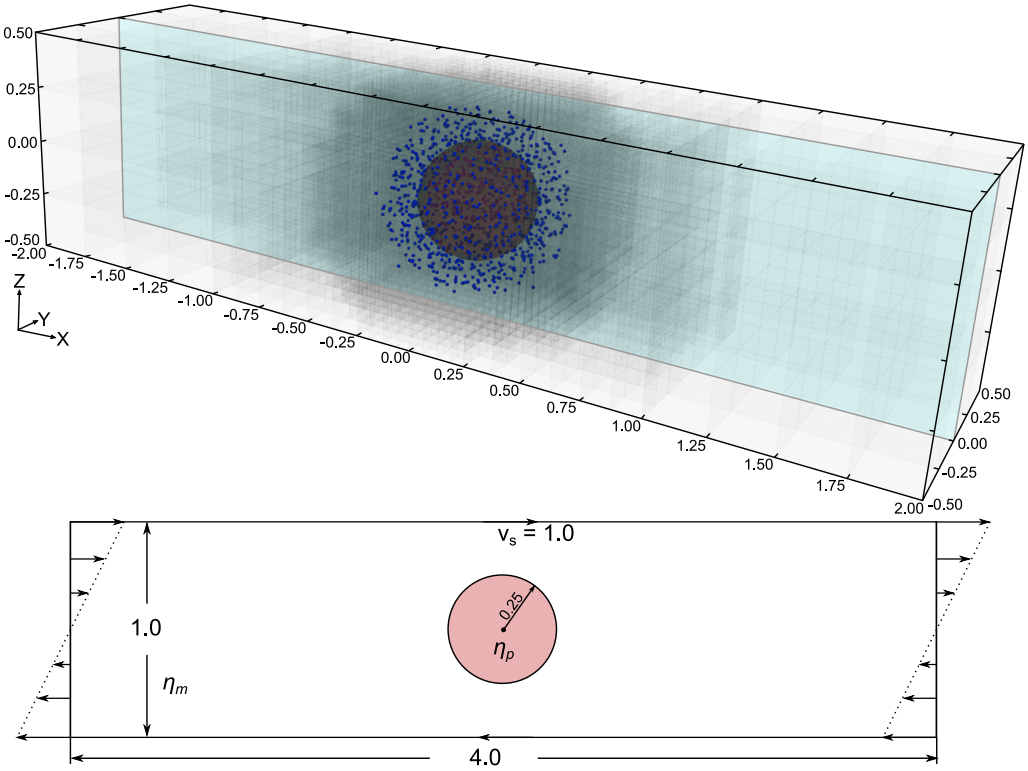
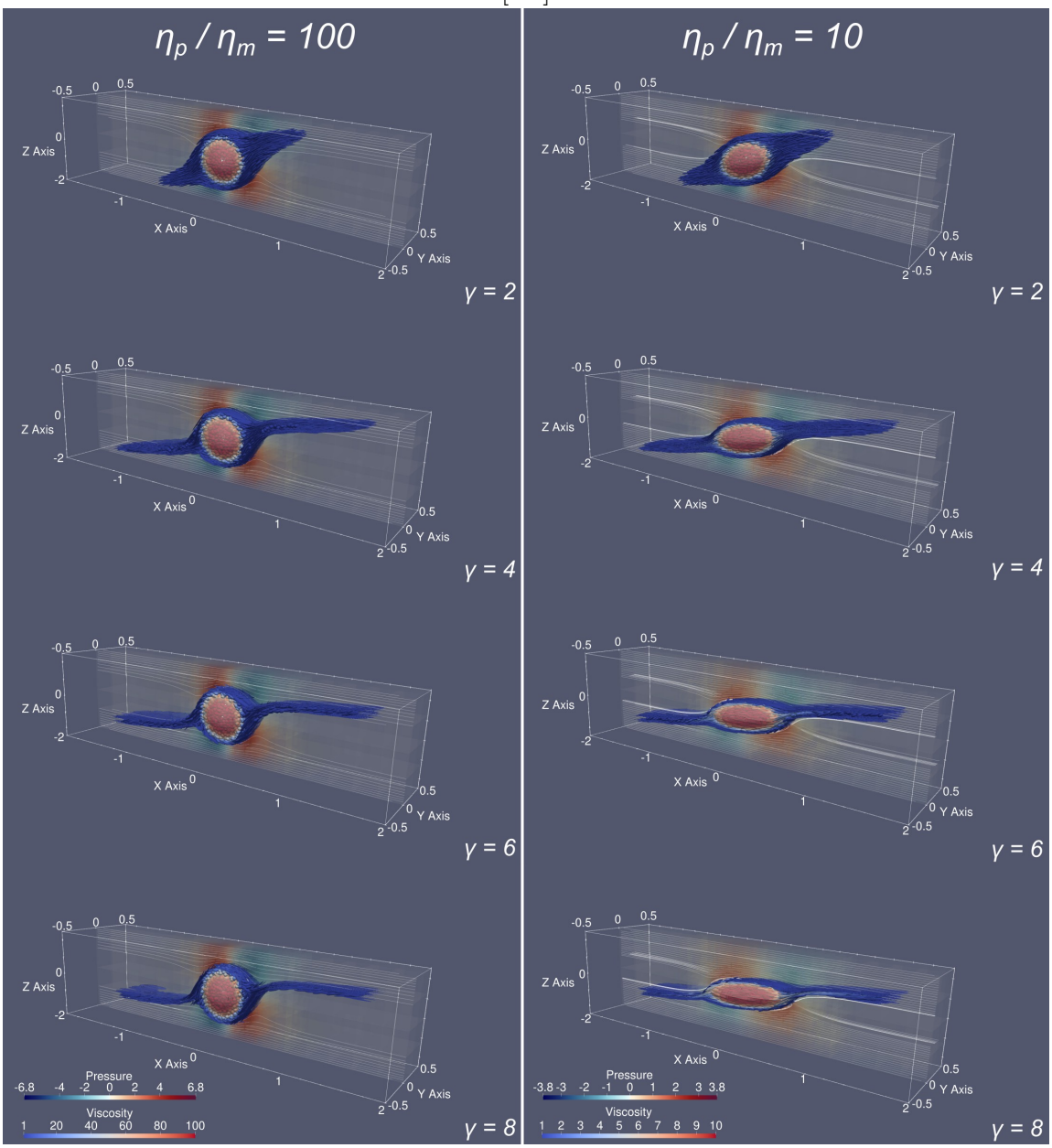


Figure 2.4: Model setup of a 3d deformable inclusion under simple shear. Upper: the 3d shear box setup at $t = 0$. The deformable inclusion (shown in dark red) is centred at the origin of the shear box. Blue dots are the tracking particles generated around the inclusion. Lower: A cross-section across the centre of the shear box which corresponds to the light blue plane in the upper diagram.

The snapshots of our results are shown in Figure 2.5. The modelling results show contrasting long-term deformation patterns for different inclusion viscosities. The results show that the behaviour of both inclusion-matrix systems are consistent with the geological understanding, which we describe as follows.

Figure 2.5 ***(following page)*:** Snapshots of the deformation for a 3d deformable inclusion in a shear box up to a shear strain $\gamma = 8$ for $\eta_p/\eta_m = 100$ (subfigures (a) to (d)) and $\eta_p/\eta_m = 10$ (subfigures (f) to (i)). The tracking particles are coloured by the viscosity value. The ellipsoids attached to the tracking particles are strain ellipsoids. The streamlines (in white) and pressure (represented by the colour shading) are plotted on an xz slice plane through the origin. Subfigures (e) and (j) show the magnified views of the strain ellipsoids on a 2d cross-section through the origin on the xz-plane for $\eta_p/\eta_m = 100$ and 10 respectively. The strain ellipsoids are coloured by the Flinn's K-value. See text for discussion.

[!ht]


$\eta_p / \eta_m = 100$
$\eta_p / \eta_m = 10$
$\gamma = 2$
$\gamma = 4$
$\gamma = 6$
$\gamma = 8$
Z Axis
X Axis
Y Axis
Pressure
Viscosity

In the case of a "more competent" inclusion ($\eta_p/\eta_m = 100$), the inclusion rotates in the flow and shows minimal internal deformation, as shown in the minimal change of the inclusion geometry and the almost spherical strain ellipsoids within the inclusion (Figure 2.5e). At the incipient stage of the shearing, the matrix material surrounding the inclusion is advected as well as deformed. The combined pattern of the particle clustering and the strain ellipsoid orientations show σ-type asymmetry. As the shearing progresses and more shear strain has accumulated, the bulk rotation of the inclusion exerts drag on the matrix material and the asymmetry gradually evolves into a δ-type. Since under a shear-box-like boundary condition (Boundary Condition 1 in Bons et al. (1997)) backflow regions develop around the inclusion, the δ-type tail in our model shows stair-stepping.

In the case of a "less competent" inclusion ($\eta_p/\eta_m = 10$), the inclusion not only rotates, but at the same time undergoes elongation approximately parallel to the instantaneous stretching axis of the simple shear velocity field and shortening perpendicular to the instantaneous shortening axis. Prolonged deformation accentuates the ellipticity of inclusion and rotates the inclusion until its long axis is almost aligned with the shear direction (x-direction) (Figure 2.5j). Eventually the orientation of the inclusion is stabilized as it continues to undergo deformation by shear flattening. The matrix material around the inclusion shows a σ-type tail at the incipient stage of the model. However, as the rotation of the inclusion gradually halts towards the stable configuration, the matrix material around the inclusion experiences mostly shear-parallel stretching and minimal rotational drag. As a result the tail remains σ-type and does not evolve into a δ-type.

2.3.2 Rayleigh-Taylor instability

The Rayleigh-Taylor instability problem is an abstract model describing the gravity-driven sinking of overlying denser materials in an inverted density profile. Modelling a Rayleigh-Taylor instability is relevant for a number of geological processes, from the origin and growth of mantle plumes (*e.g.* Davaille and Limare, 2015), the evolution of salt diapirs (Fuchs et al., 2011) to the removal of lithospheric mantle by "dripping" tectonics (Göğüş and Pysklywec, 2008; Gorczyk et al., 2012). The Rayleigh-Taylor instability is also likely to be the forming mechanism of the dome-and-keel geometry in Archean granitoid-greenstone terranes (*e.g.* Lin, 2005; Van Kranendonk et al., 2007; Robin and Bailey, 2009; Lin et al., 2013; Wiemer et al., 2018; Bédard, 2018).

We first compute the standard 2d benchmark problem in Section 2.3.2 to show that our results conform with published results with the proper order of convergence

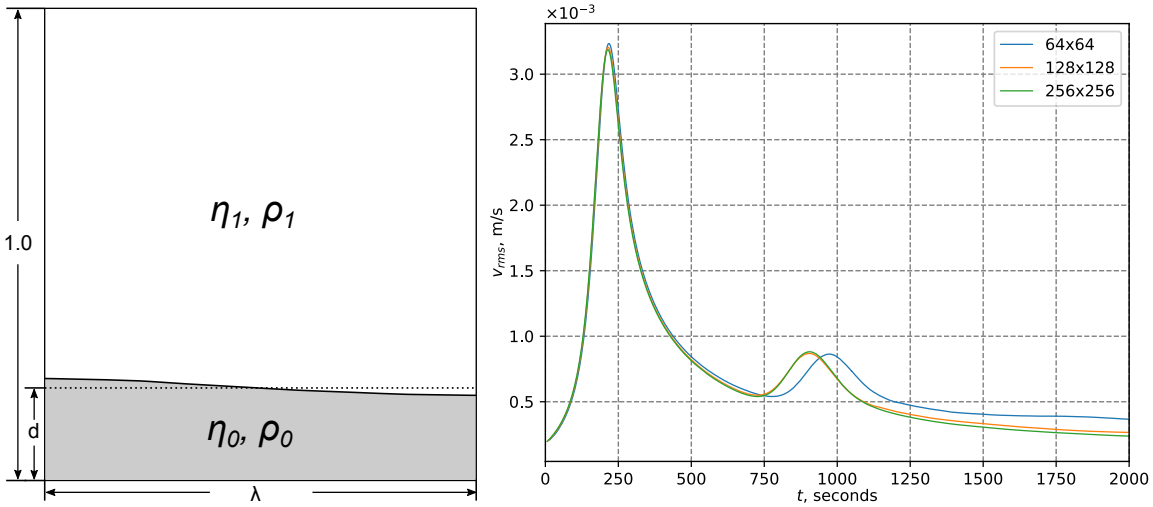


Figure 2.6: Left: Model setup of the 2d Rayleigh-Taylor instability benchmark. Right: The evolution of $\bar{v}$ up to $t = 2000$ for the isoviscous Rayleigh-Taylor instability on a grid with the finest mesh density of 64×64, 128×128 and 256×256.

so as to demonstrate our formulation produces correct results for non-steady tectonic flow with multiple materials. In Section 2.3.2 we compute a 3d Rayleigh-Taylor instability experiment with tracking particles inserted at the material interface to showcase the capability of our method to visualize the finite strain distribution at different stages of the model evolution.

2d benchmark

In this experiment we compute a viscous gravitational instability induced by an initially inverted density profile. The modelling domain is set up as in a rectangular box of height 1.0 and width $\lambda = 0.9142$. The width λ is chosen to maximize the growth rate of an isoviscous diapir (van Keken et al., 1997). In the initial setup a thin layer of buoyant material with density $\rho_0 = 1000$ and thickness 0.2 is placed beneath a layer of denser material with density $\rho_1 = 1010$ and viscosity $\eta_1 = 100$. A sinusoidal perturbation in the form of $y = 0.02\cos\left(\pi x/\lambda\right)$ is applied to the material interface. The top and bottom boundaries of the box are considered to be solid walls ($\boldsymbol{v} = \boldsymbol{0}$). A free-slip boundary condition is prescribed for the left and right boundaries. In two separate experiments, the viscosity of the buoyant layer η_0 is prescribed to be 100 (the isoviscous case) and 10 (the non-isoviscous case). The initial configuration of the model is shown in Figure 2.6. The models are computed

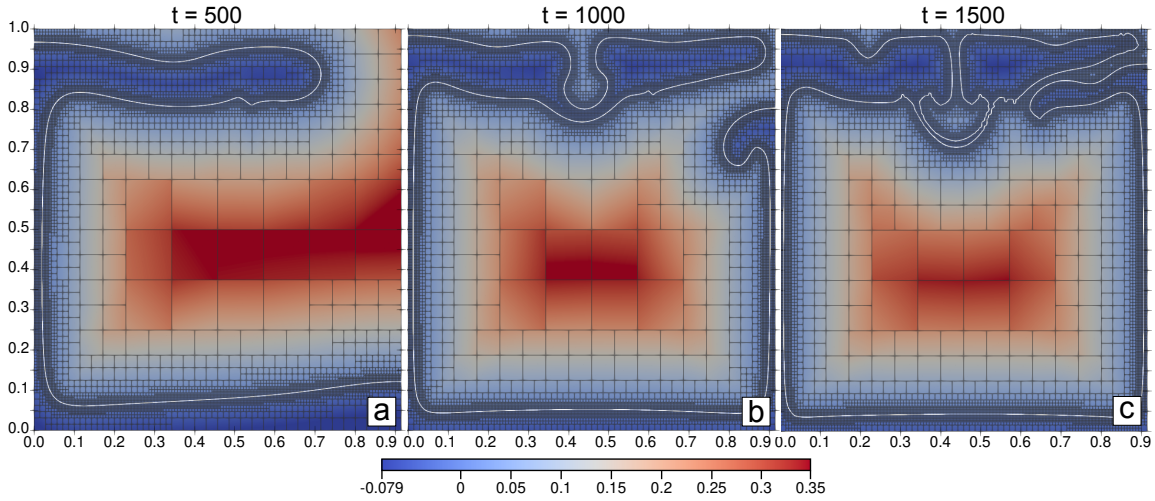


Figure 2.7: Snapshots of the mesh configuration and the level set field of the 2d Rayleigh-Taylor instability benchmark at (A) $t = 500$, (B) $t = 1000$ and (C) $t = 1500$. The solid white line outlines the material interface (the zero level set).

on a base grid of 8×8 and the meshes are successively refined near the interface up to a mesh density equivalent to $N_{\text{max}} \times N_{\text{max}}$ around the material interface. We also compute the volume-normalized velocity norm (root-mean-square velocity) to facilitate comparisons between the published results:

$$\bar{v}(t) = \frac{1}{\text{Vol}(\Omega)} \left[\int_{\Omega} \|\boldsymbol{v}(t)\|^2 \, d\Omega \right]^{1/2} \tag{2.16}$$

For the isoviscous case, the temporal evolution of the $\bar{v}$ is plotted in Figure 2.6 and the level set scalar fields at $t = 500$, $t = 1000$ and $t = 1500$ are shown in Figure 2.7. The velocity-time graph agrees in general trend with previous calculations (*e.g.* Hillebrand et al., 2014; Leng and Zhong, 2011). The results on the 128×128 and 256×256 mesh is almost identical, while the 64×64 mesh substantially deviates from the solution on finer meshes at the second peak. The deviation is attributed to the poor resolution of the interface geometry by the coarse mesh, which results in excessive interface smoothing and hinders the time at which the second gravitational instability event takes place.

To show that our modelling framework produces valid physics, we compare the value of the first peak root-mean-square velocity $\bar{v}_{\text{max}}$ and the time t_{max} at which the peak velocity is attained with established numerical results. A synthesis of published results and our data for both isoviscous and non-isoviscous cases are summarized in

Method	Mesh	$t_{\max}$	$\bar{v}_{\max}$
Tracer-in-cell (Tackley and King, 2003)	64×64	209.9	0.003098
Level set (Hillebrand et al., 2014)	60×60	213.03	0.003091
Level set (Hillebrand et al., 2014)	160×160	209.21	0.003096
Level set (Hillebrand et al., 2014)	240×240	209.19	0.003095
Tracer-in-cell (Samuel and Evonuk, 2010)	60×60	213.72	0.003135
Tracer-in-cell (Samuel and Evonuk, 2010)	120×120	214.04	0.003129
Level set (Samuel and Evonuk, 2010)	60×60	228.88	0.002925
Level set (Samuel and Evonuk, 2010)	120×120	215.87	0.003051
Level set (Samuel and Evonuk, 2010)	240×240	211.52	0.003093
Particle level set[b] (Samuel and Evonuk, 2010)	60×60	215.57	0.003087
Particle level set[b] (Samuel and Evonuk, 2010)	120×120	212.22	0.003109
DG level set, this study	64×64	220.17	0.003200
DG level set, this study	128×128	216.40	0.003185
DG level set, this study	256×256	214.56	0.003181
DG level set, this study	512×512	213.64	0.003175
DG level set, this study	1024×1024	213.18	0.003173
DG level set, this study	2048×2048	212.87	0.003172

Table 2.2: Benchmark results for the isoviscous case ($\eta_0 = \eta_1 = 100$). The mesh density for this study is reported as $N_{\max} \times N_{\max}$. The tracer density is 40 per cell for Tackley and King (2003) and 25 per cell for Samuel and Evonuk (2010).

Method	Mesh	$t_{\max}$	$\bar{v}_{\max}$
Tracer-in-cell (Tackley and King, 2003)	64×64	73.5	0.009285
Trace-in-cell (Samuel and Evonuk, 2010)	60×60	75.86	0.009193
Trace-in-cell (Samuel and Evonuk, 2010)	120×120	72.54	0.009185
Level set (Samuel and Evonuk, 2010)	60×60	78.48	0.009087
Level set (Samuel and Evonuk, 2010)	120×120	75.89	0.009269
Level set (Samuel and Evonuk, 2010)	240×240	73.45	0.009480
Particle level set (Samuel and Evonuk, 2010)	60×60	71.98	0.009375
Particle level set (Samuel and Evonuk, 2010)	120×120	74.07	0.009414
DG level set, this study	64×64	76.62	0.009302
DG level set, this study	128×128	75.52	0.009518
DG level set, this study	256×256	74.97	0.009618
DG level set, this study	512×512	74.44	0.009663
DG level set, this study	1024×1024	74.19	0.009686
DG level set, this study	2048×2048	74.07	0.009698

Table 2.3: Benchmark results for the non-isoviscous case ($\eta_0 = 10$, $\eta_1 = 100$). The mesh density for this study is reported as $N_{\max} \times N_{\max}$. The tracer density is 40 per cell for Tackley and King (2003) and 25 per cell for Samuel and Evonuk (2010).

Tables 2.2 and 2.3. The results show that for both the isoviscous and the non-isoviscous case, the DG level set formulation yields comparable results to previous studies obtained under a different discretization scheme regardless of whether the particle correction is applied or not. The results are also comparable to that obtained from a PIC method where the material information is entirely tracked by the Lagrangian particles.

A convergence test is applied to the results by testing the speed at which the relative difference in $\bar{v}_{\max}$ and $t_{\max}$ under successive mesh density contracts (Shadpour et al., 2015). The relative difference in $\bar{v}_{\max}$ and $t_{\max}$, denoted respectively as $\delta_{\bar{v}}$ and δ_t can be computed with the following expression:

$$(\delta_t, \delta_{\bar{v}})\Big|_{N_{\max}=2^m} = \frac{(t_{\max}, \bar{v}_{\max})\big|_{N_{\max}=2^{m-1}} - (t_{\max}, \bar{v}_{\max})\big|_{N_{\max}=2^m}}{(t_{\max}, \bar{v}_{\max})\big|_{N_{\max}=2^m}} \quad m = 7, 8, \ldots, 11 \tag{2.17}$$

Building upon the relative difference we can then compute the rates of contraction Λ of $\delta_{\bar{v}}$ and δ_t, as follows:

$$(\Lambda_t, \Lambda_{\bar{v}})\Big|_{N_{\max}=2^m} = \frac{(t_{\max}, \bar{v}_{\max})\big|_{N_{\max}=2^{m-2}} - (t_{\max}, \bar{v}_{\max})\big|_{N_{\max}=2^{m-1}}}{(t_{\max}, \bar{v}_{\max})\big|_{N_{\max}=2^{m-1}} - (t_{\max}, \bar{v}_{\max})\big|_{N_{\max}=2^m}} \quad m = 8, 9, 10, 11 \tag{2.18}$$

The convergence rate, shown in Table 2.4, reveals that both δ_t and $\delta_{\bar{v}}$ contracts at the same rate with respect to mesh density. Hence, our numerical formulation is overall linearly convergent. This is expected from the fact that we use $\mathcal{P}^1$ basis for the DG level set solver. This result is also in agreement with the linear rate of convergence observed in the Zalesak's disk benchmark in Appendix C. The result offers assurance that the application of the limiter does not degrade the overall rate of convergence of the numerical scheme. In summary, our results confirm that the level set formulation under DG discretization is numerically convergent and as effective as other methods for modelling multi-material geodynamic flow.

3d experiment

We compute a 3d Rayleigh-Taylor instability to showcase the capability of our numerical scheme to track finite deformation by extending the previous 2d Rayleigh-Taylor benchmark to 3d. The model is constructed in a $[0, 1]^3$ cube with a sinusoidally perturbed material interface described as:

$$z = 0.02\left(\cos(\pi r) + 1\right) + 0.2 \tag{2.19}$$

	$\eta_1/\eta_0 = 1$				$\eta_1/\eta_0 = 10$			
$N_{\max}$	δ_t	Λ_t	$\delta_{\bar{v}}$	$\Lambda_{\bar{v}}$	δ_t	Λ_t	$\delta_{\bar{v}}$	$\Lambda_{\bar{v}}$
2^7	1.22×10^{-2}	—	9.36×10^{-3}	—	1.93×10^{-3}	—	2.22×10^{-2}	—
2^8	4.58×10^{-3}	2.67	5.96×10^{-3}	1.58	1.01×10^{-2}	1.92	9.98×10^{-3}	2.20
2^9	2.01×10^{-3}	2.28	3.15×10^{-3}	1.90	6.99×10^{-3}	1.46	4.86×10^{-3}	2.04
2^{10}	2.23×10^{-3}	0.90	9.43×10^{-4}	3.33	3.37×10^{-3}	2.08	2.37×10^{-3}	2.04
2^{11}	1.35×10^{-3}	1.65	4.71×10^{-3}	2.00	1.68×10^{-3}	1.97	1.18×10^{-3}	2.01

Table 2.4: Convergence analysis for the 2d isoviscous and non-isoviscous Rayleigh-Taylor instability.

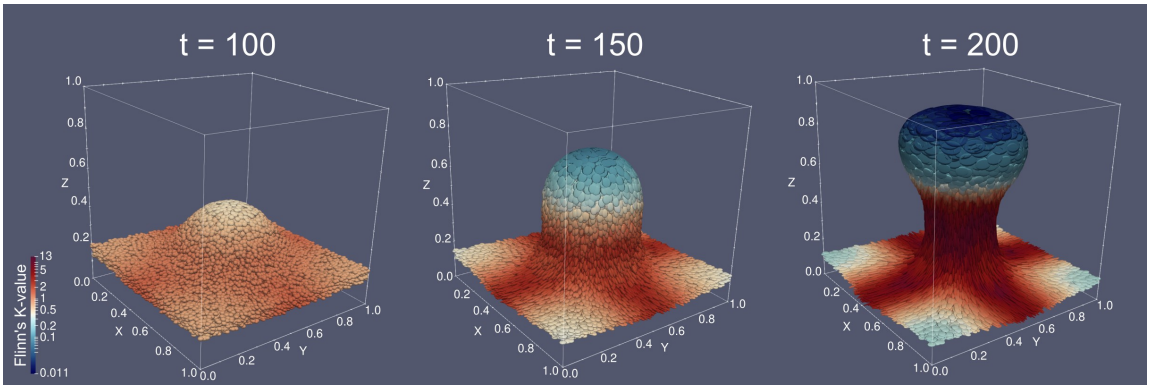


Figure 2.8: The finite strain distribution of a 3d isoviscous Rayleigh-Taylor instability at $t = 100$ (left), 150 (middle) and 200 (right). The ellipsoidal markers are strain ellipsoids coloured by Flinn slope K. The red colour range implies constrictional strain, while the blue colour range indicates flattening strain.

where $r(x, y) = \sqrt{(x - 0.5)^2 + (y - 0.5)^2}$ is the distance to the centre of the xy-plane. The boundary conditions are all free slip except for the top and bottom, where they are considered as solid walls ($\boldsymbol{v} = \mathbf{0}$). The material distribution closely resembles that of the isoviscous case of the 2d Rayleigh-Taylor benchmark. A density of 1010 is prescribed to the material above the material interface given in Equation (2.19) and 1000 to that below the interface. The viscosity is prescribed to be 100 throughout the domain.

Three snapshots of the model up to $t = 200$ are shown in Figure 2.8. In these snapshots, in addition to the geometry of the rising diapir, the strain ellipsoids are also shown at the material interface coloured by their Flinn's K-value. A red colour represents a stretching strain while a blue colour is used for flattening strain. In

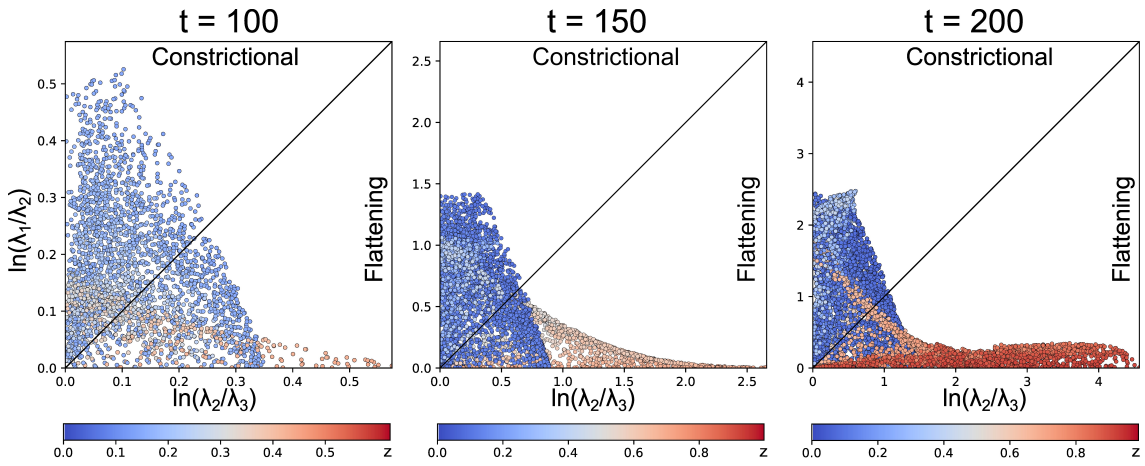


Figure 2.9: The Flinn diagram of the strain ellipsoids at the interface between the denser material on top and the lighter material below in the 3d isoviscous Rayleigh-Taylor instability test case. The model snapshots are taken at $t = 100$ (left), $t = 150$ (middle) and $t = 200$ (right). The marker points are coloured by their z-coordinates: $z = 0.0$ corresponds to the deepest level (bottom) of the model, while $z = 1.0$ corresponds to the top surface of the model. The diagonal line in each subfigure is the line of plane strain. The area above the line of plane strain represents constrictional strain while the area below the line has a flattening type of strain.

Figure 2.9, the strain ellipsoids are also plotted on the Flinn diagram in with respect to their depths (*i.e.* the z-coordinates). At $t = 0$ the strain ellipsoids are strain-free and therefore spherical. As the gravitational instability evolves, the areas at the "neck" and the bottom part of the model experiences constrictional strain in the vertical and horizontal directions due to the upward drag by the rising of the buoyant material situated at the lower part of the model. At the same time, the head of the diapir experiences compression at the material interface as the upper part of the diapir expands outwards and pushes the surrounding denser material sideways. In Figure 2.9 the same trend is revealed as the particles at deeper levels in the model show predominantly stretching strain and therefore favourable for developing lineation, while the particles at the diapir head preferentially develops strong foliation parallel to the material interface. Both lineation and foliation patterns are radially symmetric. The foliation is shallowly dipping in the centre of the diapir and gradually steepens towards the periphery of the diapir.

2.3.3 Sheared 3d Rayleigh-Taylor instability

The Rayleigh-Taylor experiments in Section 2.3.2 describe the idealized gravity-propelled density inversion processes where the material motion is predominantly vertical. Indeed, the structural pattern is overall consistent with that observed in the Archean granitoid-greenstone terranes where the partial density overturn is interpreted to be the dominant mechanism shaping the crustal architecture (*e.g.* Collins, 1989). However, in a realistic situation the vertical tectonic motion takes place under the influence of a background tectonic stress with a horizontal component. For example, in the Neoarchean terranes, evidence for horizontal and vertical tectonics coexist, and it is proposed that crustal scale density inversion may have operated simultaneously with horizontal tectonic strain (Lin, 2005; Chardon et al., 2002). The latter can be the result of far-field tectonic stress transmitted from the oblique convergence in a modern-day-like plate tectonics processes. In this experiment we construct a numerical experiment to simulate the simultaneous operation of the Rayleigh-Taylor instability and a horizontal simple shearing imposed as a boundary condition. Our primary purpose here is not to test interpretations on Archean tectonics, but to demonstrate that our modelling method can be applied to tectonic problems on a prescribed scale and can produce structural predictions readily comparable to field data, which would otherwise be impossible for 2d numerical models and prohibitively complicated for analytical solution. The bedding information and the interface geometry is difficult to obtain straight-forwardly with a particle-in-cell modelling approach. A description of the model results under different viscosity and boundary conditions, as well as an in-depth discussion of the implications for Archean tectonics is beyond the scope of this paper.

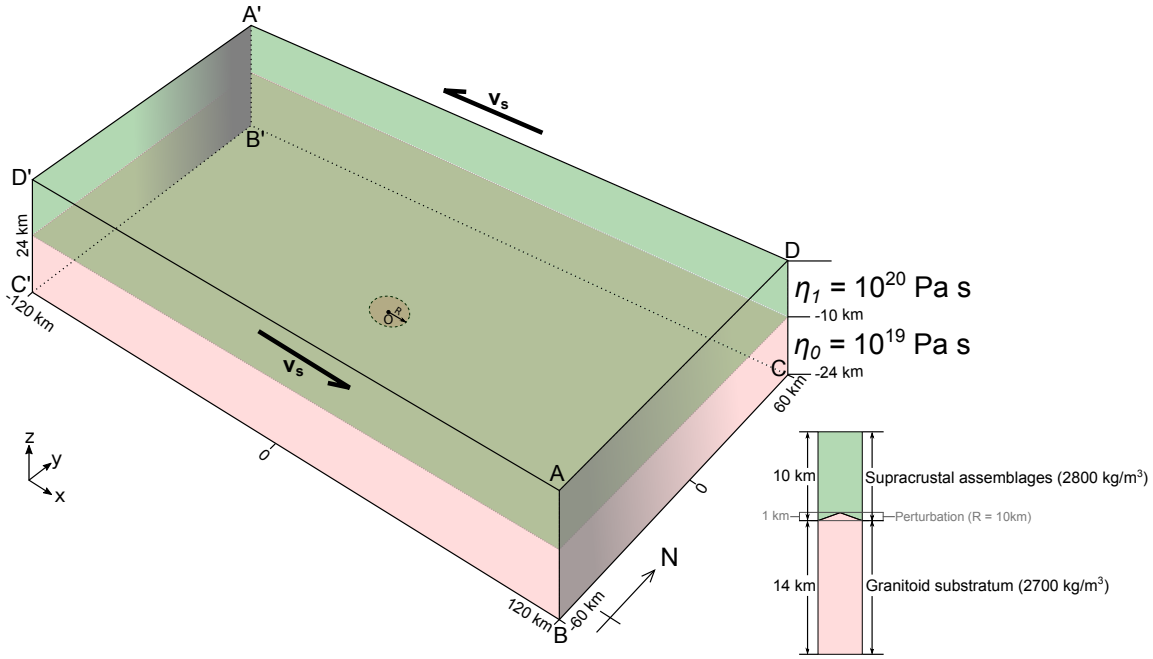


Figure 2.10: Model setup for the two-layer 3d Rayleigh-Taylor experiment with a sinistral shearing boundary conditions. v_s is the magnitude of the prescribed boundary shear velocity. The eastern and western boundary conditions are periodic with a reflection such that points A, B, C and D on the eastern boundary correspond to A', B', C' and D' on the western boundary respectively.

The model setup is illustrated in Figure 2.10. A box-shaped domain of dimensions $2.40 \times 10^2\,\text{km} \times 1.20 \times 10^2\,\text{km} \times 2.40 \times 10^1\,\text{km}$ is constructed. The geological model consists of a dense and competent supracrustal "greenstone" unit overlying a more buoyant and less viscous granitoid substratum. The upper layer and lower layer has a constant density of $2.80 \times 10^3\,\text{kg/m}^3$ and $2.70 \times 10^3\,\text{kg/m}^3$, respectively. Both units are horizontally layered except for a perturbation of radius $1.00 \times 10^1\,\text{km}$ and height $1.00\,\text{km}$ placed at the centre of the boundary between two units. Due to positive buoyancy of the granitoid intrusion, a density inversion will be initiated. The viscosity of the supracrustal assemblages η_1 is set to $1.00 \times 10^{20}\,\text{Pa}\cdot\text{s}$ to represent the typical conditions of the upper crust. The viscosity of the granitoid substratum (η_0) is set to be one order of magnitude lower than the supracrustal assemblage ($1.00 \times 10^{19}\,\text{Pa}\cdot\text{s}$) to simulate a relatively "soft" middle to lower crustal material granitoid rocks of typical tonalite-trondhjemite-granodiorite (TTG) composition.

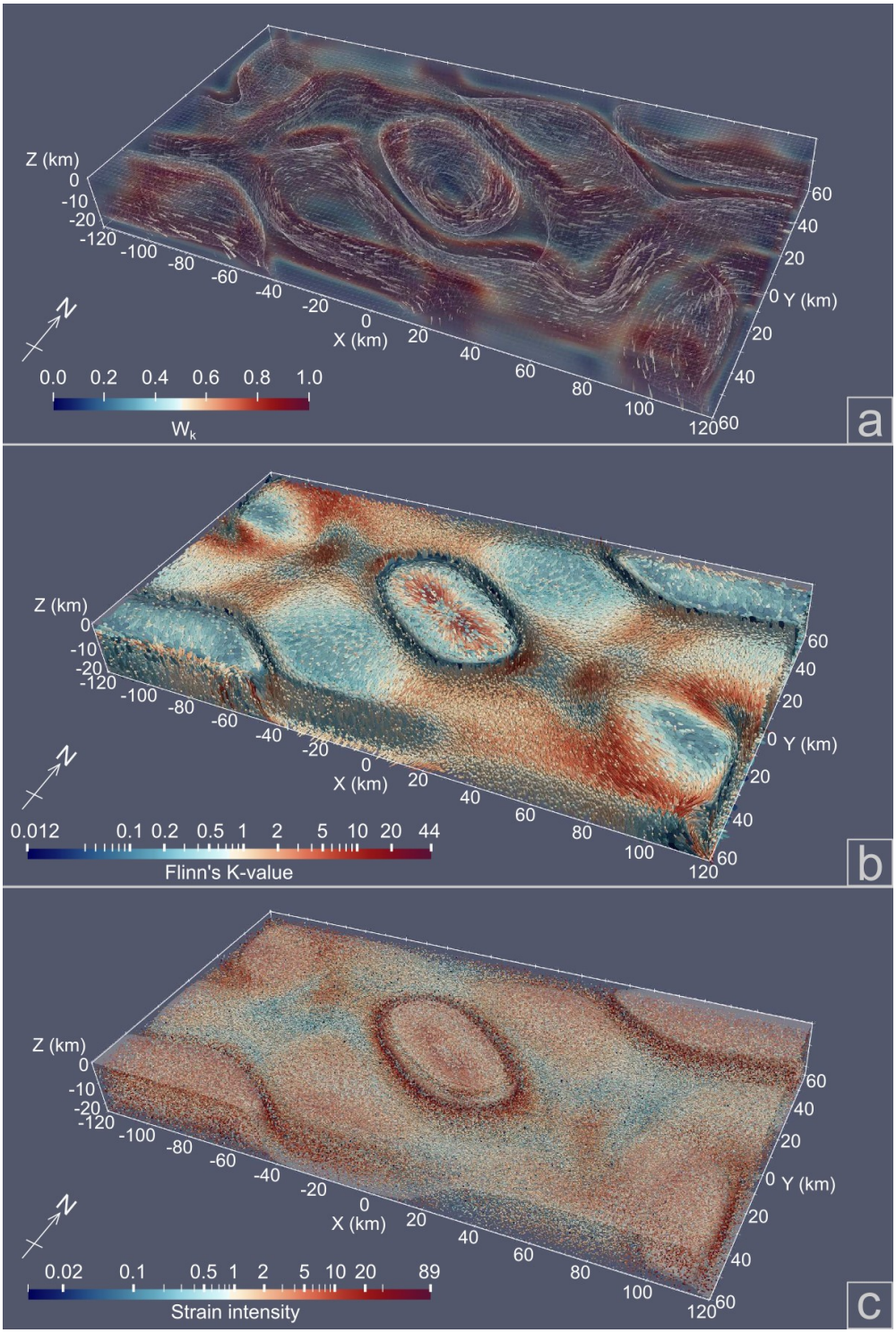
The boundary conditions of the model are set as follows. The top and bottom boundaries are both free-slip boundaries. The northern and southern boundaries have prescribed x-velocity of value $+v_s$ and $-v_s$, respectively. The eastern and

western boundaries are periodic boundaries with a reflection with respect to xz-plane model to be consistent with a monoclinic asymmetry due to the simple shear boundary conditions. In our experiment the magnitude of the shear velocity v_s is set to 5.00×10^{-1} cm/yr, equivalent to a crustal shear strain rate of 8.30×10^{-8}/yr which is on the same order of typical background strain rate of the continental crust under modern day plate tectonics (Xiong et al., 2021).

As the model evolves, the denser supracrustal assemblage sagducts into the deeper crustal level forming synclinal keels while the granitoid substratum upwells into the higher crustal levels and expands laterally. At the same time, the geometry of the granitoid intrusion is affected by sinistral shear and demonstrate an elongated geometry in the NW-SE direction due to the shear-induced elongation in this quadrant. This is in contrast with the radial symmetric diapir geometry in the 3d Rayleigh-Taylor instability without the simple shear boundary condition (Figure 2.8). To analyse the strain distribution, at the time ($t_{\max} = 1.18 \times 10^{1}\ Ma$) when the peak root-mean-square velocity ($\bar{v}_{\max} = 1.76 \times 10^{-8}$ cm/yr) is attained, we show the distribution of kinematic vorticity and the magnitude-scaled vorticity vector in Figure 2.11a, the strain ellipsoids coloured by Flinn's K-value in Figure 2.11b and the strain intensity distribution N in Figure 2.11c. The kinematic vorticity shows that strong non-coaxial rotation is concentrated at the granitoid-supracrustal assemblage boundary, while in the sagducted keels of the supracrustal rocks the strain is mainly coaxial compression or stretching. This pattern is also reflected in the finite strain distribution, where the strain ellipsoids in the greenstone keels mainly show a flattening geometry. The vorticity vectors (Figure 2.11a) clearly demonstrate granitoid-up/greenstone-down sense of shear at the granitoid-greenstone contact. Because the density inversion is a quick process, large amount of strain is accumulated at the granitoid-greenstone boundary (Figure 2.11c) as manifested by the high value of N.

Although the results obtained from the numerical model is in 3d, we acknowledge that the data collected from the field survey typically resides on a 2d plane representing the present day ground surface, above which the crustal material is eroded away.

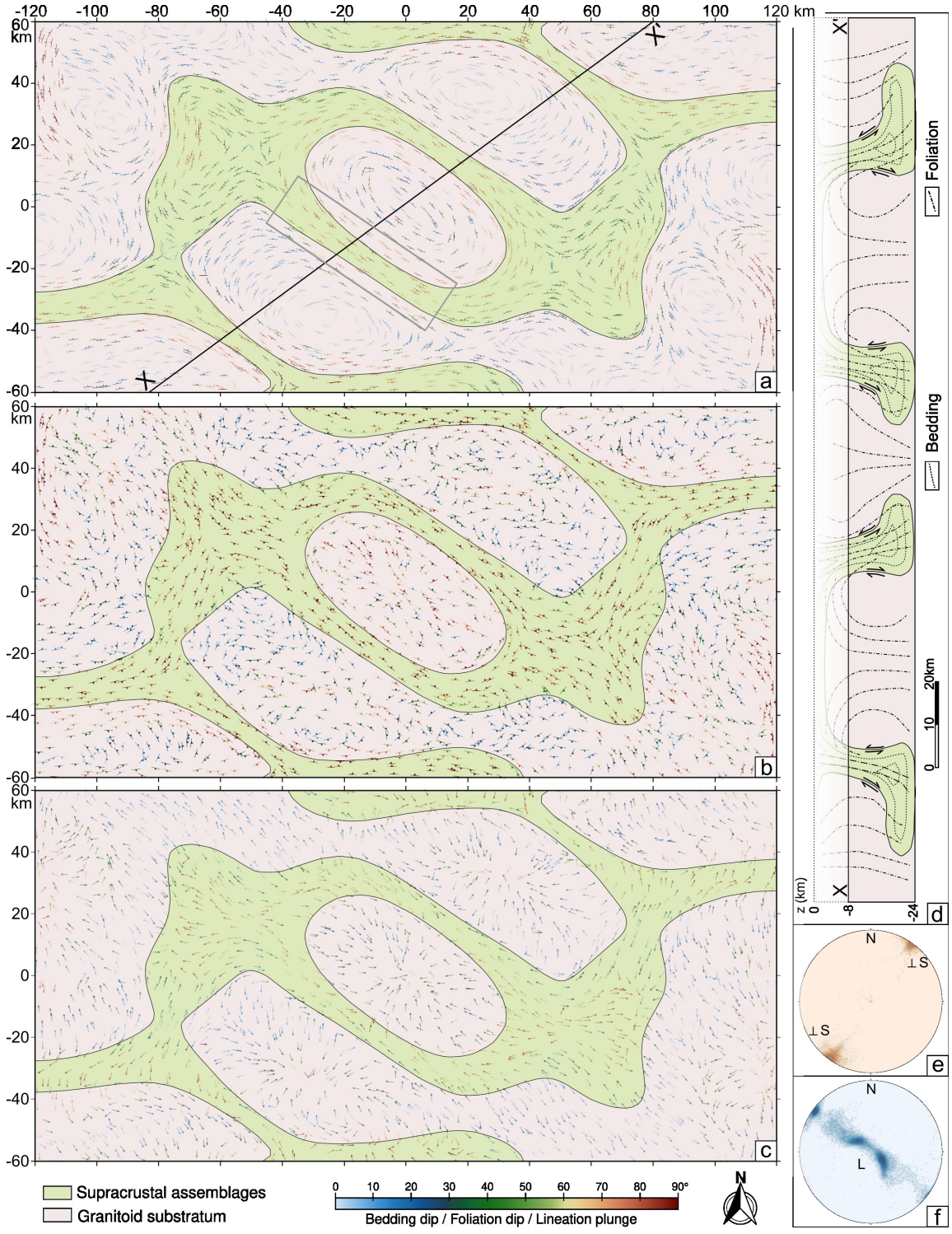
Figure 2.11 ***(following page)*:** Model results for the sheared 3d Rayleigh-Taylor instability at peak root-mean-square velocity. In (a), the faint white wireframe delineates the interface between the greenstone supracrustal assemblages and the granitoid substratum. The colour shading corresponds to the value of the kinematic vorticity number W_k value. The conical arrows are the orientations of the vorticity vectors $\boldsymbol{\omega}$ scaled by their magnitude. The computation procedures of $\boldsymbol{\omega}$ and W_k are discussed in detail in the second paragraph of Section 2.2.3. (b) shows the geometry of the strain ellipsoid coloured by the Flinn's K-value computed by Equation (2.12); (c) shows the 3d distribution of the strain intensity N computed by Equation (2.13).


Z (km)
0
-10
-20
-120
-100
-80
-60
-40
-20
0
X (km)
20
40
60
80
100
120
60
40
20
0 Y (km)
20
40
60
0.0 0.2 0.4 0.6 0.8 1.0
W_k
a
Z (km)
0
-10
-20
-120
-100
-80
-60
-40
-20
0
X (km)
20
40
60
80
100
120
60
40
20
0 Y (km)
20
40
60
0.012 0.1 0.2 0.5 1 2 5 10 20 44
Flinn's K-value
b
Z (km)
0
-10
-20
-120
-100
-80
-60
-40
-20
0
X (km)
20
40
60
80
100
120
60
40
20
0 Y (km)
20
40
60
0.02 0.1 0.5 1 2 5 10 20 89
Strain intensity
c

Assuming the erosion level is known from the knowledge of the regional geology, we can then construct a slice plane of the 3d model at that depth. The lithological distribution and the structural pattern on that 2d plane is directly comparable to field survey data. To demonstrate this process, a slice surface is constructed at a depth of 8.00 km of the 3d model. The depth of the slice plane is so chosen because most Archean greenstone terranes display a greenschist facies metamorphism. On top of the lithological pattern, orientation of the primary structures (S_0, also see Section 2.4.1), the foliation and the lineation are respectively shown in Figure 2.12a, Figure 2.12b and Figure 2.12c along with the lithological pattern. A simulated geological cross-section approximately perpendicular to the regional NW-SE structural grain is also constructed in Figure 2.12d. Local lineation and foliation patterns in a greenstone keel SW of the central granitoid dome are shown in the stereonets in Figure 2.12e and Figure 2.12f. The primary structures, which can be interpreted as the bedding in the supracrustal assemblages and pre-tectonic subhorizontal foliation in the granitoid substratum, show that the greenstone keel corresponds to regional syncline while the granitoid dome forms the core of the regional anticline.

The finite strain patterns in the keels of the supracrustal rocks west-southwest of the granitoid dome is analysed in detail (with the approximate location shown in Figure 2.12a). The stereographic projection of the poles to the foliation (Figure 2.12e) shows that the foliation in the keel is mostly steeply-dipping and strike in a NW-SE direction subparallel to the adjacent granitoid-greenstone boundary. The lineation orientation (Figure 2.12f) is scattered along the great circle defined by the local average foliation orientation and shows two point maxima that are moderately to steeply plunging. The moderate to steep plunge angle of the lineation is likely the result of the vertical sagduction movement. Meanwhile, the horizontal shearing component contributes to the scattering of the lineation pattern along the big circle trace and grouping of the lineation orientations into two point maxima. This structural

Figure 2.12 ***(following page)*:** Simulated geological map with structural patterns of the sheared 3d Rayleigh-Taylor instability model on a horizontal slice at 8.00 km depth. The structural patterns shown in (a), (b) and (c) are respectively the primary structures (subhorizontal planar markers before deformation, *e.g.* bedding), the foliation and the lineation. (d) is a geological cross-section along the line XX', the location of which is delineated in (a). The shear sense at the granitoid-greenstone boundary is extrapolated from the vorticity vector in Figure 2.11a. Because the simulated geological maps in (a), (b) and (c) are constructed at 8.00 km depth, the geological material above $z = -8.00$ km (shown in faint colours) is considered to have been removed due to erosion and no longer visible in the field. (e) and (f) are stereographic projections of the poles to foliation ($\perp$S) and lineation (L) measurements in the synclinal keel with location shown by the grey rectangle in (a).


-120 -100 -80 -60 -40 -20 0 20 40 60 80 100 120 km
60 km 40 20 0 -20 -40 -60
X
X'
a
b
c
Foliation
Bedding
0 10 20km
z (km)
0 -8 -24
d
N
⊥S
⊥S
e
N
L
f
Supracrustal assemblages
Granitoid substratum
0 10 20 30 40 50 60 70 80 90°
Bedding dip / Foliation dip / Lineation plunge
N

pattern is comparable to that observed in Neoarchean greenstone belts where both horizontal and vertical tectonic processes are postulated to operate synchronously on Earth (Lin, 2005; Lin et al., 2013), detailed discussion of which is beyond the scope of this contribution.

2.4 Discussion and conclusions

2.4.1 Geological interpretation of the level set field

Besides being an identifier of material domains, the level set field in our modelling approach contains geometric information that can be helpful for interpreting the modelled deformation patterns. For example, in a crustal-scale model where the initial layers of material domains correspond to the pre-deformation stratigraphic units, the orientation of the level set isosurfaces can be interpreted as the orientation of the primary structures, or S_0 (*e.g.* sedimentary beddings). The deformation-induced curving and distorting of the isosurface can be interpreted as the regional folding of the beddings of the stratigraphy units. The orientation of the bedding can be extracted by taking the gradient of the level set function ($\boldsymbol{\nabla}\phi$). Assuming the level of erosion is available from the knowledge of the local geology (*e.g.* mineral assemblages and or thermodynamic modelling) a 2d cut surface at that erosional level can be constructed within the 3d model which shows the lithological distribution and the bedding orientation on that particular 2d surface. Such data can be compared with the present-day geological map pattern and field bedding measurement as a validation for the modelled results. Moreover, the level set field itself represents the distance to the material interface, therefore making our approach suitable for exploring the relationship between variations of structural patterns with respect to distance to the lithological boundaries.

As a side note, one can also extract the curvature of the material interface by taking the Laplacian of the level set field ($\nabla^2\phi$). The boundary curvature is related to the boundary mobility and therefore controls the rate of grain boundary migration (GBM) in microstructure simulations (Humphreys and Hatherly, 2004, Chapter 5).

2.4.2 Geological interpretation on deformation analysis

We remark that compared to the pure kinematic modelling approaches which frequently utilizes the assumption of a steady-state velocity gradient $\boldsymbol{L}$, our formulation

has the ability to incorporate non-steady and inhomogeneous deformation states by allowing $\boldsymbol{L}$ to vary naturally as the strain state changes with the material flow. The finite deformation field is the direct integration of the instantaneous deformation field as the tracer particles are advected through the model. In this way by incorporating the full dynamics, our approach simulates deformation patterns in a more general sense than the traditional kinematic modelling. In fact, the latter can be considered as a steady-state approximation in a small enough interval in both space and time from the viewpoint of a model with complete dynamics.

The foliation and lineation patterns obtained from our modelling formulation are based upon the assumption that the lineation and the pole to foliation always follow the principal strain axes of the local strain ellipsoids. However, we acknowledge that this assumption is by itself a simplification because the alignment of the lineation- or foliation-defining mineral grains does not necessarily track the principal axes of the local strain ellipsoid in a precise and predictive manner. To probe into the microstructural evolution of the deformation fabric at each tracer particle, our modelling method framework can couple with an efficient solver based on micromechanics to model such processes on a finer scale (Jiang and Bentley, 2012). Furthermore, the information about the strain ellipsoids can not only be compared to the field-observable alignment of minerals, it can also be extended to strain ellipsoid geometry obtained through other techniques *e.g.* the anisotropy of magnetic susceptibility (AMS) measurements (Benn, 1994).

Because the deformation field that the numerical model takes into account is not steady-state, the structural patterns recorded on the particles are dependent upon the interval in time through which the deformation is recorded. Taking the quartz crystals deformed in a ductile shear zone as an example, in the temperature regime of subgrain rotation recrystallization, large quartz porphyroclasts are transformed into ribbon grains and meanwhile newly born recrystallized grains will emerge (Stipp et al., 2002). If we spread particles evenly throughout the domain, then the particle corresponding to the recrystallized grain will have to reset its $\boldsymbol{F}$ when the recrystallization takes place, while those corresponding with the ribbon porphyroclast will keep recording $\boldsymbol{F}$ for a longer period of time (Means, 1981). The same situation also applies to geological bodies on outcrop or even regional scale (*e.g.* boudinage of veins and dykes). Unfortunately, a widely accepted criteria as to the choice of this time interval is problem dependent and the modeller is cautioned to take this into consideration when interpreting the modelled structural pattern.

We also caution that the vorticity-related quantities (*e.g.* kinematic vorticity W_k) herein obtained are computed on a stationary Eulerian coordinate and therefore not

objective. Direct usage of such quantities for determining flow classification and understanding fabric development may be invalid unless corrections are made for external vorticity caused by the spin of the ISA (Astarita, 1979; Means et al., 1980). One algorithm for implementing such corrections using the ISA as a reference is proposed by Jiang (1999).

2.4.3 Summary and future extensions

In this study we have developed a modelling scheme by coupling a level set solver with DG discretization for capturing material interface and a finite element solver for resolving flow dynamics. A combination of Eulerian mesh and Lagrangian tracer particles allows us to model large deformation without sacrificing the capability to track deformation history. A complete set of kinematic information from the instantaneous flow field as well as the finite deformation field can be extracted from the numerical model, making it well-suited for analysing spatially and temporally variant structural responses as a result of the processes on a larger scale and the partitioning of larger-scale tectonic movement into material domains with contrasting mechanical properties. Our model technique also provides the possibility for ground-truthing tectonic models by comparing field observations of the geological map patterns, the strain distribution and the structural patterns with model predictions of material domain geometries and deformation patterns, thus building the bridge between abstract numerical models and concrete field evidence.

Our implementation serves as a proof of concept of integrating DG-discretized level set method into a modelling framework for tectonic flow and is therefore simplified in many aspects. However, this modelling method can be further developed in many ways, making it possible to simulate real world tectonic problems with ever more challenging physical complexities. Future improvements and extensions of the modelling framework will proceed in the following directions:

1. Implementation of more realistic rheological models. This includes, for example, a nonlinear (power-law) viscosity model for dislocation creep processes, evolving anisotropic mechanical properties due to the preferred alignment of minerals in the flow (*e.g.* Ran et al., 2019; Mühlhaus et al., 2003; Lev and Hager, 2008) and temperature-dependent viscosity model by coupling with a convection-diffusion solver for heat transport.

2. Communicating the deformation field from our tectonic modelling approach to an efficient analytical microstructural solver for fabric development and lattice

preferred orientations (*e.g.* Jiang and Bentley, 2012; Jiang, 2016). With this coupling scheme, a direct correlation of deformations across multiple scales can be made possible.

Chapter 3

Neoarchean synchronous vertical and horizontal tectonism in the southern Swayze greenstone belt, Superior Province: Insights from structural analysis and numerical modelling

3.1 Introduction

The crustal dynamics of the Neoarchean Earth, especially in granitoid-greenstone terranes showing a dome-and-keel geometry, has remained a controversial topic. Due to the elevated heat flow and the softened crustal strength for the early Earth and a lithological architecture with an inverted density profile, the Neoarchean crust may experience a "vertical" tectonism in the form of gravitational overturn (also known as *sagduction/diapirism*, *Rayleigh-Taylor instability* or *partial convective overturn*) (*e.g.* Wiemer et al., 2018; Van Kranendonk, 2011; Hamilton, 1998; Chardon et al., 1996; Collins, 1989; Lin et al., 2013; Zhao et al., 2021). On the other hand, it is argued that Neoarchean crust has enough strength not only to inhibit the development of gravitational overturn, but also to sustain the long-distance transmission of far-field regional tectonic stress, and therefore it is not necessary to explain the geom-

etry of the Neoarchean terranes by invoking non-uniformitarian processes (*e.g.* van der Velden et al., 2006; de Wit, 1998; Kusky and Polat, 1999).

If we recognize the above-mentioned regimes of crustal dynamics as two end members of an evolving spectrum from the early Earth to the present day due to the secular dissipation of primordial heat, a transitional style of crustal deformation pattern is postulated to have existed in between where the crust exhibits coexisting structural signatures of both tectonic regimes (Lin, 2005, 2007). From the standpoint of structural analysis, how this transition of crustal dynamics is manifested in the rock record (*e.g.* the spatial distribution of lithological units and the structural patterns) is of profound interest to field geologists.

In conjunction with the transition in crustal dynamics, the lithospheric-scale tectonic processes of the Earth on a larger scale was also undergoing transition from the possible bottom-up stagnant-lid-type tectonics to a top-down plate tectonics-like process in Archean or early Proterozoic (Bédard, 2018; Harris and Bédard, 2014; Johnson et al., 2014), although the exact temporal bracket of this transition remains debatable. Understanding how the crustal deformation style fits into the grand scheme of lithospheric-scale tectonic evolution constitutes a vital stroke in painting a detailed picture of the secular evolution of our planet's tectonic style.

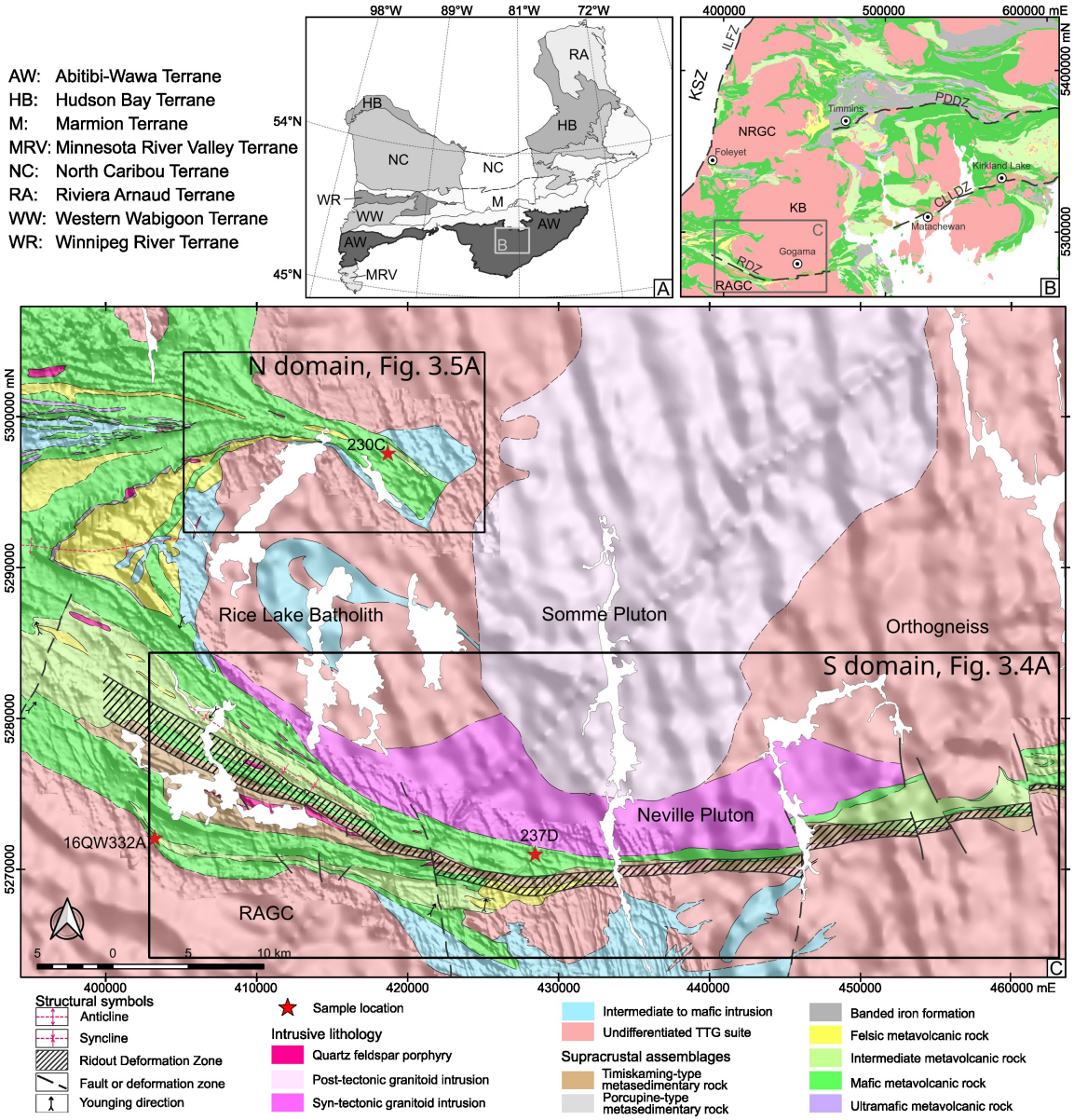
In this study, we provide insights into one example of this transitional style of crustal dynamics by conducting structural investigation in the Neoarchean Swayze greenstone belt (SGB) located in the southeastern Superior Craton (Section 3.3). To demonstrate that the structural pattern is likely the result of the simultaneous operation of gravitational instability and the far-field transmission of regional tectonic stress in the form of dextral shearing, we compare the lithological distribution and the structural pattern obtained from field mapping to a 3d crustal-scale numerical model where both "vertical" and "horizontal" tectonism are taken into account in the model configuration (Section 3.4). We show that various aspects of field mapping results can be reproduced in the numerical model, thus providing a viable explanation for the general deformation pattern and lithological distribution in the SGB. We argue, based on the coexistence of both tectonic processes, that the structural evolution of the SGB and possibly other Neoarchean terranes bear witness to the transition in crustal dynamics as the Earth dissipates heat and evolves from a vertical tectonism to present-day horizontal tectonism, as is first proposed in Lin (2005). Under the backdrop of a tectonic shift in the Superior Craton in Neoarchean documented in multiple studies (*e.g.* Mathieu et al., 2023; Mole et al., 2021), our study presents one example of the deformation pattern when a transition in tectonic regime takes place both on the crustal and the lithospheric scale (Lin, 2007).

3.2 Geological settings

The Archean Superior Craton (Figure 3.1A) consists of multiple subprovinces interpreted to be microcontinents, remnant arcs, oceanic terranes and accretionary prisms (Percival et al., 2006). It is suggested that the assembly of the Superior Craton is achieved by the northward subduction-accretion process based on the following pieces of evidence (*e.g.* Percival et al., 2012, and references therein): (1) Consistent southward-younging ages of regional deformation, syn- to post-tectonic magmatism and the deposition of the orogenic-related sedimentary assemblages. This age progression is interpreted to be the result of successive terrane accretion towards the south. (2) North-dipping lithospheric reflectors interpreted as remnant subducted slabs (Calvert et al., 1995; Calvert and Ludden, 1999). (3) Terrane boundaries traceable up to 1.00×10^3 km with possible horizontal movements bordered with greywacke belts implied to be collisional flysch belts.

The SGB is the western extension of the Abitibi greenstone belt. It is located in the Abitibi-Wawa terrane in the southern Superior Craton (Figure 3.1A,B). It is bounded by the Nat River granitoid complex to the north, the Ramsey-Algoma granitoid complex to the south and the Kenogamissi batholith to the east. To the west the SGB is bounded by the Kapuskasing structural zone, which exposes the lower to middle crustal sections of the Abitibi-Wawa subprovince due to the southeastward thrusting on the Ivanhoe Lake fault zone (Percival and West, 1994). In the following sections, we present a brief summary of the major lithological units and structural features of the SGB.

Figure 3.1 ***(following page)*:** A: Simplified subprovince and terrane map of the Superior Province, modified from Montsion et al. (2018) and Percival et al. (2012). Subprovinces belonging to the same terrane are filled with the same colour. The extent of the Abitibi greenstone belt and Swayze greenstone belt (SGB) is labelled and shown in detail in B. B: Simplified geological map of the Abitibi greenstone belt and SGB showing the overall Archean lithological units and the crustal-scale structures, modified from Ayer et al. (2004). CLLDZ: Cadillac-Larder Lake deformation zone; ILFZ: Ivanhoe Lake fault zone. KB: Kenogamissi batholith; KSZ: Kapuskasing structural zone; NRGC: Nat River granitoid complex; PDDZ: Porcupine-Destor deformation zone; RAGC: Ramsey-Algoma granitoid complex; RDZ: Ridout deformation zone; C: Simplified geological map of the southern Swayze greenstone belt. The geology is compiled from Heather (2001); Berger (2012); Ayer and Trowell (2002), complemented by the field data obtained in this study. The extents of the southern domain (see Figure 3.4) and northern domain (see Figure 3.5) are also labelled. The red stars show the locations where the geochronology samples were taken. The geochronology data are listed and discussed in Appendices D and E.


AW: Abitibi-Wawa Terrane
HB: Hudson Bay Terrane
M: Marmion Terrane
MRV: Minnesota River Valley Terrane
NC: North Caribou Terrane
RA: Riviera Arnaud Terrane
WW: Western Wabigoon Terrane
WR: Winnipeg River Terrane
98°W
89°W
81°W
72°W
54°N
45°N
RA
HB
NC
WR
WW
M
AW
MRV
A
400000
500000
600000 mE
5400000 mN
5300000
ILFZ
KSZ
PDDZ
Timmins
NRGC
Foleyet
Kirkland Lake
CLDZ
KB
Matachewan
Gogama
RDZ
RAGC
B
C
N domain, Fig. 3.5A
230C
Rice Lake Batholith
Somme Pluton
Orthogneiss
S domain, Fig. 3.4A
Neville Pluton
16QW332A
237D
RAGC
5300000 mN
5290000
5280000
5270000
5 0 5 10 km
400000
410000
420000
430000
440000
450000
460000 mE
Structural symbols
Anticline
Syncline
Ridout Deformation Zone
Fault or deformation zone
Younging direction
Sample location
Intrusive lithology
Quartz feldspar porphyry
Post-tectonic granitoid intrusion
Syn-tectonic granitoid intrusion
Intermediate to mafic intrusion
Undifferentiated TTG suite
Supracrustal assemblages
Timiskaming-type metasedimentary rock
Porcupine-type metasedimentary rock
Banded iron formation
Felsic metavolcanic rock
Intermediate metavolcanic rock
Mafic metavolcanic rock
Ultramafic metavolcanic rock

3.2.1 Supracrustal stratigraphy

Regional mapping (Heather, 2001) and U-Pb geochronology (van Breemen et al., 2006) in the SGB reveals a coherent, upward-facing autochthonous stratigraphy. The fact that the stratigraphically higher units contain zircons with ages of the underlying units implies that the stratigraphic sequences in both the Abitibi greenstone belt and the SGB are coherent rather than the result of amalgamation of allochthonous terranes (*e.g.* Jackson et al., 1994; Ayer et al., 2002; Thurston et al., 2008).

The metavolcanic assemblages in the SGB consist of ultramafic to mafic flows as well as intermediate to felsic volcaniclastic rocks with intermittent deposition of chemical sedimentary rocks in the form of the banded iron formation. Heather (2001) identifies five groups of metavolcanic rocks deposited from 2740 Ma to 2696 Ma which closely resembles the volcanic episodes of the Abitibi greenstone belt (Ayer et al., 2002; Thurston et al., 2008). The metavolcanic assemblages are overlain by the clastic metasedimentary rocks of the Opeepeesway Formation of the Ridout Group, which is the youngest of the supracrustal sequence and consists of siltstone, sandstone and conglomerate with intrusive, felsic or mafic metavolcanic and banded iron formation clasts. Recent geochronology results of the Opeepeesway Formation conglomerate yields a maximum depositional age of 2680 ± 3 Ma (Hastie et al., 2016) and the porphyry suites cross-cutting the conglomerate were dated at 2684 ± 3 Ma and 2680 ± 4 Ma, although several individual zircon grains of ages between *ca.* 2676 Ma and 2670 Ma were also found (MacDonald et al., 2017). In addition to the age data, the proximal source of the clasts and the alluvial-fluvial depositional environment of the Opeepeesway Formation supports a correlation to the Timiskaming-type metasedimentary package in the Abitibi greenstone belt. In the following discussions, we use the term Timiskaming-type assemblage to refer to the Opeepeesway Formation in the SGB due to their comparable age, sedimentary source and relative position in the local stratigraphy.

3.2.2 Kenogamissi batholith

The Kenogamissi batholith separates the stratigraphy of the SGB to the west and the Abitibi greenstone belt to the east (Figure 3.1B and C). It consists of multiple phases of intrusions of tonalitic, granodioritic and granitic compositions with crystallization ages ranging from 2747 Ma to 2660 Ma (Benn, 2004; Becker and Benn, 2003; van Breemen et al., 2006). They are broadly divided into synvolcanic, syntectonic and post-tectonic phases with minor *ca.* 2850 Ma xenocrystic zircons, interpreted as

the possible influence of a rifted continental crust substrate exposed in the Wawa area (Ketchum et al., 2008).

Synvolcanic intrusions are the volumetrically dominant phases in the Kenogamissi batholith, composed of brecciated gabbro, hornblende/biotite diorite and tonalite-trondhjemite-granodiorite (TTG). Various phases of the synvolcanic intrusions have crystallization ages that overlap with the age ranges of the supracrustal metavolcanic assemblages. In the western part of the Kenogamissi batholith, the synvolcanic phases are grouped into the Rice Lake pluton consisting of weakly- to well-foliated diorite, tonalite and granodiorite. A study of the macroscopic and magnetic structural pattern by Becker and Benn (2003) reveals that the foliation near the batholith-granitoid contact is generally boundary-parallel while assuming a NW-SE to E-W trend towards the interior of the batholith. In the eastern part of the Kenogamissi batholith, the *ca.* 2723 Ma orthogneiss with a composition of hornblende biotite tonalite is the dominant synvolcanic intrusive phase (Benn, 2004).

The most prominent syntectonic phase of the Kenogamissi batholith is the Neville pluton situated at the southern boundary of the Kenogamissi batholith. It is of hornblende biotite quartz monzodiorite to granodiorite in composition and yielded an intrusive age of 2682 ± 3 Ma (Heather, 2001).

The post-tectonic phase of the Kenogamissi batholith is the Somme Pluton located at the core of the Kenogamissi batholith. Dykes with a composition similar to that of the Somme pluton cross-cut all other intrusion phases in the Kenogamissi batholith. Various ages of this pluton are reported at *ca.* 2660 Ma (Benn, 2004), *ca.* 2665 Ma (Heather, 2001) and 2676 ± 4 Ma (Ketchum et al., 2008). It is composed of homogeneous undeformed coarse-grained granodiorite or granite.

3.2.3 The Ridout deformation zone

The Ridout deformation zone (RDZ) in the southern SGB is a less than 1.00 km-wide E-W-trending high strain zone nucleated in the metavolcanic rocks and has recorded multiple generations of shear deformation (Heather, 2001). The RDZ was initially defined in the narrow greenstone septum at the southern boundary of the Neville Pluton (Heather, 2001). To the west where the greenstone stratigraphy widens and is better preserved, multiple high strain zones can be traced continuously along strike within the greenstone belt as well as at the granitoid-greenstone boundaries. In this study we trace the RDZ to a high strain zone localized at the northern boundary of the Timiskaming-type basin in contact with the metavolcanic assemblages. The

lithologies within the RDZ are strongly foliated quartz-feldspathic sericite schist and chlorite schist. Younging indicators in the weakly deformed sandstone layer of the Timiskaming-type metasedimentary rocks indicate a consistent northward younging direction towards the RDZ (*e.g.* MacDonald et al., 2017; Hastie, 2017; Haugaard et al., 2017), suggesting only half of the Timiskaming-type basin is preserved.

The RDZ has been inferred to be the western extension of the gold-prolific Cadillac-Larder Lake deformation zone (CLLDZ) in the Abitibi greenstone belt (Heather, 2001). Direct geological evidence of this interpretation is masked by Proterozoic sedimentary assemblage of the Huronian Supergroup. This interpretation is recently questioned by Berger (2011) on the ground of the differing kinematics and contrasting stratigraphic locations of the deformation zones with respect to the Timiskaming-type sedimentary assemblage.

3.3 Deformation analysis

When presenting the sequence of the deformation events in the SGB, we adopt the notation of generation (G) because more than one generation of overprinting structures may develop in one progressive deformation (D) event (*e.g.* Lin, 2001). Based on the overprinting relationships, four generations (G_1–G_4) of ductile structures are identified in the SGB. G_1 structures are only preserved in the TTG infrastructure as folded S_1 gneissosity and its tectonic significance remain to be determined. G_2 is a thicked-skinned deformation event that affects both the Kenogamissi batholith and the supracrustal assemblages throughout the SGB. G_3 deformation is characterized by an oblique north-side-up and sinistral shearing in the RDZ. G_4 deformation is a regional strike-slip dextral reactivation of pre-existing high strain zones and lithological contacts.

Among the four generations of structures, the G_2 deformation is interpreted to have established the regional crustal architecture of the SGB. The tectonic mechanism leading to the formation of the dome-and-keel map pattern and structural trends will be explored in the numerical study in Section 3.4. Subsequent deformation episodes (G_3 and G_4) only modifies G_2 structures by localized shear reactivations and therefore does not significantly alter the regional-scale map pattern. Therefore, in this section we only present the G_2 structures in detail due to its importance in the tectonic evolution of the SGB. The detailed description of G_1, G_3 and G_4 structures, the timing of the deformation events as well as the timing and the regional significance in the context of the greater Abitibi greenstone belt of all generations of

deformations are discussed in Appendix D.

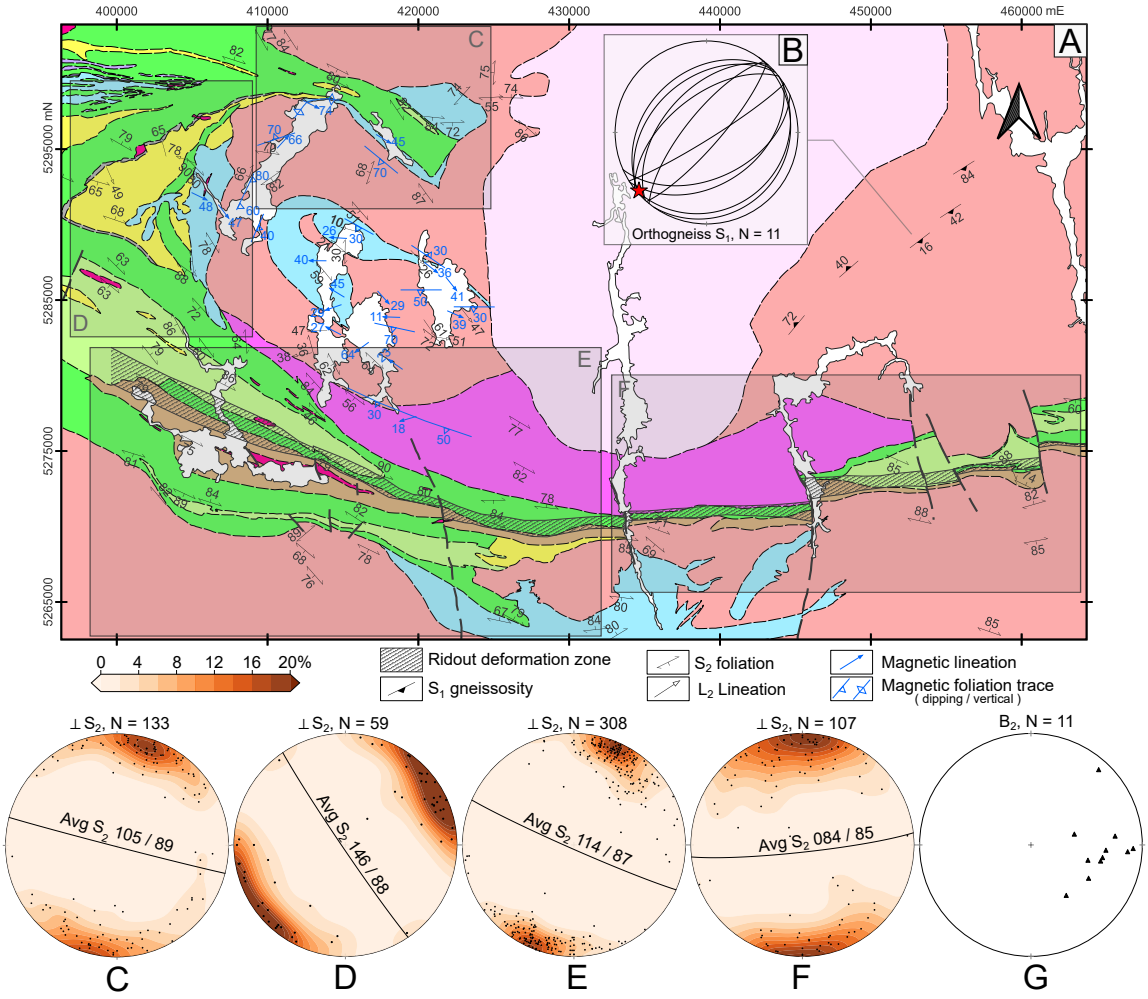


Figure 3.2: Structural data related to the G_2 deformation. A: Simplified geological map of the southern SGB with G_1 and G_2 structural patterns. The colouring of the lithological units follows that in Figure 3.1. The magnetic foliation and lineation data are compiled from (Becker and Benn, 2003). B: stereographic projection of the S_1 gneissosity in the orthogneiss. The red star is the best-fit F_2 fold axis calculated from the S_1 foliation data. C-F: Stereographic projections of the poles to S_2 fabric in corresponding areas of the greenstone belt delineated in A. The average strike and dip of S_2 in each area are also shown as the big circle trace. G: Stereographic projection of the F_2 fold hinge measurements.

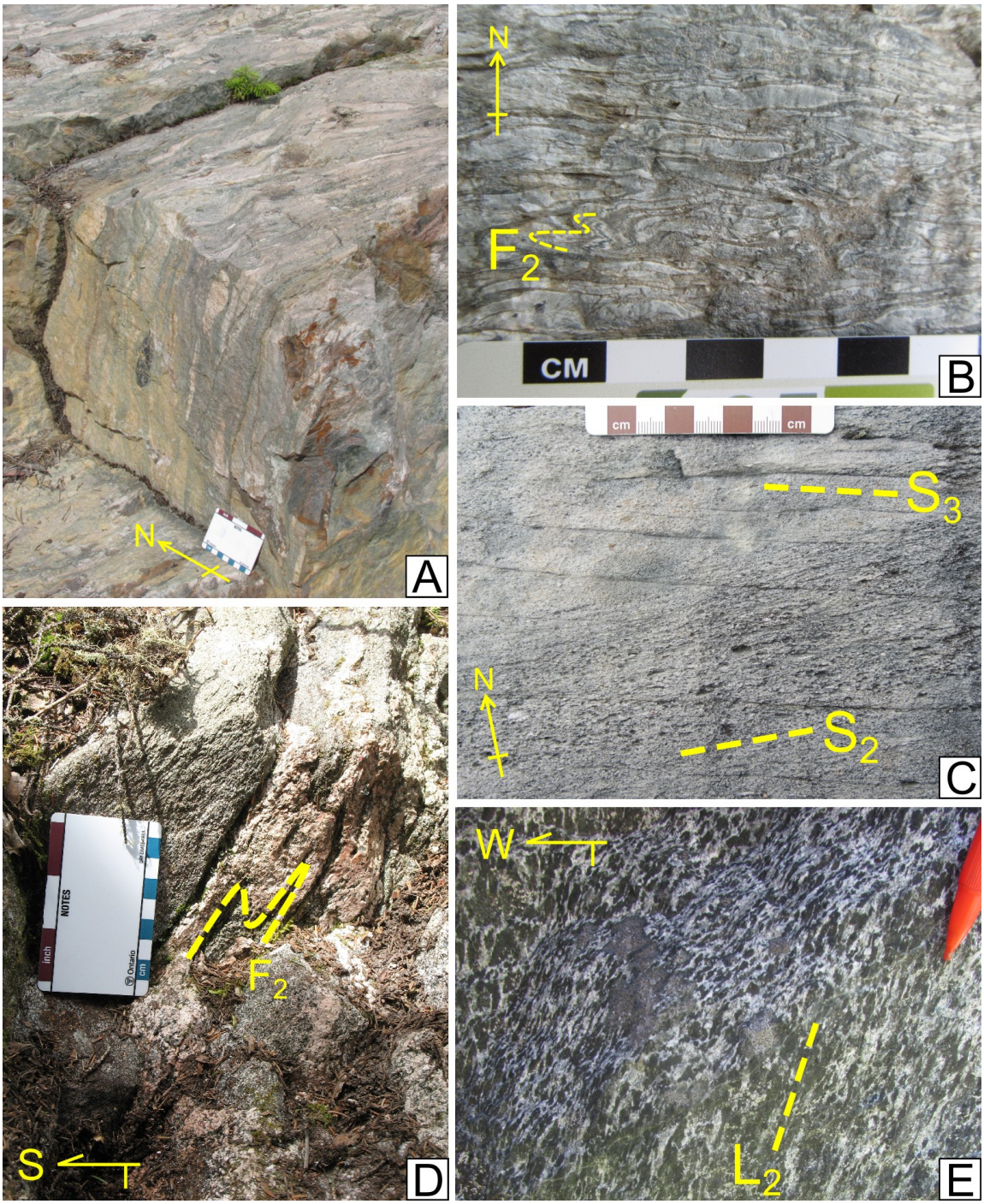
The G_2 structures are associated with regional thick-skinned F_2 folding, the associated S_2 regional foliation and L_2 mineral or stretching lineation. The first order

F_2 folding is inferred from the repetition and younging direction reversals of the supracrustal stratigraphy (Figure 3.1). On the outcrop scale, the F_2 folds are tight to isoclinal with shallowly to moderately plunging fold axes (Figure 3.2G), consistent with the interpretation that the F_2 corresponds to regional upright non-cylindrical folding of the SGB stratigraphy. The existence of the F_2 can also be inferred from the tilting of sedimentary bedding (S_0) in the Timiskaming-type sandstones to its current subvertical attitude, establishing the timing of G_2 deformation to be synchronous or postdate the deposition of the Timiskaming-type sedimentary rocks, consistent with the age relationship between deposition and deformation in the northwestern Superior Craton (Lin et al., 2013).

Associated with the G_2 folding is the S_2 axial planar foliation. In the greenstone supracrustal assemblages, S_2 is defined by a differentiated cleavage consisting of aligned chlorite in the mafic metavolcanic rocks and aligned sericite or muscovite in the felsic metavolcanic or metasedimentary rocks. The S_2 foliation is also defined by flattened pillow structures in the basaltic layers, flattened lapillis in the pyroclastic rocks as well as flattened (and isoclinally-folded) clasts (Figure 3.3A,B) in the Timiskaming-type conglomerates, attesting to a flattening type of strain (Flinn's K-value < 1) associated with the G_2 deformation. The S_2 foliation in the greenstone belt is steeply-dipping, while the strike is spatially variable and subparallel to the orientation of granitoid-greenstone contact (Figure 3.2C–F).

In the Kenogamissi batholith, the S_2 foliation is best exemplified as aligned hornblende crystals and quartz aggregates in the Neville pluton. The Neville pluton is increasingly strongly foliated closer to the granitoid-greenstone boundary with a boundary-parallel steeply-dipping foliation defined by aligned amphibole. In the Rice Lake pluton of the Kenogamissi batholith, the macroscopic and magnetic foliation shows boundary-parallel trend close to the granitoid-greenstone contact, while the foliation orientation in the interior of the batholith is generally SE-NW-trending. The exact generation of the dominant foliation is unclear due to the lack of overprinting relationship with respect to known deformation generations. However, even if the observed foliation is associated with earlier deformation events, they are likely

Figure 3.3 ***(following page)*:** Field photos showing the strain patterns of the G_2 deformation. A: Timiskaming-type conglomerate with clasts flattened parallel to S_2. B: A fragmental unit in the Timiskaming-type assemblage where the flattened clasts are folded by isoclinal F_2 folds. C: Overprinting relationship between S_2 foliation and S_3 spaced cleavage in the Timiskaming-type sandstone. D: G_2 isoclinal fold of a *syn*-G_2 granodioritic dyke. E: Amphibolite at the northern granitoid-greenstone contact of the northern domain affected by G_2 deformation and show an L-tectonized fabric.


N
A
N
F2
CM
B
cm
cm
S3
N
S2
C
W
NOTES
inch
cm
F2
S
D
L2
E

to have been transposed under the strain field of the G_2 deformation.

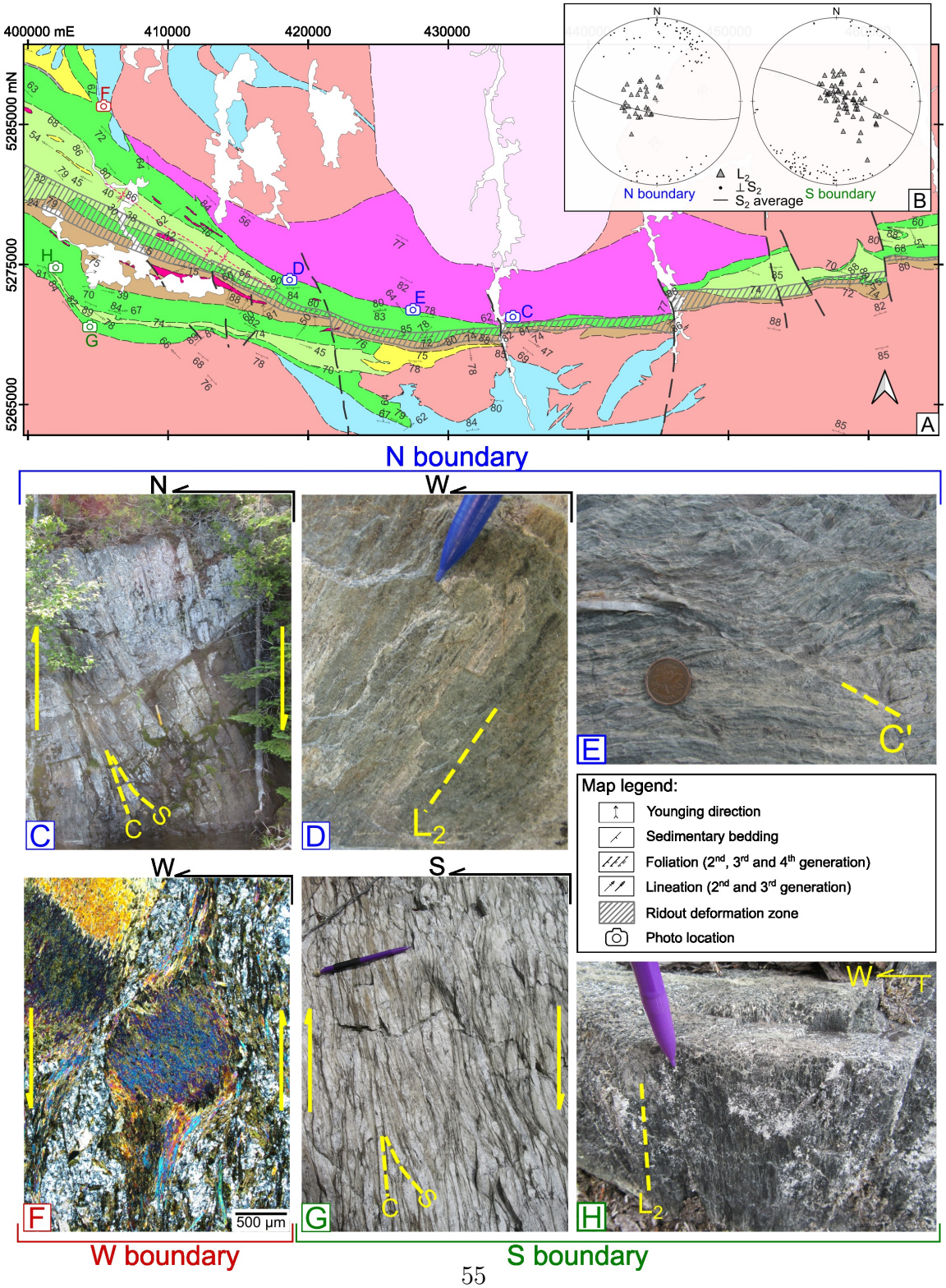
The G_2 deformation is most strongly developed in the corridors of high strain close to the granitoid-greenstone boundary. To characterize the shear kinematics of G_2 and the L_2 stretching lineation patterns therein, the study area is subdivided into a southern domain encompassing the greenstone assemblages south of the Kenogamissi batholith transected by the RDZ, and a northern domain where the greenstone assemblages extends as a narrow arm in an WNW-ESE direction into the Kenogamissi batholith. The spatial extents of the two subdomains are shown in Figure 3.1C. The structural patterns in each domain are described in detail as follows.

3.3.1 The southern domain

In the southern domain, the boundary between the Neville pluton in the north and the SGB is an intrusive contact. Dykes with the composition of the Neville granodiorite cross-cut S_2 in the mafic metavolcanic wall rock and is isoclinally folded with a S_2-parallel axial plane (Figure 3.3D), consistent with the interpretation that the emplacement of Neville pluton was *syn*-G_2 with intense flattening strain. The shear sense indicators at this contact show a granitoid-(*i.e.* north-)side-up sense of shear (Figure 3.4C). The same granitoid-(*i.e.* east-)side-up shear sense is also observed along Rice Lake pluton-greenstone contact further west (Figure 3.4F). Close to the boundary between the SGB and the Ramsey-Algoma granitoid complex in the south, the shear sense recorded in the felsic lapilli tuff is south-side-up (Figure 3.4D).

The L_2 patterns along both the northern and southern contacts of the SGB are moderately- to steeply-plunging, whereas the plunge directions are opposite from contact to contact: At the Kenogamissi batholith-greenstone contact the L_2 plunges westward (Figure 3.4B,D), while at the Ramsey-Algoma granitoid complex-

Figure 3.4 ***(following page)*:** Field photos and stereographic projections of G_2 structures. A: structural map of the southern domain of the SGB. B: stereographic projection of the L_2 lineation at the northern (left) and southern (right) granitoid-greenstone contact. C: S-C fabric on a vertical surface at the northern granitoid-greenstone contact showing a north-side-up sense of shear. D: moderately west-plunging L_2 mineral stretching lineation defined by aligned hornblende crystals in metavolcanic rocks. E: mylonitized volcanic rocks at the northern granitoid-greenstone contact with intense S_2 shear fabric. The C' shear band shows a dextral sense of shear. F: σ-type porphyroclast indicating a west-side-up sense of shear at the western granitoid-greenstone boundary. G: S-C fabric in the felsic tuff at the southern granitoid-greenstone contact indicating a south-side-up sense of shear. H: subvertical L_2 mineral stretching lineation in amphibolite at the contact between the greenstone and Ramsey-Algoma granitoid complex. The locations of C-H are labelled in A.

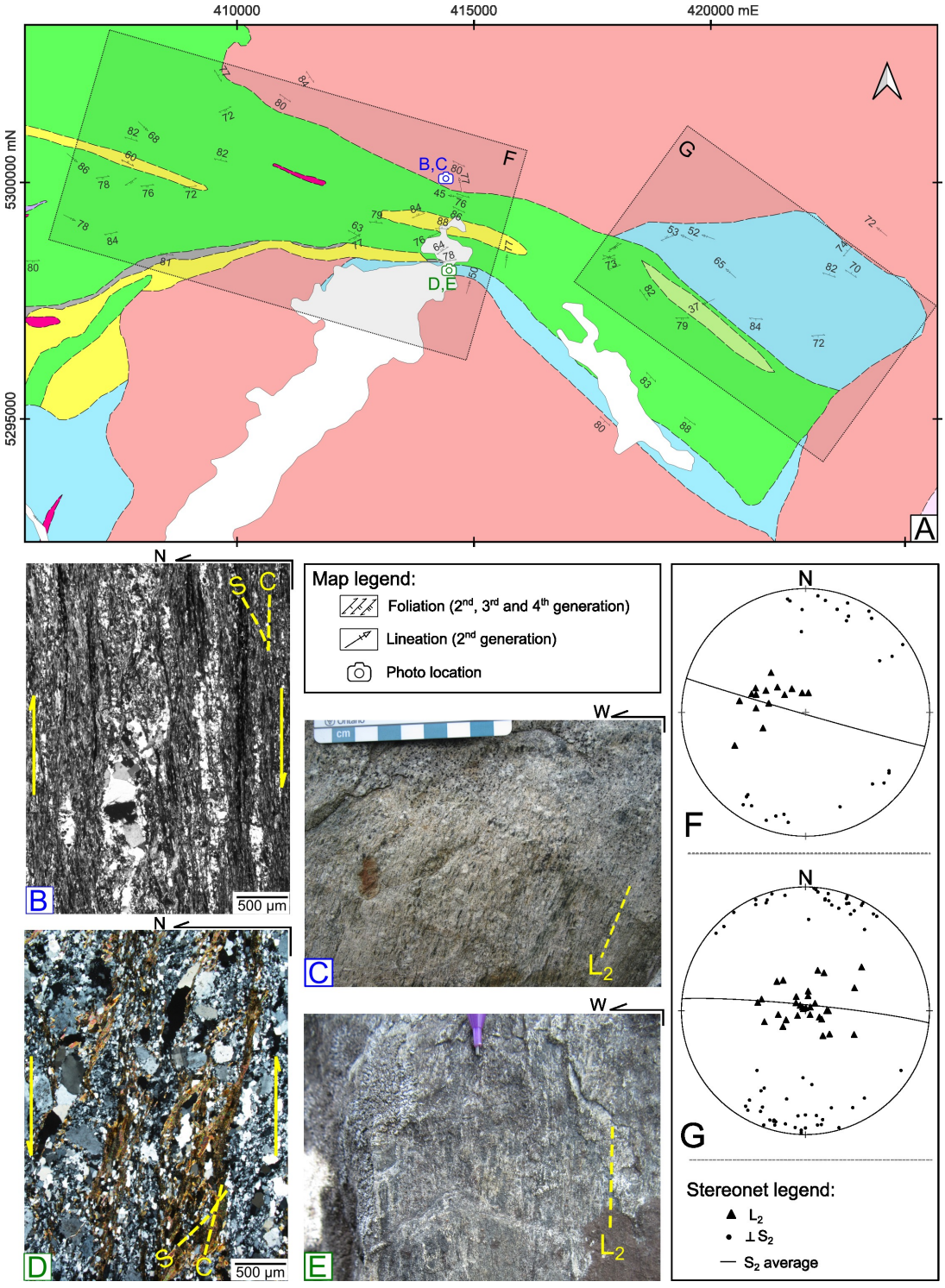

400000 mE
410000
420000
430000
5285000 mN
5275000
5265000
F
H
G
D
E
C
A
B
N
N boundary
S boundary
L_2
$\perp S_2$
S_2 average
N boundary
C
C
S
D
L_2
E
C'
W
W
F
500 µm
S
G
C
S
H
W
T
L_2
Map legend:
Younging direction
Sedimentary bedding
Foliation (2nd, 3rd and 4th generation)
Lineation (2nd and 3rd generation)
Ridout deformation zone
Photo location
W boundary
S boundary

greenstone contact, the dominant L_2 plunge direction is eastward (Figure 3.4B,H). The horizontal shearing component associated with G_2 granitoid-up/greenstone-down movement at the north granitoid-greenstone contact is observed to be dextral (Figure 3.4E), although direct field evidence of horizontal shearing component is otherwise rare due to the dominantly vertical kinematics associated with G_2. The shear sense indicators, combined with the orientation of the L_2 mineral stretching lineation, implies that kinematics in the southern domain is characterized by dominantly granitoid-up/greenstone-down shearing with a minor component of dextral shearing.

3.3.2 The northern domain

In the northern domain (Figure 3.5A), an eastward increase in the deformation intensity is observed in the greenstone arm as it narrows into the granitoid intrusion. The shear sense indicators at the granitoid-greenstone boundaries both north and south are best preserved in microstructures due to strong mylonitization and shows a consistent granitoid-up/greenstone-down kinematics (Figure 3.5B,D). Lineation data were collected in two separate subdomains in the western (Figure 3.5F) and eastern parts (Figure 3.5G) of the greenstone arm. In both subdomains, the L_2 stretching lineations are moderately- to steeply-plunging and are defined by aligned hornblende needles in the supracrustal volcanic rocks and locally garnet-bearing amphibolite. The latter is interpreted to be the metamorphosed equivalence of the supracrustal metavolcanic rocks. In the western part, the amphibolite units are locally deformed into L-tectonite, bearing only weak foliation but strong alignment of dark minerals (Figure 3.5C, E). The lineation is down-dip and subvertical (Figure 3.5G). In the eastern part, the L_2 lineation shows a moderate westward plunge (Figure 3.5F). In contrast to the southern domain, L_2 lineation does not display an asymmetrical pattern with respect to the north and south granitoid-greenstone boundaries. Therefore, any regional horizontal shearing component for the G_2 deformation is probably

Figure 3.5 ***(following page)*:** A: structural map of the northern domain of the SGB. B: S-C fabric in the mylonitized felsic volcanic rocks at the northern granitoid-greenstone contact showing a north-side-up sense of shear. C: steeply-plunging L_2 mineral stretching lineation in the metavolcanic rocks defined by aligned amphibole crystals. D: S-C fabric in the mylonitized quartzo-feldspathic porphyry at the southern granitoid-greenstone contact, showing a south-side-up sense of shear. E: steeply-plunging mineral stretching lineation in the felsic metavolcanic rocks defined by aligned amphibole aggregates. The locations of the photos B-E are all labelled in A. F-G: stereographic projections of L_2 lineation in various areas of the northern domain delineated in A.


410000
415000
420000 mE
5300000 mN
5295000
B,C
D,E
F
G
A
N
S
C
B
500 µm
D
Map legend:
Foliation (2nd, 3rd and 4th generation)
Lineation (2nd generation)
Photo location
W
cm
C
L2
E
F
G
Stereonet legend:
L2
⊥S2
S2 average

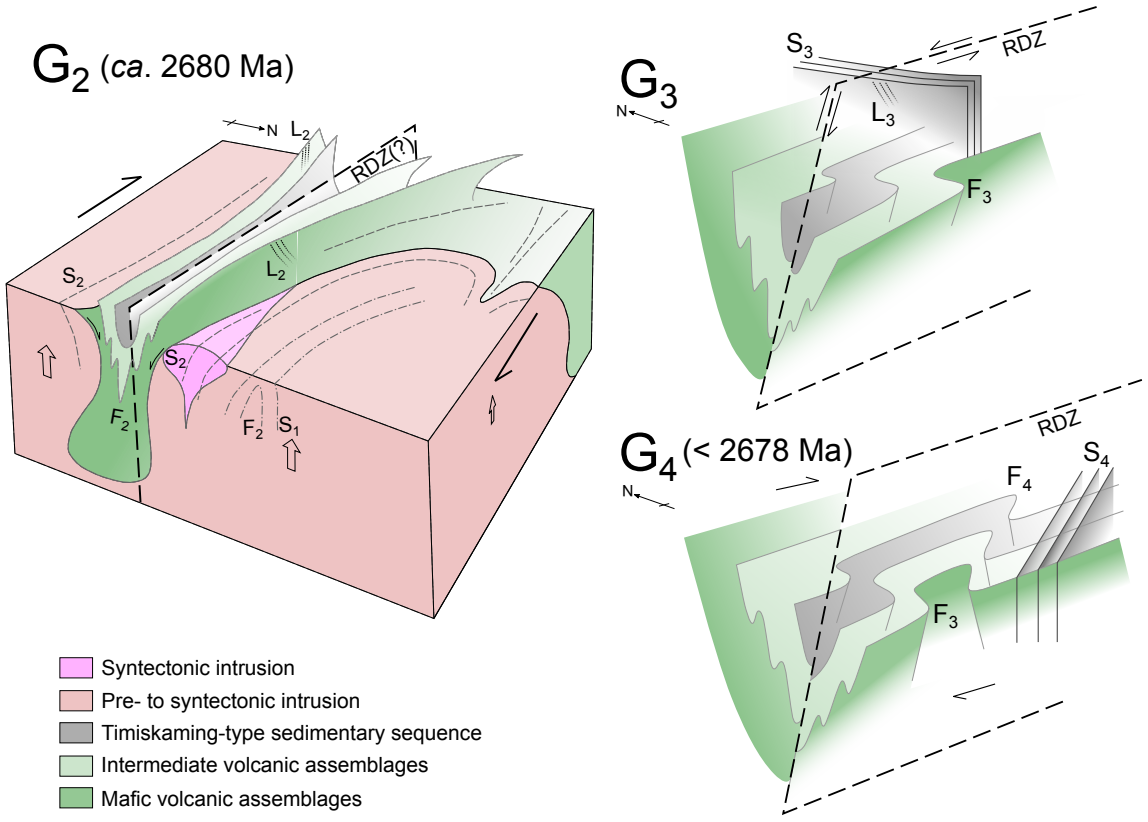


Figure 3.6: Summary of major generations of structures in the SGB and their timing. See text for further discussions.

minor in the northern domain.

3.3.3 Summary of deformation and timing

In this section we summarize the main structural patterns and the timing of the deformation generations discussed in the previous section as well as in Appendix D. A graphical summary of the deformation generations is shown in Figure 3.6.

G_1 deformation is only preserved in the synvolcanic granitoid intrusion at amphibolite facies conditions, consistent with the interpretation of Benn (2004). Heather (2001) identifies foliation-bearing intrusive clasts in the Timiskaming-type assemblage. Assuming this foliation corresponds to S_1 in this study, we can bracket the timing of G_1 deformation to between the emplacement age of the orthogneiss at

2722.5 ± 0.8 Ma (van Breemen et al., 2006) and the depositional age of the Timiskaming-type assemblage at *ca.* 2680 Ma.

G_2 deformation (Figure 3.6B) is associated with regional thick-skinned folding and therefore is identified as the major phase of deformation that establishes the crustal architecture of the SGB. G_2 is associated with S_2 subparallel to granitoid-greenstone contact and upright F_2 regional folding that affects both the supracrustal assemblages and the granitoid infrastructure. The shear kinematics associated with the G_2 high strain zones at the granitoid-greenstone contacts are invariably granitoid-up/greenstone-down. The steeply-plunging L_2 lineation pattern and the granitoid-up/greenstone-down kinematics and the boundary parallel S_2 pattern may be explained by the gravity-induced sagduction of the dense supracrustal assemblage and the complementary diapiric movement of granitoid intrusion (see Lin, 2005, and discussions therein). At the same time, the consistent dextral shearing component in the linear greenstone belt in the southern domain shows that the G_2 deformation also possesses a component of horizontally-directed simple shearing. The timing of the G_2 deformation is constrained at around 2680 Ma.

The G_3 deformation is localized within the RDZ and is characterized by an oblique sinistral and north-side-up shearing. The exact timing of G_3 deformation remains poorly constrained. The G_4 deformation represents a regional dextral strike-slip reactivation of pre-existing weak planes such as high strain zones and lithological boundaries and probably took place later than *ca.* 2678 Ma. G_2 and G_3 structures are local and do not change the overall patterns of G_2 structures.

3.4 Numerical modelling

As is discussed in the previous section, the crustal architecture of SGB is probably a result of combined operation of the vertically-directed gravitational overturn and far-field horizontally-directed tectonic stress. Due to the coherent dextral component of shearing in the southern domain for the G_2 deformation, we deduce that the gravitational overturn is likely to have happened simultaneously with the dextral shearing event. To test this hypothesis, a crustal-scale numerical model of gravity-induced crustal overturn is constructed with dextral shearing applied simultaneously as the boundary condition. The results of the model computation will be compared to field observations to test the validity of our assumed tectonic model.

3.4.1 Modelling methods

The long term crustal flow in the SGB is approximated by a creeping flow model with linear viscosity. The flow is assumed to be incompressible because no significant density-altering metamorphic reactions are observed in the study area. We solve the following set of partial differential equations within a given crustal block:

$$\begin{cases} \boldsymbol{\nabla} \cdot \big(2\eta \boldsymbol{D}(\boldsymbol{v})\big) - \boldsymbol{\nabla} p + \rho \boldsymbol{g} = 0 \\ \boldsymbol{\nabla} \cdot \boldsymbol{v} = 0 \end{cases} \tag{3.1}$$

where $\eta = \eta(\boldsymbol{x}, t)$ and $\rho = \rho(\boldsymbol{x}, t)$ are respectively the material viscosity and density, which vary in both space and time due to material movement and deformation following the tectonic flow field. $\boldsymbol{D} = \frac{1}{2}\left(\boldsymbol{L} + \boldsymbol{L}^{\top}\right)$ is the rate-of-deformation tensor and $\boldsymbol{L} = \boldsymbol{\nabla}\boldsymbol{v}$ is the velocity gradient tensor. The geological boundary between the granitoid infrastructure and the greenstone supracrustal assemblages is tracked by a level set function. Upon solving Equation (3.1), the obtained flow velocity allows us to extract information related to both the instantaneous and finite deformation field. The right-hand screw of the vorticity vector can be computed from the velocity gradient tensor and retrieves the local sense of rotation with respect to a fixed reference frame (Jiang and Williams, 1999; Means et al., 1980).

The three principal axes of the strain ellipsoids (with lengths $\lambda_1 \geqslant \lambda_2 \geqslant \lambda_3$) in the model can be obtained by the eigendecomposition of the Cauchy-Green tensor $\boldsymbol{C} = \boldsymbol{F}\boldsymbol{F}^{\top}$, where the deformation gradient tensor $\boldsymbol{F}$ can be obtained by integrating the well-known relationship $\dot{\boldsymbol{F}} = \boldsymbol{L}\boldsymbol{F}$ (Malvern, 1969) through time with a suitable integration scheme. The Flinn's K-value can be obtained by

$$K = \frac{\ln\left(\lambda_1/\lambda_2\right)}{\ln\left(\lambda_2/\lambda_3\right)} \tag{3.2}$$

where $K > 1$ and $K < 1$ implies the constrictional strain and the flattening strain, respectively. The intensity of the strain can be measured by the amount of deviation of the strain ellipsoid from a sphere (Ramsay and Huber, 1983).

$$N = \sqrt{\left(\sqrt{\frac{\lambda_1}{\lambda_2}} - 1\right)^2 + \left(\sqrt{\frac{\lambda_2}{\lambda_3}} - 1\right)^2} \tag{3.3}$$

For a detailed exposition of the technique for capturing geological contacts by the level set method and structural analysis of the flow field, the reader is referred to Wú et al. (2023) and Jiang (2023).

3.4.2 Model setup

We set up a numerical model to investigate the strain distribution in a tectonic regime where horizontal shearing operates synchronously as the crust undergoes deformation related to density inversion. Several studies have conducted numerical modelling on Archean crustal dynamics. The pioneer study by Mareschal and West (1980) constructed a two-layer model and concluded that crustal density overturn is feasible in Archean under suitable thermal and viscosity conditions. The study by Robin and Bailey (2009), using a similar model setup, concludes that the crustal density inversion can be the unifying mechanism behind the generation of voluminous TTG intrusions, buoyant subcratonic lithospheric mantle (SCLM) and the dome-and-keel map pattern in the granitoid-greenstone terranes. The evolution of crustal thermal conditions and p-T-t paths during the vertical tectonism processes have also been investigated in several studies (*e.g.* Thébaud and Rey, 2013; François et al., 2014; Yu et al., 2022). The major limitation of the previous studies is the absence of a 3d picture of the deformation. As a result, the 3d strain ellipsoids collapse into 2d ellipses, making the differentiation between the foliation patterns (finite flattening) from the lineation patterns (finite stretching) impossible. The horizontally-directed shearing boundary conditions, which are to be applied synchronously with crustal gravitational overturn, is also infeasible to be implemented in 2d models.

Our model setup complements the previous studies by extending the numerical model into 3d so that far-field tectonic stress can be incorporated and the 3d analysis of both instantaneous and finite deformation patterns becomes possible (Figure 3.7). A modelling domain of 2.40×10^2 km in the east-west direction, 1.60×10^2 km in the north-south direction and 2.50×10^1 km in depth is chosen so that the rising granitoid domes in the middle of the model and the surrounding greenstone belts can fully develop without being strongly affected by the boundary flow. We set up one 1.50×10^1 km layer of granitoid of density 2.70×10^3 kg/m^3 at the bottom of the domain, which is overlain by 1.00×10^1 km of mafic volcanic rocks of density 2.90×10^3 kg/m^3, to simulate the granitoid-greenstone crustal architecture. The density setup and thickness follows Robin and Bailey (2009) and Mareschal and Jaupart (2006) except that the lower metabasite layer is omitted from our model because it has limited influence on both the development of the gravitational overturn and the structural patterns of upper to middle crustal levels. Our material profile also conforms with the first-order estimates of crustal section in the Neoarchean terranes in general (*e.g.* Percival and Card, 1983; Bodorkos and Sandiford, 2006) and the paleopressure measurement of up to 7.00 kbar at the core of the Kenogamissi batholith (Beakhouse, 2011).

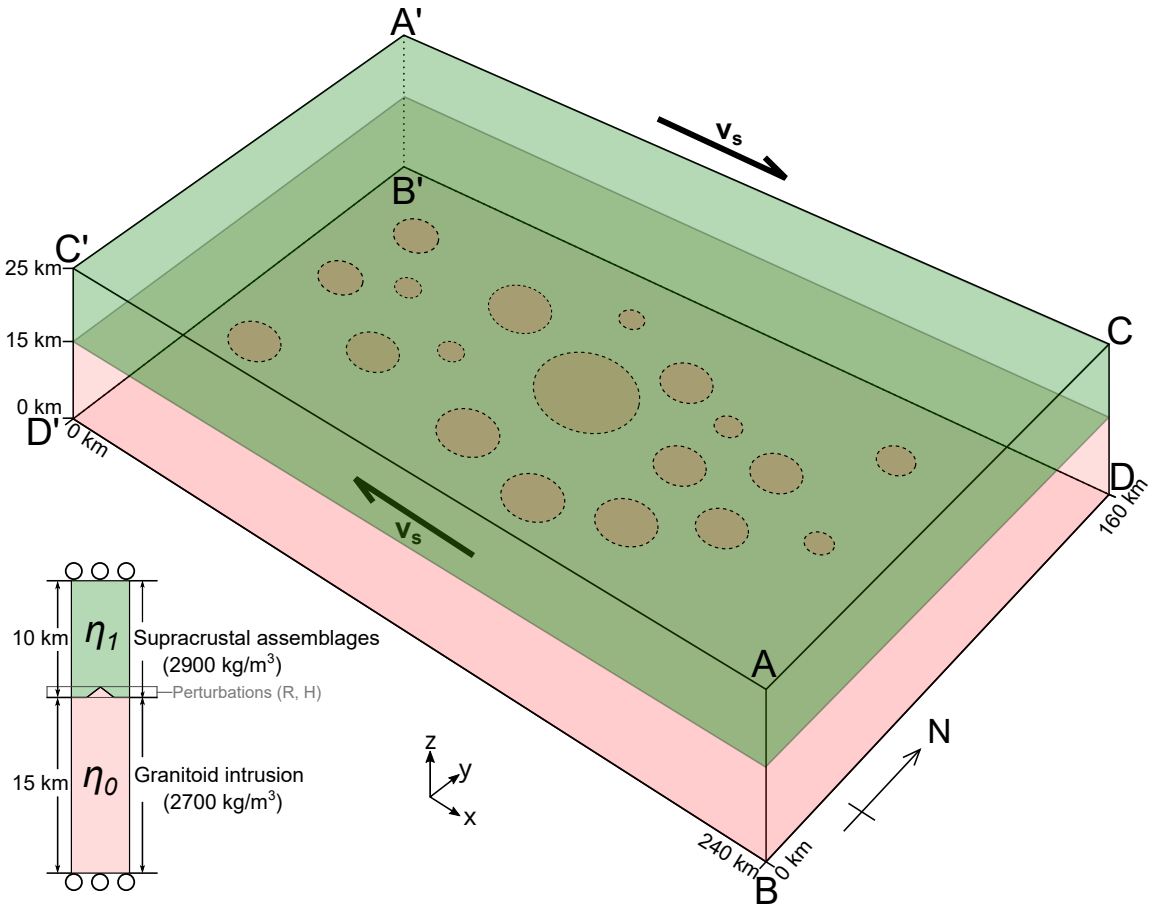


Figure 3.7: The configuration of the numerical model for the synchronous vertical and horizontal tectonism for the SGB. Randomized perturbations (with radius R and amplitude H) on the contact between the supracrustal unit and the granitoid unit are shown schematically and hence do not represent the actual size and location of the perturbations.

At the granitoid-greenstone interface, a set of sinusoidal perturbations of randomized radius (R) and amplitude (H) are generated to simulate an uneven granitoid-greenstone interface and to initiate gravitational overturn. Various randomizations of the interface perturbation cause changes in the spatial distribution of the granitoid domes. However, the structural pattern and the strain distribution within each dome and the surrounding greenstone belt remains consistent in each individual randomizations.

The boundary conditions of the model are configured in a way that far-field tectonic stress in the form of simple shearing is evenly distributed in the crustal block by applying a constant horizontal shear velocity ($+v_s$ for the northern boundary and $-v_s$ for the southern boundary). For the eastern and western boundaries, we prescribe horizontal velocity vectors which change linearly from $+v_s$ at $y = 1.60 \times 10^2\,\mathrm{km}$ and $-v_s$ at $y = 0\,\mathrm{km}$. Free slip boundary conditions are prescribed to both the top and bottom boundaries.

For a qualitative understanding of the general model behaviour, a set of numerical models are tested with a fixed viscosity for the middle crustal granitoid complex η_0, whereas the viscosity of the supracrustal assemblage η_1 as well as the horizontal shear speed v_s are varied in numerous experiments. We remark that due to the linear nature of our viscosity model, an inversely proportional relationship exists between the flow velocity (both the velocity solution $\boldsymbol{v}$ and the boundary shear velocity v_s) and the prescribed material viscosity (η_0 and η_1). The experiments show that a relatively more rigid (therefore probably "cold") supracrustal assemblage impede the onset and rate of gravitational overturn. The magnitude of v_s has minor impact on the growth of gravitational overturn and the resultant structural pattern, but will induce more shear strain localization in the model and contribute to an elongated granitoid dome geometry.

Despite these discrepancies, the general process of the dome-and-keel formation and the structural patterns are similar across various crustal strain rates and upper crustal viscosities. Therefore, we refrain from providing a detailed comparison of the model behaviours across parameter sets, which will be covered in Chapter 4. Instead, we describe in detail one type model to distill the recurring structural features under the synchronous horizontal and vertical tectonic framework.

In the type model, we choose a viscosity of $\eta_0 = 1.00 \times 10^{19}\,\mathrm{Pa \cdot s}$ for the granitoid infrastructure by taking a slightly lower value than the average viscosity of the Robin and Bailey (2009) to take into consideration the possible weakening effect by syntectonic magmatism. The viscosity of the supracrustal assemblages is set at $\eta_1 = 2.00 \times 10^{20}\,\mathrm{Pa \cdot s}$ to take into account that the upper crust is likely relatively

more rigid due to its lower temperature. The horizontal shear speed v_s is prescribed at 1.50 cm/yr, which corresponds to a crustal strain rate of 6.00×10^{-15}/yr. With the lack of a definitive estimate for the average crustal strain rate in Neoarchean, this strain rate is chosen to be consistent with the present-day average strain rate of the crust (Xiong et al., 2021). In fact, it is argued that due to the elevated crustal geotherm, Archean crust may sustain higher crustal strain rate than present day (Mai and Korenaga, 2022).

3.4.3 Modelling results and comparison with field data

We begin by qualitatively describing the temporal evolution of the model. As the model starts, both horizontal shearing and gravitational overturn operate simultaneously. The perturbations at the granitoid-greenstone contacts are amplified and coalesced into granitoid domes. However, the vertical velocity caused by gravitational overturn is smaller in magnitude than the horizontal velocity and therefore the bulk deformation is dominated by the latter. As time progresses a fast increase in the vertical velocity is observed as the dome-and-keel crustal architecture is established. The simultaneous bulk simple shearing contributes to the geometry of the elongated granitoid domes and the preferred alignment of the greenstone belts. The magnitude of vertical velocity will reach a peak and then decline after a considerable volume of greenstone has sagducted. Under the viscosity condition and boundary velocity of the type model, the peak velocity will be attained within 6 Ma.

The lithological distribution and the deformation pattern at the instant when the peak velocity is attained are analysed in detail. This point in time is chosen because it is representative of the crustal structure when both horizontal shearing and vertical gravitational overturn are well-developed. Due to the operation of vertical gravitational overturn, the vorticity vectors at the granitoid-greenstone contact show uniform granitoid-up/greenstone-down kinematics (Figure 3.8A). This is consistent with the G_2 shearing kinematics observed at granitoid-greenstone boundary in the SGB (Figure 3.4C, F, G and Figure 3.5B, D). As a result of the vertical tectonic movement, the sinking supracrustal rocks between the granitoid domes are folded into synclinal keels (Figure 3.8A), which corresponds to the F_2 regional synclinal folding of the greenstone stratigraphy.

The distribution of the strain ellipsoids are shown in Figure 3.8B. The colouring of the ellipsoids differentiates two types of strain: Blue colour corresponds to the flattening strain (Flinn's $K < 1$, "pancake" shape) while red colour represents the constrictional strain (Flinn's $K > 1$, "cigar" shape). The strain distribution shows

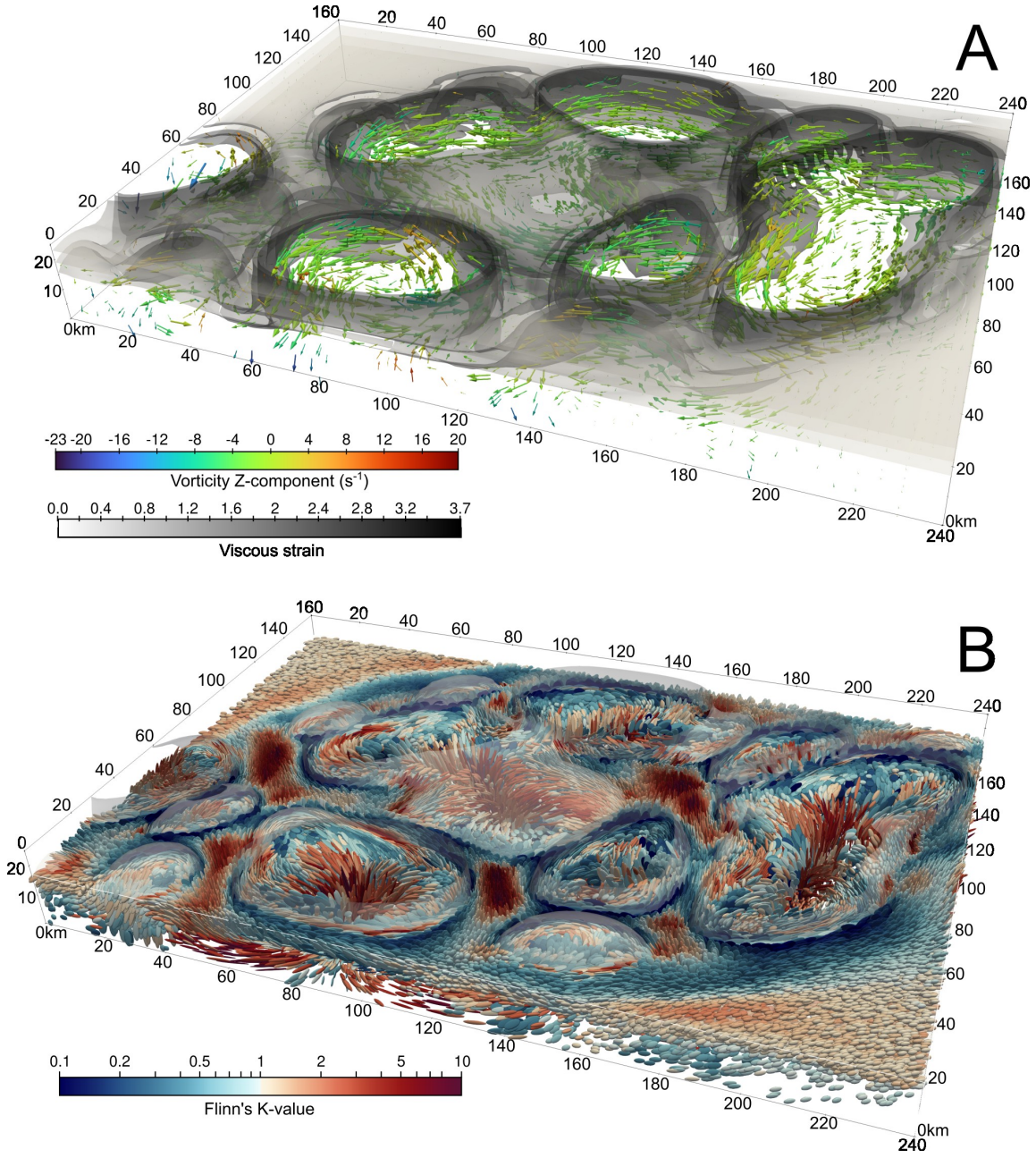


Figure 3.8: 3d results of the numerical model for the SGB. A: Vorticity and strain distribution of the modelled crust. The arrows are the local vorticity vector coloured by the z-component of the vorticity vector. The contour surfaces are isosurfaces of the level set function, *i.e.* simulated bedding surfaces. Deeper shades of the bedding surfaces represents higher amount of the accumulated strain. B: The geometry of the strain ellipsoids coloured by the Flinn's K-value. See text for further discussions.

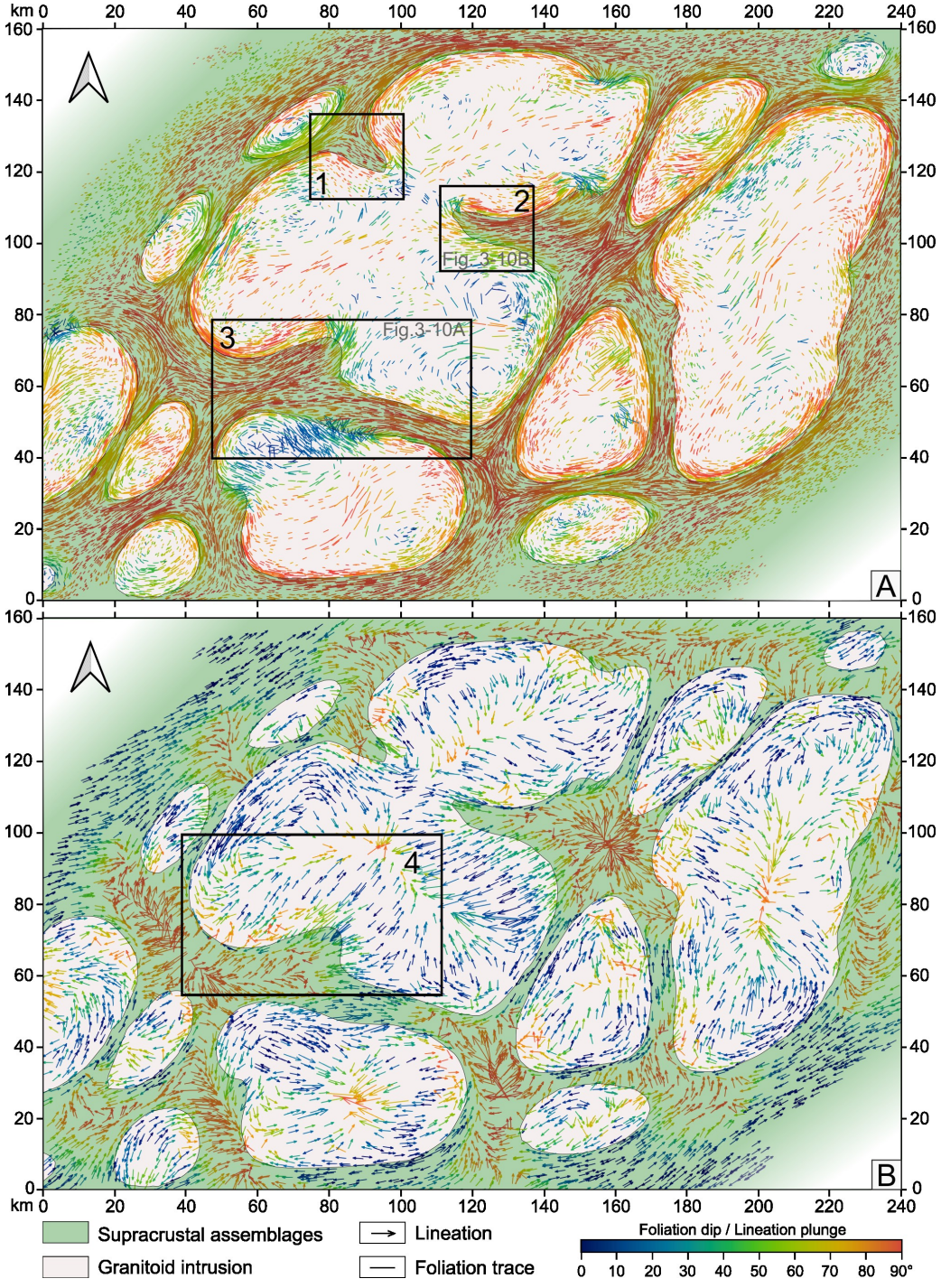
predominantly flattening strain in the greenstone keels between granitoid plutons, which agrees with the flattening strain marker in the greenstone supracrustal rocks (Figure 3.3A, B). The flattening intensity is greater (*i.e.* smaller Flinn's K-value) at the granitoid-greenstone contact, as exemplified by the upright isoclinal folding of syntectonic dykes and the preferential development of high strain zones at the granitoid-greenstone contact (Figure 3.3D). Constrictional strain, or L-tectonites, is predicted to develop preferentially at the core of the granitoid domes and at the triple junctions in the sinking supracrustal rocks between granitoid domes. The L-tectonite in the amphibolite unit of greenstone arm in the northern domain of the SGB (Figure 3.3E and Figure 3.5C) is interpreted to have developed possibly due to its closeness to a possible triple junction to the west.

The structural pattern and the lithological distribution of the numerical model are shown in Figure 3.9. The foliation traces and lineation patterns are extracted from the orientation of the principal axes of the modelled strain ellipsoids. The data is presented on a horizontal slice surface at a depth of *ca.* 8.00 km, corresponding to the regional greenschist facies metamorphism in the SGB. The foliation traces are coloured by the dip angle and scaled proportionally to the logarithm of the strain intensity computed by Equation (3.3). The strain is strongly concentrated within the greenstone belt and at the granitoid-greenstone contact, while in comparison the granitoid domes are less deformed. This is consistent with the observation that the high strain zones are more commonly distributed within the supracrustal assemblages and near the granitoid-greenstone boundaries.

The foliation is steeply-dipping within the greenstone belt and in most areas track the granitoid-greenstone boundary. However, in areas where the greenstone belt shows an "interfingering" relationship with the granitoid domes (area 1, area 2 and part of area 3 in Figure 3.9), the strike of the foliation is parallel to the elongation direction of the greenstone belt and may be at an angle to the granitoid-greenstone contact because of the localized strain within a narrow arm of the greenstone belt.

Within granitoid domes, separate lobes of granitoid subdomes are delineated by shallowly-dipping concentric foliation patterns. This is in agreement with the observation of both the macroscopic and magnetic foliation in the Kenogamissi batholith

Figure 3.9 ***(following page)*:** Modelled lithological distribution and structural pattern on a slice plane at *ca.* 8.00 km depth. A: modelled foliation trend coloured by dip angle. The length of the lines representing foliation strike is proportional to deformation intensity. B: modelled lineation pattern coloured by plunge angle. Rectangles 1, 2, 3 and 4 delineate areas of the numerical model that can be compared with specific domains within the SGB field areas. See text for further discussions.


km 0 20 40 60 80 100 120 140 160 180 200 220 240
1
2
Fig. 3-10B
3
Fig.3-10A
4
A
B
Supracrustal assemblages
Granitoid intrusion
Lineation
Foliation trace
Foliation dip / Lineation plunge
0 10 20 30 40 50 60 70 80 90°

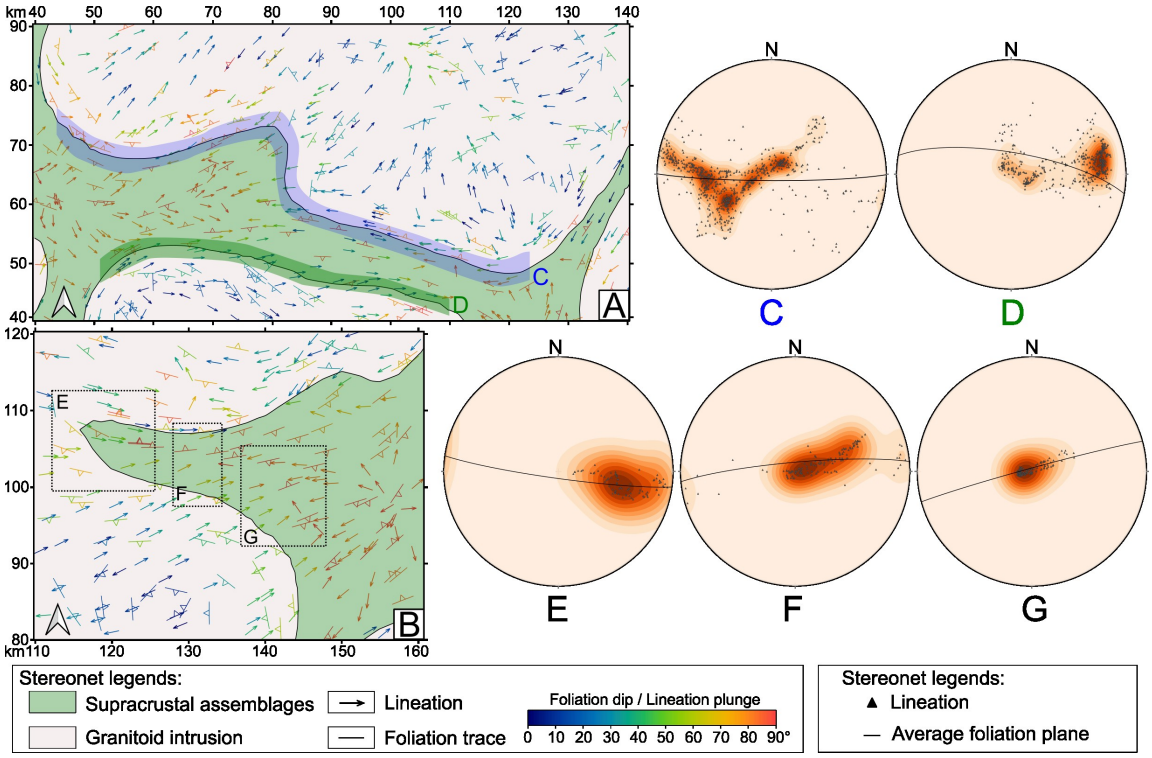


Figure 3.10: Simulated lineation and foliation patterns in the southern (A) and northern (B) domains of the numerical model. The location of both domains are shown in Figure 3.9. In the southern domain, the lineation patterns at the northern and southern granitoid-greenstone contacts are shown in C and D, respectively. In the northern domain, the lineation patterns at three subdomains (locations delineated in B) are shown in E, F and G.

where foliation near with the Rice Lake pluton shows strike directions almost concentric to the boundary. The lineation patterns in the interior of the granitoid domes are highly variable both in the numerical model and the field structural data. However, the lineation patterns of the modelled area 4 of Figure 3.9B and the Rice Lake pluton (see Figure 3.2A), both situated at southwestern part of a granitoid dome, are comparable in both overall E-W plunge direction and moderate to shallow plunge angles.

To facilitate comparisons of lineation patterns between the numerical models for the southern and northern domains of the SGB, we choose the areas 2 and 3 respectively from the modelled geological map for detailed analysis (Figure 3.9A). Area 2 is chosen due to its location on the southern margin on a modelled granitoid complex and its E-W-trending direction analogous to the southern domain. Areas

1 and 2 in Figure 3.9 have a similar geometry of a greenstone arm extending into the granitoid complex as the northern domain. However, area 2 is chosen because the presence of a granitoid dome northwest of area 1, causing interference to the structural pattern. From our field mapping, the granitoid dome is non-existent in reality.

The structural pattern of area 3 is shown in detail in Figure 3.10A. The lineation and average foliation data of the northern and southern granitoid-greenstone boundaries are plotted in Figure 3.10C and Figure 3.10D, respectively. The computed lineation patterns show an opposing lineation pattern from west-plunging at the northern boundary to east-plunging at the southern boundary. The lineation plunge direction and the asymmetry thereof agree with the measured data in Figure 3.4B.

A similar comparison is made between the northern domain of the SGB and area 2 of the numerical model (Figure 3.9 and Figure 3.5B). Three regions (Figure 3.10E, F and G) are selected from the westernmost tip of the greenstone arm progressively towards the east. The lineation patterns in each area are plotted and compared to the lineation patterns in subdomains G and F of Figure 3.5, respectively. Due to the reversed narrowing direction of the greenstone arm in the numerical model (westward) from the field observation (eastward), the modelled lineation plunge direction is a mirror image of the field observation in the SGB. Both modelled and observed lineation patterns show a similar trend: The lineation at the narrowed tip of the greenstone arm plunges towards wider main body of the greenstone belt, *i.e.* westward in the SGB (Figure 3.5H) and eastward in the numerical model (Figure 3.10H). As we approach the main body of the greenstone belt, the lineation pattern gradually changes to a vertical down-dip plunge (Figure 3.10E to G versus Figure 3.5F to G).

3.5 Discussion

3.5.1 Model assumptions and limitations

Our model is purposefully simple in design so that we may isolate a minimum set of geological conditions to reproduce the lithological and structural patterns in the SGB and potentially in other Neoarchean granitoid-greenstone terranes in general. Therefore, certain assumptions are made in this model and some geological processes are not taken into consideration in this study. The justifications for these simplifications as well as their potential influence on the operation of the Neoarchean crustal dynamics are discussed in this section.

Both the governing equations and the rheological laws are considered to be temperature independent. Hence, the temperature variable does not appear in the governing equations or the constitutive model. With this assumption the thermal weakening of the material as well as the weakening by the generation of partial melt at super-solidus temperature (possibly by orders of magnitude) (*e.g.* McKenzie and Bickle, 1988) is not considered in this model. Therefore, it is predicted that the constant viscosity in the numerical model is likely an underestimation of the variations of the real-life crustal strength. However, once the gravitational overturn begins, the emerging structural pattern predicted in our model will likely remain unchanged. In Chapter 4, we consider a more sophisticated model with a temperature-related stress-strain relationship.

The rheological model of the upper crust in our model is approximated by a linearly viscous rheology, whereas in reality the crustal deformation shallower than the brittle-ductile transition is controlled by brittle or a mixture of brittle-ductile processes. Furthermore, the dependency of viscosity with respect to strain rate ("strain-weakening") is not considered in our current model. Therefore, future incorporation of a power-law viscoplastic rheological model for the crustal material will yield a more realistic estimate of the crustal strength as well as the initiation, the evolution and the spatial distribution of high strain zones as they develop naturally under the modelled tectonic framework. An extended crustal model with the viscoplastic rheological model is discussed in Chapter 4.

Considering all the above-mentioned assumptions and simplifications, we point out that the deformation mechanisms of the geological material in nature, which involves various weakening mechanisms of the granitoid substrate as well as the supracrustal assemblages, can probably facilitate or impede the gravitational overturn in many ways. In this light, the timing estimate of the dome-and-keel development of our model should not be considered as reliable but rather more likely to represent an upper limit. Despite this, the dynamics of the sagduction/diapirism is similar and structural patterns of our numerical model will likely remain valid.

3.5.2 Implications for the Neoarchean tectonics

Several recurrent structural trends in our model are also observed in Archean terranes where gravitational overturn is postulated to be the underlying physical process for controlling the tectonic evolution. These features are also observed in the SGB and are reproducible with our current 3d model: (1) a dominant foliation trajectory

mostly parallel to the granitoid-greenstone boundary (*e.g.* Bouhallier et al., 1995; Zibra et al., 2020); (2) the granitoid-up/greenstone-down shearing kinematics recorded at the granitoid-greenstone boundary (*e.g.* Zibra et al., 2020); (3) the strong localized deformation in the form of high strain zones close the granitoid-greenstone contact (*e.g.* Chardon et al., 1998); (4) the strong flattening strain within the linear greenstone belt and (5) the development of local constrictional strain and radial lineation traces within the greenstone (*e.g.* Parmenter et al., 2006; Chardon et al., 1998; Zibra et al., 2020), *e.g.* at the triple junctions (Figure 3.5F and G). A radially outward-plunging lineation pattern can also be observed at the core of the granitoid domes (*e.g.* Bouhallier et al., 1995) The agreement between the modelled structural pattern and field observations implies that the gravitational overturn is a viable process to explain the Archean dynamics. Our field investigation and numerical model of the G_2 deformation reveals the coexistence of two modes of deformation in the SGB around *ca.* 2680 Ma: (1) a vertical component characterized by greenstone-down/granitoid-up kinematics and moderately- to steeply-plunging L_2 lineation, and (2) a horizontal component of dextral shearing, characterized by the opposite plunge of the L_2 lineation at opposing granitoid-greenstone boundaries and local preservation of dextral kinematics on the horizontal plane. Our numerical modelling confirms that the gravitational overturn ("vertical tectonism") which develops under the backdrop of synchronous far-field dextral shearing (imposed as boundary conditions) is a viable explanation for the lithological distribution, strain distribution and foliation/lineation trends. The map pattern and structural trends reported in this study of granitoid-up/greenstone-down kinematics and asymmetrical lineation pattern is a recurring pattern in various parts of the Superior Craton, although the horizontal shear sense may differ for each field area (Lin, 2005; Lin and Beakhouse, 2013). The coexisting evidence of both horizontal and vertical regional strain is also documented in multiple Neoarchean terranes. In the Dharwar Craton, the vertical sagduction of the greenstone belt was accompanied by the intracratonic coaxial E-W shortening and N-S stretching due to regional contraction following terrane accretion at *ca.* 2500 Ma (Krogstad et al., 1989). In the Yilgarn Craton, there existed a secular change from gravity-driven tectonics in the form of polydiapirism at *ca.* 2750 Ma to regional E-W shortening due to the onset of Yilgarn Orogeny *ca.* 2730 Ma (Clos et al., 2019; Zibra et al., 2020). From this synthesis we may infer that the density, thermal and rheological conditions of the Neoarchean crust in multiple cratons are both "weak" enough for the development crustal-scale gravitational tectonism and at the same time "strong" to support far-field transmission of regional tectonic stress.

Multiple lines of evidence point towards the operation of a subduction-accretion process for the Abitibi-Wawa terrane tectonics around 2680 Ma. Based on the geo-

chemical characteristics of mantle signatures of the *ca.* 2680 Ma syn-deformation pluton phases, Beakhouse et al. (2011) and Lin and Beakhouse (2013) suggest that they are the result of slab breakoff and orogenic collapse following subduction termination. Mole et al. (2021), based on isotopic and trace element geochemical data as well as zircon U-Pb geochronology, suggests a tectonic evolution of subduction initiation between 2704 Ma and 2695 Ma leading up to continental collision and cratonization (2685-2670 Ma) in the southeast Superior Craton. Under this framework, the gravitational overturn, interpreted as the cause of the vertical component of the G_2 deformation, is inferred to have taken place under the backdrop of horizontally-directed subduction-accretion-like processes following a geodynamic shift towards collisional tectonics in Neoarchean (Mathieu et al., 2023). This implies that the local development of vertical tectonism involving individual greenstone belts and the adjacent granitoid domes is not in contradiction with the simultaneous operation of horizontal plate tectonic-like processes on a subprovince and lithospheric scale, as initially proposed by Lin (2005). Furthermore, we speculate that in the context of southern Abitibi-Wawa terrane, the dextral component of the G_2 sagduction/diapirism in the SGB may be explained by oblique partitioning of the D_1 N-S shortening identified across CLLDZ onto the NW-SE-trending greenstone geometry analogous to the scenario proposed by Wilkinson et al. (1999) for the CLLDZ (*e.g.* Lin and Jiang, 2001).

3.6 Conclusion

Our field structural analysis in the southern SGB identifies four generations of regional deformation (G_1 to G_4): from G_1 high-temperature subhorizontal flow in the granitoid infrastructure, followed by (G_2) granitoid-up/greenstone-down vertical movement synchronous with dextral horizontal shearing which establishes the crustal architecture of the SGB, G_3 oblique north-side-up sinistral shearing on the RDZ and finally to the G_4 regional dextral shear reactivation. Zircon U-Pb geochronology results of the deformation generations constrains the age of G_2 to around 2680 Ma and dextral strike-slip movement to be no earlier than 2678 Ma. Our deformation analysis reveals a comparable G_2 strain field and an analogous structural history between the RDZ and CLLDZ. Therefore, both deformation zones likely developed and evolved under the same tectonic setting. However, the discrepancy in G_3 kinematics and stratigraphical relationship with respect to Timiskaming-type sedimentary package likely precludes the possibility that they belong to a single coherent crustal-scale high strain zone.

A numerical model is constructed to test whether a synchronous horizontal and vertical tectonic regime, governed by the simultaneous operation of gravitational overturn and horizontal shearing probably due to far-field tectonic stress, can explain the G_2 structural pattern. The results show agreement with field mapping in terms of lithological pattern, the strain distribution and the shear kinematics. The reversal in the lineation plunge directions on opposing granitoid-greenstone boundaries in the southern domain and the convergent lineation pattern in the greenstone arm in the northern domain are also reproduced in the 3d numerical model. Therefore, we conclude that the synchronous vertical and horizontal tectonism is a viable first-order explanation for the structural pattern of the SGB. Therefore, the lithological and structural pattern of the SGB is compatible with the simultaneous operation of vertical movement due to gravity-induced density inversion and the horizontal shearing. Assuming the latter is possibly related to the far-field stress due to terrane accretion, we propose that the G_2 strain pattern serves as a natural example of the coexistence of the vertical crustal-scale diapirism/sagduction process and horizontal plate interactions as the Earth transitions towards a mature modern-day plate tectonics in the Neoarchean.

Chapter 4

Neoarchean crustal architecture and structural patterns under synchronous horizontal and vertical tectonism: Insights from numerical modelling

4.1 Introduction

As the Earth dissipates heat through its geological history and evolves from its early lithospheric dynamics of the stagnant lid tectonics to the present-day plate tectonics, the crustal dynamics may have mirrored this trend. With the increase of the crustal strength due to the gradually lowered planet-wide heat budget, crustal-scale tectonic processes may have transitioned from the vertically-directed gravitational instability (*i.e.* sagduction/diapirism) in response to an inverted density profile to a horizontally-directed folding and faulting in response to far-field tectonic forcing between rigid crustal blocks or plates. Furthermore, it is conceivable that this transition happens in a gradual manner and therefore at some time in the geological history, both vertical and horizontal tectonic processes coexist to various extents (Lin, 2005). Two outstanding questions remain regarding this transition in crustal dynamics: (a) If vertical and horizontal tectonic processes operate synchronously, what are the structural patterns and crustal architecture resultant from such a tectonic

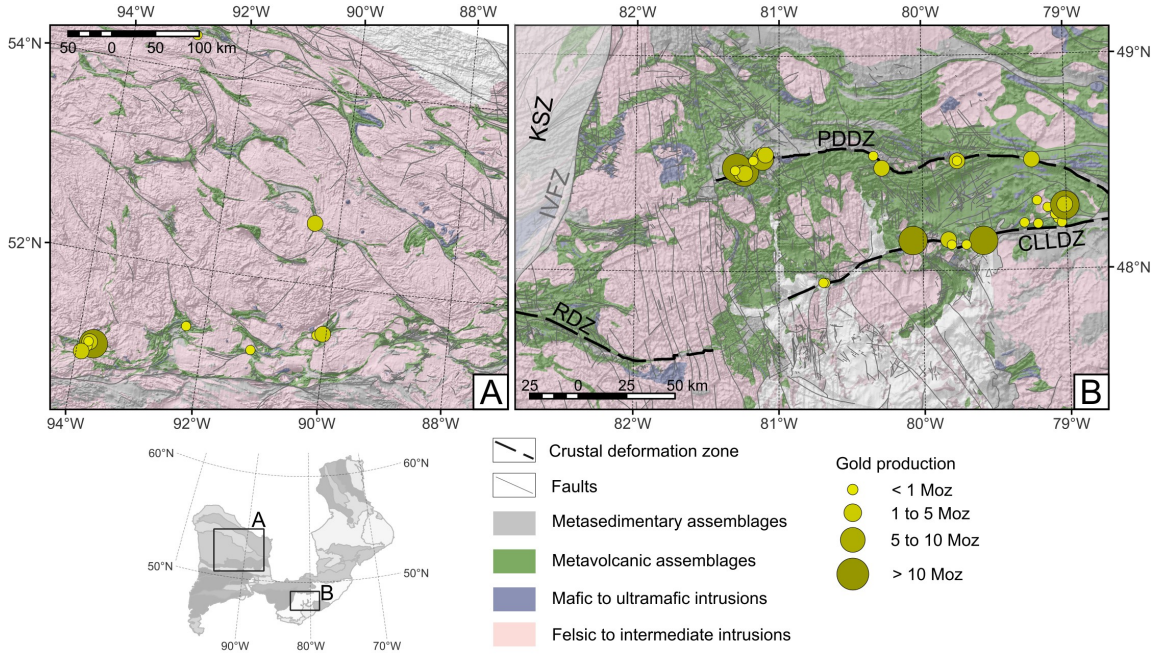


Figure 4.1: Simplified geological maps (A and B) of various parts of the Superior Craton (locations shown in the inset) representative of the Neoarchean granitoid-greenstone terranes. The major gold deposits and crustal-scale deformation zones are also shown. A: The northwestern Superior Craton including the areas of Oxford-Stull terrane, the Island Lake terrane, North Caribou terrane and Uchi terrane. B: Abitibi-Wawa terrane in the southern Superior Craton. CLLDZ: Cadillac-Larder Lake deformation zone; IVFZ: Ivanhoe Lake fault zone; KSZ: Kapuskasing structural zone; PDDZ: Porcupine-Destor deformation zone; RDZ: Ridout deformation zone.

process? (b) What are the possible conditions that drives this transition from the vertical to horizontal tectonism?

The Archean granitoid-greenstone terranes are type localities for studying this transition in crustal dynamics. The Paleo- to Mesoarchean granitoid-greenstone terranes are characterized by a "dome-and-keel" geometry where mostly circular granitoid domes are surrounded by narrow greenstone belts and are generally regarded as the type localities for crustal-scale gravitational instability (*e.g.* Van Kranendonk et al., 2004; Wiemer et al., 2018). The Neoarchean granitoid-greenstone terrane, on the other hand, show evidence of horizontal shearing or flattening deformation in the form of linearly aligned greenstone belts surrounding elliptical granitoid complexes (Figure 4.1A), with the structural trend of the former coinciding with the long axis of the latter. Crustal-scale deformation zones develop sub-parallel to the structural trend in the greenstone belts and are often the preferred localities for gold mineral-

ization (Figure 4.1B). This pattern has led to the interpretation that the strength of Neoarchean crust is sufficiently strong to support the horizontal transmission of tectonic stress. In either case, the field observations imply that the transition of crustal dynamics from a vertical style to horizontal style may be an ongoing process during the Neoarchean era. Elucidating the structural signature of this transition under the Neoarchean conditions has profound implications for both the Earth's tectonic evolution and gold mineralization.

Field studies of the Neoarchean granitoid-greenstone belts in the Superior Craton, the Dharwar Craton and the Yilgarn Craton have yielded ample information concerning the crustal architecture, the structural pattern and the deformation history (*e.g.* Collins et al., 1998; Chardon et al., 1998). Possible interplay between horizontal and vertical tectonic processes has also been discussed in these studies by comparing the structural pattern from the field observations with that obtained from the analogue modelling (*e.g.* Bouhallier et al., 1995; Dixon, 1975; Dixon and Summers, 1983). The latter has the limitation of neither accounting for the thermal effects on rheology, nor the possible synchronous operation of far-field simple or pure shear deformation field. Numerical thermomechanical modelling of the crustal-scale gravitational instability has been conducted in order to shed light on the geometry of gravitational instability (Mareschal and Jaupart, 2006; Weinberg and Podladchikov, 1994), intra-crustal differentiation process (Robin and Bailey, 2009), hydrothermal fluid circulation (Thébaud and Rey, 2013) or the pressure-temperature-time (p-T-t) evolution (François et al., 2014; Yu et al., 2022) as a result of the vertical tectonic processes. However, these models are limited by are the 2d plane-strain formulation and therefore lack information on the 3d crustal architecture as well as the full picture of strain patterns of the modelled crustal section. 3d numerical studies of the diapiric process under the interference of a regional strain field have also been investigated (Guglielmo, 1993, 1994). However, these models are subject to a prescribed strain field and hence do not incorporate the dynamical picture of the crustal deformation.

To overcome the aforementioned limitations, we construct 3d thermomechanical model of the crustal dynamics assuming a synchronous operation between both the horizontal and vertical tectonic processes under a lithological framework and thermal conditions appropriate for the Neoarchean granitoid-greenstone belt. The vertical tectonic process initiated spontaneously under the synchronous operation of imposed simple shearing. The latter represent a regional deformation caused by some far-field tectonic stress. One possible cause for this far-field deformation may be related to the oblique convergence between geological bodies. Reduction in thermal input and the

strain rate of the imposed horizontal movement are systematically varied to explore their effects on the evolution of crustal architecture and deformation patterns.

Our current model serves as a generalization to the numerical model constructed in Chapter 3 by: (a) considering the heat conduction and advection in the model by solving the additional conservation of energy (Equation (4.1c)), (b) applying a more sophisticated non-linear and temperature-dependent rheology for long term flow of the crustal materials and (c) adding the Drucker-Prager plasticity to simulate the spontaneous development of crustal high deformation zones. With the application of thermal and rheological parameters as well as a crustal structure appropriate to Neoarchean conditions, these improvements result in a numerical model which can be of general implications to the Neoarchean crustal dynamics.

Our model results are consistent with those from previous analogue and numerical models. Furthermore, our simulated crustal architecture and structural pattern compare favourably with those in the Neoarchean granitoid-greenstone terranes worldwide in terms of the foliation/lineation patterns, the strain distribution and the shear kinematics. The low total pressure area in the greenstone belt are coincident with the areas of greenstone sagduction and are enveloped by the crustal deformation zones, thus making the latter preferred localities for fluid transfer and gold mineralization. The reduced thermal input produces unfavourable conditions for the gravitational overturn, possibly explaining the transition to a present-day dominantly horizontal style of crustal-scale tectonics due to planet heat dissipation.

In this study we first introduce the governing physics and configuration of the numerical model in Section 4.2. The model results are then presented in Section 4.3. Finally, the comparison of our results to previous analogue and numerical models and the relevance to field observations and Archean tectonic evolution are both discussed in Section 4.4.

4.2 Methodology and model setup

4.2.1 Governing physics

We model the flow of the Earth's lithosphere on a tectonic timescale by solving the following set of equations which respectively describe the conservation of incompressible rock mass, the highly viscous dissipation of momentum as well as heat convection

and conduction (*e.g.* Ranalli, 1995; Gerya, 2019):

$$\begin{cases} \boldsymbol{\nabla} \cdot \boldsymbol{v} = 0 & \text{(4.1a)} \\ \boldsymbol{\nabla} \cdot (2\eta_{\text{eff}}\, \boldsymbol{D}) - \boldsymbol{\nabla} p + \rho \boldsymbol{g} = 0 & \text{(4.1b)} \\ \rho C_p \left(\dfrac{\partial T}{\partial t} + \boldsymbol{v} \cdot \boldsymbol{\nabla} T \right) = \boldsymbol{\nabla} \cdot (k \boldsymbol{\nabla} T) + \rho H(\boldsymbol{x}) + 2\eta_{\text{eff}}\, \boldsymbol{D} : \boldsymbol{D} & \text{(4.1c)} \end{cases}$$

where the unknowns $\boldsymbol{v}$, p and T are the flow velocity, the pressure and the temperature. The material parameters ρ, C_p and k are respectively the density, the specific heat and heat conductivity. $\boldsymbol{D} = \frac{1}{2}\left(\boldsymbol{\nabla}\boldsymbol{v} + (\boldsymbol{\nabla}\boldsymbol{v})^\top\right)$ is the rate-of-deformation tensor. The $\boldsymbol{g}$ is the constant gravity vector pointing in the negative z-direction. The total pressure p thus obtained from solution should be interpreted as the sum of the lithostatic pressure and the tectonic overpressure and is fixed to be zero at the top surface of the model. The mechanical part of the governing equations, *i.e.* Equations (4.1a) and (4.1b), are completed by appropriate velocity boundary conditions described in detail in Section 4.2.2. The thermal part (Equation (4.1c)) requires the prescription of an initial temperature field and temperature boundary conditions. Both are described in Section 4.2.2.

A visco-plastic model is used to model the crustal rheology by taking into account both the viscous creep and brittle failure (Glerum et al., 2018). The viscous part of the model is described by the combined operation of the dislocation creep and diffusion creep. The effective viscosity formulation of the dislocation creep is

$$\eta_{\text{disl}} = \frac{1}{2} A_{\text{disl}}^{-\frac{1}{n}}\, \mathrm{D}_{\text{II}}^{\frac{1-n}{n}} \exp\left(\frac{Q + pV}{nRT}\right) \tag{4.2}$$

where A_{disl} is the constant viscosity prefactor, $\mathrm{D}_{\text{II}} = \sqrt{\frac{1}{2}(\boldsymbol{D} : \boldsymbol{D})}$ is the square root of the second invariant of the rate-of-deformation tensor $\boldsymbol{D}$. The diffusion creep mechanism is dominant under low differential stress (10–100 MPa, Ranalli, 1995) and therefore is taken into consideration in our numerical model. The flow law of the diffusion creep assumes the following form:

$$\eta_{\text{diff}} = \frac{1}{2} A_{\text{diff}}^{-1} \exp\left(\frac{Q + pV}{RT}\right) \tag{4.3}$$

where A_{diff} stands for the prefactor for the diffusion creep. Due to the lack of experimental data for the diffusion creep, we adopt the approximation in (Thébaud and Rey, 2013; Robin, 2010) and assume that the creep mechanisms produce the

same strain rate at an equilibrium stress level and back-calculate the prefactor for the diffusion creep A_{diff}. The activation energy is assumed to be the same for both dislocation and diffusion creep. The final effective viscosity is computed by taking the harmonic mean of the dislocation creep viscosity as well as the diffusion creep viscosity:

$$\eta_{\text{eff}}^{\text{visc}} = \frac{2}{1/\eta_{\text{diff}} + 1/\eta_{\text{disl}}} \tag{4.4}$$

The brittle failure of the lithosphere is described by the Drucker-Prager plasticity criterion, which defines a yield stress σ_{yield} as a function of pressure:

$$\sigma_{\text{yield}} = \frac{6\alpha_C C\cos(\alpha_\phi\phi) + 6p\sin(\alpha_\phi\phi)}{\sqrt{3}(3-\sin(\alpha_\phi\phi))} \tag{4.5}$$

If the stress computed by the viscosity formulation in Equation (4.4) exceeds σ_{yield}, the effective viscosity is rescaled so that the stress remains bounded by the yield surface:

$$\eta_{\text{eff}}^{\text{plas}} = \frac{\sigma_{\text{yield}}}{2\text{D}_{\text{II}}} \tag{4.6}$$

The amount of plasticity-induced strain is integrated throughout the modelled duration to show corridors (*i.e.* deformation zones) where strain is preferentially localized. Weakening of the cohesion C and the internal angle of friction ϕ is prescribed when the plastic strain reaches $\epsilon_{\text{min}}^{\alpha}$. To simulate the effect of strain weakening, a weakening coefficient is prescribed to the cohesion (α_C) and the internal angle of friction (α_ϕ) respectively, both decreasing linearly from 1.0 (no weakening) to α_C or α_ϕ as the accumulated plastic strain increase from $\epsilon_{\text{min}}^{\alpha}$ to $\epsilon_{\text{max}}^{\alpha}$ The final effective viscosity is taken as the smaller value among both the creep-related viscosity and plasticity-related viscosity:

$$\eta_{\text{eff}} = \min\left(\eta_{\text{eff}}^{\text{visc}}, \eta_{\text{eff}}^{\text{plas}}\right) \tag{4.7}$$

To analyse the finite strain accumulated through time in the numerical model, tracer particles are generated in the numerical model. The position of each particle is advected with the predicted velocity field and the temporal evolution of deformation is visualized by the local reconstruction of a strain ellipsoid per particle. A wealth of information concerning the finite deformation field can be extracted from the strain ellipsoids *e.g.* the strain intensity, strain type distribution (*i.e.* stretching versus flattening) and foliation/lineation trajectories (*e.g.* Lin et al., 1998). For a more comprehensive exposition of extracting this information, the reader is referred to Wú et al. (2023) and Jiang (2023). The tools applied for implementation of finite deformation analysis on tracer particles are described in Appendix F.

4.2.2 Model setup

Geometry and material parameters

We construct a numerical model consisting of three layers of geological materials to represent the crustal architecture of a generalized crustal structure of the Neoarchean terranes (*e.g.* Robin and Bailey, 2009; Bodorkos and Sandiford, 2006). A geometrical representation of the numerical model is shown in Figure 4.2. All rheological parameters used in the model are listed in Table 4.1. The topmost layer of the numerical model consists of a mixture of a minor component (10%) of serpentinite and a major component (90%) of fresh diabase to simulate an upper crustal greenstone assemblage composed of predominantly of mafic or ultramafic volcanic rocks, following the upper crustal lithology in Robin (2010). We improve upon the material definition of the middle crust of Robin (2010) by also considering granite (10%) in addition to quartz diorite (90%) to represent the middle crust made up of a tonalite-trondhjemite-granodiorite (TTG) composition. The effective viscosity for each layer is computed as a result of the mixture of n materials. Assuming the i-th material in this mixture has an effective viscosity $\eta_{\mathrm{eff},i}$, the effective viscosity of the mixed material can be computed by a weighted harmonic average:

$$\eta_{\mathrm{eff}} = \frac{\sum_{j=1}^{n} w_j}{\sum_{i=1}^{n} \left(w_i / \eta_{\mathrm{eff},i} \right)} \tag{4.8}$$

Therefore if large viscosity contrasts exist within the material mixture, the resultant effective viscosity is controlled by the material with the smallest magnitude in viscosity. On the interface between the upper and middle crust, circular random perturbations of heights between 1.00 km and 5.00 km and radius between 5.00 km and 2.00×10^1 km are distributed to simulate the initiation of diapirism/sagduction process on a probably uneven upper/middle crust interface, similar to the setup for Chapter 3.

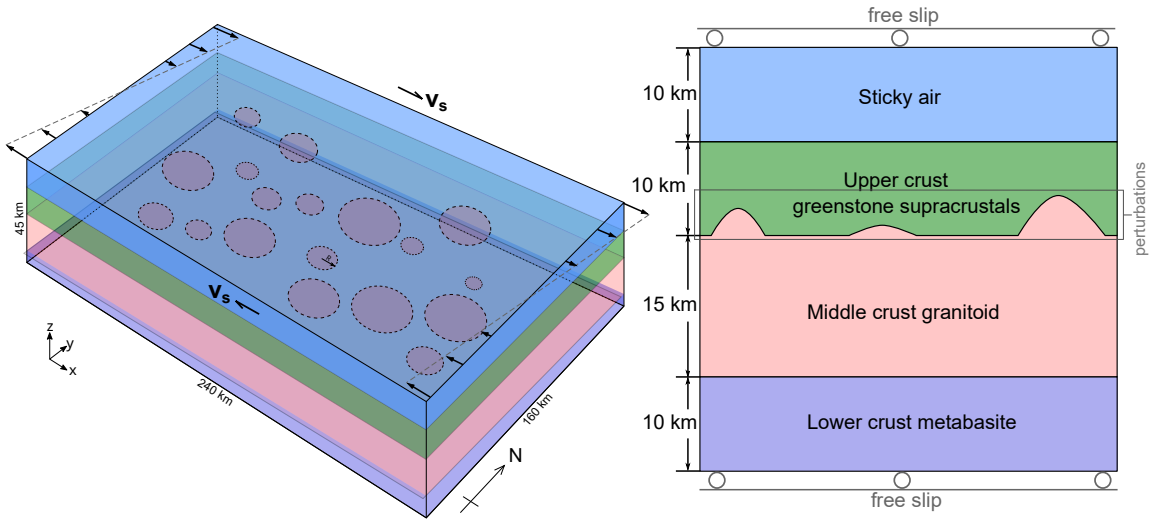


Figure 4.2: Model setup and boundary conditions of the Neoarchean synchronous crustal-scale gravitational overturn and horizontal shearing in 3d view (left) and cross-sectional view (right). In the 3d view, the ellipses on the interface between the supracrustal rocks of the upper crust and the middle crustal granitoid represent the perturbations schematically. v_s stands for the prescribed boundary speed of horizontal shearing.

	Lower crust	Middle crust		Upper crust		Sticky air
	Microgabbro[1]	Wet diorite (90%)[2]	Wet granite (10%)[3]	Diabase (90%)[4]	Serpentinite (10%)[5]	
Thermal parameters						
Density (ρ, kg/m^3)	2.90×10^3	2.70×10^3	2.70×10^3	2.90×10^3	2.90×10^3	1.0
Heat conductivity (k,W/(m $\cdot$ K))	2.90	2.70	2.70	2.90	2.90	2.90×10^2
Heat capacity (C_p, J/(K $\cdot$ kg))	1000	1000	1000	1000	1000	1000
Heat production (H, µW/m^3)	0.5	1.0	1.0	0.1	0.1	0.0
Viscous rheology						
Stress exponent (n)	3.4	2.4	1.9	3.05	2.8	1.0
Activation enthalpy (Q, kJ/mol)	497	212	140	276	66	0
Dislocation creep prefactor (A_{disl}, Pa^{-n}1/s)	1.99×10^{-11}	1.27×10^{-16}	7.96×10^{-16}	3.08×10^{-20}	9.99×10^{-24}	2.50×10^{-19}
Diffusion creep prefactor (A_{diff}, 1/(Pa $\cdot$ s))	1.75×10^7	3.74×10^{-6}	4.27×10^{-9}	6.40×10^{-5}	4.27×10^{-9}	2.50×10^{-19}
Plastic rheology						
Cohesion (C, MPa)	4.00×10^1	1.00×10^1	1.00×10^1	1.00×10^1	1.00×10^1	$+\infty$
Internal angle of friction (ϕ, $^\circ$)	25	15	15	5	5	0
Plastic strain weakening range ($[\epsilon_{\min}^{\alpha,\text{plas}}, \epsilon_{\max}^{\alpha,\text{plas}}]$)	[0.0, 0.5]	[0.0, 0.5]	[0.0, 0.5]	[0.0, 0.5]	[0.0, 0.5]	n/a
Cohesion weakening factor (α_C)	0.2	0.2	0.2	0.2	0.2	n/a
Friction angle weakening factor (α_ϕ)	0.2	0.2	0.2	0.2	0.2	n/a

[1] Wilks and Carter (1990)
[2] Ranalli (1995)
[3] Burov (2011)
[4] Caristan (1982)
[5] Raleigh and Paterson (1965)

Table 4.1: List of the values of material parameters used in the numerical model.

Above the geological units, a less viscous top layer of sticky air is prescribed to model the effect of a free surface (Crameri et al., 2012). In our simulation we prescribe a constant viscosity of $5.00 \times 10^{18}\,\mathrm{Pa} \cdot \mathrm{s}$ for the sticky air layer, which is two orders of magnitude lower than the viscosity at the ground surface. The heat conductivity (k) of the sticky air is prescribed to be two orders of magnitude higher than that of the underlying lithological units so that temperature within the sticky air layer will not deviate for more than $5.00\,^{\circ}\mathrm{C}$ throughout the duration of the model.

Velocity boundary conditions

The top and bottom boundaries of the model are treated as free slip boundaries to ensure the well-posedness of the governing equations. The north (south) boundaries are prescribed a fixed velocity v_s ($-v_s$) in the x ($-x$) direction. The east and west boundaries of the model are prescribed a horizontal velocity that varies linearly from v_s to $-v_s$ from north to south. In this configuration, the velocity boundary conditions prescribe a background horizontal shearing to the model. The induced shear strain rate of the model can be computed by $1.25 \times 10^{-7} \times v_s$ (1/yr), assuming v_s is in the unit of cm/yr. The effects of various v_s on the crustal deformation are explored in Section 4.3.2.

Thermal conditions

The top boundary is prescribed a constant temperature of $0\,^{\circ}\mathrm{C}$ (*e.g.* Robin and Bailey, 2009; Yu et al., 2022), which is approximately equivalent to the ground surface temperature. The base of the crust is prescribed a steady state heat flux q_m. The values of q_m are varied, resulting in a corresponding change in basal temperature (in this case, equivalent to the Moho temperature) to explore the change of deformation behaviour on a variety of crustal thermal conditions (see Section 4.3.3). The other boundaries in the model are treated as insulating (*i.e.* zero heat flow) boundaries. The radioactive heating of the modelled crust is prescribed according to the measured values of the concentration of radioactive elements in a crustal transect of the Kapuskasing Structural Zone (Kinney et al., 2023), where a section of the Archean upper to lower crust is exposed due to later faulting.

The initial thermal condition of the crust can be calculated by assuming that the temperature field has been fully equilibrated prior to the beginning of the model under the given basal flux q_m and heat conductivities of each lithological unit. We remark that with this assumption, the initiation of the gravitational overturn in

this study is faster than the studies assuming an instantaneous emplacement of the supracrustal greenstone rocks at surface temperature conditions (*e.g.* Robin and Bailey, 2009; Thébaud and Rey, 2013) and similar in spirit with Yu et al. (2022).

4.3 Modelling results

In this section the 3d lithological architecture and structural patterns predicted by the synchronous horizontal/vertical tectonism model are presented. Firstly, a model without background horizontal shearing ($v_s = 0$) is computed in Section 4.3.1. Building upon the baseline model, we systematically vary the boundary shear speed (v_s) in Section 4.3.2 to assess the effect of higher contribution of horizontal shearing on the crustal dynamics and the structural pattern. We then proceed to test a various range of geotherms in Section 4.3.3 to show the effect of thermal profile on the sagduction process. For both sets of experiments, $v_{\max}$, *i.e.* the peak value of maximum velocity magnitude within the entire modelled time span, along with the time points ($t_{\max}$) at which $v_{\max}$ values are attained, are tabulated for increasing horizontal strain rates (Table 4.2) and basal heat fluxes (Figure 4.9). Finally, we explore the geometry of crustal deformation zones and pressure distribution in Section 4.3.4.

4.3.1 Baseline model without horizontal shearing

We first compute a baseline model with the sole operation of gravitational overturn (pure "vertical tectonism"). A basal heat flux of $q_m = 4.20 \times 10^{-2}\,\mathrm{W/m^2}$ is imposed, resulting in a Moho temperature of approximately $7.50 \times 10^2\,^{\circ}\mathrm{C}$ which is in range for the Neoarchean lower crustal temperature estimated by Sun et al. (2021) assuming the prescribed thermal parameters and a steady-state geotherm. Under this thermal

v_s (cm/yr)	Horizontal strain rate (1/yr)	Peak $v_{\max}$ (cm/yr)	$t_{\max}$ (Myr)
0	0	7.40	1.63
1	1.25×10^{-7}	7.03	1.62
2	2.50×10^{-7}	6.58	1.66
4	5.00×10^{-7}	5.66	1.65

Table 4.2: Maximum velocity magnitude ($v_{\max}$) and the time at which the gravitational overturn reaches peak velocity ($t_{\max}$) under increasing boundary shear velocity (v_s). The background crustal horizontal strain rates as a result of the imposed v_s are also listed.

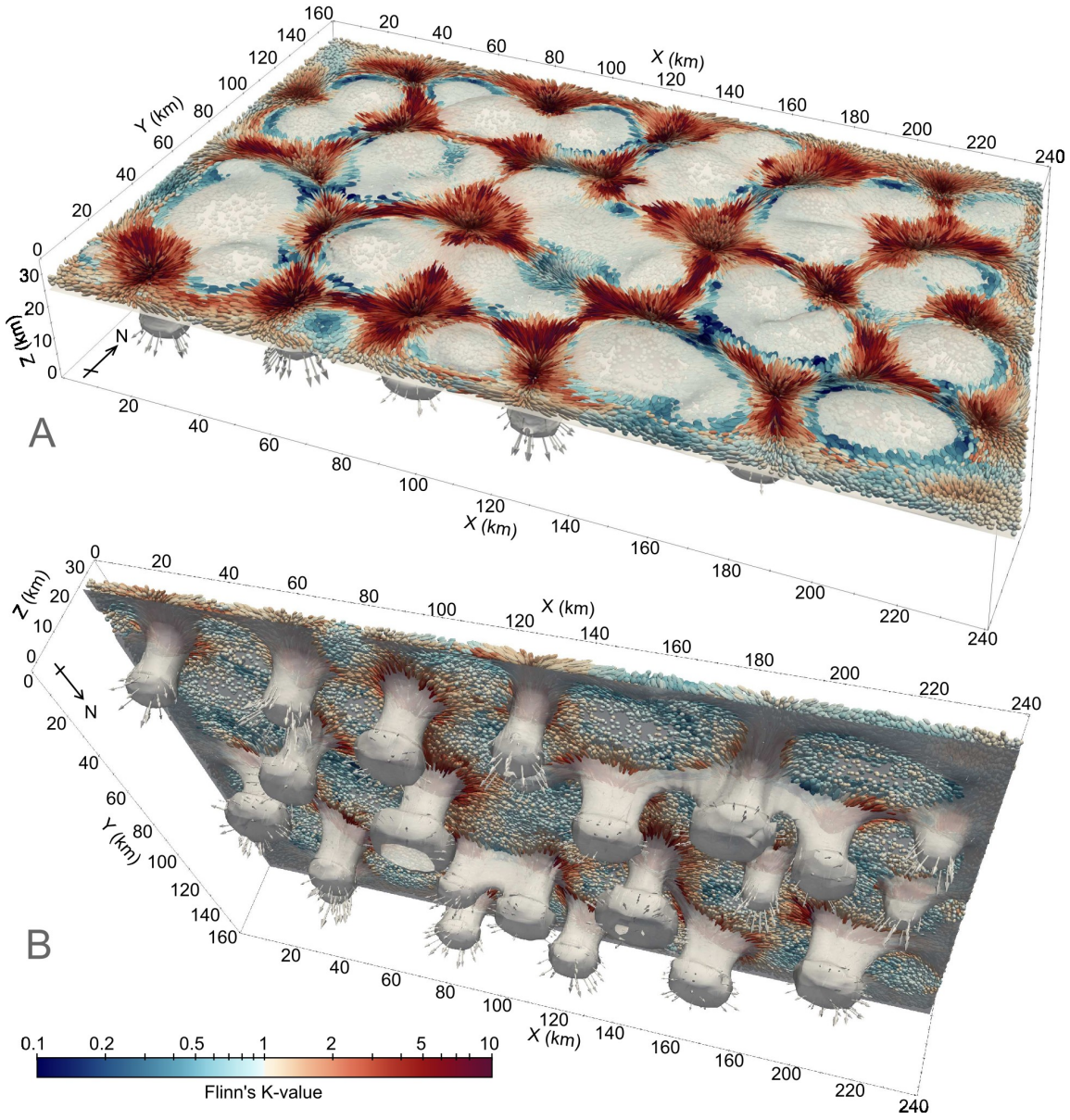


Figure 4.3: 3d geometry of the granitoid-greenstone interface and the strain ellipsoid distribution of the base model. The strain ellipsoids are coloured by the Flinn's K-value. The arrows represent orientation of the local velocity field. A: The view from the top; B: the view from underneath.

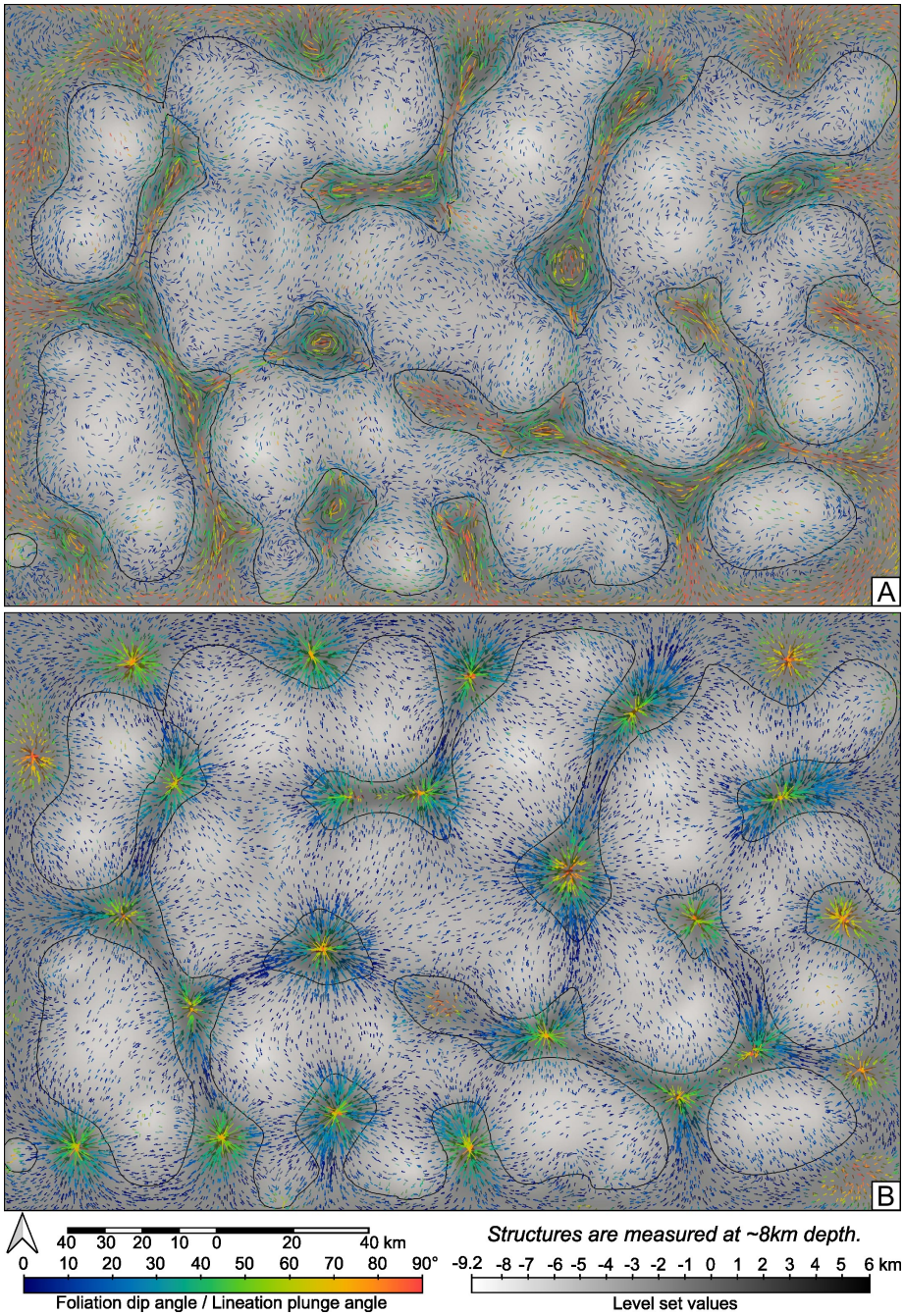


Figure 4.4: Structural patterns of the baseline model at *ca.* 8.00 km depth. In (A) the lines are parallel to the strike direction of the foliation and are coloured by the dip angle. In (B) the arrows point to the plunge direction of the lineation and are coloured by the plunge angle. The lineation arrows are scaled by the logarithm of the Flinn's K-value.

Basal heat flux q_m (W/m^2)	Moho T (°C)	$v_{\max}$ (cm/yr)	$t_{\max}$ (Myr)
0.031	606.14	3.40	5.69
0.0375	697.40	5.11	2.33
0.042	760.58	6.58	1.66
0.045	802.70	7.61	1.44
0.052	900.98	9.59	1.10

Table 4.3: Maximum velocity magnitude ($v_{\max}$) and the time at which the gravitational overturn reaches peak velocity ($t_{\max}$) under increasing basal heat flux q_m (*i.e.* basal temperature). The corresponding temperatures at Moho depth (Moho T), which corresponds to the basal plane of our model, are also given.

and rheological conditions, the maximum velocity of crustal flow as a result of the sagduction of the supracrustal assemblages reaches a peak value of (7.40 cm/yr) at *ca.* 1.63 Myr (Table 4.2). The granitoid-greenstone interface and the geometry of strain ellipsoids are shown in Figure 4.3. The foliation and lineation patterns on a horizontal slice plane placed at *ca.* 8.00 km depth are shown in Figure 4.4, where the foliation lines (Figure 4.4A) are scaled by the strain intensity and the lineation arrows (Figure 4.4B) are scaled by the logarithm of the Flinn's K-value.

In the supracrustal assemblages, the crustal structure is characterized by the "dripping" of the greenstone assemblages at preferential locations, most notably at the triple junction in the greenstone belt between multiple granitoid domes (Figure 4.3). Elsewhere, the supracrustal assemblages coalesce into linear greenstone belts by connecting adjacent sinking centres, forming a "saddle"-like geometry between sinking centres. The lineations close to the triple junctions show a moderately- to steeply-plunging radial pattern and correspond to a strong constrictional strain, which is favourable for the development of *L*-tectonites. In the saddle area between the sinking centres, the strain is characterized by flattening and the lineation is shallowly-plunging towards the closest sinking centre. The foliations in general are parallel to the granitoid-greenstone contact and steepen from the granitoid-greenstone contact towards the centre of the greenstone belt. Near the sinking centres, the foliations are characterized by a triangular or concentric pattern.

The strain is strongly localized in the supracrustal assemblages compared to the granitoid domes. The foliation in the interior of the granitoid domes are shallowly-dipping and may be further subdivided into subdomes, each characterized by a concentric group of foliation. The strain type is generally flattening strain probably due to the impedance of the diapiric rise of the pluton by the low-temperature high-

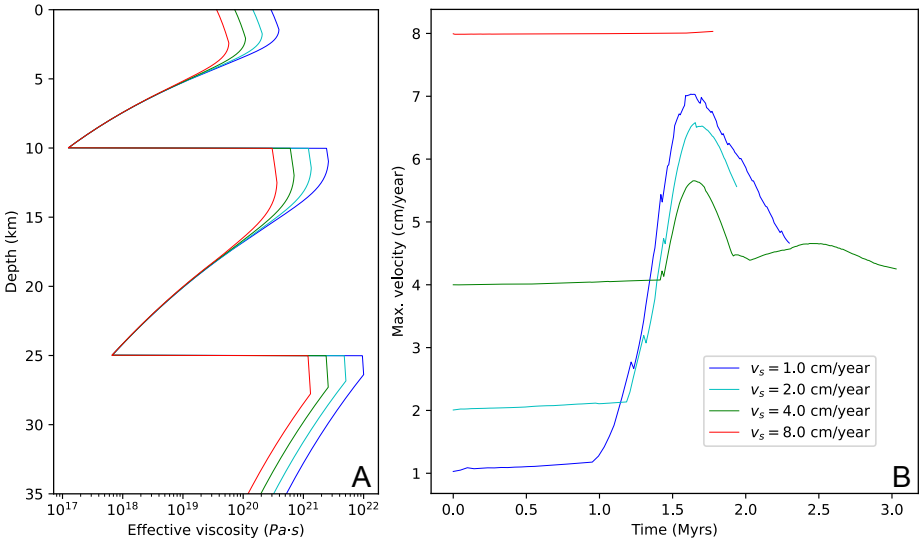


Figure 4.5: A: Profile of effective viscosity with respect to depth. B: Evolution of maximum velocity magnitude with respect to time. The line colours shown in the legends of B also apply to A.

viscosity shallow crust (Figure 4.5A). The lineations in the granitoid dome are generally shallowly-plunging towards the nearby sinking centres located in the supracrustal rocks.

4.3.2 Models with horizontal shearing of varying strain rates

In this set of experiments, building upon the rheological and thermal structures of the vertical baseline model (Section 4.3.1), we impose various magnitude of horizontal shearing (v_s). The increase in the horizontal strain rate generally has a reducing effects on the rheology in the upper part of the upper and middle crust where the deformation mechanism is dominated by the Drucker-Prager plasticity, or in the lower crust where dislocation creep is the main deformation mechanism (Figure 4.5A). The evolution of maximum velocity ($v_{\max}$) is shown in Figure 4.5B. The highly similar values of $t_{\max}$ for various v_s values implies that the reduction in viscosity due to higher horizontal strain rate is not significant enough to result in a faster onset of gravitational overturn. Faster horizontal strain rate, on the contrary, leads to a decreasing trend in the peak $v_{\max}$ and eventually results in no visible sagduction of the greenstone supracrustal.

We plot the 3d crustal structure and the strain ellipsoids for two v_s values of

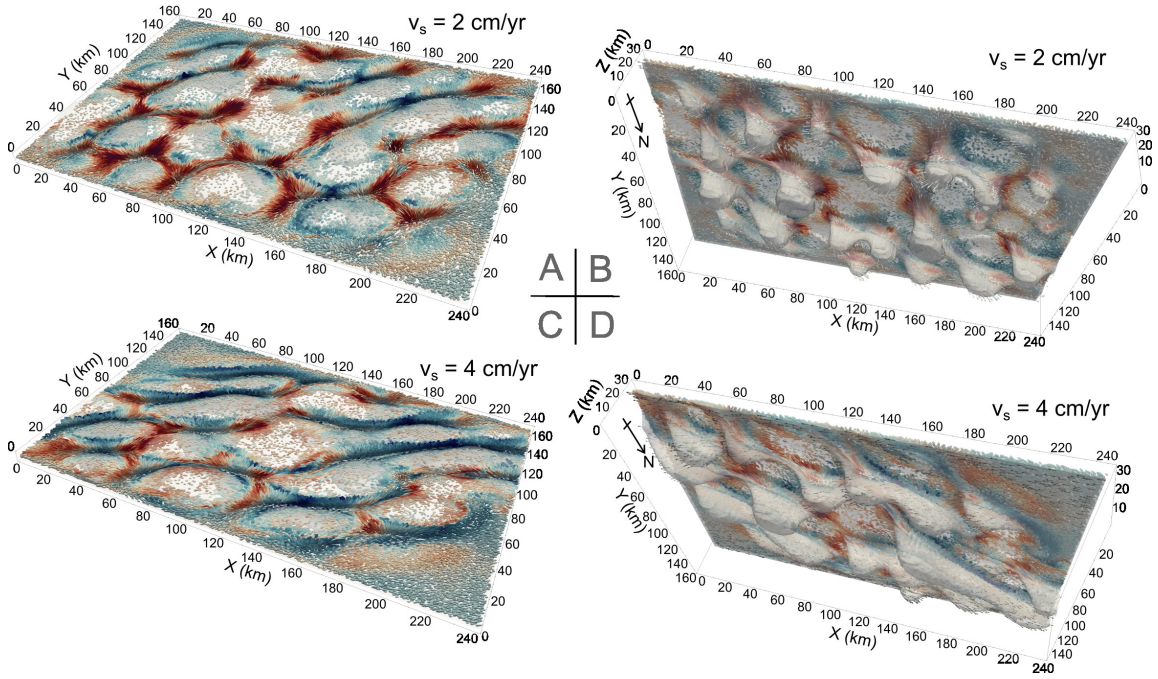


Figure 4.6: The geometry of the strain ellipsoids at *ca.* 8.00 km depth (A and C) and the granitoid-greenstone interface (shown as white surface in B and D) for the boundary shear velocities (v_s) of 2.00 cm/yr (A and B) and 4.00 cm/yr (C and D). The snapshots are taken at the $t_{\max}$ time of *ca.* 1.62 Myr for both v_s values. The strain ellipsoids are coloured by the Flinn's K-value as in Figure 3.8 with the same colour scale.

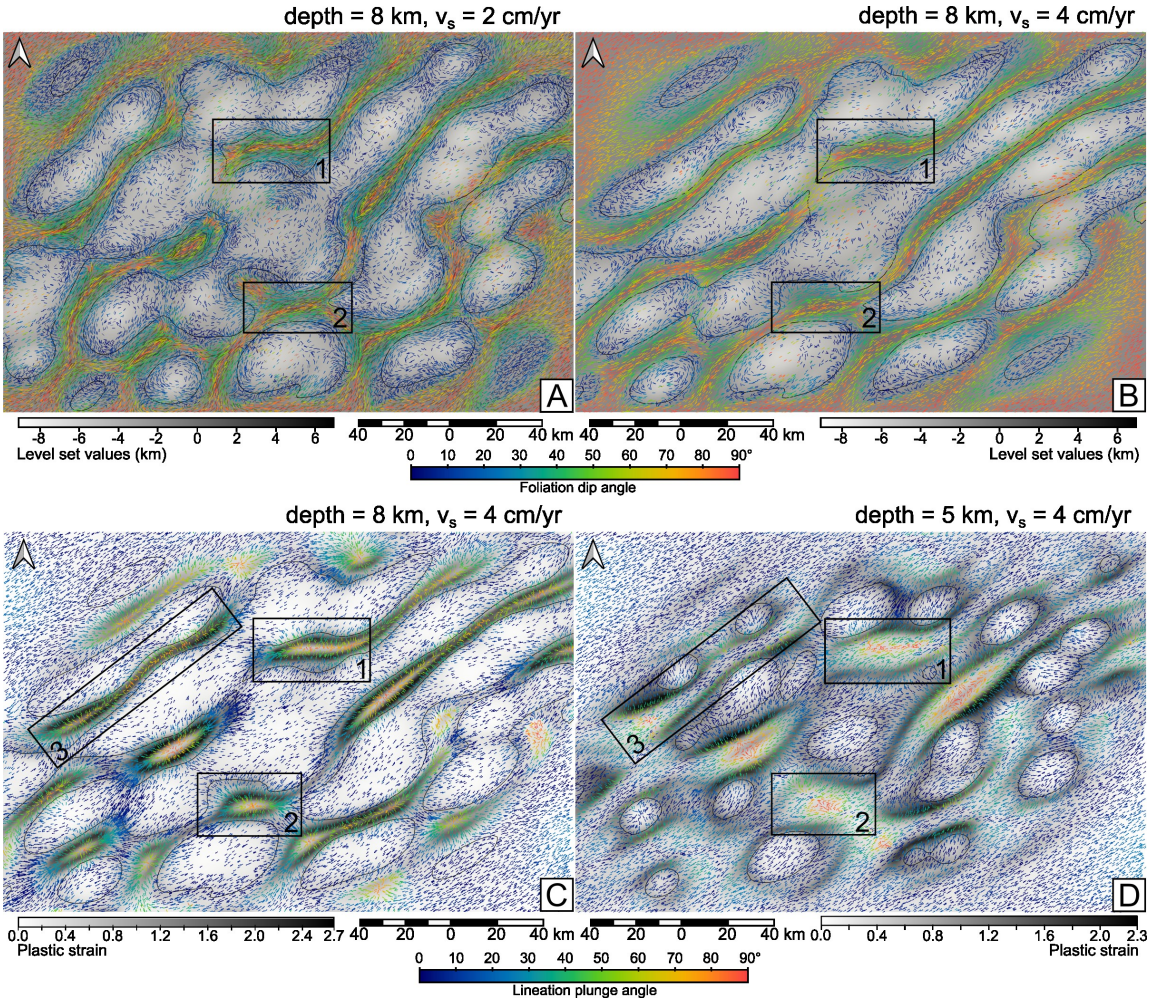


Figure 4.7: Foliation patterns (A and B) at *ca.* 8.00 km depth shown by lines parallel to strike direction coloured by dip angle for boundary shear velocity at 2.00 cm/yr (A) and 4.00 cm/yr (B). Lineation patterns (C and D) at *ca.* 8.00 km depth shown by arrows pointing towards the plunge direction and coloured by plunge angle for the same boundary shear speed (v_s = 4.00 cm/yr) but at different depth (8.00 km for C and 5.00 km for D). Various areas are labelled with numbers and are further discussed in the text.

2.00 cm/yr and 4.00 cm/yr at *ca.* 8.00 km depth in Figure 4.6. The foliation patterns on an 8.00 km-deep slice of the 3d model are shown in Figure 4.7A and Figure 4.7B. All data are plotted at $t_{\max}$ time of *ca.* 1.62 Myr. A comparison between Figure 4.6A and Figure 4.6C shows that the model with a higher v_s accumulates greater amount of horizontal shearing strain evident by the elongated geometry of the granitoid dome. During the incipient stage of the sagduction, elevated rate of horizontal shearing also results in more prominent elongation of the supracrustal assemblages into a trough-like geometry, which later serve as the preferential location when the sagduction process fully develops. The sagduction behaviour also changes from localized dripping (see baseline model and Figure 4.6B) to sheet-like sagduction (Figure 4.6D), due to the combined effects of the folded geometry of the supracrustal rocks when the density instability is initiated and the *syn*-sagduction shear flattening of the down-going supracrustal assemblages attributed to the horizontal shearing (Figure 4.6B and Figure 4.6D). In accordance with the changes of the sagduction behaviour, sheet-like sagduction results in dominantly flattening strain, with minor area of constrictional strain only at either end of the sheet. With the increase of the horizontal shear strain rate, the sheet-like sagduction becomes more pervasive, due to the along-strike lengthening of the sinking sheet, the strain type in the supracrustal assemblage evolves from dominantly constrictional strain (Figure 4.3A) and radial lineation pattern (Figure 4.4B) to wide-spread flattening strain and steeply-plunging down-dip lineation (Figure 4.6C).

The moderately- to steeply-dipping foliation in the supracrustal rocks are in general almost parallel to the granitoid-greenstone contacts. A slight deviation from the contact orientation is attributed to the presence of background shearing. In areas where the granitoid-greenstone contacts are of E-W orientation (*e.g.* in areas 1 and 2 labelled in Figure 4.7A and Figure 4.7B), the foliation assumes a small clockwise angle with respect to the contact, reminiscent of the relationship between the S- and the C-fabric in a mesoscale ductile shear zone.

The lineation patterns can vary depending on both the orientation of the greenstone belt and the crustal level. In Figure 4.7C and Figure 4.7D we plot the lineation patterns for $v_s = 4.00$ cm/yr at two depth levels of 8.00 km and 5.00 km respectively. The lineations in the NE-SW-oriented greenstone belts for both depth levels are moderately- to steeply-plunging and converge towards the centre of the sinking sheet (see area 3 in Figure 4.7C and Figure 4.7D). In the E-W trending greenstone belts, the lineation pattern at the shallow level shows opposing plunge direction from one granitoid-greenstone contact to the other: at the northern granitoid-greenstone contact the lineation is generally west-plunging while the plunge direction reversed to

east-plunging at the southern contact (see areas 1 and 2 in Figure 4.7D). Knowing that the greenstone is displaced downwards with respect to the granitoid intrusion, the stretching lineation is consistent with the regional dextral sense of shearing. However, at a deeper crustal level this opposing plunge direction is no longer obvious and the lineation converges towards the centre of the sinking greenstone assemblages (see areas 1 and 2 in Figure 4.7C). This discrepancy in the lineation pattern is inferred to be the results of the difference in rheological structure of the upper crustal layer (Figure 4.5): at the shallow depth, due to the low temperature and the high viscosity of the crust, the gravitational sinking of the crust does not operate as actively compared to low viscosity crust at deeper levels. However, the shallow crust still records the distributed strain caused by the horizontal shearing and therefore display a lineation pattern affected by regional distributed shearing. At the base of upper crust where the thermal weakening plays a more prominent role, the deformation is dominated by the active sagduction of the greenstone and therefore shows a lineation pattern strongly attracted to the sinking centres.

4.3.3 Models with horizontal shearing at various basal heat fluxes

In this section we explore the response of the crust under a range of geothermal gradients by systematically decreasing the basal heat flux q_m from $5.20 \times 10^{-2}\,\mathrm{W/m^2}$ to $3.10 \times 10^{-2}\,\mathrm{W/m^2}$ while maintaining the boundary shear speed at v_s=2.00 cm/yr. This corresponds to a decrease of the Moho temperature (*i.e.* in this case, the basal temperature of the model, shown in Table 4.3) and results in a range of crustal geotherms shown in Figure 4.8A. This lowering of the basal heat flux results in an overall increase in the crustal viscosity (Figure 4.8B), especially where the crustal deformation is dominated by ductile creep. The increase in the viscosity at lower q_m translates to overall less active sagduction behaviour of the greenstone supracrustal rocks, manifested by (a) the delayed onset of the sagduction process and (b) the smaller magnitude of the sagduction velocity.

When q_m is low enough (*e.g.* $q_m = 2.40 \times 10^{-2}\,\mathrm{W/m^2}$) the overall high crustal viscosity prevents the development of the gravitational overturn and the crustal deformation is characterized by the continual horizontal shearing. Both the delayed onset and the slow sagduction result in greater amount of localized shear strain and the coalescing of sagducted greenstone into sheet at the onset of the gravitational overturn (Figure 4.9). The behaviour of the numerical model with reducing q_m is analogous to increasing v_s discussed in Section 4.3.2.

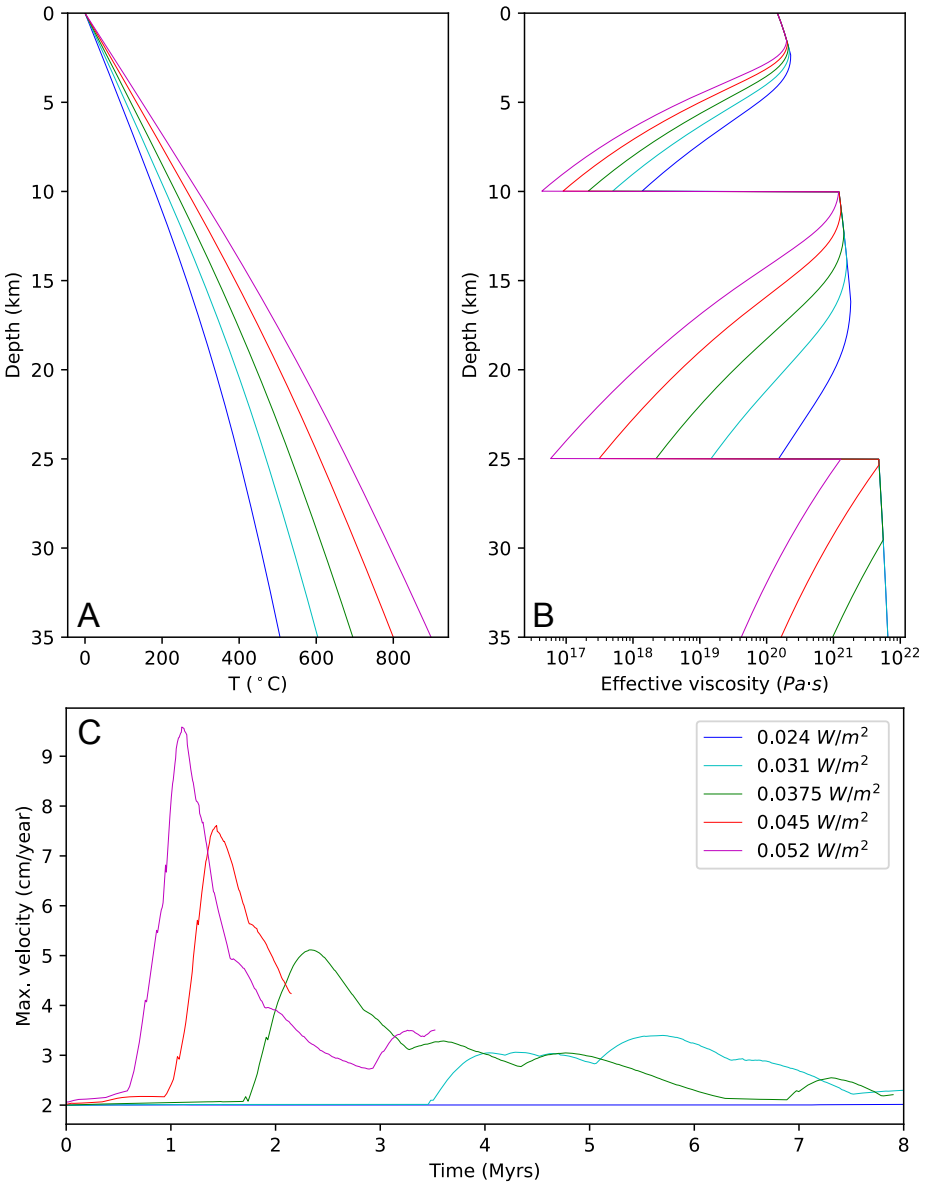


Figure 4.8: Crustal temperature profile (A), effective viscosity profile (B) and the temporal evolution of maximum velocity magnitude (C) in the modelling domain under increasing basal heat fluxes q_m.

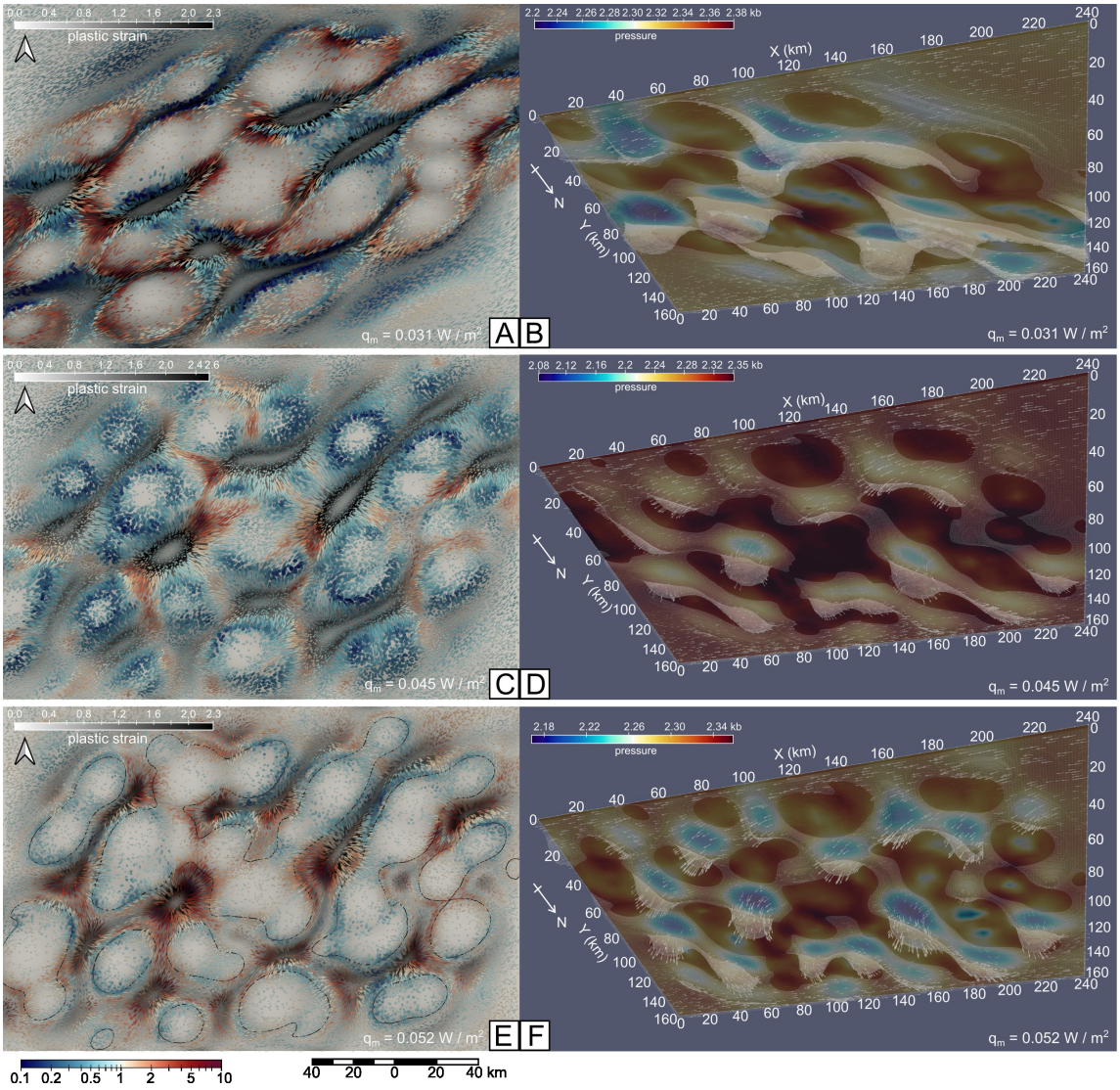


Figure 4.9: Simulated structure of the granitoid-greenstone interface under various basal heat fluxes. A, C and E are the views from the top. B, D and F are the views from below. q_m = 3.10×10^{-2} W/m^2 for A, B; 4.50×10^{-2} W/m^2 for C, D and 5.20×10^{-2} W/m^2 for E, F. A, C and E show the strain ellipsoids coloured by Flinn's K-value and the magnitude of accumulated plastic strain in greyscale shading. B, D and F show the geometry of the granitoid-greenstone interface. The flow velocities in B, D and F, shown in arrows, are scaled by the velocity magnitude. The tectonic pressure at the *ca.* 8.00 km depth are also shown by the colour shading.

We also remark that with reducing q_m the sagduction of the greenstone assemblages evolves towards a time-transgressive process: the sagduction event in each individual greenstone belt may be activated at different times, producing extended period of crustal deformation with multiple pulses of greenstone $v_{\max}$ in Figure 4.8C. The interval between these events can be several million years apart. Therefore, the numerical model supports the possibility of a diachronous process of deformation in granitoid-greenstone terranes under a uniform crustal dynamic framework.

4.3.4 Distribution of total pressure and deformation zones

In the numerical experiments in Section 4.3.2 and Section 4.3.3 we compute the intensity of accumulated plastic strain at a given depth in Figure 4.7C and Figure 4.7D as well as in Figure 4.9A, Figure 4.9C and Figure 4.9E. The higher accumulated plastic strain is interpreted as the high strain zones where relatively higher amount of deformation is localized. If compared with the corresponding 3d crustal structures, we may find that the geometry of the deformation zones approximately delineates the boundary of the sinking greenstone "drip" and "sheet" deeper in the crust. The geometry of the high strain zones is preferentially aligned in the NE-SW orientation parallel to the finite stretching axis of dextral shearing and are situated close to, but not necessarily strictly coincide with the granitoid-greenstone contact. With the continual sagduction and shearing of the greenstone assemblages, an additional deformation zone may develop in the middle of the greenstone belt at the shallow crustal level.

In Figure 4.9B, Figure 4.9D and Figure 4.9F we explore the total pressure p on the 8.00 km-deep slice plane under various temperature conditions and their relationship with the deeper 3d crustal structures. In all cases, the areas above the sinking greenstone "drips" or "sheets" correspond to an area of low total pressure. The pressure difference ΔP_{total} at 8.00 km depth is *ca.* 2.00×10^{-1} kbar. We note that the lithostatic pressure at a given depth within the greenstone belt is higher due to the greater density of the supracrustal assemblages. Therefore, the difference in the dynamic pressure, or the "tectonic over-/underpressure", due to the synchronous vertical and horizontal tectonic process, is likely to be underestimated. An upper bound of this difference in the dynamic pressure may be found by adding the maximum possible pressure difference caused by the density difference (Δp_ρ), which can

be computed as

$$\begin{aligned}\Delta p_\rho &= \Delta\rho\, gh \\ &= (2.90 \times 10^3\,\mathrm{kg/m^3} - 2.70 \times 10^3\,\mathrm{kg/m^3}) \times 9.80\,\mathrm{m/s^2} \times 8.00 \times 10^3\,\mathrm{m} \\ &= 1.57 \times 10^{-1}\,\mathrm{kbar}\end{aligned}$$

Therefore the maximum dynamic pressure difference at 8.00 km depth $\Delta p_\mathrm{d} = \Delta p_\rho + \Delta p_\mathrm{total}$ will not exceed 5.00×10^{-1} kbar. In this sense, the sinking centre of the greenstone assemblage, the high strain zones and the areas of low total pressure are found to be closely related spatially.

4.4 Discussions

4.4.1 Model assumptions and limitations

The initial temperature condition in our model is assumed to have attained a steady-state geotherm profile prior to the start of the model. This treatment is also adopted by Yu et al. (2022) but is different from the starting temperature assumption of Thébaud and Rey (2013) and Robin and Bailey (2009) where the supracrustal assemblages are considered to have been emplaced instantaneously at the temperature of the ground surface. The latter results in a longer time of tectonic quiescence prior to the initiation of the sagduction/diapirism during which the geotherm is equilibrated until adequate thermal weakening of the crust is achieved. However, we refrain from adopting the latter geotherm because doing so results in excessive accumulation of horizontal shearing strain to the extent that the strain caused by vertical tectonism is obliterated. Therefore, in this study, the onset time of sagduction/diapirism should be interpreted as the delay from the thermal weakening of the crust rather than the duration since the deposition of the supracrustal assemblage. A more geologically realistic treatment of the numerical model for a given granitoid-greenstone terrane would be to start the model at the deposition of the first volcanic package of the supracrustal assemblage and impose the horizontal shearing according to timing constraints provided from regional tectonic analysis.

The rheological model is simplified by not considering the melt-induced weakening of the crust with a prescribed solidus and liquidus formulation. The interstitial melt present between the grains may reduce the viscosity by orders of magnitude (Rosenberg and Handy, 2005). However, incorporating melt weakening will probably have limited effect on the crustal response because the rigid upper crust will unlikely be

strongly affected by melt weakening. The granitoid dome, on the other hand, may produce higher volume of melt and therefore the modelled viscosity is likely to be an overestimation of the real-world viscosity conditions, implying that the estimate of $t_{\max}$ ($v_{\max}$) of greenstone sagduction in our model may be an overestimation (underestimation) in our model.

4.4.2 Comparison with previous modelling studies

The crustal-scale gravitational overturn has been the focus of multiple modelling studies, both analogue and numerical, addressing various aspects of this vertical tectonic regime. We hereby compare our modelling results with these previous studies to show broad compatibility and new insights into the Archean crustal dynamics.

Our 3d model agrees with previous models in terms of the crustal architecture, shear kinematics and strain pattern. In all cases the models produces a dome-and-keel architecture as a result of the granitoid-up/greenstone-down kinematics (*e.g.* Dixon, 1975). Mareschal and Jaupart (2006) modelled the 2d sagduction/diapirism process with a temperature-dependent linear rheology and concluded that the process can be initiated if the effective viscosity of the greenstone belts falls below $1.00 \times 10^{21}\,\mathrm{Pa \cdot s}$, which is consistent with the viscosity range in our model. This model configuration is extended by Robin and Bailey (2009) to a power-law viscoelastic rheology and concludes that the density overturn (as fast as $1.00 \times 10^{1}\,\mathrm{Myr}$) is an efficient and viable mechanism for forming TTG and a dunitic restite from the sunken greenstone volcanics, subsequently contributing to the vertical growth of the subcratonic lithospheric mantle. The fast timescale of the overturn agrees with our model.

The base case ($v_s = 0$) of our model is characterized by the point-wise "dripping" of supracrustal greenstone at triple junctions of the granitoid domes, connected by greenstone belts in the "saddle" area (Figure 4.3). Our pattern is identical with the analogue results by Talbot et al. (1991) and Koyi (1988), which describes a "finger"-type diapiric pattern connected by "spokes" coincident with the greenstone belts in our model. Furthermore, Talbot et al. (1991) predicts that the sheet-like (or "wall"-like in their terminology) diapiric pattern does not develop without being affected by boundary or external forces. This is supported by our observation that the sheet-like sinking only develops with the presence of horizontal shearing.

With the horizontal shearing incorporated, the active sheet-like sagduction of the greenstone belt results in a strain pattern identical to Dixon and Summers (1983)

where materials in the saddle areas of the sagducted trough flow towards the sinking center. The strain is mainly of a flattening type in the trough area and is of strongly constrictional type in the sinking centers. In this sense, higher horizontal far-field strain rate (Section 4.3.2) may promote the formation of laterally coherent synclinal keel geometry of the greenstone assemblages. We thereby postulate that linear greenstone belts with regionally aligned structural grain and a tight synclinal geometry are likely formed under the synchronous operation of horizontal and vertical tectonic processes.

Nevertheless, aspects of our model deviates from vertical tectonic models featuring an active role of diapirism (*e.g.* Dixon, 1975; Mareschal and West, 1980; Weinberg and Schmeling, 1992; Weinberg, 1997; Yu et al., 2022). This family of "active diapirism" models show upward vertical constrictional strain at the core of the rising diapir, which corresponds to radial flattening at the top. This pattern is also reproduced in our linear viscous model (Figures 3.8 and 3.9). In our current thermomechanical model, however, the upward rising of the diapir appears passive and does not evolve into a funnel-shaped diapir. In contrast, the "active sagduction" of the greenstone assemblages is the major manifestation of the gravitational overturn and localizes the dominant part of the strain in the model. This discrepancy is likely caused by the combination of following crustal thermomechanical conditions:

1. The shallow crust, being cold and rheologically rigid, impedes the upward movement and the lateral expansion of the buoyant granitoid dome. This is consistent with the hypothesis that the crustal brittle-ductile transition may serve as the upper limit of the diapir emplacement (Weinberg, 1997).

2. The shear-softening power-law rheology of the greenstone assemblages promotes and sustains the sagduction of the greenstone once a sinking center is localized.

3. When the sagducted greenstone assemblages penetrates to the middle to lower crustal level, the higher temperatures at these levels will likely make sagduction self-sustainable.

At the current stage of modelling it remains premature to unequivocally conclude which mechanism (active diapirism or active sagduction) is the dominant behavior governing the Neoarchean crustal dynamics. Indeed, several potentially viscosity-altering mechanisms of the crustal material, especially the weakening of the granitoid materials, has not yet been taken into account in our model either due to

simplification or lack of consensus on parameterization (see Section 4.4.1). However, the thermal and melt weakening is unlikely to alter the high competence of the supracrustal assemblages at shallower level. Therefore, we may postulate that the crustal dynamics in the Neoarchean granitoid-greenstone terranes is likely a combination of both end-member processes of active diapirism and active sagduction depending upon the local crustal conditions.

4.4.3 Comparison with field structural observations

In individual Archean granitoid and gneiss domes, the foliation patterns may outline several circular or elliptical subdomes (*e.g.* Schwerdtner, 1990; Bouhallier et al., 1995), while the lineations are generally shallowly-plunging (Chardon et al., 2002; Lin and Beakhouse, 2013). In terranes where the evidence for a far-field tectonic strain is present, the lineation is aligned in the direction of the regional strain (*e.g.* Chardon et al., 2002; Bouhallier et al., 1995; Lin and Jiang, 2001). This is consistent with the modelled structural pattern where the lineation is subparallel to the finite stretching axis of the horizontal shearing.

On the other hand, field studies in the Youanmi Terrane in the Yilgarn Craton report a feeder zone at the core of the granitoid domes characterized by vertical sheath folds, an upward movement of the migmatitic material and a strongly constrictional strain pattern (*e.g.* Zibra et al., 2020; Clos et al., 2019). Outside this feeder zone, the lineations show a radial pattern (Zibra et al., 2020). This lineation pattern is consistent with the regional deformation pattern modelled with a uniform viscosity within the granitoid dome and a weak viscosity contrast between the dome and the supracrustal assemblages (*e.g.* Wú et al., 2023, figures 10 and 11). The structural patterns presented in these studies is likely indicative of a more active role of active granitoid diapirism due to the possible low viscosity contributed possibly in part by the presence of melt. In this sense, the deformation pattern in a granitoid-greenstone terrane may be a combination of active sagduction and active diapirism.

In the greenstone belts, the lineations mostly plunge down-dip. The trend direction of the lineation may be dictated by the regional tectonic strain field. In particular, the strain is of constrictional type at the triple junctions of granitoid domes and changes into a flattening type in the synclinal keel (figure 10d, page 35 of Bouhallier et al., 1995). Furthermore, structural studies in multiple Neoarchean greenstone belts in the Superior Craton reveal a granitoid-up/greenstone-down kinematics in the high strain zones close to the granitoid-greenstone boundary. Meanwhile, the plunge direction of the stretching lineations in the greenstone belts are reversed on opposing

granitoid-greenstone boundaries (*e.g.* Lin, 2005; Lin and Beakhouse, 2013) with a granitoid-up/greenstone-down kinematics. This kinematics and lineation pattern leads to the interpretation that the deformation of these high strain zones is composed of a vertical component due to the gravitational overturn and a uniform horizontal shearing attributed to the regional far-field tectonic stress. On the other hand, in the lower amphibolite facies Kolar greenstone belt of Dharwar craton, Chardon et al. (2002) reports that the lineation converges towards the interior of the greenstone belt. In both cases, the field structures record a greenstone-down/granitoid-up kinematics. The vertical kinematics are consistently reproduced by our numerical model, while the lineation asymmetry, interpreted to be the results of horizontal tectonism, is best developed at shallow crustal levels (Figure 4.7C). At deeper crustal levels (*e.g.* Figure 4.7D), the lowered crustal viscosity leads to a lineation pattern which is strongly attracted by the downward sagducted greenstone "sheet" or "drips". Therefore, we infer that the lineation patterns observed in the granitoid-greenstone terranes may vary as a result of the crustal level, which is in turn a function of the temperature condition: the cold shallow crust showing an intimate mechanical coupling to the distributed far-field tectonic strain, while the crust at deeper level records a more dominant component of vertical sinking.

Our numerical model shows that sagduction/diapirism process within the granitoid-greenstone terrane, once initiated, can be a diachronous process lasting for several million years, With a warmer crust, a major initial sagduction event of the greenstone assemblages begins early as "drips" and develop almost synchronously throughout the entire terrane. Minor sagduction event may follow at later stage. For colder crustal conditions, the sagduction event in each individual greenstone belt of the terrane develop in a temporally staggered manner and with variations in structural patterns, in accordance with the local strain and viscosity conditions. This variation in timing and the deformation patterns agrees with the observation by Zibra et al. (2014) in the Yilgarn Craton that the multiphase deformation in the granitoid-greenstone terranes may be unique to the pluton and its adjacent greenstone belts. In the southern Abitibi province of the Superior Craton, the first phase of regional folding differs by several million years along the Cadillac-Larder Lake deformation zone (CLLDZ) (2674 Ma – 2670 Ma; Lafrance, 2015) and along the Ridout deformation zone (RDZ) (2679 Ma–2683 Ma,Appendix D.2). This gap in timing can likely be explained by the time-transgressive natural of the synchronous vertical and horizontal model.

4.4.4 Transition mechanism of crustal dynamics

The increase in the imposed boundary shear velocity in our model results in the alignment of the greenstone belts prior to the onset of sagduction, the promotion of sheet-like sagduction of the supracrustal assemblages as well as a more stretched geometry of the granitoid domes. The rate of horizontal shearing has negligible effect on the initiation time of the gravitational overturn. On the other hand, higher shear strain rate exerts a suppressing trend on the rate of greenstone sagduction.

It is widely inferred that a major difference between the Archean Earth and the present day is the high mantle potential temperature (*e.g.* Condie and Benn, 2006), which in turn translates to a higher Moho heat flux. In this light, the systematic reduction of the basal heat flux in the numerical model may be interpreted as the gradual shift in crustal behavior from the hotter Archean geotherm to the modern-day cooler geotherm. Our results show that the reduction of the crustal heat budget results in an increase in crustal strength, thus delaying the onset and suppressing the rate at which the gravitational overturn operates. Therefore, we speculate that on a broader scale, lithospheric tectonic processes with a positive heat input to the crust leads to a more active role of vertical tectonism (Bodorkos and Sandiford, 2006). Such process may take the forms of *e.g.* the mantle heat influx from sub-lithospheric mantle under crustal extension due to slab break-off (*e.g.* Lin and Beakhouse, 2013) or mantle plume events (*e.g.* Kloppenburg et al., 2001). On the other hand, the secular reduction of heat flux through the geological history, which leads to the increase of the crustal strength, may explain the reason why the gravitational overturn no longer significantly contributes to crustal architecture in modern day crustal dynamics. Furthermore, the secular increase of the crustal viscosity promotes the transmission of far-field tectonic stress, leading to possible higher strain rate in the weak supracrustal rocks, which in turn leads to slower rate of sagduction and therefore suppresses the operation of vertical tectonic processes.

4.4.5 Crustal-scale deformation zones

The geometry of deformation zones in our model is strongly controlled by the sinking of the greenstone assemblages and shows a more complicated relationship with respect to the granitoid-greenstone boundary than previous models. Robin (2010) concludes that high strain zones of the granitoid-greenstone terranes coincides simply with the granitoid-greenstone interface. In our model, however, the deformation zones outline the sinking greenstone "drips" or "sheet" at deeper crustal levels and

may develop in the greenstone belt with a distance from the granitoid-greenstone boundary, leaving a gap of weak deformation between the deformation zone and the granitoid-greenstone boundary. At deeper crustal levels, this gap may become obscured as the synclinal keel tightens due to continued sagduction and the non-coaxial deformation due to horizontal shearing. The greenstone belt-bounding deformation zones become tangential to the granitoid-greenstone boundary and can be traced for long distance in the direction of the regional finite extension axis. This geometry of the deformation zones at various crustal levels can be interpreted as the result of combined horizontal and vertical tectonic strain. The deformation zones are initiated by sagduction at deeper crustal level. The upward extension of the deformation zones to the brittle shallow crust, on the other hand, is controlled by the internal angle of friction of the Drucker-Prager plasticity law.

The geometry of the deformation zones outlines areas of active sagduction in the greenstone belt and roughly follows the granitoid-greenstone contact. With the influence of the horizontal shearing, the deformation zones are aligned into regionally continuous deformation corridors analogous to the crustal breaks in the Neoarchean terranes. These deformation corridors can be traced coherently for long distance and record multiple phases of ductile deformation (*e.g.* Nassif et al., 2018; Ispolatov et al., 2008). Our model evolution shows that the strain partition and localization due to active greenstone sagduction, which happens under the backdrop horizontally-directed tectonic stress, is a viable mechanism to initiate the laterally coherent geometry of crustal-scale deformation zones. Our results are also consistent with the observations that the late Archean crustal-scale deformation zones record little evidence of large displacements (Chardon et al., 2008, 2009; Lin and Jiang, 2001).

Horizontal sections through the numerical model at a middle crustal depth show that the sinking centers in the greenstone assemblage yield a lower total pressure than elsewhere in the greenstone belt as well as that of the surrounding granitoid domes. If the deformation mechanism at this crustal depth is governed by viscous deformation (without the presence of pervasive brittle fracture), the pore fluid pressure is controlled by the total pressure (Fournier, 1999), which shows a negative pressure gradient towards the sinking center. As a result, hydrothermal fluids, which may be magmatic or metamorphic origin, may be directed by the pressure gradient towards the sinking center in the greenstone belt. The total pressure gradient, as well as the presence of the high strain zones around the sinking centers to serve as possible fluid pathways, provides a possible transport mechanism for mineralization fluids towards the deformation zones, which then serves as the preferred locality for

gold mineralization in Neoarchean terranes (Goldfarb et al., 2001; Vearncombe and Zelic, 2015).

4.5 Conclusions

In this study we construct a 3d thermomechanical model to explore the crustal architecture and deformation pattern resultant from the synchronous operation of horizontal tectonism in the form of far-field simple shearing and vertical tectonism in the form of gravitational overturn with the thermal, rheological and boundary conditions appropriate for the Neoarchean Earth. In particular, we assess the role that the basal heating and the horizontal strain rate play in the crustal deformation by systematically varying the Moho heat flux and the boundary strain rate of horizontal shearing.

The main conclusions of the numerical model are summarized as follows:

1. Due to the high strength of the brittle upper crust, the foundering of the greenstone assemblages may play a more active role in driving the vertical tectonic component, a pattern in contrast to previous models of vertical tectonism where a more active role of granitoid diapirism is proposed.

2. Imposed horizontal shearing facilitates a sheet-like sagduction of the greenstone supracrustal assemblages. Otherwise, the sagduction takes the form of pointwise dripping at the triple junctions in the greenstone belt.

3. In the granitoid domes, intrusions show low strain intensity and the foliation pattern outlines elliptical subdomes. The lineations are in most cases shallowly-plunging.

4. In the greenstone belt the foliations are steeply dipping and subparallel to the granitoid-greenstone contact. The lineations are generally steeply plunging. At the shallow crustal level, the lineation shows opposite plunge directions on opposing granitoid-greenstone boundaries conformable with the kinematics of the regional oblique far-field shearing as well as the sagduction kinematics. At the deep crustal level, the lineation converges towards the sinking centres.

5. The crustal deformation in a synchronous horizontal and vertical tectonic regime can be a diachronous process. The timing of the major phase of deformation may progress from one greenstone belt to the other in a staggered manner through an extended period.

6. Lowered Moho heat flux results in a delayed initiation of the gravitational overturn and a reduced rate of sagduction, while higher horizontal strain rate results in a reduction in the rate of sagduction without affecting the time of sagduction initiation. The evolution of the crustal deformation pattern under decreasing Moho heat flux are likely representative of the secular evolution of crustal condition as the Earth cools down from the Neoarchean time towards modern-day thermal and rheological conditions.

7. The sagduction of the supracrustal assemblages leads to low-pressure zones above the sinking centres in the greenstone belts and also the initiation of the crustal scale deformation zones near the granitoid-greenstone contact, possibly creating an environment conducive for the transport of mineralizing fluids towards the deformation zones.

Chapter 5

Summary of conclusions and future directions

5.1 Summary of conclusions

This thesis proposes a modelling framework to simulate the structural patterns emergent from ductile tectonic flow in an extensible computationally efficient manner. Our modelling framework produces simulation results of lithological distributions and structural patterns that can be directly compared to results of geological mapping and field-based structural analysis. The framework is subsequently applied to the simulation of crustal architecture and structural patterns of the Neoarchean terranes. Our modelling results reveal that the synchronous operation of two styles of tectonic processes, *i.e.* the vertical tectonism in the form of gravitational instability and the horizontal tectonism in response to the far-field boundary forces, can explain various aspects of the crustal architecture and deformation observed in Neoarchean granitoid-greenstone terranes, thereby establishing the Neoarchean era as a possible transition period in crustal dynamics. The main conclusions of this thesis are summarized in the following sections.

5.1.1 The discontinuous Galerkin level set method for modelling structural patterns

1. A numerical modelling framework is constructed to capture both the lithological distribution and structural pattern of tectonic flows by coupling a level set

solver of the material interface with a Stokes flow solver.

2. The interface solver and the flow solver use different variations of the finite element method (the discontinuous Galerkin (DG) method and the continuous Galerkin method, respectively) to maintain accuracy and flexibility.

3. Passive tracer particles can be generated in the model where deformation tracking is needed. However, they are not essential to model computations and therefore can be placed sparingly for improved computational efficiency.

4. The modelling framework can potentially be extended to encompass more complicated rheological models and to couple with additional solvers for multi-physics modelling.

5.1.2 The deformation pattern and crustal dynamics of the Swayze greenstone belt

1. Four generations of regional ductile structures (G_1–G_4) are identified in the Swayze greenstone belt (SGB).

2. Limited evidence of G_1 structures are preserved in the granitoid infrastructure characterized by subhorizontal flow.

3. The *ca.* 2680 Ma thick-skinned G_2 structures established the dome-and-keel crustal architecture of the SGB. G_2 structures are characterized by an oblique shearing with both a granitoid-up/greenstone-down vertical component and dextral horizontal component.

4. The G_3 and G_4 structures are regional reactivation events. G_3 is characterized by oblique sinistral and north-side-up shearing on the Ridout deformation zone (RDZ). G_4 is characterized by regional dextral transcurrent shearing on pre-existing high strain zones and lithological boundaries. G_4 happened no earlier than 2678 Ma.

5. Simulated crustal deformation patterns with the Neoarchean thermal and rheological conditions under synchronous operation of gravitational overturn and horizontal shearing agree with the observed lithological distribution, the structural pattern and the shearing kinematics in Neoarchean granitoid-greenstone terranes. Our model supports the coexistence of both horizontal and vertical tectonic processes in Neoarchean terranes.

5.1.3 Implications for Neoarchean tectonics in general

1. The vertical tectonism in the granitoid-greenstone belt is characterized by the active diachronous sagduction of the supracrustal assemblage, either in the form of pointwise "dripping" at the triple junctions, or in the form sheet-like sagduction in the greenstone keels. The latter is favoured under the presence of horizontal shearing.

2. The foliations in the granitoid domes are shallowly-dipping and outlines the subdomes in the granitoid dome complex. The foliation in the greenstone belt, on the other hand, is moderately- to steeply-dipping and is largely parallel to the granitoid-greenstone belt contact but may be slightly oblique to the contact due to the non-coaxial shearing.

3. The lineations in the granitoid domes are generally shallowly plunging while being moderately to steeply plunging in the greenstone belt. Furthermore, the lineations in the greenstone belt may show opposite plunge directions on the two opposing sides of the greenstone belt in the shallow crustal level in accordance with the far-field regional shearing.

4. The reduction of the basal heat flux results in the delayed onset of and the decreased rate of the sagduction. As the Earth dissipates heat and transitions towards a modern-day tectonic style characterized by the horizontal interaction between rigid plates, the component of crustal-scale vertical tectonism is likely diminished through time.

5. The increase in horizontal shear rate results in higher accumulation of horizontal shear strain, possibly generating regionally aligned linear structural pattern of the greenstone belts. The rate of sagduction is also slightly decreased, but the overall timing of sagduction onset is not affected.

6. The crustal-scale high strain zones are nucleated during the sagduction process around the sinking centres and are characterized by low total pressure, possibly producing a favourable condition for the transport of mineralizing fluids in the crust towards the deformation zones.

5.2 Future directions

The DG level set modelling methodology can be extended and improved in many ways. As of its current state the discontinuous Galerkin discretization for the level set reinitialization can present numerical instability when the degree of polynomial basis $p \geqslant 2$. A few possible routes to tame numerical oscillation is by using a different discretization for the Hamilton-Jacobi (HJ) formulation (*e.g.* Hu and Shu, 1999; Li and Shu, 2005; Zhang et al., 2019) or experiment with artificial viscosity methods for oscillation suppression (*e.g.* Mousavi, 2014; Barter, 2008). In this way, the level set method can be extended to high-order accuracy in a straightforward manner. The rheological model in our model at the current stage of development, which can be linear or non-linear with respect to the strain rate, is assumed to be isotropic. This assumption may be valid if the rheological properties of the lithological units are averaged through large areas. However, this assumption falls short on mesoscale structures when strong alignment of minerals is present in localized high strain zones due to deformation, which in turn will serve as the preferential location for future strain partitioning parallel to the shear plane.

Moreover, the elements defining the foliation and lineation patterns are assumed to be passive to the flow in the current formulation. This is asymptotically true when the lithological unit has been subject to the deformation for sufficiently long period. However, this assumption is invalid if the transposition of a foliation defined by mechanically active elements needs to be modelled. One possible solution to this problem is to couple the tectonic flow solver to an efficient micromechanics solver, where the latter takes the strain field from the tectonic solver to compute the geometry and orientation of shape elements (Jiang, 2012). The homogenized material property of the latter can then be used as the material property for modelling tectonic flow (chapters 13 and 17 of Jiang, 2023, and references therein). In this way, models taking into account of both shape preferred orientation and lattice preferred orientation under a large-scale tectonic flow on multiple scales can be achieved.

The application of the numerical model to the Neoarchean tectonics can also be further explored in numerous directions by taking into consideration more sophisticated physical processes. For example, the generation and the transport of melt within the granitoid-greenstone terrane are not taken into account in our current model, which may affect the behaviour of the numerical model thermally and mechanically: The presence of melt in the crystal framework of the lithological unit has the effect of decreasing the viscosity possibly by several orders of magnitude (Rosenberg and Stünitz, 2003). Furthermore, the preferential enrichment of incompatible

radioactive elements in the melt and the transportation of the latter contributes to the redistribution of heat-producing elements and may eventually contribute to the stabilization of the cratonic crust (Reimink and Smye, 2024). Taking the above-mentioned factors into account will result in a more realistic estimation of crustal thermomechanical structure and leads to deeper insights into the thermal-mechanical process of the cratonization process. The combination of low pressure distribution and the high strain zones in the synchronous vertical and horizontal tectonism model is also worth exploring in terms of its role in the transport of the mineralizing fluids. To achieve this, the total pressure field provided by our tectonic flow model can be coupled to a fluid flow solver based on Darcy's law to identify preferable locations of mineralization (*e.g.* Zhang et al., 2011).

References

Allmendinger, R.W., Cardozo, N., Fisher, D.M., 2012. Structural Geology Algorithms: Vectors and Tensors. Cambridge University Press, Cambridge ; New York.

Arndt, D., Bangerth, W., Davydov, D., Heister, T., Heltai, L., Kronbichler, M., Maier, M., Pelteret, J.P., Turcksin, B., Wells, D., 2021. The deal.II finite element library: Design, features, and insights. Computers & Mathematics with Applications 81, 407–422. doi: 10.1016/j.camwa.2020.02.022.

Astarita, G., 1979. Objective and generally applicable criteria for flow classification. Journal of Non-Newtonian Fluid Mechanics 6, 69–76. doi: 10.1016/0377-0257(79)87004-4.

Ayer, J., Amelin, Y., Corfu, F., Kamo, S., Ketchum, J., Kwok, K., Trowell, N., 2002. Evolution of the southern Abitibi greenstone belt based on U–Pb geochronology: Autochthonous volcanic construction followed by plutonism, regional deformation and sedimentation. Precambrian Research 115, 63–95. doi: 10.1016/S0301-9268(02)00006-2.

Ayer, J., Trowell, N., 2002. Geological Compilation of the Swayze Area, Abitibi Greenstone Belt, Preliminary Map P.3511, Ontario Geological Survey.

Ayer, J., Trowell, N., Josey, S., 2004. Geological compilation of the Abitibi greenstone belt, Miscellaneous Release Data 143, Ontario Geological Survey.

Barter, G.E., 2008. Shock Capturing with PDE-based Artificial Viscosity for an Adaptive, Higher-Order Discontinuous Galerkin Finite Element Method. Ph.D. thesis. Massachusetts Institute of Technology. Dept. of Aeronautics and Astronautics. Cambridge, Massachusetts, USA.

Beakhouse, G.P., 2011. The Abitibi Subprovince Plutonic Record: Tectonic and Metallogenic Implications. Technical Report 6288. Ontario Geological Survey.

Beakhouse, G.P., Lin, S., Kamo, S.L., 2011. Magmatic and tectonic emplacement of the Pukaskwa batholith, Superior Province, Ontario, Canada. Canadian Journal of Earth Sciences 48, 187–204. doi: 10.1139/E10-048.

Beaumont, C., Jamieson, R.A., Nguyen, M.H., Lee, B., 2001. Himalayan tectonics explained by extrusion of a low-viscosity crustal channel coupled to focused surface denudation. Nature 414, 738–742. doi: 10.1038/414738a.

Becker, J., Benn, K., 2003. The Neoarchean Rice Lake Batholith and Its Place in the Tectonomagnetic Evolution of the Swayze and Abitibi Granite-Greenstone Belts, Northeastern Ontario. Technical Report 6105. Ontario Geological Survey.

Becker, J., Bons, P., Jessell, M., 2008. A new front-tracking method to model anisotropic grain and phase boundary motion in rocks. Computers & Geosciences 34, 201–212. doi: 10.1016/j.cageo.2007.03.013.

Bédard, J.H., 2018. Stagnant lids and mantle overturns: Implications for Archaean tectonics, magmagenesis, crustal growth, mantle evolution, and the start of plate tectonics. Geoscience Frontiers 9, 19–49. doi: 10.1016/j.gsf.2017.01.005.

Bedeaux, P., Pilote, P., Daigneault, R., Rafini, S., 2017. Synthesis of the structural evolution and associated gold mineralization of the Cadillac Fault, Abitibi, Canada. Ore Geology Reviews 82, 49–69. doi: 10.1016/j.oregeorev.2016.11.029.

Benn, K., 1994. Overprinting of magnetic fabrics in granites by small strains: Numerical modelling. Tectonophysics 233, 153–162. doi: 10.1016/0040-1951(94)90238-0.

Benn, K., 2004. Late Archaean Kenogamissi complex, Abitibi Subprovince, Ontario, Canada: Doming, folding and deformation-assisted melt remobilisation during syntectonic batholith emplacement. Earth and Environmental Science Transactions of the Royal Society of Edinburgh 95, 297–307. doi: 10.1017/S0263593300001085.

Berger, B.R., 2011. Geological Investigations South of Gogama. Open File Report 6270. Ontario Geological Survey.

Berger, B.R., 2012. Precambrian geology, south of Gogama area, Preliminary Map P.3762—Revised, Ontario Geological Survey.

Bhandari, A., Jiang, D., 2021. A Multiscale Numerical Modeling Investigation on the Significance of Flow Partitioning for the Development of Quartz c-Axis Fabrics. Journal of Geophysical Research: Solid Earth 126, e2020JB021040. doi: 10.1029/2020JB021040.

Bodorkos, S., Sandiford, M., 2006. Thermal and mechanical controls on the evolution of archean crustal deformation: Examples from Western Australia, in: Benn, K., Mareschal, J.C., Condie, K.C. (Eds.), Geophysical Monograph Series. American Geophysical Union, Washington, D. C.. volume 164, pp. 131–147. doi: 10.1029/164GM10.

Bons, P., Barr, T., ten Brink, C., 1997. The development of δ-clasts in non-linear viscous materials: A numerical approach. Tectonophysics 270, 29–41. doi: 10.1016/S0040-1951(96)00174-6.

Bouhallier, H., Chardon, D., Choukroune, P., 1995. Strain patterns in Archaean dome-and-basin structures: The Dharwar craton (Karnataka, South India). Earth and Planetary Science Letters 135, 57–75. doi: 10.1016/0012-821X(95)00144-2.

Bouhallier, H., Choukroune, P., Ballèvre, M., 1993. Diapirism, bulk homogeneous shortening and transcurrent shearing in the Archaean Dharwar craton: The Holenarsipur area, southern India. Precambrian Research 63, 43–58. doi: 10.1016/0301-9268(93)90004-L.

Bourgouin, L., Mühlhaus, H.B., Jane Hale, A., Arsac, A., 2007. Studying the influence of a solid shell on lava dome growth and evolution using the level set method. Geophysical Journal International 170, 1431–1438. doi: 10.1111/j.1365-246X.2007.03471.x.

Brackbill, J., Kothe, D., Ruppel, H., 1988. Flip: A low-dissipation, particle-in-cell method for fluid flow. Computer Physics Communications 48, 25–38. doi: 10.1016/0010-4655(88)90020-3.

Braun, J., Thieulot, C., Fullsack, P., DeKool, M., Beaumont, C., Huismans, R., 2008. DOUAR: A new three-dimensional creeping flow numerical model for the solution of geological problems. Physics of the Earth and Planetary Interiors 171, 76–91. doi: 10.1016/j.pepi.2008.05.003.

Burov, E.B., 2011. Rheology and strength of the lithosphere. Marine and Petroleum Geology 28, 1402–1443. doi: 10.1016/j.marpetgeo.2011.05.008.

Calvert, A.J., Ludden, J.N., 1999. Archean continental assembly in the southeastern Superior Province of Canada. Tectonics 18, 412–429. doi: 10.1029/1999TC900006.

Calvert, A.J., Sawyer, E.W., Davis, W.J., Ludden, J.N., 1995. Archaean subduction inferred from seismic images of a mantle suture in the Superior Province. Nature 375, 670–674. doi: 10.1038/375670a0.

Caristan, Y., 1982. The transition from high temperature creep to fracture in Maryland diabase. Journal of Geophysical Research: Solid Earth 87, 6781–6790. doi: 10.1029/JB087iB08p06781.

Chardon, D., Choukroune, P., Jayananda, M., 1996. Strain patterns, décollement and incipient sagducted greenstone terrains in the Archaean Dharwar craton (south India). Journal of Structural Geology 18, 991–1004. doi: 10.1016/0191-8141(96)00031-4.

Chardon, D., Choukroune, P., Jayananda, M., 1998. Sinking of the Dharwar Basin (South India): Implications for Archaean tectonics. Precambrian Research 91, 15–39. doi: 10.1016/S0301-9268(98)00037-0.

Chardon, D., Gapais, D., Cagnard, F., 2009. Flow of ultra-hot orogens: A view from the Precambrian, clues for the Phanerozoic. Tectonophysics 477, 105–118. doi: 10.1016/j.tecto.2009.03.008.

Chardon, D., Jayananda, M., Chetty, T.R.K., Peucat, J.J., 2008. Precambrian continental strain and shear zone patterns: South Indian case. Journal of Geophysical Research: Solid Earth 113. doi: 10.1029/2007JB005299.

Chardon, D., Peucat, J.J., Jayananda, M., Choukroune, P., Fanning, C.M., 2002. Archean granite-greenstone tectonics at Kolar (South India): Interplay of diapirism and bulk inhomogeneous contraction during juvenile magmatic accretion. Tectonics 21, 7–1–7–17. doi: 10.1029/2001TC901032.

Cho, M.H., Choi, H.G., Yoo, J.Y., 2011. A direct reinitialization approach of level-set/splitting finite element method for simulating incompressible two-phase flows. International Journal for Numerical Methods in Fluids 67, 1637–1654. doi: 10.1002/fld.2437.

Choi, E., Tan, E., Lavier, L.L., Calo, V.M., 2013. DynEarthSol2D: An efficient unstructured finite element method to study long-term tectonic deformation: DYNEARTHSOL2D. Journal of Geophysical Research: Solid Earth 118, 2429–2444. doi: 10.1002/jgrb.50148.

Chung, E.T., Lam, C.Y., Qian, J., 2015. A staggered discontinuous Galerkin method for the simulation of seismic waves with surface topography. GEOPHYSICS 80, T119–T135. doi: 10.1190/geo2014-0413.1.

Clos, F., Weinberg, R.F., Zibra, I., Fenwick, M.J., 2019. Archean diapirism recorded by vertical sheath folds in the core of the Yalgoo Dome, Yilgarn Craton. Precambrian Research 320, 391–402. doi: 10.1016/j.precamres.2018.11.010.

Cockburn, B., Shu, C.W., 1989. TVB Runge-Kutta Local Projection Discontinuous Galerkin Finite Element Method for Conservation Laws II: General Framework. Mathematics of Computation 52, 411. doi: 10.2307/2008474, arXiv:2008474.

Cockburn, B., Shu, C.W., 1991. The Runge-Kutta local projection P^1-discontinuous-Galerkin finite element method for scalar conservation laws. ESAIM: Mathematical Modelling and Numerical Analysis - Modélisation Mathématique et Analyse Numérique 25, 337–361.

Collins, W., 1989. Polydiapirism of the Archean Mount Edgar Batholith, Pilbara Block, Western Australia. Precambrian Research 43, 41–62. doi: 10.1016/0301-9268(89)90004-1.

Collins, W., Van Kranendonk, M., Teyssier, C., 1998. Partial convective overturn of Archaean crust in the east Pilbara Craton, Western Australia: Driving mechanisms and tectonic implications. Journal of Structural Geology 20, 1405–1424. doi: 10.1016/S0191-8141(98)00073-X.

Condie, K.C., Benn, K., 2006. Archean geodynamics: Similar to or different from modern geodynamics?, in: Benn, K., Mareschal, J.C., Condie, K.C. (Eds.), Geophysical Monograph Series. American Geophysical Union, Washington, D. C.. volume 164, pp. 47–59. doi: 10.1029/164GM05.

Crameri, F., Schmeling, H., Golabek, G.J., Duretz, T., Orendt, R., Buiter, S.J.H., May, D.A., Kaus, B.J.P., Gerya, T.V., Tackley, P.J., 2012. A comparison of numerical surface topography calculations in geodynamic modelling: An evaluation of the 'sticky air' method: Modelling topography in geodynamics. Geophysical Journal International 189, 38–54. doi: 10.1111/j.1365-246X.2012.05388.x.

Davaille, A., Limare, A., 2015. Laboratory Studies of Mantle Convection, in: Treatise on Geophysics. Elsevier, pp. 73–144. doi: 10.1016/B978-0-444-53802-4.00128-7.

de Montserrat, A., Morgan, J.P., Hasenclever, J., 2019. LaCoDe: A Lagrangian two-dimensional thermo-mechanical code for large-strain compressible visco-elastic geodynamical modeling. Tectonophysics 767, 228173. doi: 10.1016/j.tecto.2019.228173.

de Wit, M.J., 1998. On Archean granites, greenstones, cratons and tectonics: Does the evidence demand a verdict? Precambrian Research 91, 181–226. doi: 10.1016/S0301-9268(98)00043-6.

Dixon, J.M., 1975. Finite strain and progressive deformation in models of diapiric structures. Tectonophysics 28, 89–124. doi: 10.1016/0040-1951(75)90060-8.

Dixon, J.M., Summers, J.M., 1983. Patterns of total and incremental strain in subsiding troughs: Experimental centrifuged. models of inter-diapir synclines. Canadian Journal of Earth Sciences 20, 1843–1861. doi: 10.1139/e83-175.

Donéa, J., 2003. Finite Element Methods for Flow Problems. Wiley, Chichester ; Hoboken, NJ.

Elliott, D., 1972. Deformation Paths in Structural Geology. Geological Society of America Bulletin 83, 2621. doi: 10.1130/0016-7606(1972)83[2621:DPISG]2.0.CO;2.

Elman, H., Golub, G., 1994. Inexact and Preconditioned Uzawa Algorithms for Saddle Point Problems. SIAM Journal on Numerical Analysis 31, 1645–1661. doi: 10.1137/0731085.

Enright, D., Fedkiw, R., Ferziger, J., Mitchell, I., 2002. A Hybrid Particle Level Set Method for Improved Interface Capturing. Journal of Computational Physics 183, 83–116. doi: 10.1006/jcph.2002.7166.

Fletcher, R.C., Pollard, D.D., 1999. Can we understand structural and tectonic processes and their products without appeal to a complete mechanics? Journal of Structural Geology 21, 1071–1088. doi: 10.1016/S0191-8141(99)00056-5.

Fournier, R.O., 1999. Hydrothermal processes related to movement of fluid from plastic into brittle rock in the magmatic-epithermal environment. Economic Geology 94, 1193–1211. doi: 10.2113/gsecongeo.94.8.1193.

François, C., Philippot, P., Rey, P., Rubatto, D., 2014. Burial and exhumation during Archean sagduction in the East Pilbara Granite-Greenstone Terrane. Earth and Planetary Science Letters 396, 235–251. doi: 10.1016/j.epsl.2014.04.025.

Fraters, M.R.T., Billen, M.I., 2021. On the Implementation and Usability of Crystal Preferred Orientation Evolution in Geodynamic Modeling. Geochemistry, Geophysics, Geosystems 22. doi: 10.1029/2021GC009846.

Fu, C., Guo, Q., Gast, T., Jiang, C., Teran, J., 2017. A polynomial particle-in-cell method. ACM Transactions on Graphics 36, 1–12. doi: 10.1145/3130800.3130878.

Fuchs, L., Schmeling, H., Koyi, H., 2011. Numerical models of salt diapir formation by down-building: The role of sedimentation rate, viscosity contrast, initial amplitude and wavelength: Numerical models of salt diapir formation. Geophysical Journal International 186, 390–400. doi: 10.1111/j.1365-246X.2011.05058.x.

Fullsack, P., 1995. An arbitrary Lagrangian-Eulerian formulation for creeping flows and its application in tectonic models. Geophysical Journal International 120, 1–23. doi: 10.1111/j.1365-246X.1995.tb05908.x.

Gerya, T., 2019. Introduction to Numerical Geodynamic Modelling. Second edition ed., Cambridge University Press, Cambridge, United Kingdom ; New York, NY.

Gerya, T.V., Yuen, D.A., 2007. Robust characteristics method for modelling multiphase visco-elasto-plastic thermo-mechanical problems. Physics of the Earth and Planetary Interiors 163, 83–105. doi: 10.1016/j.pepi.2007.04.015.

Ghia, U., Ghia, K., Shin, C., 1982. High-Re solutions for incompressible flow using the Navier-Stokes equations and a multigrid method. Journal of Computational Physics 48, 387–411. doi: 10.1016/0021-9991(82)90058-4.

Ghosh, S., Ramberg, H., 1976. Reorientation of inclusions by combination of pure shear and simple shear. Tectonophysics 34, 1–70. doi: 10.1016/0040-1951(76)90176-1.

Glerum, A., Thieulot, C., Fraters, M., Blom, C., Spakman, W., 2018. Nonlinear viscoplasticity in ASPECT: Benchmarking and applications to subduction. Solid Earth 9, 267–294. doi: 10.5194/se-9-267-2018.

Göğüş, O.H., Pysklywec, R.N., 2008. Near-surface diagnostics of dripping or delaminating lithosphere. Journal of Geophysical Research 113, B11404. doi: 10.1029/2007JB005123.

Goldfarb, R., Groves, D., Gardoll, S., 2001. Orogenic gold and geologic time: A global synthesis. Ore Geology Reviews 18, 1–75. doi: 10.1016/S0169-1368(01)00016-6.

Gorczyk, W., Hobbs, B., Gerya, T., 2012. Initiation of Rayleigh–Taylor instabilities in intra-cratonic settings. Tectonophysics 514–517, 146–155. doi: 10.1016/j.tecto.2011.10.016.

Griera, A., Llorens, M.G., Gomez-Rivas, E., Bons, P.D., Jessell, M.W., Evans, L.A., Lebensohn, R., 2013. Numerical modelling of porphyroclast and porphyroblast rotation in anisotropic rocks. Tectonophysics 587, 4–29. doi: 10.1016/j.tecto.2012.10.008.

Groß, S., Reichelt, V., Reusken, A., 2006. A finite element based level set method for two-phase incompressible flows. Computing and Visualization in Science 9, 239–257. doi: 10.1007/s00791-006-0024-y.

Guglielmo, G., 1993. Interference between pluton expansion and non-coaxial tectonic deformation: Three-dimensional computer model and field implications. Journal of Structural Geology 15, 593–608. doi: 10.1016/0191-8141(93)90150-9.

Guglielmo, G., 1994. Interference between pluton expansion and coaxial tectonic deformation: Three-dimensional computer model and field implications. Journal of Structural Geology 16, 237–252. doi: 10.1016/0191-8141(94)90107-4.

Hamilton, W.B., 1998. Archean magmatism and deformation were not products of plate tectonics. Precambrian Research 91, 143–179. doi: 10.1016/S0301-9268(98)00042-4.

Harris, L.B., Bédard, J.H., 2014. Crustal Evolution and Deformation in a Non-Plate-Tectonic Archaean Earth: Comparisons with Venus, in: Dilek, Y., Furnes, H. (Eds.), Evolution of Archean Crust and Early Life. Springer Netherlands, Dordrecht. volume 7, pp. 215–291. doi: 10.1007/978-94-007-7615-9_9.

Hastie, E., 2017. Gold Metallogeny of the Southern Swayze Area, Abitibi Greenstone Belt: A Field Trip Guidebook. Open File Report 6334. Ontario Geological Survey. Sudbury.

Hastie, E., Kontak, D.J., Lafrance, B., 2016. Update on Activities Related to a Gold Metallogenic Study of the Southern Swayze Greenstone Belt. Open File Report 6323. Ontario Geological Survey. Sudbury.

Haugaard, R., Gemmell, T.P., Ayer, J.A., Thurston, P.C., 2017. Lithological and Stratigraphic Relationships of the Swayze Area, Abitibi Greenstone Belt. Open File Report 6333. Ontario Geological Survey. Sudbury.

Heather, K.B., 2001. The Geological Evolution of the Archean Swayze Greenstone Belt, Superior Province, Canada. Ph.D. thesis. Keele University. Keele, United Kingdom.

Heister, T., Dannberg, J., Gassmöller, R., Bangerth, W., 2017. High accuracy mantle convection simulation through modern numerical methods – II: Realistic models and problems. Geophysical Journal International 210, 833–851. doi: 10.1093/gji/ggx195.

Hesthaven, J.S., Warburton, T., 2007. Nodal Discontinuous Galerkin Methods: Algorithms, Analysis, and Applications. 1st ed., Springer Publishing Company, Incorporated.

Hillebrand, B., Thieulot, C., Geenen, T., van den Berg, A.P., Spakman, W., 2014. Using the level set method in geodynamical modeling of multi-material flows and Earth's free surface. Solid Earth 5, 1087–1098. doi: 10.5194/se-5-1087-2014.

Hu, C., Shu, C.W., 1999. A Discontinuous Galerkin Finite Element Method for Hamilton-Jacobi Equations. SIAM Journal on Scientific Computing 21, 666–690. doi: 10.1137/S1064827598337282.

Humphreys, F.J., Hatherly, M., 2004. Recrystallization and Related Annealing Phenomena. 2nd ed ed., Elsevier, Amsterdam ; Boston.

Ispolatov, V., Lafrance, B., Dube, B., Creaser, R., Hamilton, M., 2008. Geologic and Structural Setting of Gold Mineralization in the Kirkland Lake-Larder Lake Gold Belt, Ontario. Economic Geology 103, 1309–1340. doi: 10.2113/gsecongeo.103.6.1309.

Jackson, S.L., Fyon, J., Corfu, F., 1994. Review of Archean supracrustal assemblages of the southern Abitibi greenstone belt in Ontario, Canada: Products of microplate interaction within a large-scale plate-tectonic setting. Precambrian Research 65, 183–205. doi: 10.1016/0301-9268(94)90105-8.

Jeffery, G.B., 1922. The motion of ellipsoidal particles immersed in a viscous fluid. Proceedings of the Royal Society of London. Series A, Containing Papers of a Mathematical and Physical Character 102, 161–179. doi: 10.1098/rspa.1922.0078.

Jeẑek, J., 1994. Software for modeling the motion of rigid triaxial ellipsoidal particles in viscous flow. Computers & Geosciences 20, 409–424. doi: 10.1016/0098-3004(94)90049-3.

Ježek, J., Saic, S., Segeth, K., Schulmann, K., 1999. Three-dimensional hydrodynamical modelling of viscous flow around a rotating ellipsoidal inclusion. Computers & Geosciences 25, 547–558. doi: 10.1016/S0098-3004(98)00165-4.

Jiang, D., 1999. Vorticity decomposition and its application to sectional flow characterization. Tectonophysics 301, 243–259. doi: 10.1016/S0040-1951(98)00246-7.

Jiang, D., 2007. Numerical modeling of the motion of deformable ellipsoidal objects in slow viscous flows. Journal of Structural Geology 29, 435–452. doi: 10.1016/j.jsg.2006.09.009.

Jiang, D., 2012. A general approach for modeling the motion of rigid and deformable ellipsoids in ductile flows. Computers & Geosciences 38, 52–61. doi: 10.1016/j.cageo.2011.05.002.

Jiang, D., 2014. Structural geology meets micromechanics: A self-consistent model for the multiscale deformation and fabric development in Earth's ductile lithosphere. Journal of Structural Geology 68, 247–272. doi: 10.1016/j.jsg.2014.05.020.

Jiang, D., 2016. Viscous inclusions in anisotropic materials: Theoretical development and perspective applications. Tectonophysics 693, 116–142. doi: 10.1016/j.tecto.2016.10.012.

Jiang, D., 2023. Continuum Micromechanics: Theory and Application to Multiscale Tectonics. Springer, Cham.

Jiang, D., Bentley, C., 2012. A micromechanical approach for simulating multiscale fabrics in large-scale high-strain zones: Theory and application. Journal of Geophysical Research: Solid Earth 117. doi: 10.1029/2012JB009327.

Jiang, D., Bhandari, A., 2018. Pressure variations among rheologically heterogeneous elements in Earth's lithosphere: A micromechanics investigation. Earth and Planetary Science Letters 498, 397–407. doi: 10.1016/j.epsl.2018.07.010.

Jiang, D., Williams, P.F., 1998. High-strain zones: A unified model. Journal of Structural Geology 20, 1105–1120. doi: 10.1016/S0191-8141(98)00025-X.

Jiang, D., Williams, P.F., 1999. A fundamental problem with the kinematic interpretation of geological structures. Journal of Structural Geology 21, 933–937. doi: 10.1016/S0191-8141(99)00068-1.

Jibben, Z., Herrmann, M., 2017. An arbitrary-order Runge–Kutta discontinuous Galerkin approach to reinitialization for banded conservative level sets. Journal of Computational Physics 349, 453–473. doi: 10.1016/j.jcp.2017.08.035.

Johnson, T.E., Brown, M., Kaus, B.J.P., VanTongeren, J.A., 2014. Delamination and recycling of Archaean crust caused by gravitational instabilities. Nature Geoscience 7, 47–52. doi: 10.1038/ngeo2019.

Karakus, A., Warburton, T., Aksel, M.H., Sert, C., 2016a. A GPU-accelerated adaptive discontinuous Galerkin method for level set equation. International Journal of Computational Fluid Dynamics 30, 56–68. doi: 10.1080/10618562.2016.1155704.

Karakus, A., Warburton, T., Aksel, M.H., Sert, C., 2016b. A GPU accelerated level set reinitialization for an adaptive discontinuous Galerkin method. Computers & Mathematics with Applications 72, 755–767. doi: 10.1016/j.camwa.2016.05.025.

Karakus, A., Warburton, T., Aksel, M.H., Sert, C., 2018. An adaptive fully discontinuous Galerkin level set method for incompressible multiphase flows. International Journal of Numerical Methods for Heat & Fluid Flow 28, 1256–1278. doi: 10.1108/HFF-03-2017-0098.

Ketchum, J.W.F., Ayer, J.A., van Breemen, O., Pearson, N.J., Becker, J.K., 2008. Pericontinental Crustal Growth of the Southwestern Abitibi Subprovince, Canada–U-Pb, Hf, and Nd Isotope Evidence. Economic Geology 103, 1151–1184. doi: 10.2113/gsecongeo.103.6.1151.

Kinney, C., Kendrick, J., Duguet, M., Yakymchuk, C., 2023. Redistribution of heat-producing elements during melting of Archean crust. Journal of Metamorphic Geology , jmg.12751doi: 10.1111/jmg.12751.

Kloppenburg, A., White, S., Zegers, T., 2001. Structural evolution of the Warrawoona Greenstone Belt and adjoining granitoid complexes, Pilbara Craton, Australia: Implications for Archaean tectonic processes. Precambrian Research 112, 107–147. doi: 10.1016/S0301-9268(01)00172-3.

Koyi, H., 1988. Experimental Modeling of Role of Gravity and Lateral Shortening in Zagros Mountain Belt. AAPG Bulletin 72. doi: 10.1306/703C99AB-1707-11D7-8645000102C1865D.

Krivodonova, L., Xin, J., Remacle, J.F., Chevaugeon, N., Flaherty, J., 2004. Shock detection and limiting with discontinuous Galerkin methods for hyperbolic conservation laws. Applied Numerical Mathematics 48, 323–338. doi: 10.1016/j.apnum.2003.11.002.

Krogstad, E.J., Balakrishnan, S., Mukhopadhyay, D.K., Rajamani, V., Hanson, G.N., 1989. Plate Tectonics 2.5 Billion Years Ago: Evidence at Kolar, South India. Science 243, 1337–1340. doi: 10.1126/science.243.4896.1337.

Kronbichler, M., 2021. The Discontinuous Galerkin Method: Derivation and Properties, in: Kronbichler, M., Persson, P.O. (Eds.), Efficient High-Order Discretizations for Computational Fluid Dynamics. Springer International Publishing, Cham. volume 602, pp. 1–55. doi: 10.1007/978-3-030-60610-7_1.

Kronbichler, M., Diagne, A., Holmgren, H., 2018. A fast massively parallel two-phase flow solver for microfluidic chip simulation. The International Journal of High Performance Computing Applications 32, 266–287. doi: 10.1177/1094342016671790.

Kusky, T.M., Polat, A., 1999. Growth of granite–greenstone terranes at convergent margins, and stabilization of Archean cratons. Tectonophysics 305, 43–73. doi: 10.1016/S0040-1951(99)00014-1.

Lafrance, B., 2015. Geology of the orogenic Cheminis gold deposit along the Larder Lake – Cadillac deformation zone, Ontario. Canadian Journal of Earth Sciences 52, 1093–1108. doi: 10.1139/cjes-2015-0067.

Leng, W., Zhong, S., 2011. Implementation and application of adaptive mesh refinement for thermochemical mantle convection studies. Geochemistry, Geophysics, Geosystems 12. doi: 10.1029/2010GC003425.

Lev, E., Hager, B.H., 2008. Rayleigh-Taylor instabilities with anisotropic lithospheric viscosity. Geophysical Journal International 173, 806–814. doi: 10.1111/j.1365-246X.2008.03731.x.

Li, F., Shu, C.W., 2005. Reinterpretation and simplified implementation of a discontinuous Galerkin method for Hamilton–Jacobi equations. Applied Mathematics Letters 18, 1204–1209. doi: 10.1016/j.aml.2004.10.009.

Lin, S., 2001. Stratigraphic and Structural Setting of the Hemlo Gold Deposit, Ontario, Canada. Economic Geology 96, 477–507. doi: 10.2113/gsecongeo.96.3.477.

Lin, S., 2005. Synchronous vertical and horizontal tectonism in the Neoarchean: Kinematic evidence from a synclinal keel in the northwestern Superior craton, Canada. Precambrian Research 139, 181–194. doi: 10.1016/j.precamres.2005.07.001.

Lin, S., 2007. Comment: When did the life of plate tectonics begin? GSA Today 17, 12. doi: 10.1130/GSAT01703C.1.

Lin, S., Beakhouse, G.P., 2013. Synchronous vertical and horizontal tectonism at late stages of Archean cratonization and genesis of Hemlo gold deposit, Superior craton, Ontario, Canada. Geology 41, 359–362. doi: 10.1130/G33887.1.

Lin, S., Jiang, D., 2001. Using along-strike variation in strain and kinematics to define the movement direction of curved transpressional shear zones: An example from northwestern Superior Province, Manitoba. Geology 29, 767. doi: 10.1130/0091-7613(2001)029<0767:UASVIS>2.0.CO;2.

Lin, S., Jiang, D., Williams, P.F., 1998. Transpression (or transtension) zones of triclinic symmetry: Natural example and theoretical modelling. Geological Society, London, Special Publications 135, 41–57. doi: 10.1144/GSL.SP.1998.135.01.04.

Lin, S., Parks, J., Heaman, L.M., Simonetti, A., Corkery, M.T., 2013. Diapirism and sagduction as a mechanism for deposition and burial of "Timiskaming-type" sedimentary sequences, Superior Province: Evidence from detrital zircon geochronology and implications for the Borden Lake conglomerate in the exposed middle to lower crust in the Kapuskasing uplift. Precambrian Research 238, 148–157. doi: 10.1016/j.precamres.2013.09.012.

MacDonald, P., Hastie, E., Davis, D., 2017. Preliminary Geology of Osway and Huffman Townships and Parts of Eric, Fingal and Arbutus Townships, Southern Swayze Area, Abitibi Greenstone Belt. Open File Report 6333. Ontario Geological Survey. Sudbury.

Mai, V.V., Korenaga, J., 2022. What controlled the thickness of continental crust in the Archean? Geology 50, 1091–1095. doi: 10.1130/G50350.1.

Malvern, L., 1969. Introduction to the Mechanics of a Continuous Medium. Prentice-Hall Series in Engineering of the Physical Sciences, Prentice-Hall.

Mareschal, J.C., Jaupart, C., 2006. Archean thermal regime and stabilization of the cratons, in: Benn, K., Mareschal, J.C., Condie, K.C. (Eds.), Geophysical

Monograph Series. American Geophysical Union, Washington, D. C.. volume 164, pp. 61–73. doi: 10.1029/164GM06.

Mareschal, J.C., West, G.F., 1980. A model for Archean tectonism. Part 2. Numerical models of vertical tectonism in greenstone belts. Canadian Journal of Earth Sciences 17, 60–71. doi: 10.1139/e80-006.

Marques, F.O., 2016. Mineral lineation produced by 3-D rotation of rigid inclusions in confined viscous simple shear. Tectonophysics 684, 92–99. doi: 10.1016/j.tecto.2016.01.013.

Masuda, T., Mizuno, N., 1996. Deflection of non-Newtonian simple shear flow around a rigid cylindrical body by the finite element method. Journal of Structural Geology 18, 1089–1100. doi: 10.1016/0191-8141(96)00030-2.

Mathieu, L., Mole, D., Tóth, Z., Rubingh, K., Haugaard, R., White, S., Ma, C., Frieman, B., Lodge, R., Sherlock, R., Lafrance, B., 2023. The Neoarchean, a Turning Point for Geodynamic and Magmatic Processes within the Superior Craton?. Geological Society of America. pp. 43–54. doi: 10.1130/2022.1220(03).

May, D.A., Brown, J., Pourhiet, L.L., 2014. pTatin3D: High-Performance Methods for Long-Term Lithospheric Dynamics, in: SC14: International Conference for High Performance Computing, Networking, Storage and Analysis, IEEE, New Orleans, LA, USA. pp. 274–284. doi: 10.1109/SC.2014.28.

McKenzie, D., Bickle, M.J., 1988. The Volume and Composition of Melt Generated by Extension of the Lithosphere. Journal of Petrology 29, 625–679. doi: 10.1093/petrology/29.3.625.

Means, W., 1981. The concept of steady-state foliation. Tectonophysics 78, 179–199. doi: 10.1016/0040-1951(81)90013-5.

Means, W., Hobbs, B., Lister, G., Williams, P., 1980. Vorticity and non-coaxiality in progressive deformations. Journal of Structural Geology 2, 371–378. doi: 10.1016/0191-8141(80)90024-3.

Merriman, B., Bence, J.K., Osher, S.J., 1994. Motion of Multiple Junctions: A Level Set Approach. Journal of Computational Physics 112, 334–363. doi: 10.1006/jcph.1994.1105.

Mole, D., Thurston, P., Marsh, J., Stern, R., Ayer, J., Martin, L., Lu, Y., 2021. The formation of Neoarchean continental crust in the south-east Superior Craton by two distinct geodynamic processes. Precambrian Research 356, 106104. doi: 10.1016/j.precamres.2021.106104.

Montsion, R., Thurston, P., Ayer, J., 2018. 1:2000000 Scale Geological Compilation of the Superior Craton - Version 1.

Moresi, L., Dufour, F., Mühlhaus, H.B., 2003. A Lagrangian integration point finite element method for large deformation modeling of viscoelastic geomaterials. Journal of Computational Physics 184, 476–497. doi: 10.1016/S0021-9991(02)00031-1.

Moresi, L.N., Solomatov, V.S., 1995. Numerical investigation of 2D convection with extremely large viscosity variations. Physics of Fluids 7, 2154–2162. doi: 10.1063/1.868465.

Mousavi, R., 2014. Level Set Method for Simulating the Dynamics of the Fluid-Fluid Interfaces: Application of a Discontinuous Galerkin Method. Ph.D. thesis. Technische Universität. Darmstadt.

Mousavi, R., Kummer, F., Oberlack, M., Pelz, P., 2016. Level set method for simulating the interface kinematics: Application of a discontinuous Galerkin method, in: ECCOMAS Congress 2016, pp. 7182–7221. doi: 10.7712/100016.2327.9241.

Mühlhaus, H.B., Moresi, L., Čada, M., 2003. Anisotropy model for mantle convection, in: Computational Fluid and Solid Mechanics 2003. Elsevier, pp. 1044–1046. doi: 10.1016/B978-008044046-0.50255-4.

Nassif, M., Kuiper, Y., Goldfarb, R., Monecke, T., Holm-Denoma, C., 2018. Structural evolution of a gold-bearing transtensional zone within the Archean Porcupine-Destor deformation zone, southern Abitibi greenstone belt, eastern Ontario, Canada. Journal of Structural Geology 117, 203–218. doi: 10.1016/j.jsg.2018.09.012.

Osher, S.J., Fedkiw, R., 2003. Level Set Methods and Dynamic Implicit Surfaces. Springer, New York.

Owkes, M., Desjardins, O., 2013. A discontinuous Galerkin conservative level set scheme for interface capturing in multiphase flows. Journal of Computational Physics 249, 275–302. doi: 10.1016/j.jcp.2013.04.036.

Parmenter, A.C., Lin, S., Corkery, M.T., 2006. Structural evolution of the Cross Lake greenstone belt in the northwestern Superior Province, Manitoba: Implications for relationship between vertical and horizontal tectonism. Canadian Journal of Earth Sciences 43, 767–787. doi: 10.1139/e06-006.

Passchier, C., 1998. Monoclinic model shear zones. Journal of Structural Geology 20, 1121–1137. doi: 10.1016/S0191-8141(98)00046-7.

Pennacchioni, G., Fasolo, L., Cecchi, M.M., Salasnich, L., 2000. Finite-element modelling of simple shear flow in Newtonian and non-Newtonian fluids around a circular rigid particle. Journal of Structural Geology 22, 683–692. doi: 10.1016/S0191-8141(99)00180-7.

Percival, J.A., Card, K.D., 1983. Archean crust as revealed in the Kapuskasing uplift, Superior province, Canada. Geology 11, 323. doi: 10.1130/0091-7613(1983)11<323:ACARIT>2.0.CO;2.

Percival, J.A., Sanborn-Barrie, M., Skulski, T., Stott, G.M., Helmstaedt, H., White, D.J., 2006. Tectonic evolution of the western Superior Province from NATMAP and Lithoprobe studies. Canadian Journal of Earth Sciences 43, 1085–1117. doi: 10.1139/e06-062.

Percival, J.A., Skulski, T., Sanborn-Barrie, M., Stott, G.M., Leclair, A.D., Corkery, M.T., Boily, M., 2012. Geology and tectonic evolution of the Superior Province, Canada, in: Percival, J., Clowes, R., Cook, F.A., Geological Association of Canada (Eds.), Tectonic Styles in Canada: The Lithoprobe Perspective. Geological Association of Canada, St. John's, NL. number 49 in Geological Association of Canada Special Paper, pp. 321–378.

Percival, J.A., West, G.F., 1994. The Kapuskasing uplift: A geological and geophysical synthesis. Canadian Journal of Earth Sciences 31, 1256–1286. doi: 10.1139/e94-110.

Pysklywec, R.N., Beaumont, C., Fullsack, P., 2002. Lithospheric deformation during the early stages of continental collision: Numerical experiments and comparison with South Island, New Zealand. Journal of Geophysical Research: Solid Earth 107, ETG 3–1–ETG 3–19. doi: 10.1029/2001JB000252.

Qiu, J., Shu, C.W., 2005. A Comparison of Troubled-Cell Indicators for Runge–Kutta Discontinuous Galerkin Methods Using Weighted Essentially Nonoscillatory

Limiters. SIAM Journal on Scientific Computing 27, 995–1013. doi: 10.1137/04061372X.

Raleigh, C.B., Paterson, M.S., 1965. Experimental deformation of serpentinite and its tectonic implications. Journal of Geophysical Research 70, 3965–3985. doi: 10.1029/JZ070i016p03965.

Ramsay, J., 1980. Shear zone geometry: A review. Journal of Structural Geology 2, 83–99. doi: 10.1016/0191-8141(80)90038-3.

Ramsay, J.G., Graham, R.H., 1970. Strain variation in shear belts. Canadian Journal of Earth Sciences 7, 786–813. doi: 10.1139/e70-078.

Ramsay, J.G., Huber, M.I., 1983. The Techniques of Modern Structural Geology. Vol. 1, Strain Analysis. Academic Press, London ; New York.

Ran, H., de Riese, T., Llorens, M.G., Finch, M.A., Evans, L.A., Gomez-Rivas, E., Griera, A., Jessell, M.W., Lebensohn, R.A., Piazolo, S., Bons, P.D., 2019. Time for anisotropy: The significance of mechanical anisotropy for the development of deformation structures. Journal of Structural Geology 125, 41–47. doi: 10.1016/j.jsg.2018.04.019.

Ranalli, G., 1995. Rheology of the Earth. 2nd ed ed., Chapman & Hall, London ; New York.

Reed, W.H., Hill, T.R., 1973. Triangular Mesh Methods for the Neutron Transport Equation. Technical Report NSA-28-001270. Los Alamos Scientific Lab.. New Mexico, USA.

Reimink, J.R., Smye, A.J., 2024. Subaerial weathering drove stabilization of continents. Nature 629, 609–615. doi: 10.1038/s41586-024-07307-1.

Rhebergen, S., Cockburn, B., van der Vegt, J.J., 2013. A space–time discontinuous Galerkin method for the incompressible Navier–Stokes equations. Journal of Computational Physics 233, 339–358. doi: 10.1016/j.jcp.2012.08.052.

Robin, C., Bailey, R., 2009. Simultaneous generation of Archean crust and subcratonic roots by vertical tectonics. Geology 37, 523–526. doi: 10.1130/G25519A.1.

Robin, C.M., 2010. Diapirism on Venus and the Early Earth and The Thermal Effect of Fluid Flows in AECL's Tunnel Sealing Experiment. Ph.D. thesis. University of Toronto. Toronto, Canada.

Rosenberg, C.L., Handy, M.R., 2005. Experimental deformation of partially melted granite revisited: Implications for the continental crust. Journal of Metamorphic Geology 23, 19–28. doi: 10.1111/j.1525-1314.2005.00555.x.

Rosenberg, C.L., Stünitz, H., 2003. Deformation and recrystallization of plagioclase along a temperature gradient: An example from the Bergell tonalite. Journal of Structural Geology 25, 389–408. doi: 10.1016/S0191-8141(02)00036-6.

Samuel, H., Evonuk, M., 2010. Modeling advection in geophysical flows with particle level sets. Geochemistry, Geophysics, Geosystems 11. doi: 10.1029/2010GC003081.

Schmid, D.W., Podladchikov, Y.Y., 2003. Analytical solutions for deformable elliptical inclusions in general shear. Geophysical Journal International 155, 269–288. doi: 10.1046/j.1365-246X.2003.02042.x.

Schmid, D.W., Podladchikov, Y.Y., 2005. Mantled porphyroclast gauges. Journal of Structural Geology 27, 571–585. doi: 10.1016/j.jsg.2004.09.005.

Schwerdtner, W.M., 1990. Structural tests of diapir hypotheses in Archean crust of Ontario. Canadian Journal of Earth Sciences 27, 387–402. doi: 10.1139/e90-035.

Shadpour, A., Unger, A.J.A., Knight, M.A., Haas, C.T., 2015. Numerical DAE Approach for Solving a System Dynamics Problem. Journal of Computing in Civil Engineering 29, 04014054. doi: 10.1061/(ASCE)CP.1943-5487.0000349.

Shu, C.W., 2014. Discontinuous Galerkin Method for Time-Dependent Problems: Survey and Recent Developments, in: Feng, X., Karakashian, O., Xing, Y. (Eds.), Recent Developments in Discontinuous Galerkin Finite Element Methods for Partial Differential Equations. Springer International Publishing, Cham. volume 157, pp. 25–62. doi: 10.1007/978-3-319-01818-8_2.

Silvester, D., Wathen, A., 1994. Fast Iterative Solution of Stabilised Stokes Systems Part II: Using General Block Preconditioners. SIAM Journal on Numerical Analysis 31, 1352–1367. doi: 10.1137/0731070.

Sizova, E., Gerya, T., Brown, M., Perchuk, L., 2010. Subduction styles in the Precambrian: Insight from numerical experiments. Lithos 116, 209–229. doi: 10.1016/j.lithos.2009.05.028.

Smith, J., 2016. An Integrated Structural and Geochemical Study of Auriferous Sheeted Quartz Veins within the 2740 Ma Côté Gold Deposit, Swayze Greenstone Belt, Ontario. Master's thesis. Laurentian University. Sudbury.

Stahr, D.W., Law, R.D., 2011. Effect of finite strain on clast-based vorticity gauges. Journal of Structural Geology 33, 1178–1192. doi: 10.1016/j.jsg.2011.05.002.

Stipp, M., Stünitz, H., Heilbronner, R., Schmid, S.M., 2002. The eastern Tonale fault zone: A 'natural laboratory' for crystal plastic deformation of quartz over a temperature range from 250 to 700°C. Journal of Structural Geology 24, 1861–1884. doi: 10.1016/S0191-8141(02)00035-4.

Sun, G., Liu, S., Cawood, P.A., Tang, M., Van Hunen, J., Gao, L., Hu, Y., Hu, F., 2021. Thermal state and evolving geodynamic regimes of the Meso- to Neoarchean North China Craton. Nature Communications 12, 3888. doi: 10.1038/s41467-021-24139-z.

Sussman, M., Fatemi, E., Smereka, P., Osher, S., 1998. An improved level set method for incompressible two-phase flows. Computers & Fluids 27, 663–680. doi: 10.1016/S0045-7930(97)00053-4.

Sussman, M., Smereka, P., Osher, S., 1994. A Level Set Approach for Computing Solutions to Incompressible Two-Phase Flow. Journal of Computational Physics 114, 146–159. doi: 10.1006/jcph.1994.1155.

Tackley, P.J., King, S.D., 2003. Testing the tracer ratio method for modeling active compositional fields in mantle convection simulations: TRACER RATIO METHOD. Geochemistry, Geophysics, Geosystems 4. doi: 10.1029/2001GC000214.

Talbot, C., Rönnlund, P., Schmeling, H., Koyi, H., Jackson, M., 1991. Diapiric spoke patterns. Tectonophysics 188, 187–201. doi: 10.1016/0040-1951(91)90322-J.

Thébaud, N., Rey, P., 2013. Archean gravity-driven tectonics on hot and flooded continents: Controls on long-lived mineralised hydrothermal systems away from continental margins. Precambrian Research 229, 93–104. doi: 10.1016/j.precamres.2012.03.001.

Thieulot, C., 2014. ELEFANT: A User-Friendly Multipurpose Geodynamics Code. Preprint. Geodynamics. doi: 10.5194/sed-6-1949-2014.

Thurston, P.C., Ayer, J.A., Goutier, J., Hamilton, M.A., 2008. Depositional Gaps in Abitibi Greenstone Belt Stratigraphy: A Key to Exploration for Syngenetic Mineralization. Economic Geology 103, 1097–1134. doi: 10.2113/gsecongeo.103.6.1097.

Tikoff, B., Fossen, H., 1995. The limitations of three-dimensional kinematic vorticity analysis. Journal of Structural Geology 17, 1771–1784. doi: 10.1016/0191-8141(95)00069-P.

Tornberg, A.K., Engquist, B., 2000. A finite element based level-set method for multiphase flow applications. Computing and Visualization in Science 3, 93–101. doi: 10.1007/s007910050056.

Tryggvason, G., Bunner, B., Esmaeeli, A., Juric, D., Al-Rawahi, N., Tauber, W., Han, J., Nas, S., Jan, Y.J., 2001. A Front-Tracking Method for the Computations of Multiphase Flow. Journal of Computational Physics 169, 708–759. doi: 10.1006/jcph.2001.6726.

Turcksin, B., Kronbichler, M., Bangerth, W., 2016. WorkStream - A Design Pattern for Multicore-Enabled Finite Element Computations. ACM Transactions on Mathematical Software 43, 1–29. doi: 10.1145/2851488.

Uphoff, C., May, D.A., Gabriel, A.A., 2022. A discontinuous Galerkin method for sequences of earthquakes and aseismic slip on multiple faults using unstructured curvilinear grids. Geophysical Journal International 233, 586–626. doi: 10.1093/gji/ggac467.

ur Rehman, M., Geenen, T., Vuik, C., Segal, G., MacLachlan, S.P., 2011. On iterative methods for the incompressible Stokes problem. International Journal for Numerical Methods in Fluids 65, 1180–1200. doi: 10.1002/fld.2235.

van Breemen, O., Heather, K., Ayer, J.A., 2006. U-Pb Geochronology of the Neoarchean Swayze Sector of the Southern Abitibi Greenstone Belt. Technical Report 2006-F1. Geological Survey of Canada. doi: 10.4095/223016.

van der Velden, A.J., Cook, F.A., Drummond, B.J., Goleby, B.R., 2006. Reflections of the Neoarchean: A global perspective, in: Benn, K., Mareschal, J.C., Condie, K.C. (Eds.), Geophysical Monograph Series. American Geophysical Union, Washington, D. C.. volume 164, pp. 255–265. doi: 10.1029/164GM16.

van Keken, P.E., King, S.D., Schmeling, H., Christensen, U.R., Neumeister, D., Doin, M.P., 1997. A comparison of methods for the modeling of thermochemical convection. Journal of Geophysical Research: Solid Earth 102, 22477–22495. doi: 10.1029/97JB01353.

Van Kranendonk, M.J., 2011. Cool greenstone drips and the role of partial convective overturn in Barberton greenstone belt evolution. Journal of African Earth Sciences 60, 346–352. doi: 10.1016/j.jafrearsci.2011.03.012.

Van Kranendonk, M.J., Collins, W., Hickman, A., Pawley, M.J., 2004. Critical tests of vertical vs. horizontal tectonic models for the Archaean East Pilbara Granite–Greenstone Terrane, Pilbara Craton, Western Australia. Precambrian Research 131, 173–211. doi: 10.1016/j.precamres.2003.12.015.

Van Kranendonk, M.J., Smithies, R.H., Hickman, A.H., Champion, D.C., 2007. Chapter 4.1 Paleoarchean Development of a Continental Nucleus: The East Pilbara Terrane of the Pilbara Craton, Western Australia, in: Developments in Precambrian Geology. Elsevier. volume 15, pp. 307–337. doi: 10.1016/S0166-2635(07)15041-6.

Vearncombe, J., Zelic, M., 2015. Structural paradigms for gold: Do they help us find and mine? Applied Earth Science 124, 2–19. doi: 10.1179/1743275815Y.0000000003.

Wallstedt, P.C., Guilkey, J.E., 2011. A weighted least squares particle-in-cell method for solid mechanics. International Journal for Numerical Methods in Engineering 85, 1687–1704. doi: 10.1002/nme.3041.

Weinberg, R.F., 1997. Diapir-driven crustal convection: Decompression melting, renewal of the magma source and the origin of nested plutons. Tectonophysics 271, 217–229. doi: 10.1016/S0040-1951(96)00269-7.

Weinberg, R.F., Podladchikov, Y., 1994. Diapiric ascent of magmas through power law crust and mantle. Journal of Geophysical Research: Solid Earth 99, 9543–9559. doi: 10.1029/93JB03461.

Weinberg, R.F., Schmeling, H., 1992. Polydiapirs: Multiwavelength gravity structures. Journal of Structural Geology 14, 425–436. doi: 10.1016/0191-8141(92)90103-4.

Wiemer, D., Schrank, C.E., Murphy, D.T., Wenham, L., Allen, C.M., 2018. Earth's oldest stable crust in the Pilbara Craton formed by cyclic gravitational overturns. Nature Geoscience 11, 357–361. doi: 10.1038/s41561-018-0105-9.

Wilkinson, L., Cruden, A.R., Krogh, T.E., 1999. Timing and kinematics of post-Timiskaming deformation within the Larder Lake - Cadillac deformation zone,

southwest Abitibi greenstone belt, Ontario, Canada. Canadian Journal of Earth Sciences 36, 627–647. doi: 10.1139/e99-015.

Wilks, K.R., Carter, N.L., 1990. Rheology of some continental lower crustal rocks. Tectonophysics 182, 57–77. doi: 10.1016/0040-1951(90)90342-6.

Wú, Q., Lin, S., Unger, A., 2023. Modeling Multi-Material Structural Patterns in Tectonic Flow With a Discontinuous Galerkin Level Set Method. Journal of Geophysical Research: Solid Earth 128, e2023JB026806. doi: 10.1029/2023JB026806.

Xiong, Z., Zhuang, J., Zhou, S., Matsu'ura, M., Hao, M., Wang, Q., 2021. Crustal strain-rate fields estimated from GNSS data with a Bayesian approach and its correlation to seismic activity in Mainland China. Tectonophysics 815, 229003. doi: 10.1016/j.tecto.2021.229003.

Yan, J., Osher, S., 2011. A local discontinuous Galerkin method for directly solving Hamilton–Jacobi equations. Journal of Computational Physics 230, 232–244. doi: 10.1016/j.jcp.2010.09.022.

Yu, C., Yang, T., Zhang, J., Zhao, G., Cawood, P.A., Yin, C., Qian, J., Gao, P., Zhao, C., 2022. Coexisting diverse P–T–t paths during Neoarchean Sagduction: Insights from numerical modeling and applications to the eastern North China Craton. Earth and Planetary Science Letters 586, 117529. doi: 10.1016/j.epsl.2022.117529.

Zalesak, S.T., 1979. Fully multidimensional flux-corrected transport algorithms for fluids. Journal of Computational Physics 31, 335–362. doi: 10.1016/0021-9991(79)90051-2.

Zhang, J., Lin, S., Linnen, R., Martin, R., 2014. Structural setting of the Young-Davidson syenite-hosted gold deposit in the Western Cadillac-Larder Lake Deformation Zone, Abitibi Greenstone Belt, Superior Province, Ontario. Precambrian Research 248, 39–59. doi: 10.1016/j.precamres.2014.04.007.

Zhang, J., Yue, P., 2019. A high-order and interface-preserving discontinuous Galerkin method for level-set reinitialization. Journal of Computational Physics 378, 634–664. doi: 10.1016/j.jcp.2018.11.029.

Zhang, Q., Fossen, H., 2020. The dilemma of asymmetric porphyroclast systems and sense of shear. Journal of Structural Geology 130, 103893. doi: 10.1016/j.jsg.2019.103893.

Zhang, Y., Gao, J., Han, W., He, Y., 2019. A discontinuous Galerkin method for seismic wave propagation in coupled elastic and poroelastic media. Geophysical Prospecting 67, 1392–1403. doi: 10.1111/1365-2478.12781.

Zhang, Y., Robinson, J., Schaubs, P., 2011. Numerical modelling of structural controls on fluid flow and mineralization. Geoscience Frontiers 2, 449–461. doi: 10.1016/j.gsf.2011.05.011.

Zhao, C., Zhang, J., Zhao, G., Yin, C., Chen, G., Liu, J., Liu, X., Chen, W., 2021. Kinematics and structural evolution of the Anziling dome-and-keel architecture in east China: Evidence of Neoarchean vertical tectonism in the North China Craton. GSA Bulletin doi: 10.1130/B36225.1.

Zhao, H.K., Chan, T., Merriman, B., Osher, S., 1996. A Variational Level Set Approach to Multiphase Motion. Journal of Computational Physics 127, 179–195. doi: 10.1006/jcph.1996.0167.

Zhong, X., Shu, C.W., 2013. A simple weighted essentially nonoscillatory limiter for Runge–Kutta discontinuous Galerkin methods. Journal of Computational Physics 232, 397–415. doi: 10.1016/j.jcp.2012.08.028.

Zhou, X., Li, Z.H., Gerya, T.V., Stern, R.J., Xu, Z., Zhang, J., 2018. Subduction initiation dynamics along a transform fault control trench curvature and ophiolite ages. Geology 46, 607–610. doi: 10.1130/G40154.1.

Zhu, J., Zhong, X., Shu, C.W., Qiu, J., 2013. Runge–Kutta discontinuous Galerkin method using a new type of WENO limiters on unstructured meshes. Journal of Computational Physics 248, 200–220. doi: 10.1016/j.jcp.2013.04.012.

Zibra, I., Gessner, K., Smithies, H., Peternell, M., 2014. On shearing, magmatism and regional deformation in Neoarchean granite-greenstone systems: Insights from the Yilgarn Craton. Journal of Structural Geology 67, 253–267. doi: 10.1016/j.jsg.2013.11.010.

Zibra, I., Lu, Y., Clos, F., Weinberg, R., Peternell, M., Wingate, M., Prause, M., Schiller, M., Tilhac, R., 2020. Regional-scale polydiapirism predating the Neoarchean Yilgarn Orogeny. Tectonophysics 779, 228375. doi: 10.1016/j.tecto.2020.228375.

APPENDICES

Appendix A

Linear system solver details

In this document we tabulate the solver iteration counts and timing results for the experiments carried out in Section 2.3. Each problem is solved first with Schur complement reduction (SCR) method, conjugate gradient (CG) iterative solver and the level based incomplete LU (ILU) preconditioner. The problem is then solved again with fully coupled (FC) method, generalized minimal residue (GMRES) iterative solver and the ILU as well as algebraic multigrid (AMG) preconditioners. The number of orthogonalization basis vector is chosen at 100 for the GMRES iterative solver.

In the Rayleigh-Taylor experiment, the simulation is run up to $t = 50$. In the inclusion experiment, the simulation is run up to $t = 0.5$. The "CPU time" column reports the average execution of the linear solver per each time step. The CPU time is reported in seconds as well as in normalized time in the parenthesis with respect to the SCR method with and the ILU preconditioner at level of fill $k = 0$. The mesh density is reported in $N_{\max} \times N_{\max}$ in 2d and $N_{\max} \times N_{\max} \times N_{\max}$ in 3d where $N_{\max}$ represents the mesh density for the most refined mesh.

A.1 The Rayleigh-Taylor instability

32×32	$\eta_1/\eta_0 = 100$			$\eta_1/\eta_0 = 10$		
Method	N_{iter}		CPU time	N_{iter}		CPU time
FC						
GMRES w. ILU(0)	244		0.1468 (0.28)	119		0.0726 (0.14)
GMRES w. ILU(1)	70		0.0665 (0.12)	48		0.0441 (0.08)
GMRES w. ILU(2)	61		0.0794 (0.15)	40		0.0531 (0.10)
GMRES w. AMG	63		0.3068 (0.58)	29		0.2164 (0.41)
SCR	Inner	Outer		Inner	Outer	
CG w. ILU(0)	87	27	0.5328 (**1.00**)	79	14	0.2751 (0.52)
CG w. ILU(1)	39	27	0.4311 (0.81)	36	14	0.2219 (0.42)
CG w. ILU(2)	29	27	0.4526 (0.85)	28	14	0.2379 (0.45)

Table A.1: Number of iterations and CPU time of the 2d Rayleigh-Taylor instability test case on an adaptively refined mesh up to 32×32. The CPU time is measured in seconds. The maximum mass error is 0.22% for $\eta_1/\eta_0 = 100$ test cases and 0.034% for $\eta_1/\eta_0 = 10$ test cases.

64×64	$\eta_1/\eta_0 = 100$			$\eta_1/\eta_0 = 10$		
	N_{iter}		CPU time	N_{iter}		CPU time
FC						
GMRES w. ILU(0)	2041		2.8012 (1.32)	351		0.4464 (0.21)
GMRES w. ILU(1)	118		0.2516 (0.12)	66		0.1319 (0.06)
GMRES w. ILU(2)	82		0.2624 (0.12)	52		0.1592 (0.07)
GMRES w. AMG	76		1.1251 (0.53)	31		0.7103 (0.33)
SCR	Inner	Outer		Inner	Outer	
CG w. ILU(0)	140	28	2.1260 (**1.00**)	126	14	0.9250 (0.44)
CG w. ILU(1)	62	28	1.7407 (0.82)	55	14	0.7631 (0.36)
CG w. ILU(2)	45	28	2.0316 (0.96)	42	14	0.8770 (0.41)

Table A.2: Number of iterations and CPU time of the 2d Rayleigh-Taylor instability test case on an adaptively refined mesh up to 64×64. The maximum mass error is 0.62% for $\eta_1/\eta_0 = 100$ test cases and 0.0056% for $\eta_1/\eta_0 = 10$ test cases.

$16 \times 16 \times 16$	$\eta_1/\eta_0 = 100$			$\eta_1/\eta_0 = 10$		
Method	N_{iter}		CPU time	N_{iter}		CPU time
FC						
GMRES w. ILU(0)	898		33.3836 (0.58)	319		13.0696 (0.23)
GMRES w. ILU(1)	170		45.4202 (0.79)	75		35.4928 (0.61)
GMRES w. AMG	56		2.6603 (0.05)	33		1.8031 (0.03)
SCR	Inner	Outer		Inner	Outer	
CG w. ILU(0)	98	20	57.7545 (**1.00**)	94	10	32.8875 (0.57)
CG w. ILU(1)	43	20	104.6918 (1.81)	42	10	70.6880 (1.22)

Table A.3: Number of iterations and CPU time of the 3d Rayleigh-Taylor instability test case on an adaptively refined mesh up to $16 \times 16 \times 16$. The CPU time is measured in seconds. The maximum mass error is 0.36% for $\eta_1/\eta_0 = 100$ test cases and 0.013% for $\eta_1/\eta_0 = 10$ test cases.

$32 \times 32 \times 32$	$\eta_1/\eta_0 = 100$			$\eta_1/\eta_0 = 10$		
Method	N_{iter}		CPU time	N_{iter}		CPU time
FC						
GMRES w. ILU(0)			N/A	3260		641.2159 (1.10)
GMRES w. AMG	57		16.7669 (0.03)	34		10.2218 (0.02)
SCR	Inner	Outer		Inner	Outer	
CG w. ILU(0)	180	18	582.9235 (**1.00**)	167	8	279.1082 (0.48)

Table A.4: Number of iterations and CPU time of the 3d Rayleigh-Taylor instability test case on an adaptively refined mesh up to $32 \times 32 \times 32$. The maximum mass error is 0.42% for $\eta_1/\eta_0 = 100$ test cases and 0.066% for $\eta_1/\eta_0 = 10$ test cases.

A.2 Competent inclusion in simple shear flow

$16 \times 16 \times 16$	$\eta_1/\eta_0 = 100$			$\eta_1/\eta_0 = 10$		
Method	N_{iter}		CPU time	N_{iter}		CPU time
FC						
GMRES w. ILU(0)	210		17.6472 (0.38)	136		11.2886 (0.24)
GMRES w. ILU(1)	73		64.9483 (1.39)	53		55.0291 (1.18)
GMRES w. AMG	45		10.8627 (0.23)	39		9.4438 (0.20)
SCR	Inner	Outer		Inner	Outer	
CG w. ILU(0)	99	47	46.8049 (**1.00**)	85	40	131.6576 (2.81)
CG w. ILU(1)	47	47	347.2301 (7.42)	40	40	229.2119 (4.90)

Table A.5: Number of iterations and CPU time of the 3d inclusion test case on an adaptively refined mesh up to $16 \times 16 \times 16$. The maximum mass error is 0.32% for $\eta_1/\eta_0 = 100$ test cases and 0.1% for $\eta_1/\eta_0 = 10$ test cases.

$32 \times 32 \times 32$	$\eta_1/\eta_0 = 100$			$\eta_1/\eta_0 = 10$		
Method	N_{iter}		CPU time	N_{iter}		CPU time
FC						
GMRES w. ILU(0)	368		98.3485 (0.08)	497		123.6282 (0.10)
GMRES w. ILU(1)	98		339.7347 (0.27)	80		325.4592 (0.26)
GMRES w. AMG	41		36.9965 (0.03)	36		32.9449 (0.03)
SCR	Inner	Outer		Inner	Outer	
CG w. ILU(0)	175	49	1261.1562 (**1.00**)	146	41	811.9788 (0.65)
CG w. ILU(1)			N/A	68	41	1627.2463 (1.29)

Table A.6: Number of iterations and CPU time of the 3d inclusion test case on an adaptively refined mesh up to $32 \times 32 \times 32$. The maximum mass error is 0.12% for $\eta_1/\eta_0 = 100$ test cases and 0.1% for $\eta_1/\eta_0 = 10$ test cases.

A.3 Discussions

We have tested our SCR (CG) and FC (GMRES) solver in 2d/3d numerical experiments under different viscosity contrasts, grid densities and levels of fill k. In the Rayleigh-Taylor instability experiments, solver comparisons are carried out for both 2d and 3d for multiple time steps up to $t = 50$, while the solvers are tested up to $t = 0.5$ for the 3d inclusion experiments. The zero level set contours are plotted in Figures A.1 to A.3. The results show that the solutions obtained from different preconditioner and linear solver combinations agree within the solver tolerance. We hereby summarize our observations and make recommendations for the optimal choice.

In all test cases, with the same ILU preconditioner and convergence criteria, the SCR method requires significantly more computation time to achieve convergence than the FC GMRES solver due to substantial number of inner iterations needed to be performed.

For both iterative solvers and preconditioning techniques, the total iteration counts of FC method and outer iteration counts of the SCR method increase slightly for denser mesh configuration, while the increase is more significant under the higher viscosity contrast. The inner iteration counts of the SCR methods, however, are sensitive to the grid configuration while being relatively independent of viscosity contrast. Increasing the level of fill k in the $\boldsymbol{A}$ preconditioner reduces the total iteration counts in the GMRES solver and the inner iteration counts for SCR at the expense of larger memory consumption and slow per-cycle computation time.

Our numerical experiments on the linear solver underscores the importance of a high-quality preconditioner for the velocity block of the steady-state Stokes system to achieve reasonably fast convergence with the FC approach. The level-based ILU preconditioner can be viewed as an approximate "inverse" of the velocity block $\boldsymbol{A}$. A higher level-of-fill corresponds to an "inverse" that more closely approximates $\boldsymbol{A}^{-1}$. Although ILU has been successful in preconditioning elliptical problems on a uniform grid for weakly non-homogeneous and strongly anisotropic media, the combined effect of a non-uniform mesh structure and the viscosity contrast in our problem results in a highly stiff system that requires a higher ILU level-of-fill ($k \geqslant 1$) to smooth out the error effectively. On the other hand, the choice of k is limited by the additional memory and computation time in the forward/backward substitution phase due to the induced fill-ins. In 2d a balanced choice is $k = 1$. In 3d the quality of the ILU preconditioner is more difficult to maintain as the wide grid support of the Taylor-Hood element induces too many fill-ins to be practical for the

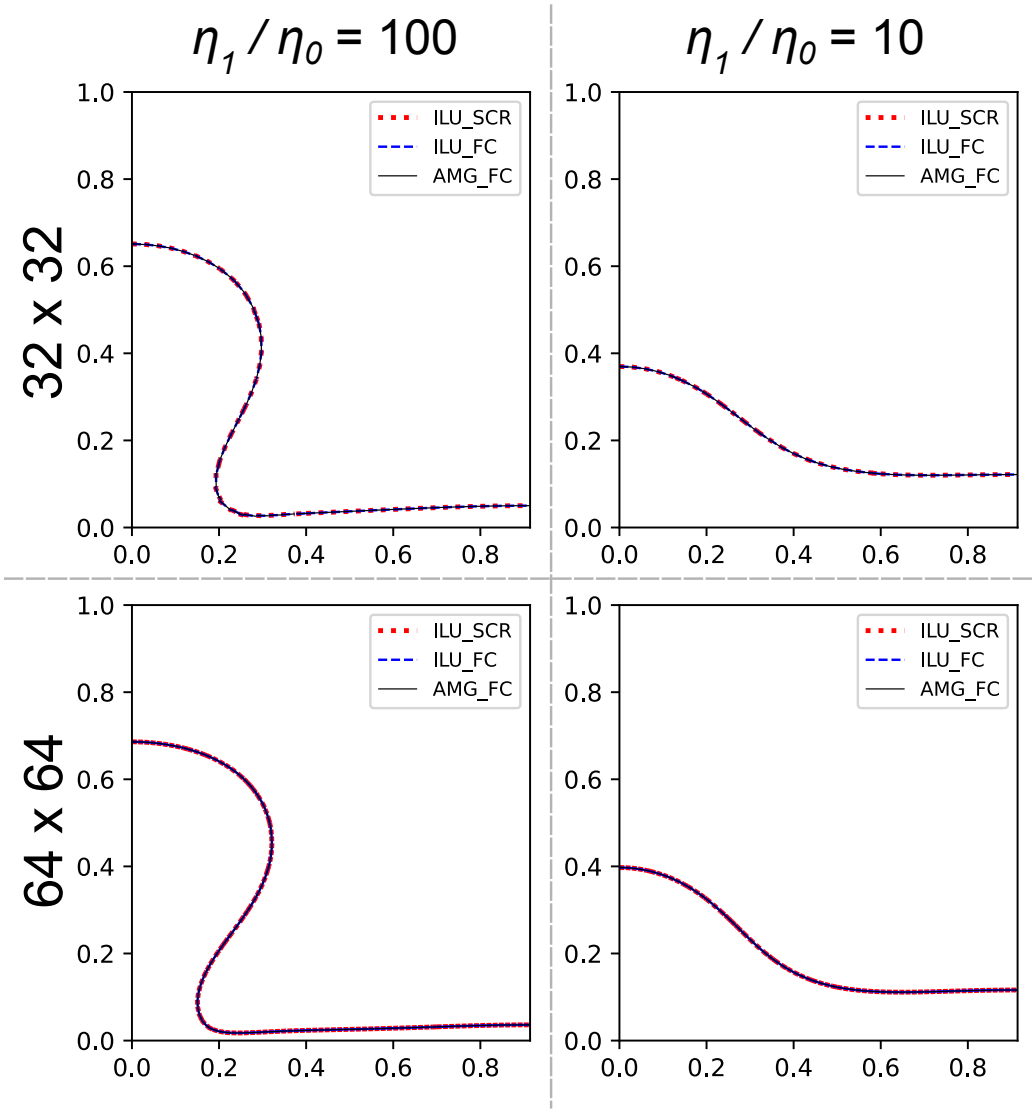


Figure A.1: The zero level set contour of the 2d Rayleigh-Taylor benchmark.

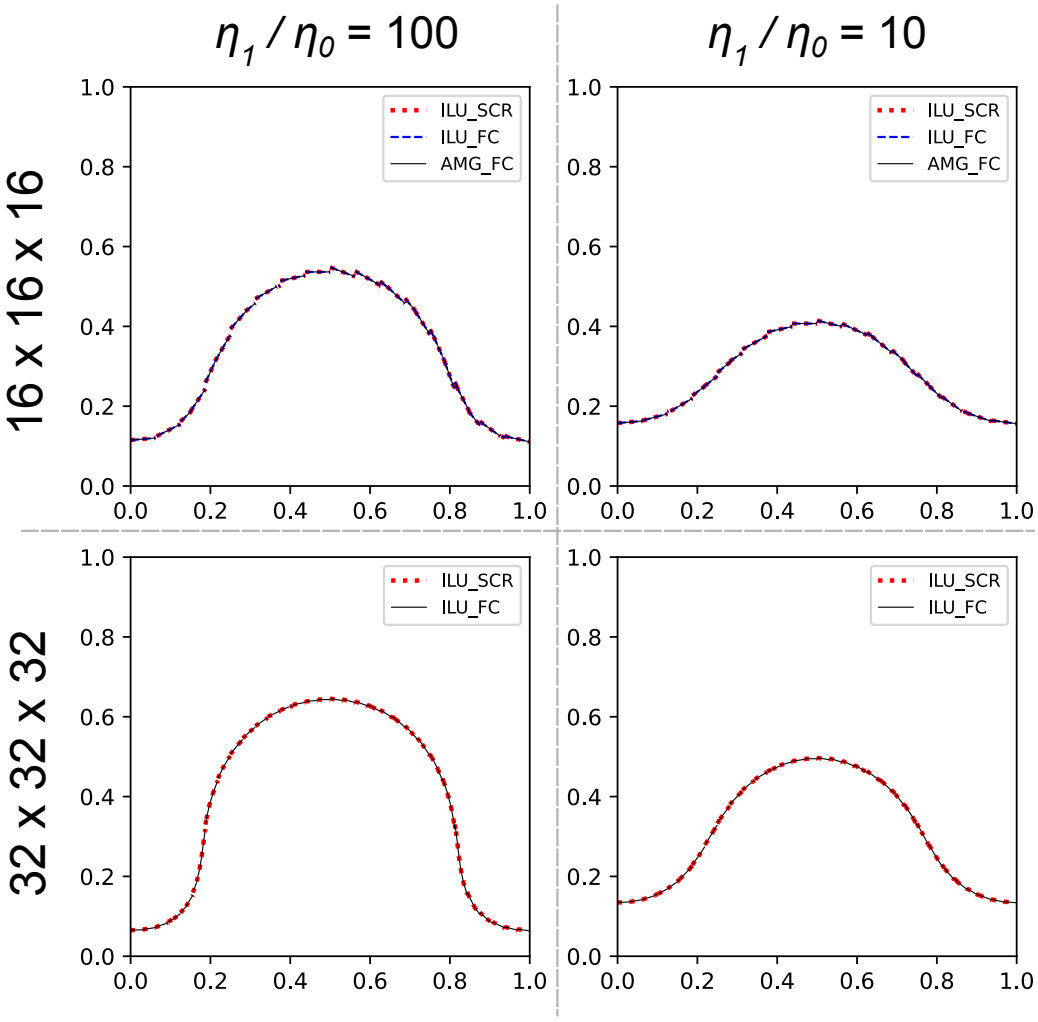


Figure A.2: The zero level set contour of the 3d Rayleigh-Taylor experiment on a yz slice plane through the origin.

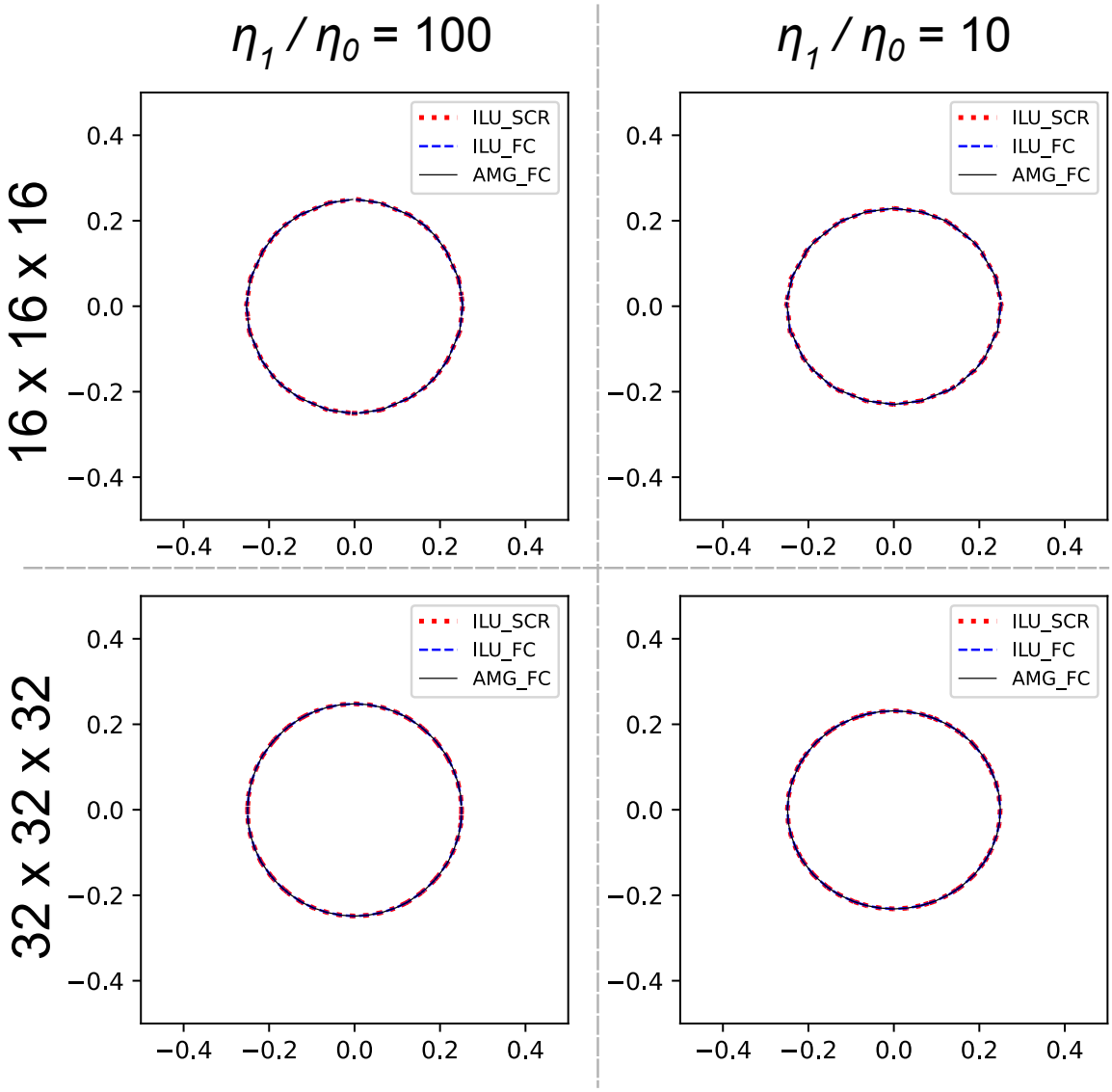


Figure A.3: The zero level set contour of the 3d inclusion on a yz slice plane through the origin.

ILU preconditioning even for $k = 1$. The AMG preconditioner, on the other hand, operates by interpolating the velocity block $\boldsymbol{A}$ on a hierarchy of grid structures defined by the influences between grid points (ur Rehman et al., 2011). In this way AMG is effective in smoothing out errors on a wide range of length scales and achieves convergence independent of the mesh configuration, making AMG a very efficient high-quality preconditioner in 3d, although the overhead for setting up the

AMG preconditioner makes it less attractive in 2d.

We also remark that better preconditioner results in a reduction of the orthogonalization vectors for GMRES. In 2d test cases the GMRES requires at least 100 temporary basis vectors to orthogonalize against for ILU(0) preconditioner. This number drop to 50 for ILU(1) and can be as low as 10 for AMG preconditioner.

Appendix B

Level set details

B.1 Level set reinitialization

The discretization of level set reinitialization as a Hamilton-Jacobi (HJ) problem share similarities with the discretization of hyperbolic conservation law and is traditionally done with high order essential non-oscillatory scheme (ENO) and weighted essential non-oscillatory scheme (WENO) scheme under finite difference and finite volume methods (Osher and Fedkiw, 2003). Under discontinuous Galerkin (DG) discretization, Zhang and Yue (2019) proposes a reinitialization scheme using a weighted local projection in the interface cells and the HJ formulation of Hu and Shu (1999) with a modified Lax-Friedrichs flux elsewhere. In this study, we apply the local discontinuous Galerkin (LDG) method for a direct solution to the HJ reinitialization problem (Yan and Osher, 2011; Karakus et al., 2016a), the procedure of which we shall summarize below.

The DG discretization seek approximation to the level set field in the "broken" space V_h^k of polynomials of degree no more than k, which is the space where the polynomial approximations of the level set function ϕ_h and the test function ψ_h reside in.

We begin by seeking a component-wise DG approximation of the level set gradient $\boldsymbol{u} = \boldsymbol{\nabla}\phi$. Let ω_h and $u_{h,i}\,(i = 1, \ldots, d)$ respectively be the test function and the i-th component of the level set gradient, both residing in V_h^k space. Through integration by parts we obtain a one-sided upwind gradient approximation for each component

of $\boldsymbol{u}_h$:

$$\begin{aligned}
\int_{\Omega_e} \omega_h^{\leftarrow} u_{h,i}^{\leftarrow}\, d\Omega &= \int_{\partial\Omega_e} \omega_h^{\leftarrow} n_i \phi_{h,e}^{\leftarrow}\, dS - \int_{\Omega_e} \frac{\partial \omega_h^{\leftarrow}}{\partial x_i} \phi_h\, d\Omega \quad \forall\, \omega_h^{\leftarrow} \in V_h^k \\
\int_{\Omega_e} \omega_h^{\rightarrow} u_{h,i}^{\rightarrow}\, d\Omega &= \int_{\partial\Omega_e} \omega_h^{\rightarrow} n_i \phi_{h,e}^{\rightarrow}\, dS - \int_{\Omega_e} \frac{\partial \omega_h^{\rightarrow}}{\partial x_i} \phi_h\, d\Omega \quad \forall\, \omega_h^{\rightarrow} \in V_h^k
\end{aligned} \tag{B.1}$$

where $\phi_{h,e}^{\leftarrow}$ and $\phi_{h,e}^{\rightarrow}$ are the left and right upwind values at the faces of cell e. They are defined as:

$$\phi_{h,e}^{\leftarrow} = \begin{cases} \phi_{h,e}^{-} & n_i \leqslant 0 \\ \phi_{h,e}^{+} & n_i > 0 \end{cases} \quad ; \quad \phi_{h,e}^{\rightarrow} = \begin{cases} \phi_{h,e}^{+} & n_i \leqslant 0 \\ \phi_{h,e}^{-} & n_i > 0 \end{cases} \tag{B.2}$$

Here $\phi_{h,e}^{-}$ and $\phi_{h,e}^{+}$ are the internal and external values of ϕ_h at the cell face of element e.

With the one-sided gradients obtained at each degree of freedom, we are ready to discretize the reinitialization problem by replacing the reinitialization operator $H(\boldsymbol{\nabla}\phi)$ by a monotone and consistent numerical HJ operator $\hat{H}(u_{h,i}^{\leftarrow}, u_{h,i}^{\rightarrow})$ with a suitable numerical flux. In this study we use the numerically non-dissipative Godunov flux, which resolves the flow and shock propagation by considering the velocity component in each spatial dimension (Karakus et al., 2016b; Mousavi, 2014):

$$\hat{H}(\boldsymbol{u}_h^{\leftarrow}, \boldsymbol{u}_h^{\rightarrow}) = \mathrm{sgn}_h(\phi_0) \begin{cases} \left(\sum_{i=1}^{d} \max\left\{ (\widehat{u_{h,i}^{\leftarrow}})^2,\ (\widetilde{u_{h,i}^{\rightarrow}})^2 \right\} \right)^{1/2} - 1, & \text{if} \quad \mathrm{sgn}_h(\phi_0) \geqslant 0 \\ \left(\sum_{i=1}^{d} \max\left\{ (\widetilde{u_{h,i}^{\leftarrow}})^2,\ (\widehat{u_{h,i}^{\rightarrow}})^2 \right\} \right)^{1/2} - 1, & \text{else} \end{cases} \tag{B.3}$$

where $\widehat{u_{h,i}} := \max\left\{u_{h,i}\ ,\ 0\right\}$ and $\widetilde{u_{h,i}} := -\min\left\{u_{h,i}\ ,\ 0\right\}$. Finally, the nodal level set values can be updated by testing the reinitialization equation against a test function $\psi_h \in V_h^k$:

$$\sum_e \int_{\Omega_e} \psi_h \frac{\partial \phi_h}{\partial t}\, d\Omega = -\sum_e \int_{\Omega_e} \psi_h \hat{H}(\boldsymbol{u}_h^{\leftarrow}, \boldsymbol{u}_h^{\rightarrow})\, d\Omega \tag{B.4}$$

the temporal aspect of the equation is treated with an explicit Runge-Kutta (RK) total variance diminishing (TVD) scheme.

B.2 Slope Limiting

Our solution scheme for the level set method is in most cases stable. However, when cells close to the interface are highly refined or a degree of polynomial $k \geqslant 1$ approximation is used, the discontinuities in the first derivative of the discretized level set (appearing geometrically as "kinks" or "cusps") may evolve into numerical oscillations. If not contained, the spurious oscillations may grow and eventually affect the physical behaviour of the modelled problem. In the studies by Kronbichler (2021) and Karakus et al. (2016a), the numerical oscillation is damped by judiciously applying artificial viscosity to shock-affected cells. In Zhang and Yue (2019) a minmod-type limiter is applied to the gradient of the level set values in cells with a high curvature. Our implementation adopts the WENO limiter proposed in Zhu et al. (2013) and Zhong and Shu (2013). Here we briefly discuss summarize the idea of the WENO limiter algorithm.

We denote the target cell under consideration as Ω_0 with a local polynomial approximation $\phi_{h,0}(\boldsymbol{x})$. Its neighbouring cells are denoted as Ω_m where $m = 1, 2, \ldots$ up to N_{nb}, the total number of neighbouring cells. The local polynomial approximations of the neighbouring cells are similarly denoted as $\phi_{h,m}(\boldsymbol{x})$. In 2d, $N_{\text{nb}} = 4$ if no neighbouring cells are more refined than Ω_0 and N_{nb} can reach up to 8 if all neighbouring cells are on a higher refinement level than Ω_0. The limiter operates by first constructing shifted approximations $\tilde{\phi}_{h,i}(\boldsymbol{x})$ on all cells Ω_i $(i = 0, 1, 2, \ldots, N_{\text{nb}})$, target cell and neighbouring cells included:

$$\tilde{\phi}_{h,i}(\boldsymbol{x}) = \phi_{h,i}(\boldsymbol{x}) - \frac{1}{\text{Vol}(\Omega_0)} \int_{\Omega_0} \phi_{h,i}(\boldsymbol{x})\, d\boldsymbol{x} + \frac{1}{\text{Vol}(\Omega_0)} \int_{\Omega_0} \phi_{h,0}(\boldsymbol{x})\, d\boldsymbol{x} \quad (i = 0, 1, 2, \ldots) \tag{B.5}$$

where $\text{Vol}(\Omega_i)$ gives the volume of the cell Ω_i. The shifting is needed so that the modified approximations of the neighbouring cells have the same cell average of the target cell. The next step is to replace the target cell approximation $\phi_{h,0}$ with a limited $\phi_{h,0}^{\text{lim}}$, which is a linear combination of the modified approximations $\tilde{p}_i$:

$$\phi_{h,0}^{\text{lim}}(\boldsymbol{x}) = \sum_i \omega_i \tilde{\phi}_{h,i}(\boldsymbol{x}) \tag{B.6}$$

where ω_i is a weighting coefficient associated with the smoothness of the local solution. To obtain ω_i, we begin by evaluating the smoothness indicator for each local polynomial approximation $\tilde{\phi}_{h,i}$:

$$\beta_i = \sum_{|l|=1}^{k} \big(\text{Vol}(\Omega_0)\big)^{2|l|-1} \int_{\Omega_0} \left(\frac{\partial^{l_1}}{\partial x_1^{l_1}} \cdots \frac{\partial^{l_d}}{\partial x_d^{l_d}} \tilde{\phi}_{h,i}(\boldsymbol{x}) \right)^2 d\boldsymbol{x} \tag{B.7}$$

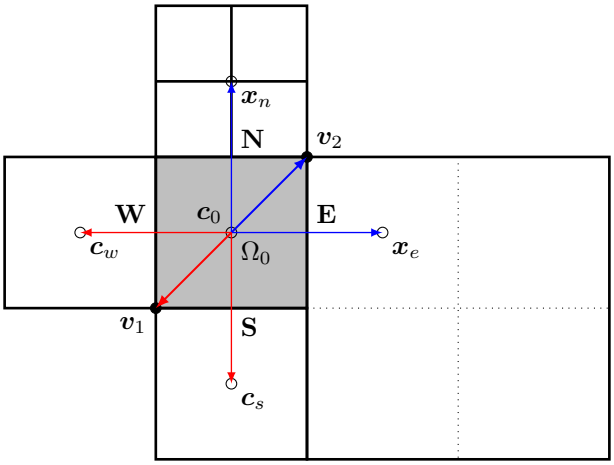


Figure B.1: The minmod shock detector acting on the vertex $\boldsymbol{v}_1$ and $\boldsymbol{v}_2$ of the target cell Ω_0 with the barycentre at $\boldsymbol{c}_0$. N, S, W and E respectively marks the northern, southern, western and eastern facet of the cell Ω_0. See text for detailed explanation.

where $l = (l_1, l_2)$ if the spatial dimension $d = 2$ and $l = (l_1, l_2, l_3)$ for $d = 3$ and $|l| = \sum_i l_i$. A high value of β_i signifies the possibility of non-smooth behaviour in the local solution $\tilde{\phi}_{h,i}$ and therefore $\tilde{\phi}_{h,i}$ is assigned a smaller weight. ω_i is related to the smoothness indicators β_i by the following relations:

$$\omega_i = \frac{\bar{\omega}_i}{\sum_{j=0}^{n} \bar{\omega}_j}, \quad \text{where } \bar{\omega}_j = \frac{\gamma_j}{(\epsilon + \beta_j)^2} \tag{B.8}$$

where $\epsilon = 10^{-6}$ is a small number to avoid division by zero. γ_j are a set of linear weights assigned to the cells under the constraint that $\sum_{j=0}^{n} \gamma_j = 1$. The modified local approximation will not alter the cell average of the target cell because all local approximations $\tilde{p}_i$ preserve target cell average. In our computation we use a uniform value of $\gamma_i = 0.001$ $(i = 1, 2, \ldots, N_{\text{nb}})$ for all the neighbouring cells as recommended in Zhu et al. (2013). The linear weight for the target cell Ω_0 is then $\gamma_0 = 1 - \sum_{j=1}^{N_{\text{nb}}} \gamma_i$. We remark that the γ values for the neighbouring cells should be chosen to be the smallest possible value to suppress oscillations. Although the choice in theory does not affect the accuracy of the overall scheme, values greater than necessary introduce excessive numerical diffusion and spurious interface movements especially in long term simulations.

To avoid introducing excessive numerical diffusion due to indiscriminate limiting on all cells, the limiter is only applied when the cell is identified as being affected by spurious oscillations (*i.e.* "troubled" cell). Numerous effective shock cell

indicators have been proposed for hyperbolic conservation laws based on minmod function (Cockburn and Shu, 1989), modal expansion (Karakus et al., 2016b) and superconvergence on the outflow cell boundary (Krivodonova et al., 2004). The reader is referred to Qiu and Shu (2005) for a detailed review. In this work we use a vertex-based minmod shock detector similar in spirit to Zhang and Yue (2019) and the process is illustrated in Figure B.1. We consider the process for two vertices $\boldsymbol{v}_1$ and $\boldsymbol{v}_2$ of the target cell Ω_0 with the barycentre $\boldsymbol{c}_0$. The process is similar for all other vertices. If any of the vertices of a cell has an activated shock detector, the cell will be marked as a "troubled" cell and its local solution will be modified by the WENO limiter.

In the case of vertex $\boldsymbol{v}_1$, we consider the neighbouring cells on the southern and western facet of Ω_0 with cell centres at $\boldsymbol{c}_s$ and $\boldsymbol{c}_w$ respectively. Let $\tilde{\phi}_{h,0}$, $\tilde{\phi}_{h,w}$ and $\tilde{\phi}_{h,s}$ be the cell average of ϕ_h in the target cell, neighbouring cell at western facet and neighbouring cell at southern facet. The difference between the vertex ϕ_h value and the cell average is:

$$\Delta_\phi \boldsymbol{v}_1 = \phi(\boldsymbol{v}) - \phi(\boldsymbol{c}_0) \tag{B.9}$$

This difference can also be approximated with an interpolation based on neighbouring cell averages, which we denote as $\tilde{\Delta}_\phi \boldsymbol{v}_1$. Using the fact that

$$\boldsymbol{v}_1 = \boldsymbol{c}_0 + \alpha_1(\boldsymbol{c}_s - \boldsymbol{c}_0) + \alpha_2(\boldsymbol{c}_w - \boldsymbol{c}_0) \tag{B.10}$$

We approximate the difference between the vertex value and cell average by combining the difference in cell average in each coordinate direction:

$$\tilde{\Delta}_\phi \boldsymbol{v}_1 = \alpha_1(\tilde{\phi}_{h,s} - \tilde{\phi}_{h,0}) + \alpha_2(\tilde{\phi}_{h,w} - \tilde{\phi}_{h,0}) \tag{B.11}$$

The vertex-cell average differences, $\Delta_\phi \boldsymbol{v}_1$ and $\tilde{\Delta}_\phi \boldsymbol{v}_1$ are then passed as arguments into the minmod function. The minmod function is defined as:

$$\text{minmod}(a, b) = \begin{cases} s \min(|a|, |b|) & \text{if} \quad s = \text{sgn}(a) = \text{sgn}(b) \\ 0 & \text{else} \end{cases} \tag{B.12}$$

If $\Delta_\phi \boldsymbol{v}_1 = \text{minmod}(\Delta_\phi \boldsymbol{v}_1, \nu \tilde{\Delta}_\phi \boldsymbol{v}_1)$, with the scaling coefficient $1 \leqslant \nu \leqslant 2$, *i.e.* the minmod function does not change the value of $\Delta_\phi \boldsymbol{v}_1$, the shock detector is activated.

In the case of vertex $\boldsymbol{v}_2$, the situation is complicated by the fact that the neighbouring cells are on different refinement levels. On the northern facet, the neighbouring cells are finer than the target cell Ω_0. In this case we compute the cell average of the parent cell of the four refined cells with the barycentre located at $\boldsymbol{x}_n$. On the

eastern facet, the neighbouring cell is coarser than Ω_0. In this case, the cell average is computed on the top-left subcell with barycentre at $\boldsymbol{x}_e$. Then the same procedure is for vertex $\boldsymbol{v}_1$ can be applied for shock detection with cell averages computed on the parent cell centred at $\boldsymbol{x}_n$ and the subcell centred at $\boldsymbol{x}_e$.

B.3 Efficient coupling scheme

To improve the efficiency in coupling the material description (facilitated by the level set solver for each material) and the flow solver, we design a multithreaded parallelization scheme to assemble the Stokes matrix so that the shared-memory multicore *WorkStream* scheme in the `deal.II` library can be fully exploited (Turcksin et al., 2016). We illustrate our parallelization strategy in Figure B.2 assuming two threads (1 and 2), working on two different cells with different sets of quadrature points. For each thread as it iterates through cells to assemble the Stokes system, a `StokesIterator`, which is a cell iterator associated with Stokes flow solver, and a `MaterialAccessor` object, with a pointer to the `MaterialStack` object, are both constructed. The `MaterialAccessor` shares the same set of quadrature points as the `StokesIterator`. At the quadrature points, the former queries the flow solver for the velocity $\boldsymbol{v}$ and the velocity gradient $\boldsymbol{L}$. Meanwhile the `MaterialAccessor` queries the level set solvers in the `MaterialStack` for level set values. If $\big(1 - h_\epsilon(\phi_i)\big)$ for material i is non-zero, (*i.e.* the quadrature point is in the material domain or in the transition zone), the material parameters associated with the level set will be retrieved from the `MaterialStack` and the effective viscosity will be computed according to the rheological model. The resultant effective viscosity will be into the local viscosity matrix. Eventually, the local viscosity matrix is assembled into the global viscosity matrix $\boldsymbol{A}$.

In this way it is not necessary for each thread to retain a copy of all material parameters. The material parameters will be read on-the-fly into the `MaterialAccessor` to reduce the memory footprint. Because the cells that are worked on by different threads likely has different states (in this case, the level set values and the kinematic quantities), a race condition will occur if one instance of the `MaterialStack` is solely responsible for computing material parameters. Our implementation circumvents this difficulty by distribute the task of compositing material parameters to the thread-local `MaterialAccessor`. In this way we avoid the explicitly locking the threads and offers better scalability on multithreaded matrix assembly processes.

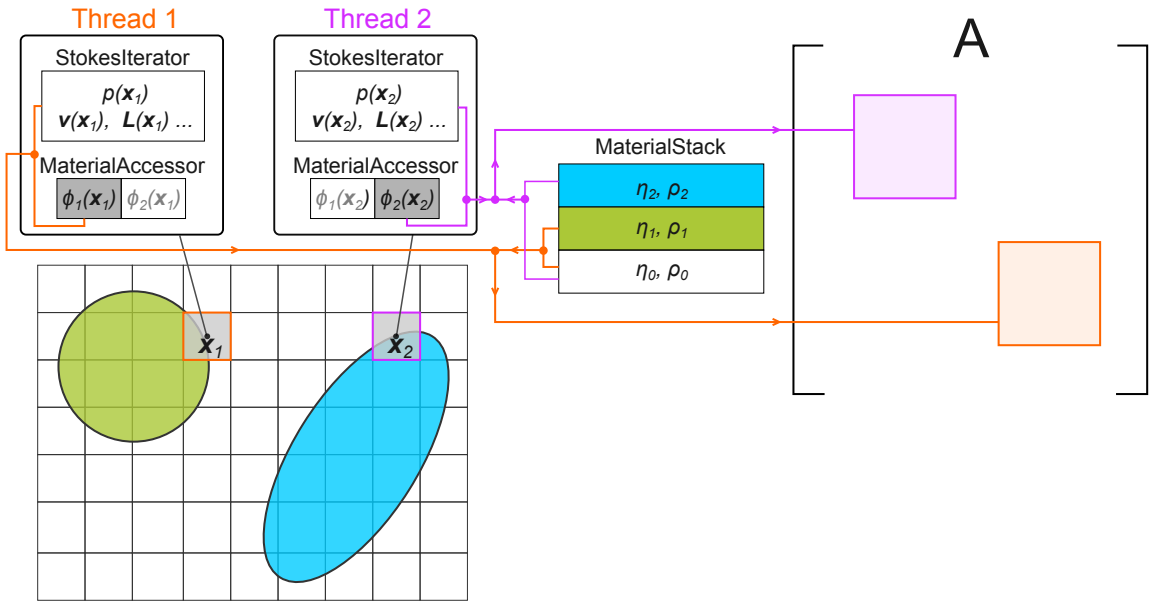


Figure B.2: Illustration of a multithreaded level set-flow solver coupling scheme. Thread 1 and Thread 2 have their thread-local copies of `StokesIterator` and `MaterialAccessor`. Both threads are working on different cells with different materials distribution. Each thread will retrieve level set values at quadrature points (We illustrate with single quadrature point per cell, but the concept is the same for multiple quadrature points.) Depending on the level set values, the threads will retrieve the corresponding material parameters from the `MaterialStack`, compute the correct local viscosity matrix and assemble into the global matrix $\boldsymbol{A}$. See text for detailed explanation.

Appendix C

Additional benchmark problems

C.1 The lid-driven cavity flow

In this numerical experiment we compute the classical flow benchmark for mono-phase fluid flow to verify that the flow solver by itself is stable and accurate for a wide range of flow conditions. The configuration of the model is shown in Figure C.1, where a square 2d box, whose length and height are both 1.00 m, is configured. The box is filled with a Newtonian fluid with viscosity η and density ρ. The left, right and bottom boundaries of the box are considered to be solid walls (*i.e.* $v_x = v_y = 0$), while the top boundary is an infinite lid moving strictly horizontally in the $+x$ direction at a speed of 1.00 m/s.

Instead of solving the Stokes problem, we do not omit the non-steady and inertial effects in the momentum equation and effectively solve the Navier-Stokes equations:

$$\begin{cases} \dfrac{\mathrm{D}\boldsymbol{v}}{\mathrm{D}t} = \dfrac{1}{Re}\nabla^2\boldsymbol{v} - \dfrac{1}{\rho}\boldsymbol{\nabla}p \\ \boldsymbol{\nabla}\cdot v = 0 \end{cases} \tag{C.1}$$

where $^{\mathrm{D}}/_{\mathrm{D}t}$ is the material derivative and $Re = {}^{\rho}/_{\eta}$ is the Reynold's number. In an Eulerian formulation the material derivative of the velocity $\mathrm{D}\boldsymbol{v}/\mathrm{D}t = \partial\boldsymbol{v}/\partial t + \boldsymbol{v}\cdot\boldsymbol{\nabla}\boldsymbol{v}$ expands to a non-steady term and non-linear convective term, the solution of which requires iterations. However, in a Lagrangian description the material derivative is simply a first-order derivative of time. This prompts us to use a dual representation: a stationary mesh for modelling the viscous dissipation of velocity and a set of Lagrangian particles for modelling the convective transport. The coupling between the

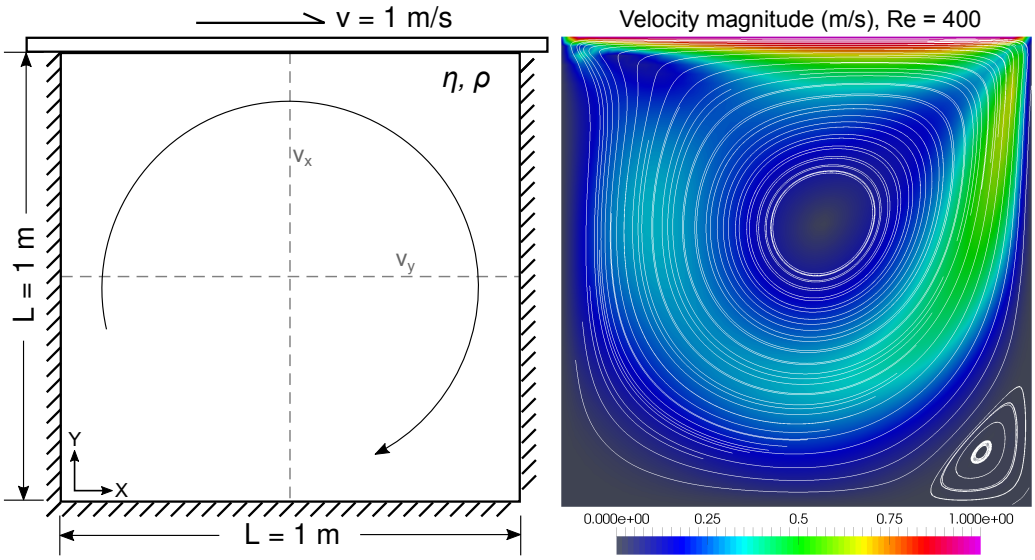


Figure C.1: Left: model setup for the lid-driven cavity flow. The dashed lines are profile lines for v_x (vertical) and v_y (horizontal) to be compared with the standard solution. Right: the steady-state velocity magnitude of the lid-driven cavity computed at Re = 400. The white lines are the streamlines of velocity field.

moving particles and the background mesh is realized by the particle-in-cell (PIC) method. We hereby briefly review the mechanism of PIC method for one incremental time step $[t^n, t^{n+1}]$. A schematic diagram of weighted least square (WLS)-PIC workflow is shown in Figure C.2.

At time t^n, the particle velocities $\boldsymbol{v}_p^n$ are projected component-wise onto the nodes of the Cartesian computational mesh by a WLS regression (Wallstedt and Guilkey, 2011) to obtain nodal velocity $\boldsymbol{v}_I^n$. The WLS regression seeks to minimize the weighted squared L_2-norm E_I around the node I for an arbitrary scalar field $f(\boldsymbol{x})$:

$$E_I(\boldsymbol{x}) = \sum_p W_I(\boldsymbol{\xi}_{pI}) \Big(f_p - \hat{f}_I(\boldsymbol{x}) \Big)^2 \tag{C.2}$$

where f_p is the value of f on the particle p and $\hat{f}_I(\boldsymbol{x})$ is the least square function at grid point I. $\boldsymbol{\xi}_{pI} = (\boldsymbol{x}_p - \boldsymbol{x}_I)/\Delta x$ is the normalized relative position of the particle with respect to the grid point located at $\boldsymbol{x}_I$ and grid spacing Δx. We assume the latter is a linear function $\hat{f}(\boldsymbol{x}) = c_0 + c_1 x + c_2 y + c_3 z$. The coefficient vector $\boldsymbol{c}$ can

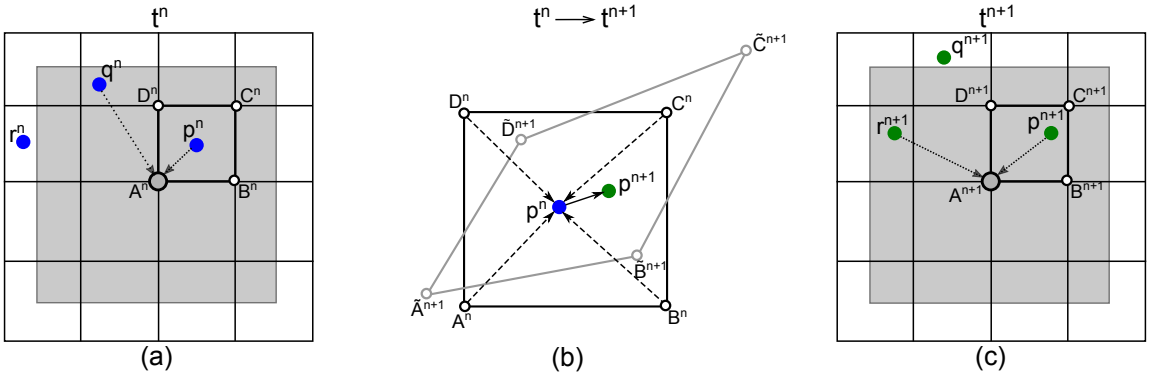


Figure C.2: General procedure of the WLS-PIC method. (a): At time t^n, the particle momentum is projected onto the computational grid by a WLS method. The grey area is the support domain of the weight function centred at grid point A^n. (b): the velocities are obtained on mesh points $A^nB^nC^nD^n$ by solving Equation (C.1) on the computational mesh. The grid velocities are interpolated onto the in-cell particle p^n and it is advected to location p^{n+1}. The cell is also deformed to the configuration $\tilde{A}^{n+1}\tilde{B}^{n+1}\tilde{C}^{n+1}\tilde{D}^{n+1}$. However, this configuration is never used and a new mesh in the same configuration as t^n is generated. (c): At time t^{n+1}, the cycle restarts by each newly generated mesh point, *e.g.* A^{n+1}, accepting information from particles within its weight function support domain.

be obtained by solving a 4×4 linear system at each grid point for 3d:

$$\begin{bmatrix} \sum_p W_{Ip} & \sum_p W_{Ip}x_p & \sum_p W_{Ip}y_p & \sum_p W_{Ip}z_p \\ \sum_p W_{Ip}x_p & \sum_p W_{Ip}x_p^2 & \sum_p W_{Ip}x_py_p & \sum_p W_{Ip}x_pz_p \\ \sum_p W_{Ip}y_p & \sum_p W_{Ip}x_py_p & \sum_p W_{Ip}y_p^2 & \sum_p W_{Ip}y_pz_p \\ \sum_p W_{Ip}z_p & \sum_p W_{Ip}z_px_p & \sum_p W_{Ip}z_py_p & \sum_p W_{Ip}z_p^2 \end{bmatrix} \begin{bmatrix} c_0 \\ c_1 \\ c_2 \\ c_3 \end{bmatrix} = \begin{bmatrix} \sum_p W_{Ip}f_p \\ \sum_p W_{Ip}f_px_p \\ \sum_p W_{Ip}f_py_p \\ \sum_p W_{Ip}f_pz_p \end{bmatrix} \tag{C.3}$$

where we have used the shorthand $W_{Ip} = W_I(\boldsymbol{\xi}_{pI})$. Many choices of the weight functions are available among literatures and they typically span the several grids so that sufficient information about the particle field can be represented by the grid points. In this benchmark we choose the cubic spline function, which in 1d is defined as:

$$W_i(\xi) = \begin{cases} \frac{1}{2}|\xi|^3 - |\xi|^2 + \frac{2}{3} & (|\xi| < 1) \\ -\frac{1}{6}|\xi|^3 + |\xi|^2 - 2|\xi| + \frac{4}{3} & (1 \leqslant |\xi| \leqslant 2) \\ 0 & (|\xi| > 2) \end{cases} \tag{C.4}$$

The weight function in higher spatial dimensions is the tensor product of the 1d weight function.

After particle velocities are projected onto the mesh, Equation (C.1) is solved with the finite element discretization to obtain the nodal velocities $\tilde{\boldsymbol{v}}_I^{n+1}$. The implicit Euler scheme is used for temporal integration. The updated nodal velocity differences $\tilde{\boldsymbol{v}}_I^{n+1} - \boldsymbol{v}_I^n$ will be interpolated back onto the particles through the finite element basis of the velocity approximation space. The technique of updating particle velocity by difference instead by velocity itself, also known as the fluid implicit particle (FLIP) method, significant reduces numerical diffusion by treating velocity as a Lagrangian quantity (Brackbill et al., 1988). However, the nodal velocity $\tilde{\boldsymbol{v}}^{n+1}$ is directly interpolated onto the particle when updating particle locations by the explicit Euler scheme to avoid particle collision and multistreaming. At this stage the update for both the mesh nodes and the particle velocities are completed, and we are ready to begin the computation for the next time step with the particle-to-grid velocity transfer.

On a side note, the background mesh, which is constructed under an updated Lagrangian formulation, is also deformed at t^{n+1}. However, this deformed configuration does not participate in further updates and is never explicitly constructed (Fu et al., 2017). At time step t^{n+1}, a new stationary mesh, with exactly the same configuration as t^n, is regenerated to accept particle-to-grid information transfer.

The benchmark is computed on a 25×25 uniform Cartesian mesh with 25 particles per cell. Particles will be reseeded if insufficient particles are present in the support of the weight function, whose velocities $\boldsymbol{v}_p$ are directly interpolated from the mesh nodes. Two benchmarks are computed at Re = 100 and Re = 1000. In Figure C.3, the x-velocity along a vertical line and the y-velocity along a horizontal line, both drawn through the origin, are compared with the standard results obtained by Ghia et al. (1982) using a streamline-vorticity formulation.

Our results in general show good agreement with the standard results. At low Reynold's number, the match between our results and standard results is almost exact. At high Reynold's number, our numerical formulation shows more pronounced numerical diffusion from the standard solution. The added diffusion is likely to be originated from the fact that (a) the linear least square function discards higher order information and (b) the direct interpolation of the grid velocity. However, the numerical dissipation is in most applications acceptable because the long-term geological flow almost never reaches a high Reynold's number.

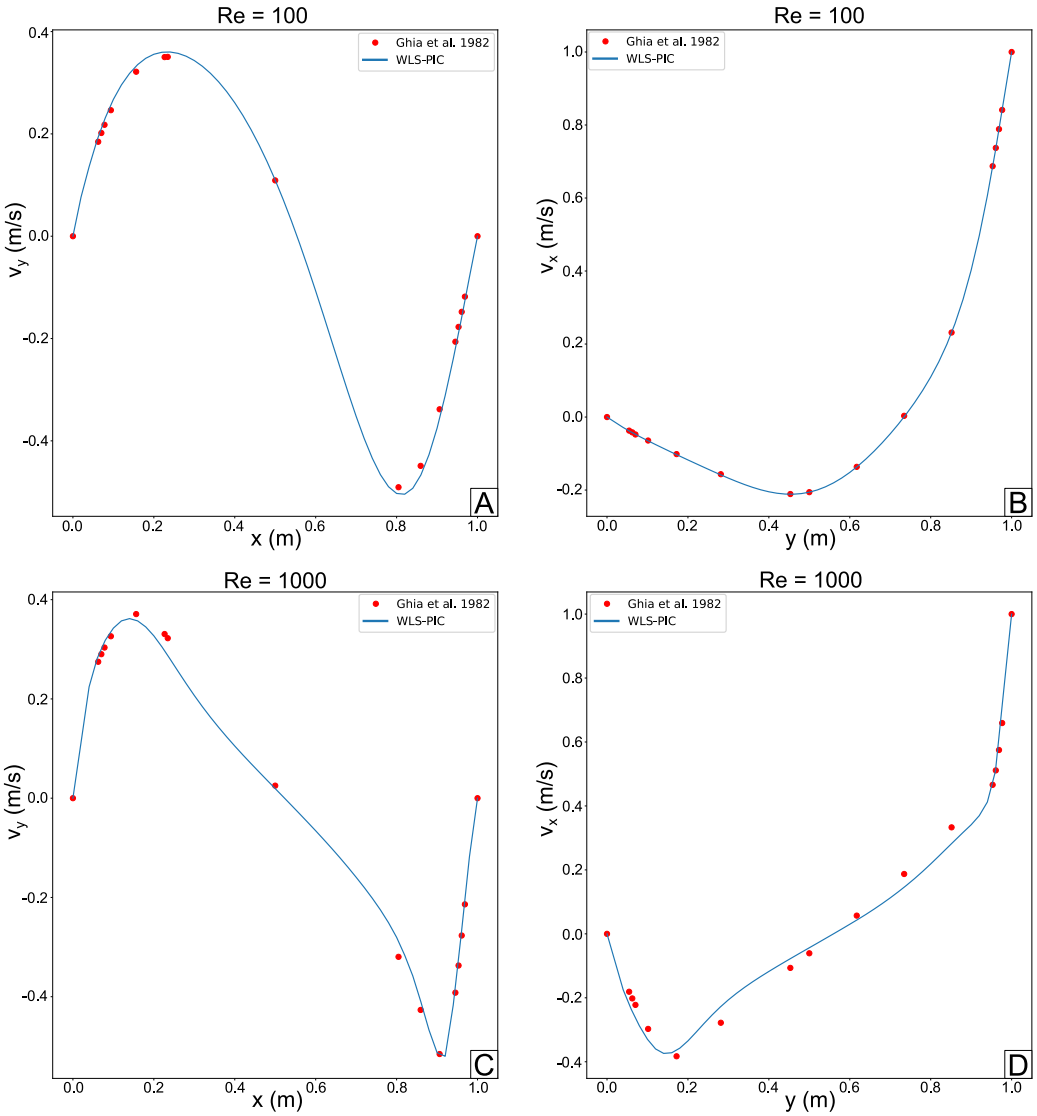


Figure C.3: The results of lid-driven cavity flow benchmark for Re = 100 (A and B) and Re = 1000 (C and D).

C.2 Zalesak's disk

In this numerical experiment we compute the passive rigid-body rotation of a slotted disk in a constant velocity field (Zalesak, 1979). This benchmark is computed in many studies related to the level set method to test mass conservation and convergence properties (*e.g.* Cho et al., 2011; Enright et al., 2002).

$$\begin{cases} v_x = \dfrac{\pi}{314} y \\ v_y = -\dfrac{\pi}{314} x \end{cases} \tag{C.5}$$

The modelling domain is a square 2d box of dimensions $[-50, 50]^2$. The diameter of the disk is 30 and is initially positioned at $(x, y) = (0, 30)$. A rectangular slot of dimension 5×25 is cut vertically through the centre of the disk. The coarsest computational mesh is 8×8 and is recursively refined near the interface up to an equivalent grid density $N_{\max} \times N_{\max}$ for better resolution while saving computational expenses away from the interface. In our benchmark $N_{\max}$ ranges from 64 to 1024. Both the model setup and the grid configuration of $N_{\max} = 256$ are shown in Figure C.4. The benchmark is computed for one full revolution (up to $t = 628$). Legendre polynomials of degree no more than one is used as the element basis function. In order to quantify the mass conservation property of our level set solver, we compute the mass error E_m by rewriting the volume integration into a sum over the smoothed Heaviside function values at quadrature points:

$$E_m = \frac{1}{V_0} \sum_e \int_{\Omega^e} \left(1 - h_\epsilon(\phi)\right) \, d\boldsymbol{x} \approx \frac{1}{V_0} \sum_e \sum_q w_q \left(1 - h_\epsilon(\phi(\boldsymbol{\xi}_q))\right) J_e(\boldsymbol{\xi}_q) \tag{C.6}$$

where V_0 is the initial volume of the disk, $(\boldsymbol{\xi}_q, w_q)$ are the pair of location vector and weight for the q-th quadrature point in the reference elements and J_e is the Jacobian from the reference element to the element e. We also compute the L_1-error to quantify the error due to solving the transport of the interface on the Eulerian mesh,

$$E_1 = \sum_I \frac{|\hat{\phi}_I(t) - \hat{\phi}_I^0|}{N_{\max}^2} \tag{C.7}$$

where $\phi_I^0 = \phi_I(t)\big|_{t=0}$. In order to remove the possible mismatch of mesh configuration caused by the adaptive mesh refinement, the E_1 errors are computed on an $N_{\max} \times N_{\max}$ uniform mesh. The geometry of the disk interface before and after one revolution is shown in Figure C.5.

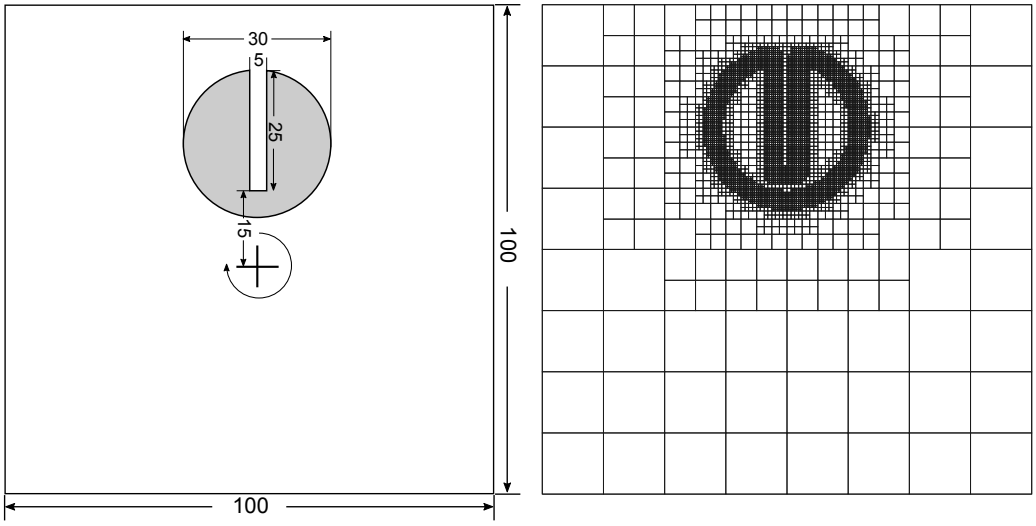


Figure C.4: Left: model setup for the Zalesak's disk benchmark. Right: The computational mesh of the Zalesak's disk benchmark. The mesh is selectively refined at the disk interface. The finest mesh density has an equivalent mesh density $N_{\max} = 256$.

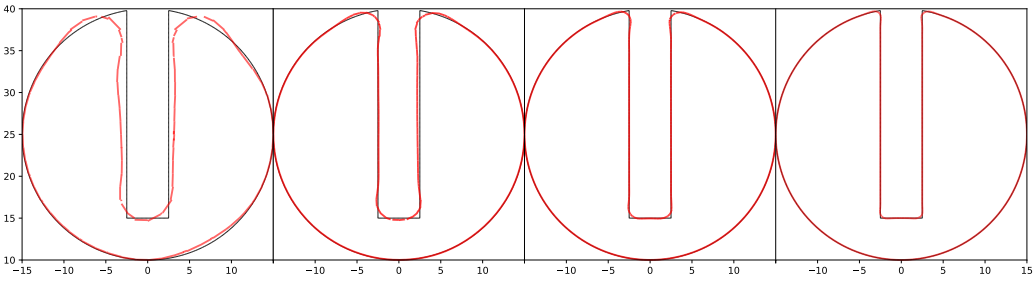


Figure C.5: The interface trace of the Zalesak's disk before (dashed line) and after (solid line) one revolution. From left to right, $N_{\max} = 64, 128, 256$ and 512.

This study				Particle level set		
$N_{\max}$	N_{cell}	E_1	E_m	Mesh	E_1	E_m
64	2604	8.15×10^{-2}	-6.90×10^{-2}	50×50	5.90×10^{-1}	1.49×10^{-1}
128	6438	3.06×10^{-2}	8.70×10^{-3}	100×100	7.00×10^{-2}	3.10×10^{-3}
256	14799	1.38×10^{-2}	-1.50×10^{-3}	200×200	2.00×10^{-2}	2.00×10^{-3}
512	30711	7.54×10^{-3}	-1.20×10^{-3}		N/A	

Table C.1: Errors of the Zalesak's disk benchmark with increasing grid densities. E_1 is the L_1 error norm. E_m is the mass error. In our study, E_1 is computed on a uniform mesh of $N_{\max} \times N_{\max}$ while E_m is computed on an adaptively refined mesh where the finest refinement level has a density of $N_{\max} \times N_{\max}$. N_{cell} is the number of finite element cells of the adaptively refined mesh. The particle level set results are obtained from (Enright et al., 2002).

The L_1 and mass errors are listed in Table C.1. The results demonstrate that our formulation converges almost linearly as we refine the grid density. The mass error E_m is also significantly reduced as finer level of adaptive mesh refinement (AMR) is used near the interface, albeit the rate of reduction does not follow a linear trend due to the competition of mass correction at areas of negative curvature versus positive curvatures.

Appendix D

Details of deformation analysis of the Swayze greenstone belt and regional implications

In this section we present systematic description of observational data for all four generations of structures (G_1–G_4) as observed in the central and southern Swayze greenstone belt (SGB), with an emphasis on deformation generations G_1, G_3 and G_4 as the G_2 deformation has been discussed in detail in Section 3.3. We also report our zircon U-Pb geochronology results, which provide constraints on the ages of deformation generations. Finally, we discuss the regional implications of our deformation analysis for the Ridout deformation zone (RDZ) in the SGB, as well as its relationship with the Cadillac-Larder Lake deformation zone (CLLDZ) in the Abitibi greenstone belt to the east of our study area.

D.1 Details of deformation analysis

D.1.1 Deformation G_1

G_1 structures are recognized in the tonalite-trondhjemite-granodiorite (TTG) infrastructure. Overprinting relationship between G_1 and G_2 structures can be identified in the orthogneiss unit of the Kenogamissi batholith, where the S_1 foliation is defined by the gneissosity of alternating dioritic and tonalitic compositions. The orientations of the foliation are NE-SW with a highly variable dip angle (Figure 3.2B), suggesting

overprinting by a regional folding event. The regional folding of S_1 is also mirrored on the outcrop scale as tight to isoclinal upright folds with subhorizontal NE-SW-trending fold axis. The NE-SW orientation of the steeply-dipping axial plane in the orthogneiss is correlated to the S_2 foliation in the supracrustal volcanic rocks to the south, supporting the interpretation that the folding affecting the orthogneiss is a G_2 event. Upon unfolding, the pre-folding orientation of the S_1 is likely to be subhorizontal.

D.1.2 Deformation G_2

The geometrical and structural patterns of the G_2 deformation as well as its significance for the tectonic evolution of the SGB has been discussed in detail in Chapter 3. The reader is referred to Section 3.3 for an in-depth description of the structural pattern of G_2. For the sake of completeness, we hereby provide a brief summary for the main features of the G_2 deformation.

The G_2 deformation is characterized by the S_2 foliation, L_2 mineral lineation or stretching lineation, as well as F_2 regional folding. The moderately- to steeply-dipping S_2 is the pervasive regional foliation in the SGB whose orientation is subparallel to the granitoid-greenstone boundary. The L_2 lineation is defined by the alignment of acicular minerals in meta-igneous rocks or stretched clasts in volcaniclastic or sedimentary rocks. The orientation of L_2 is moderately- to steeply-plunging (Figures 3.4 and 3.5). The F_2 folds are upright tight to isoclinal folds, which affect both the granitoid infrastructure and supracrustal units on both outcrop- and regional-scale.

The G_2 deformation is strongly localized in discrete high strain zones at the granitoid-greenstone contacts as well as within the greenstone belts with a strong flattening type of strain. The kinematics associated with these high strain zones have a predominantly vertical granitoid-up/greenstone-down component. In the southern domain of the study area, the L_2 shows a reversal in plunge direction from the northern contact (*i.e.* the contact between the Kenogamissi batholith and the SGB) to the southern contact (*i.e.* the contact between the Ramsey-Algoma granitoid complex and the SGB) (Figure 3.4B), consistent with a regional dextral shearing associated with the granitoid-up/greenstone-down kinematics. In the northern domain, L_2 generally plunges to the west and shows a westward steepening trend (Figure 3.5F,G).

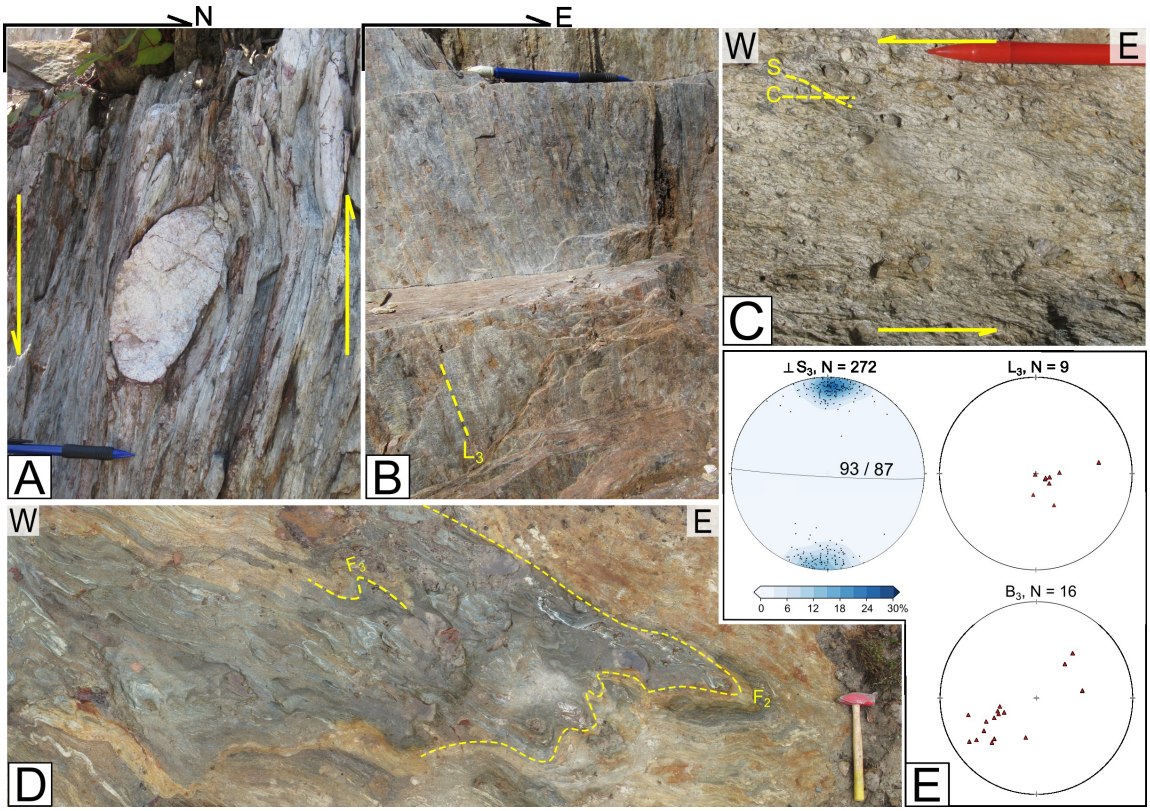


Figure D.1: Field photos and measurements of the G_3 deformations. A: A clast in the Timiskaming-type conglomerate shows a north-side-up sense of shear. B: East-plunging L_3 lineation in the Timiskaming-type conglomerate. C: S-C fabric in a quartz feldspar porphyry in the RDZ display sinistral sense of shear on the horizontal surface. D: A felsic dyke in the mafic volcanic rocks folded by a tight F_2 fold which is in turn overprinted by F_3 *s*-fold on both limbs. E: Stereographic projections of the poles to S_3 foliation ($\perp S_3$), the L_3 lineations and the F_3 fold axes.

D.1.3 Deformation G_3

G_3 deformation is associated with the subvertical S_3 foliation, the L_3 mineral stretching lineation and the F_3 shear-related folding. G_3 is strongly localized in the RDZ as well as in several minor high strain zones in the southern SGB area which may constitute splay high strain zones of the RDZ. Therefore, G_3 is postulated to be a shear reactivation event affecting the southern SGB.

The E-W-trending steeply-dipping S_3 foliation is characterized by intense shear fabric parallel to the RDZ as well as other G_2-overprinted high strain zones. The G_2-G_3 overprinting relationship is best preserved in the Timiskaming-type sandstone where the S_3 spaced cleavage overprints the bedding-parallel S_2 foliation defined by the alignment of quartz aggregates, with S_3 showing a clockwise relationship with respect to S_2 (Figure 3.3C). With higher shear strain, the differentiation between S_2 and S_3 is difficult and therefore the foliation in the G_3-affected high strain zones is likely a composite S_2/S_3 fabric.

The kinematics of the G_3 deformation is characterized by an oblique sinistral (Figure D.1A) and north-side-up shearing (Figure D.1C), The L_3 lineation is defined by the preferred orientation of chlorite and sericite in the highly deformed Timiskaming-type sandstones and conglomerates (Figure D.1B). L_3 plunges steeply to east (Figure D.1E), which is consistent with the oblique sinistral and north-side-up kinematics. The F_3 folds possess an *s*-asymmetry on the subhorizontal surface. Measurements of the F_3 fold hinges on one outcrop unaffected by later folding events shows a predominantly southwesterly plunge direction (Figure D.1E). This supports the interpretation that F_3 are shear-related drag folds caused by the G_3 oblique shearing.

D.1.4 Deformation G_4

The G_4 deformation is characterized by a dextral strike-slip shearing demonstrated by multiple shear sense indicators, *e.g.* back-rotated boudins of quartz veins (Figure D.2C), sigmoidal clasts in conglomerates and S-C fabric, consistently showing a dextral sense of shear. Also associated with G_4 deformation are the F_4 asymmetric folds with *z*-asymmetry (Figure D.2B), commonly associated with the dextral kinematic indicators, and are therefore interpreted as dextral drag folds. The F_4 fold axes are subvertical (Figure D.2D), implying that the G_4 shearing is predominantly strike-slip. The S_4 is a NE-SW-striking crenulation cleavage defined by microscopic F_4 folding of the platy minerals previously aligned as S_2 or S_3 composite cleavage

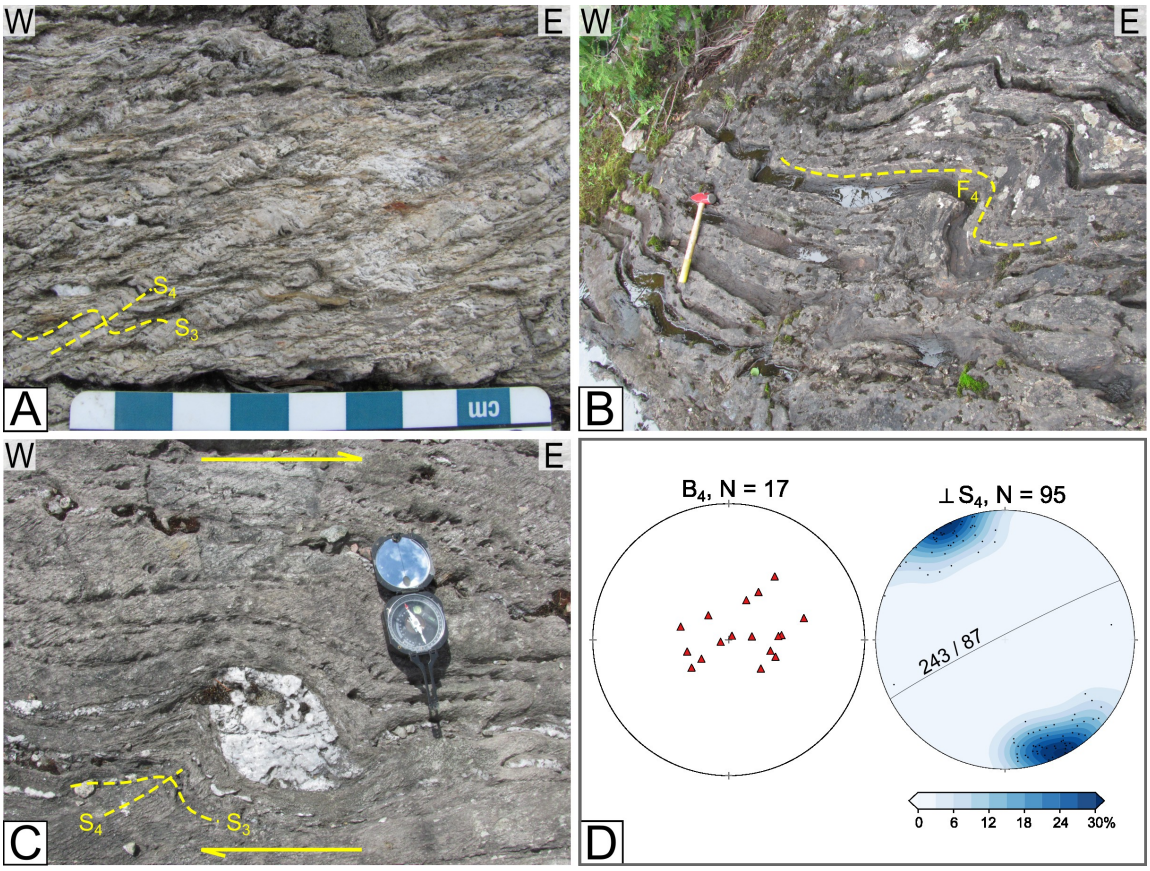


Figure D.2: Field photos and measurements of the G_4 structures. A: S_4 NE-striking S_4 crenulation cleavage in the felsic crystal tuff overprinting the S_3. B: F_4 z-fold in Timiskaming-type metasandstone. C: Back-rotated quartz vein boudin and the S_3/S_4 overprinting relationship in the felsic metavolcanic rocks, both consistent with a dextral sense of shear. D: Stereographic projections of F_4 fold axes (B_4) and poles to S_4 ($\perp S_4$).

(Figure D.2A, Figure D.2D). The G_4 deformation overprints all previous ductile structures and is only localized in pre-existing weak planes such as high strain zones and lithological boundaries.

D.2 Timing of deformation

To constrain the timing of the deformation phases, samples demonstrating relative timing relationships with respect to deformation generations were collected and dated by zircon U-Pb geochronology. The zircons are analysed with isotope dilution-thermal ionization mass spectrometry (ID-TIMS) or laser ablation-inductively coupled plasma-mass spectrometry (LA-ICP-MS) at the Jack Satterly Geochronology Lab at the University of Toronto. The analytical datasets for all samples are presented in Appendix E. The sampling locations are shown in Figure 3.1C.

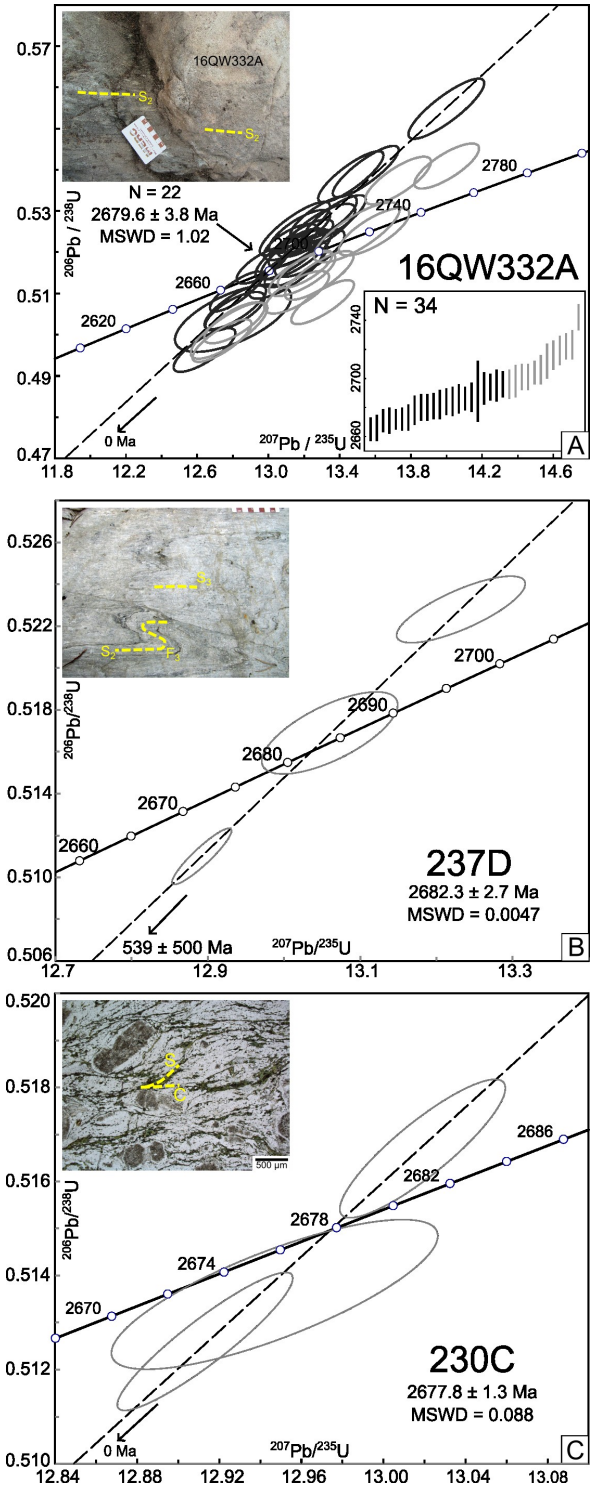
Sample 16QW332A: a *syn*-G_2 felsic dyke

To constrain the timing of the G_2 deformation at the southern contact between the SGB and the Ramsey-Algoma granitoid complex, a felsic dyke is sampled for zircon U-Pb geochronology. The felsic dyke cross-cuts the S_2 foliation and itself bears a weak S_2 foliation (Figure D.3A), indicating the intrusion age of the dyke is *syn*-G_2. A total of 36 analyses were conducted on 36 grains with LA-ICP-MS. The youngest population of 22 grains yields an average $^{207}Pb/^{206}Pb$ age of 2679.6 ± 3.8 Ma, interpreted as the emplacement age of the dyke and hence represents the approximate age of the G_2 deformation at the southern SGB contact with the Ramsey-Algoma granitoid complex.

Sample 237D: a *pre*-G_2 or early *syn*-G_2 felsic dyke

Sample 237D was taken at the northern contact of the SGB with the Kenogamissi batholith. The felsic dyke is subparallel to the local S_2 foliation and itself bears a S_2 foliation. The local S_2 foliation is folded by the F_3 *s*-folds (Figure D.3B). A

Figure D.3 ***(following page)*:** Concordia diagrams of the samples for zircon U-Pb geochronology. For sample 16QW332A the Pb-Pb age distribution for all analysed zircon grains is also shown at the bottom right. The photo in each concordia diagram shows the relationship of each sample with respect to the deformation generations. The sampling locations are labelled in Figure 3.1.


16QW332A
N = 22
2679.6 ± 3.8 Ma
MSWD = 1.02
16QW332A
N = 34
A
237D
2682.3 ± 2.7 Ma
MSWD = 0.0047
539 ± 500 Ma
B
230C
2677.8 ± 1.3 Ma
MSWD = 0.088
0 Ma
C
$^{206}Pb / ^{238}U$
$^{207}Pb / ^{235}U$
$^{206}Pb/^{238}U$
$^{207}Pb/^{235}U$

crenulation cleavage S_3 axial planar to F_3 is also present. This field relationship suggests that the intrusion of the felsic dyke is either *pre*-G_2 or early *syn*-G_2. Three zircons were analysed by ID-TIMS. The data points form a discordia line with the lower intercept at 539 ± 500 Ma and the upper intercept at 2682.3 ± 2.7 Ma. The latter is interpreted as the intrusion age. This age constrains the age of the G_2 and G_3 deformations at the contact between the SGB and the Neville pluton to be no earlier than *ca.* 2680 Ma.

Sample 230C: a *pre*-G_4 felsic dyke

The 230C is a quartz feldspar porphyry dyke intruding into mafic metavolcanic rocks in the northern domain of the study area. The dyke intrudes subparallel to the local S_2 foliation and records a dextral S-C fabric (Figure D.3C), interpreted to the result of G_4 dextral shearing. Therefore, the intrusion of the dyke is likely *pre*-G_4. Three grains were analysed with ID-TIMS and yielded an average $^{207}Pb/^{206}Pb$ age of 2677.8 ± 1.3 Ma, which is interpreted as the maximum age of G_4 dextral movement.

D.3 Regional considerations

Our sequence of deformation events is compatible with previous structural studies in the SGB in general. Heather (2001) identifies an analogous sequence of deformation beginning with the D_1 deformation, characterized by a S_1 gneissosity or a compositional layering in the synvolcanic intrusion. The D_1 is overprinted by the D_2 regional deformation characterized by thick-skinned regional folding F_2 and a moderately- to steeply-plunging stretching L_2 lineation. The D_1-D_2 structural pattern of Heather (2001) is in agreement with our G_1 and G_2 deformation. Heather (2001) also recognizes RDZ as a high strain zone initiated during D_2 with first sinistral and then dextral shearing. Smith (2016) identifies an initial oblique north-side-up and sinistral shearing followed by dextral transcurrent movement in the RDZ. In both cases, the deformation history agrees with the oblique sinistral G_3 and strike-slip dextral G_4 deformation identified in this study.

Our understanding of the deformation history of the RDZ and their timing allows us to compare with the structural studies of the CLLDZ to discuss the possible correlation between the two deformation zones. Results of numerous structural studies at various segments of the CLLDZ can be summarized into the following sequence of events (*e.g.* Bedeaux et al., 2017; Zhang et al., 2014; Wilkinson et al., 1999; Lafrance, 2015):

D_1 N-S shortening and regional upright folding of the supracrustal stratigraphy,

D_2 NE-SW shortening leading to *s*-folds, and finally

D_3 regional dextral strike-slip shearing.

Our analysis shows that our $G_{2\text{-}4}$ deformations in the southern SGB have an almost one-to-one correlation in terms of structural pattern and kinematics with those of the $D_{1\text{-}3}$ deformations in the Abitibi greenstone belt around the CLLDZ. In terms of timing, our G_2 deformation in the SGB is also broadly contemporaneous with the ages reported for the post-Timiskaming D_1 in multiple segments of the CLLDZ. In the Matachewan area, the first phase of post-Timiskaming ductile deformation represented by regional shortening and folding is contemporaneous with the syenite intrusion dated at 2676.3 ± 1.4 Ma (Zhang et al., 2014). In the Cheminis gold deposit area west of the town of Kirkland Lake, Lafrance (2015) constrains the age of D_1 regional folding to postdate the 2674 Ma–2670 Ma Timiskaming-type assemblage and predate the onset of *ca.* 2672 Ma–*ca.* 2665 Ma D_2 deformation. The SGB equivalence of this regional folding event, *i.e.* the G_2 deformation, is constrained at around 2680 Ma and is therefore slightly older but broadly synchronous with D_1 in the CLLDZ.

On the other hand, there is discrepancy in kinematics concerning the G_3 sinistral shearing in the RDZ and the comparable D_2 *s*-folding event in the CLLDZ. In the Larder Lake area, the D_2 deformation overprinting the regional folding is characterized by a south-side-up kinematics and a southward younging of the Timiskaming Group turbiditic sandstone (Lafrance, 2015). Furthermore, in the Matachewan segment of the CLLDZ, D_1 and D_2 are respectively characterized by top-to-NE and top-to-NW thrusting (Zhang et al., 2014). This is incompatible with the north-side-up shearing associated with G_3 deformation and a northward younging direction of the Timiskaming-type assemblage in the RDZ.

From the above discussion we may conclude, based on the comparable deformation style and the timing of deformation events, that the RDZ and the CLLDZ probably developed a similar terrane-scale tectonic framework. However, the discrepancy between them concerning the G_3(RDZ)/D_2(CLLDZ) kinematics and their relative position in the regional stratigraphy with respect to the Timiskaming-type metasedimentary assemblage suggest that they may have evolved, at least in their early history, as independent entities rather than as one continuous and coherent deformation corridor. With the insights from the numerical model, both deformation zones may have initially developed close to the opposing boundaries of Timiskaming-type basin (Figure 3.8) with opposite vertical kinematics under the same generation

of regional deformation. Later deformation may have been preferentially localized in one of the deformation zones and hence only preserve a one-sided younging direction of the Timiskaming-type basin. A relationship similar to that between the RDZ and CLLDZ is also reported in the Neoarchean Yilgarn Craton (Zibra et al., 2014), indicating that it may be a common pattern for the Neoarchean terranes that even in adjacent greenstone belts, one regional deformation event may partition into different deformation styles in different greenstone belts and evolve in a temporally transgressional manner.

	Ridout deformation zone, Swayze greenstone belt			*Cadillac-Larder Lake deformation zone, Abitibi greenstone belt*	
	This study	Smith (2016)	Heather (2001)	Zhang et al. (2014)	Wilkinson et al. (1999)
G_1	S_1 gneissosity in the TTG gneisses	Not observed	E-W to NW-SE S_1 cleavage in metavolcanics, S_1 gneissosity in synvolcanic pluton, intrafolial isoclinal F_1. Unknown regional significance.	Not reported	D_1 *pre*-Timiskaming E-W trending upright folding
G_2	Granitoid-up greenstone-down kinematics with dextral shearing, boundary-parallel S_2, moderately- to steeply-plunging L_2 lineation, upright tight to isoclinal F_2.	Sinistral and north-side-up shearing in RDZ, L_2 steeply-dipping stretching lineation, E-W steeply-dipping S_2, sinistral drag folds.	Regional upright folding, E-W S_2 cleavage axial planar to doubly-plunging F_2. Followed by first sinistral and then dextral shearing in RDZ.	NE-SW shortening $D_{1a,1b}$, top-to-NE thrusting, NW-SE upright isoclinal fold F_{1a}, NW-SE penetrative S_{1b}.	D_2 N-S shortening, dextral on NE segments, sinistral on SW segments, S_2 parallel to CLLDZ
G_3	Oblique sinistral and north-side-up shearing, east-plunging stretching L_3, F_3 with *s*-asymmetry.	S_3 WNW-striking foliation, L_3 steeply-plunging mineral lineation, F_3 *s*-shaped folds.	Sinistral shearing in NE-striking high strain zones, NE-striking steeply-dipping S_3	Not reported	Not reported
G_4	Dextral strike-slip shearing, F_4 *z*-shaped drag folds, S_4 NE-SW crenulation cleavage.	Dextral shearing, F_4 *z*-shaped folding, S_4 NE-SW crenulation cleavage.	NE-striking crenulation cleavage S_4, dextral crenulation fold F_4	D_2 NW-SE shortening, top-to-NW oblique thrusting with dextral shearing NE to E-W-trending S_2, F_2 with *z*-asymmetry	D_3 NW-SE shortening, dextral reactivation, subvertical NE-striking S_3

Table D.1: Deformation history obtained by multiple studies in the SGB (with an emphasis on the RDZ). The deformation history of CLLDZ, Abitibi greenstone belt is also summarized for comparison.

Appendix E

Geochronology dataset for the Swayze Greenstone Belt

Sample 16QW332A: *UTM 403234* m*E, 5272034* m*N, Zone 17T, NAD83*

No.	Th/U	$\frac{^{207}Pb}{^{235}U}$	2σ	$\frac{^{206}Pb}{^{238}U}$	2σ	Err. corr.	$\frac{^{206}Pb}{^{238}U}$ Age (Ma)	2σ	$\frac{^{207}Pb}{^{235}U}$ Age (Ma)	2σ	$\frac{^{207}Pb}{^{206}U}$ Age (Ma)	2σ	Disc. (%)
16QW332-29*	0.61	11.155	0.12	0.459	0.004	0.8121	2618	10	2536	10	2435	18	8
16QW332-24k	0.37	13.463	0.121	0.5383	0.0041	0.8433	2665	8	2713	8	2777	17	-5
16QW332-27k	0.63	13.149	0.13	0.5257	0.0043	0.8362	2666	9	2690	9	2723	18	-3
16QW332-20	0.89	13.175	0.114	0.525	0.0035	0.7703	2671	9	2692	8	2720	15	-2
16QW332-26	0.79	12.966	0.096	0.5168	0.0029	0.7495	2671	8	2677	7	2686	12	-1
16QW332-5	0.45	12.82	0.098	0.5105	0.0032	0.8189	2672	7	2667	7	2659	14	1
16QW332-7	0.79	13.547	0.122	0.5396	0.0041	0.8486	2672	8	2719	9	2782	17	-5
16QW332-21	0.75	13.125	0.1	0.5225	0.0029	0.7234	2673	9	2689	7	2710	12	-2
16QW332-13k	0.34	13.309	0.124	0.5282	0.0037	0.7445	2678	10	2702	9	2734	15	-3
16QW332-12	0.63	13.999	0.141	0.5548	0.0048	0.8524	2680	9	2750	10	2845	20	-8
16QW332-25	0.91	13.208	0.102	0.5234	0.003	0.7409	2680	9	2695	7	2714	13	-2
16QW332-22	0.83	13.156	0.102	0.521	0.003	0.7497	2681	9	2691	7	2704	13	-1
16QW332-8	0.87	13.123	0.129	0.5196	0.0041	0.7913	2682	10	2689	9	2698	17	-1
16QW332-11	0.98	13.296	0.127	0.5258	0.0039	0.7671	2684	10	2701	9	2724	16	-2
16QW332-31	0.87	12.814	0.114	0.5066	0.0035	0.7822	2684	9	2666	8	2642	15	2
16QW332-10	1.08	13.155	0.13	0.5195	0.004	0.7743	2686	10	2691	9	2697	17	0
16QW332-30	0.87	13.373	0.115	0.5282	0.0037	0.8068	2686	8	2706	8	2734	15	-2
16QW332-2	0.81	12.812	0.11	0.5057	0.0031	0.7196	2687	10	2666	8	2638	13	2
16QW332-3	0.16	12.802	0.215	0.504	0.0054	0.6335	2691	21	2665	16	2631	23	3
16QW332-33	0.84	13.1	0.137	0.5151	0.0042	0.7844	2693	11	2687	10	2679	18	1
16QW332-34	0.8	13.155	0.116	0.517	0.0036	0.7845	2694	9	2691	8	2686	15	0
16QW332-17	0.99	13.232	0.129	0.5198	0.0038	0.7444	2695	11	2696	9	2698	16	0
16QW332-28	1.05	12.809	0.112	0.5029	0.0033	0.7446	2696	10	2666	8	2626	14	3
16QW332-36k	0.4	12.641	0.115	0.4963	0.0035	0.7846	2696	9	2653	9	2598	15	4
16QW332-18*	0.22	7.927	0.419	0.3108	0.0134	0.8163	2698	50	2223	47	1745	66	40
16QW332-32	0.74	12.779	0.142	0.501	0.0045	0.8003	2698	11	2663	10	2618	19	4
16QW332-1	0.49	12.739	0.109	0.4986	0.0034	0.7921	2701	9	2661	8	2608	15	4
16QW332-14	0.86	13.728	0.122	0.5374	0.0038	0.7867	2701	9	2731	8	2772	16	-3
16QW332-23k	0.33	13.205	0.101	0.5159	0.003	0.7588	2704	8	2694	7	2682	13	1
16QW332-19	0.6	13.189	0.123	0.5147	0.0035	0.7329	2706	10	2693	9	2677	15	1
16QW332-9	0.86	13.497	0.159	0.5248	0.0048	0.7832	2712	12	2715	11	2719	20	0
16QW332-15k	0.44	13.16	0.119	0.5103	0.0034	0.7418	2716	10	2691	8	2658	15	3
16QW332-4	0.71	13.286	0.127	0.5144	0.0039	0.7953	2719	10	2700	9	2676	17	2
16QW332-6	0.83	14.002	0.12	0.5409	0.0036	0.7788	2722	9	2750	8	2787	15	-3
16QW332-16k	0.71	13.593	0.131	0.525	0.0038	0.7589	2723	10	2722	9	2720	16	0
16QW332-35	0.42	13.304	0.116	0.5079	0.0035	0.7976	2742	9	2701	8	2647	15	4

Sample 237D: *UTM 428438*m*E, 5270969*m*N, Zone 17T, NAD83*

No.	Th/U	$\frac{^{207}Pb}{^{235}U}$	2σ	$\frac{^{206}Pb}{^{238}U}$	2σ	Err. Corr.	$\frac{^{207}Pb}{^{206}U}$	2σ	$\frac{^{206}Pb}{^{238}U}$ Age (Ma)	2σ	$\frac{^{207}Pb}{^{235}U}$ Age (Ma)	2σ	$\frac{^{207}Pb}{^{206}U}$ Age (Ma)	2σ	Disc. (%)
z1	0.36	13.232	0.069	0.5228	0.0013	0.773	0.18357	0.00067	2710.9	5.5	2696.3	4.9	2685.4	6	-1.2
z2	0.29	13.06	0.073	0.5169	0.0016	0.685	0.18324	0.00076	2686	6.8	2684	5.3	2682.4	6.9	-0.2
z3	0.15	12.892	0.032	0.511	0.0011	0.916	0.18298	0.00019	2660.9	4.5	2671.8	2.4	2680.1	1.7	0.9

Sample 230C: *UTM 418678*m*E, 5297545*m*N, Zone 17T, NAD83*

No.	Th/U	$\frac{^{207}Pb}{^{235}U}$	2σ	$\frac{^{206}Pb}{^{238}U}$	2σ	Err. Corr.	$\frac{^{207}Pb}{^{206}U}$	2σ	$\frac{^{206}Pb}{^{238}U}$ Age(Ma)	2σ	$\frac{^{207}Pb}{^{235}U}$ Age(Ma)	2σ	$\frac{^{207}Pb}{^{206}U}$ Age(Ma)	2σ	Disc. (%)
z1	0.24	13.019	0.033	0.5167	0.0012	0.874	0.18273	0.00023	2685.2	5	2681	2.4	2677.8	2	-0.3
z2	0.58	12.947	0.065	0.5136	0.0013	0.783	0.18284	0.00063	2671.9	5.4	2675.8	4.8	2678.8	5.7	0.3
z3	0.39	12.913	0.035	0.5126	0.0012	0.917	0.1827	0.0002	2667.7	4.9	2673.3	2.6	2677.6	1.8	0.4

Appendix F

`stgeotk`: A `Python` package for strain analysis

After the simulation run the deformation gradient tensor $\boldsymbol{F}$ of each tracer particle will be exported to a `vtk` file. This $\boldsymbol{F}$ tensor incorporates all the information one needs to analyze the finite strain. However, in its matrix form a straightforward graphical visualization of $\boldsymbol{F}$ is almost impossible. `stgeotk` (structural geology toolkit)[1] is a lightweight library written in `Python` for reducing $\boldsymbol{F}$ so that it can be visualized in methods that are familiar to the geological community.

F.1 Reading data from export files

The algorithms in the `stgeotk` can be called from a post-processing program if it has a `Python` scripting environment which allows the user to access the `vtk` dataset. For example, in `Paraview`, this is achieved by applying `ProgrammableFilter` to the particle dataset. Note that the tensor data for each particle in `vtk` is flattened into a 1d array in a row-major (`C`-type) format. Therefore, a `numpy.reshape(dim, dim)` call with the default `order` argument will properly transform the flattened $\boldsymbol{F}$ into its `dim` $\times$ `dim` matrix representation. The `Python` implementation is outlined as follows:

Listing F.1: Obtain $\boldsymbol{F}$ on particle data

```
1  import numpy as np
```

[1] The source code is available at: https://github.com/mengtongwqh/stgeotk.git.

```
2
3   input_data = inputs[0].GetPointData()
4   F_tag = "deformation gradient"
5   npt = inputs[0].GetNumberOfPoints()
6
7   for ipt in range(0, npt):
8     F_tuple = input_data.GetArray(F_tag).GetTuple(ipt)
9     F = np.array(F_tuple).reshape(3, 3)
10    # user-defined data manipulation code on F
```

F.2 Finite deformation analysis implementations

As is discussed in Section 3.3, the deformation gradient tensor $\boldsymbol{F}$ contains enough information for us to predict a wealth of the local structural elements. All such predictions are in fact dependent upon obtaining the left stretch tensor $\boldsymbol{C} = \boldsymbol{F}\boldsymbol{F}^{\top}$ and its eigendecomposition to obtain the three principal stretching axes. Programmatically this is shown in the following code snippet:

Listing F.2: Strain ellipsoid kernel

```
1  import scipy.linalg as LA
2  import math
3
4  def strain_ellipsoid_kernel(F):
5
6      # The eigenvalues are in ascending order
7      FFt = F.dot(F.T)
8      eigval, eigvec = LA.eigh(FFt)
9
10     # Rescale the unit eigenvectors with
11     # their corresponding eigenvalues.
12     for i in range(0, 3):
13       eigvec[:, i] *= math.sqrt(eigval[i])
14
15     # Eigenvectors are returned as row vectors
16     # the row from top to bottom are
17     # foliation normal, intermediate axis and lineation
18     return eigvec.T
```

The maximum stretching and maximum compression axes are interpreted to be the lineation and the foliation normal (or pole to foliation). They can then be visualized

by stereographic projection discussed in Appendix F.3 or directly as vector data to show its spatial distribution.

It is also worth mentioning that in `Paraview` a straightforward visualization method is provided by `TensorGlyph` filter, which implements an ellipsoidal representation of symmetric tensors. This allows us to draw the strain ellipsoids directly onto the tracer particles. In this way the spatial distribution of strain type (flattening vs. constrictional, which respectively favours the formation of L-tectonite and S-tectonite) can be easily recognized. In order to visualize the strain ellipsoid, the `TensorGlyph` can be applied to the left-stretch tensor $\boldsymbol{V}$, where $\boldsymbol{F} = \boldsymbol{V}\boldsymbol{R}$ is the left polar decomposition of $\boldsymbol{F}$, or it can be applied to a 3×3 matrix whose columns consist of the eigenvectors (*i.e.* the results of the Listing F.2 need to be transposed).

Listing F.3: Eigenvectors of the strain ellipsoids within a given range

```
def strain_ellipsoid_range(F, range_begin, range_end):
    eigvecs = np.zeros((range_end-range_begin, 3, 3))
    counter = 0

    # Compute the eigenvectors for
    # the entries within the given range
    for i in range(range_begin, range_end):
        eigvecs[counter, :] = strain_ellipsoid_kernel(F[i, :])
        counter += 1
    return eigvecs
```

Due to the large number of data points that needs to be processed, the `Python concurrent` package is utilized to devise an embarrassingly parallel solution to the extraction of the principal axes of the strain ellipsoids. This is done by first defining a function to looping through only a partial range of all the given deformation gradient tensors ($\boldsymbol{F}$). Eigenvectors of each element in the range is are computed with Listing F.2. This function will be operated by different processes, each operating on different ranges for higher efficiency.

Listing F.4: Eigenvectors of all strain ellipsoids

```
import multiprocessing
import concurrent.futures

def strain_ellipsoid(F):
  # use multi-processing
  n_procs = multiprocessing.cpu_count()
  idx = (F.shape[0] + np.arange(0, n_procs))//n_procs
  idx = np.concatenate(([0], np.cumsum(idx)))
```

```
9
10  eigvecs = np.empty((0, 3, 3))
11
12  with concurrent.futures.ProcessPoolExecutor() as executor:
13    eigvecs_chunks = [ \
14      executor.submit(strain_ellipsoid_range, \
15      F, idx[iproc], idx[iproc+1]) \
16      for iproc in range(0, n_procs) \
17    ]
18
19  # retrieve the results in the future object
20  for chunk in eigvecs_chunks:
21      eigvecs = np.concatenate((eigvecs, chunk.result()), axis=0)
22
23  return eigvecs
```

The highest-level `strain_ellipsoid` function divides up the tasks by the number of available processes and handle them to each process with Listing F.3. Eventually, the results of all processes are merged into one array, in which each entry is a 3×3 matrix of eigenvectors. This is shown in Listing F.4.

F.3 Stereographic projection

By the structural geology convention 3d linear structural elements are visualized by casting them into data points on a 2d stereonet via lower-hemisphere stereographic projection. Let ϕ be plunge angle of a linear structural element and R be the radius of the 2d stereonet. Two commonly used stereographic projections are implemented in `stgeotk`: the equal-angle projection and the equal-area projection. Our implementation follows the algorithms discussed in Allmendinger et al. (2012).

The equal-angle projection, or the Wulff net, preserves the angular relationship between the line elements. On the 2d stereonet, the distance from the projected data point to the origin can be calculated by:

$$r = R \tan\left(45^\circ - \frac{\phi}{2}\right)$$

The major disadvantage of the equal-angle projection is that the area can be significantly distorted, which renders it unsuitable for density-based statistics and contouring. The equal-area projection, or the Schmidt net, is derived to overcome

this by ensuring the small circles with equal area will still occupy equal area on the stereonet after projection. This comes at the expense of sacrificing the angle-preserving property. The distance from the data point to the origin is:

$$r = \sqrt{2}R \sin\left(45^\circ - \frac{\phi}{2}\right)$$

Both projection methods are available as functions in the `stgeotk.stereonet` module. These functions take the trend azimuth θ and the plunge angle ϕ of a linear structural element as input arguments. The return values are the trend azimuth ($= \theta$ in this case) and distance to stereonet origin r. The (θ, r) pair can be subsequently graphed on a polar plot. This completes stereographic projection procedure.